

University of Southampton Research Repository ePrints Soton

Copyright © and Moral Rights for this thesis are retained by the author and/or other copyright owners. A copy can be downloaded for personal non-commercial research or study, without prior permission or charge. This thesis cannot be reproduced or quoted extensively from without first obtaining permission in writing from the copyright holder/s. The content must not be changed in any way or sold commercially in any format or medium without the formal permission of the copyright holders.

When referring to this work, full bibliographic details including the author, title, awarding institution and date of the thesis must be given e.g.

AUTHOR (year of submission) "Full thesis title", University of Southampton, name of the University School or Department, PhD Thesis, pagination

UNIVERSITY OF SOUTHAMPTON

FACULTY OF ENGINEERING AND THE ENVIRONMENT

**An Image-Based Computation of Microvascular
Dysfunction**

by

Berit Zeller-Plumhoff

A thesis submitted in partial fulfilment for the
degree of Doctor of Philosophy

January 2017

UNIVERSITY OF SOUTHAMPTON

ABSTRACT

FACULTY OF ENGINEERING AND THE ENVIRONMENT

Engineering Sciences

Doctor of Philosophy

AN IMAGE-BASED COMPUTATION OF MICROVASCULAR DYSFUNCTION

by Berit Zeller-Plumhoff

The supply of oxygen in sufficient quantity is vital for the correct functioning of all organs, in particular for skeletal muscle during exercise. Disease is often associated with a reduction of the microvascular oxygen supply capability and is thought to relate to changes in the structure of blood vessel networks.

Traditional methods of vascular perfusion or tissue staining for micro-computed tomography (μ CT), as well as phase contrast-based synchrotron radiation computed tomography (SR CT) were used to image the microvasculature of the mouse soleus. These techniques were applied to an animal model of developmental conditioning to investigate the influence of maternal fat intake on the structure and oxygen exchange capability of the microvasculature in the adult offspring. Dams and their offspring were assigned either a standard chow diet (C) or a high-fat diet (HF), resulting in four groups: HFHF, HFC, CHF, CC. Tissue staining and vascular perfusion techniques were found insufficient for imaging capillaries. SR CT imaging enabled the visualization of red blood cells (RBCs) which allowed the determination quantitative measures of capillarization. An image-based model of muscle tissue oxygenation was further created.

Quantitative measures in the CC group showed good agreement with values obtained by gold standard histology. RBC spacing was the only measure significantly different for the dietary groups ($p < 0.05$). By assessing the relationship between tissue oxygenation and the structural parameters, it was found that volume fraction ($R^2 = 0.63$) and RBC spacing ($R^2 = 0.52$) were the best predictors for muscle tissue oxygenation, followed by length density ($R^2 = 0.40$). Fractal dimension ($R^2 = 0.28$) and the 2D measures of capillary density ($R^2 = 0.30$) and capillary-to-fibre ratio ($R^2 = 0.26$) ranked last. SR CT further enabled the visualisation of fat, nerves and muscle spindles in the muscle. The mean muscle volume in the CC group was determined as $5.21 \pm 0.40 \text{ mm}^3$. The number of muscle fibres per SR CT cross-section in the medial region of the muscle was 1013 ± 45 . In the CC group an average of 11.8 ± 0.7 muscle spindles per muscle was found with a mean of 3.7 ± 0.1 intrafusal fibres per muscle spindle. The mean spacing between muscle spindles and the muscle boundary was $0.28 \pm 0.15 \mu\text{m}$. No effect of offspring or maternal diet on spindle numbers was observed. Offspring high-fat diet lead to a significant increase in intramuscular adipose tissue ($p < 0.05$) and muscle volume ($p < 0.0001$).

Contents

Declaration of Authorship	xxi
Acknowledgements	xxiii
1 Introduction	1
1.1 Image-based modelling of skeletal muscle oxygenation	3
1.1.1 Aims of this thesis	6
1.1.2 Thesis structure	6
2 Clinical and biological background	9
2.1 Anatomy of skeletal muscle	9
2.1.1 The microvasculature in skeletal muscle	10
2.1.2 Nervous tissue in skeletal muscle	12
2.1.2.1 Muscle spindles	14
2.2 Biology of oxygen uptake in skeletal muscle	15
2.3 Association of cardio-metabolic disease and microvascular structure . .	18
2.3.1 Animal models of developmental priming	20
2.3.2 Human models	23
2.4 Assessment of microvascular oxygen exchange capability	26
2.4.1 Capillary density	26
2.4.2 Capillary-to-fibre ratio	26
2.4.3 Tortuosity in Skeletal Muscle	27
2.4.4 Length Density	28
2.4.5 Volume Fraction	29
2.4.6 Fractal Analysis	29
2.4.7 Other measures	30
2.5 Summary	31
3 Literature review on soft tissue imaging	35
3.1 Overview of imaging methods	35
3.1.1 Methods for <i>ex vivo</i> imaging of murine skeletal muscle	36
3.1.1.1 Light sheet fluorescent microscopy	38
3.2 The principles of computed tomography	39
3.2.1 X-ray generation	39
3.2.1.1 X-ray generation in lab-based computed tomography .	39
3.2.1.2 X-ray generation in synchrotron radiation computed to- mography	39
3.2.2 Data acquisition	42

3.2.3	Image reconstruction	45
3.2.3.1	Filtered backprojection	45
3.2.3.2	<i>gridrec</i> algorithm	47
3.2.4	Imaging Artefacts	48
3.3	Sample preparation methods	48
3.3.1	Applications of μ CT	50
3.3.2	μ CT imaging modes	50
3.3.3	Phase contrast-based micro-computed tomography	51
3.3.3.1	Free space propagation	53
3.3.3.2	Grating interferometry	54
3.3.3.3	Diffraction enhanced imaging	56
3.3.4	Phase retrieval algorithms	57
3.3.4.1	(Modified) Bronnikov algorithm	58
3.3.4.2	Paganin algorithm	59
3.3.4.3	Reconstruction post Paganin phase retrieval	59
3.3.4.4	Other algorithms	60
3.3.5	μ CT for <i>in vivo</i> imaging	60
4	Methodology for micro-computed tomography of the microvasculature in skeletal muscle	63
4.1	Animal model of developmental priming	63
4.2	Sample preparation	64
4.2.1	Contrast by perfusion method	64
4.2.2	Contrast by staining method	64
4.2.3	Propagation-based phase contrast	67
4.3	Imaging of samples	67
4.3.1	Imaging of the Microfil-perfused samples	67
4.3.2	Imaging of the PTA-stained sample	69
4.3.3	Phase contrast-based imaging at the Swiss Light Source	69
4.3.3.1	Choice of propagation distance	70
4.3.3.2	Phase retrieval	73
4.3.3.3	Limitation by scintillator setup	75
4.4	Image segmentation	76
4.4.1	Data stitching	76
4.4.2	Microfil samples	77
4.4.3	PTA samples	79
4.4.4	Unperfused samples	79
4.5	Feature quantification	80
4.5.1	Identification of capillaries	80
4.5.2	Volumes and volume fraction	82
4.5.3	Tortuosity	82
4.5.4	Length density	82
4.5.5	Capillary density	82
4.5.6	Capillary-to-fibre ratio	83
4.5.7	Fractal dimension	83
4.5.8	Mean distance to next red blood cell (RBC spacing)	83
4.6	Statistical analysis	83

4.7	Summary	84
5	Results of micro-computed tomography of the microvasculature in skeletal muscle	85
5.1	Microfil-perfused samples	85
5.2	PTA-stained samples	89
5.3	Phase contrast-based imaging	90
5.4	3D visualisation of other intramuscular structures using phase contrast-based SR CT	91
5.4.1	Muscle spindles	91
5.4.2	Fat volume	96
5.5	Discussion	97
5.6	Summary	104
6	Validation of phase contrast-based SR CT imaging	105
6.1	Methods	105
6.1.1	Image correlation between SR CT and histology slices	106
6.1.2	Segmentation of nerves and analysis	108
6.1.3	Segmentation of red blood cells and analysis	109
6.2	Results	110
6.2.1	Nerves	110
6.2.2	Red blood cells	110
6.2.3	Structural Parameters from Histology	112
6.3	Discussion and conclusion	112
6.4	Summary	114
7	Mathematical modelling of oxygen uptake in mouse skeletal muscle	115
7.1	Literature review of image-based mathematical models	116
7.1.1	Image-based modelling	117
7.1.1.1	Limitation 1: Role of the haematocrit	121
7.1.1.2	Limitation 2: Validation of results	122
7.2	Mathematical description of oxygen exchange in skeletal muscle	123
7.2.1	Modelling oxygen diffusion	123
7.2.2	Oxygen tissue metabolism	123
7.2.3	Boundary and initial conditions	124
7.2.4	Extensions of the simple diffusion model	124
7.2.4.1	Myoglobin facilitated oxygen transport	125
7.2.4.2	Arteriolar oxygen supply	126
7.2.5	Modelling of blood flow	126
7.3	Implementation of image-based modelling of muscle tissue oxygenation	127
7.3.1	Mesh Generation and Solver Choice	127
7.3.2	Model Description and Solver Settings	130
7.3.2.1	Microfil datasets in COMSOL Multiphysics	131
7.3.2.2	Unstained dataset in OpenFOAM	132
7.4	Results	134
7.4.1	Results for Microfil sample oxygenation	134
7.4.2	Results for unperfused sample oxygenation	135
7.4.2.1	Structural parameter - oxygenation relationship	135

7.5	Discussion	136
7.6	Summary	137
8	Conclusions and future work	143
8.1	Future work	146
A	Imaging methods	149
A.1	Light based methods	149
A.1.1	Light microscopy	149
A.1.2	Confocal laser scanning microscopy	150
A.1.3	Photon laser scanning microscopy	150
A.1.4	Optical coherence tomography/optical microangiography	150
A.1.5	Laser speckle contrast imaging	150
A.1.6	Laser doppler flowmetry	151
A.2	Electron based methods	151
A.2.1	Scanning electron microscopy	151
A.2.2	Transmission electron microscopy	152
A.3	X-ray based methods	152
A.3.1	Micro-computed tomography	152
A.4	Magnetic pulse based methods	153
A.4.1	Micro-magnetic resonance imaging	153
A.5	Positron based methods	153
A.5.1	Positron emission tomography	153
A.6	Acoustic waves based methods	153
A.6.1	Photoacoustic tomography	153
B	Histology protocols	155
B.1	H&E stain	155
B.2	Avidin biotin-peroxidase technique for paraffin sections	156
B.3	Microwave pretreatment	157
B.4	Martius yellow scarlet blue (MSB) trichrome	157
C	Testing the Influence of Tortuosity	159
C.1	Hypothesis	159
C.2	Model	160
C.2.1	Results	160
C.2.2	Discussion	162
D	Phase contrast imaging using the Zeiss Versa 510	167
D.1	Repeated experiments as by Bidola <i>et al.</i> [2015]	170

List of Figures

1.1	Trajectory of the risk of chronic non-communicable disease [Gluckman <i>et al.</i> , 2009]. The risk for chronic non-communicable disease, including cardio-metabolic disease, increases during lifetime. The higher the age, the steeper the risk curve becomes. Intervention in early life may significantly change the trajectory of the curve and lead to an improved risk over lifetime.	2
1.2	Challenges and requirements in image-based modelling of biological processes. The example shown applies namely for the oxygenation in skeletal muscle.	5
1.3	Generic workflow for image-based modelling. Images are acquired by a specific imaging technique. From the resulting images, blood vessels and muscle tissue can be segmented from the background material (here air). The blood vessels can now be analysed for their 3D structure by quantitative morphometry. At the same time, the segmented tissues can be meshed for finite element modelling. The mesh is then imported into a partial differential equation (PDE) solver, which will solve equations describing the biological process at hand. Given the results of the quantitative morphometry and the solved mathematical model, an association between 3D vascular structure and function can be derived, for instance in terms of fluid flow or tissue oxygenation. Microscope clipart from ClipartPanda.com.	8
2.1	Transmission electron micrograph of mouse soleus muscle taken at 15000X magnification. The Z-disks (a) are visible, as well as the thin actin filaments (b) and the region of overlapping thick and thin filaments (c). Mitochondria are also visible (d). This image was taken during a training course on transmission electron microscopy at the Biomedical Imaging Unit (BIU) at Southampton General Hospital (SGH).	10
2.2	Location of murine soleus muscle. The soleus muscle is a muscle located below the gastrocnemius in the calf of an animal. Image taken and adapted from [Faulkes, 2016].	11
2.3	Schematic of the microvasculature, taken from Levick [2003]. The vessels denoted by the term microvasculature are the arterioles, capillaries and venules, which have a diameter of 5 – 150 μ m.	11
2.4	Schematic of the vascular wall. The vascular wall consists of connective tissue and smooth muscle cells which are separated from the endothelium by a basal lamina. Not to scale. This image is courtesy of L. Cooper. . . .	12

2.5	Transmission electron micrograph of a capillary in mouse soleus muscle at 9000X magnification. The capillary wall consists only of endothelium (a) and basal lamina (b). Vesicles are visible inside the endothelial cells (c). A red blood cell can be seen inside the capillary (d). This image was taken during a training course on transmission electron microscopy at the BIU at SGH.	13
2.6	Light micrographs of histological slices of mouse soleus muscle in transversal section, courtesy of Katy Gould. The muscle fibres are aligned parallel to each other, see subfigure 2.6(a). The capillaries between them are aligned in the same way, on average there are around 1.2-1.3 capillaries per muscle fibre. A fluorescent marker was used to visualise these (subfigure 2.6(b)).	14
2.7	Light micrograph of a muscle spindle. ICA and ECA mark internal and external capsule, respectively. Three intrafusal muscle fibres are visible within the ICA. The ECA can be significantly larger than the ICA, as can be seen in the image. Taken from Diaz-Flores <i>et al.</i> [2013]	15
2.8	Schematic of a muscle spindle. The muscle spindle consists of an external capsule (eca) that surrounds the intrafusal fibres, which can be distinguished as chain (c) and bag fibres (b). The sensory innervation (n) of the intrafusal fibres lies in the middle the fibre.	16
2.9	Schematic of oxygen delivery in muscle tissue through diffusion. Up to four oxygen molecules can be bound by one of the haemoglobin molecules present in the red blood cells (1). The partial pressure of oxygen is very high in the blood vessels, but low in the surrounding tissue. Therefore, the oxygen is released by the haemoglobin and diffuses along the gradient towards the surrounding tissue. It permeates the capillary wall (4), which consists only of the endothelium and its basement membrane. The released oxygen travels towards the mitochondria in the muscle tissue by which it will be consumed for adenosine triphosphate (ATP) generation (2). The protein myoglobin, which stores up to one oxygen molecule and releases this if the oxygen demand is very high (3), is also present in muscle tissue. Schematic is not to scale. Source code for mitochondria adapted from [Medina, 2015].	17
2.10	Maternal high fat mouse model of developmental priming of the microvasculature. Dams are fed either a normal chow diet (C) or a high-fat diet (HF) for 9 weeks prior to mating, during pregnancy and lactation. Their respective offspring is then again divided into two groups that are being fed the respective diets. Thus, the offspring can be divided into four groups: CC, CHF, HFC and HFHF. This schematic is courtesy of Moji Musa.	21
2.11	Phenotype of offspring groups of the animal model of developmental priming at 15 weeks of age. Animals of the HFHF group show a significantly worsened phenotype in body weight, fat percentage and blood pressure. Similarly, the CHF group shows elevated bodyweight, diastolic pressure, fat percentage and elevated glucose levels. Data published in Stead <i>et al.</i> [2016].	22
2.12	Oxidative stress in offspring groups of the animal model of developmental priming at 15 weeks of age. A high-fat diet (both maternal and post weaning) leads to an increase of muscle oxidative stress. Data published in Torrens <i>et al.</i> [2012].	23

2.13	Dependence of tortuosity on sarcomere length. Taken without permission from Mathieu-Costello <i>et al.</i> [1989].	28
3.1	Comparison of different imaging techniques with regard to maximum spatial resolution and tissue penetration depth. The dashed red line marks $1\ \mu\text{m}$, which is the spatial resolution required to resolve the capillaries. The dotted blue line indicates the minimal tissue penetration required, based on murine muscle dimensions of $\sim 0.2 \times 0.2 \times 0.8\text{ cm}^3$. The top left quadrant covers high-resolution 3D imaging techniques that are appropriate to assess the (muscle) microvasculature and includes micro-computed tomography (μCT), synchrotron-based CT (SR CT) and light sheet fluorescence microscopy (LSFM).	36
3.2	Sketch of the cross-section of a microfocus X-ray tube from [Xra, 2016]. A filament, the cathode, is used to generate an electron beam which travels towards the anode, the so-called target. Focus coils are used to focus the electrons to achieve as small a focal spot on the target as possible. As the electron beam hits the target, X-rays are emitted as a cone beam.	40
3.3	Exemplary X-ray spectrum of a (microfocus) X-ray tube. The X-ray spectrum emitted by the target is continuous, consisting of Bremsstrahlung and characteristic X-rays. Bremsstrahlung results from the slowing down of the electrons by the target material's nuclei. The characteristic X-rays are peaks which result from electrons in the K-M shells of the target material being ejected by the high-speed electrons and they are characteristic for each target material. Taken from chapter 2 in Hsieh [2015].	40
3.4	Sketch of an undulator array. A periodic array of magnets generates a sinusoidal oscillation of the electron beam which leads to emission of X-rays. The setup of a wiggler looks much the same in general, with longer period lengths of the dipole arrangements. This results in the angles of the emitted radiation to be much larger for the wiggler devices. The shorter period lengths in the undulator result in the X-rays being created due to relativistic effects with significantly higher brilliance than in the wiggler, where the X-rays are created by the deflection of the X-ray beam only. Image taken from [Elektronensynchrotron, 2016]	41
3.5	Setup of a synchrotron [dia, 2013]: An electron beam is created by an electron gun and accelerated in the linear accelerator (1). Here it reaches an energy of hundreds MeV. It is then further accelerated to several GeV inside the booster synchrotron (2). In the storage ring (3) it is kept at this energy. Emitted radiation reaches the experimental hutch (4), where the sample is staged and controlled via the control cabin (5).	42
3.6	Schematic of a typical modern μCT scanner. An electron beam generated by a filament at the top of the electron gun (1a) hits a metal target (1b), e.g. tungsten or molybdenum, thereby creating X-rays. The X-rays are emitted in the form of a cone beam and hit a sample located behind the source (2). When passing through the sample, the X-rays lose intensity, due to different interaction processes with the sample material. The beam then hits a scintillator (3) which emits visible light (4) that can be detected by a charge-coupled device camera (5). The sample stage can rotate, so that projections of the sample for at least 180° can be recorded.	43

3.7	X-ray energy-attenuation curves for exemplary materials. Depending on the material the attenuation coefficient μ will be overall higher or lower, i.e., iodine attenuates X-rays the strongest, followed by bone which contains as a main component calcium and finally water and soft tissue. It holds that the higher the X-ray energy, the lower the X-ray attenuation and generally the worse the contrast. Iodine is an exception with the step change at around 33 keV arising from the characteristic K-edge of iodine, i.e., the binding energy of K-shell electrons [Hsieh, 2015]. Taken from Chapter 2 in Hsieh [2015].	44
3.8	Original and rotated coordinate system in an imaging system. z is the direction of propagation of the X-rays, (x, y) is the tuple describing the perpendicular imaging plane to z , with x being the horizontal coordinate and y the vertical coordinate in an actual imaging setup. The rotated axis x around an angle θ is described as t . Adapted from Hsieh [2015], chapter 3.	46
3.9	δ (solid line) and β (dashed line) of the refractive index for iodine (blue), calcium (black) and water (red). δ and β curves are given in 3.9(a) and their ratio in 3.9(b). They depend on the material density and its interaction with X-rays. Values obtained from hen [2016], Henke <i>et al.</i> [1993].	52
3.10	Principles of Fresnel fringes through X-ray interference. Taken from [Lundstrom <i>et al.</i> , 2012]. The X-rays hitting the interfaces between different materials within the sample are refracted and if being allowed to propagate for a longer distance behind the sample they will interfere. This results in dark and light fringes around the material interfaces. . . .	53
3.11	Principle of grating interferometry. By use of two gratings, G_1 and G_2 , which are placed between sample and detector, the first two diffraction orders of the refracted X-rays are extracted (G_1) and interference patterns are transformed into intensity variations (G_2). Taken from [Weitkamp <i>et al.</i> , 2005].	55
3.12	Principle of diffraction enhanced imaging. An analyser crystal is inserted between sample and detector to convert the X-ray diffraction into intensity changes in the projections. Taken without permission from Connor & Zhong [2014].	56
4.1	Microfil-perfused vessels. In order to enhance imaging contrast, the vascular network is perfused with the radio-opaque silicone rubber Microfil®MV122 (Flow Tech Inc., US), which has a yellow colour. When the perfusion is complete, both arteries and veins can be clearly seen in yellow.	66
4.2	Sample mounting for μCT and SR CT imaging. For imaging, the wax block containing the muscle was trimmed and glued onto a SEM stub. The mounting of the muscle was such that the longitudinal direction of the muscle was perpendicular to the X-ray path.	66
4.3	Zeiss/Versa 510 scan of CC mouse soleus perfused with Microfil. Imaging was performed on the 4X lense at 80kV/7W, at 1.4 μ m pixel size, detector bin 2. Exposure time was between 2 and 3.5 seconds and a minimum of 2001 projections was used. Microfil appears bright in the reconstructed image. The muscle tissue (m) is visible against the surrounding wax (w). The Microfil appears to have shrunk in a number of blood vessels (*). . .	68

4.4	Zeiss/Versa 510 scan of CC mouse soleus stained with PTA. Imaging was performed on the 20X lense at 100kV/9W, at 0.8 μm pixel size, detector bin 2. Exposure time was 3 seconds and 2001 projections were obtained. All muscle fibres (m) and vessel walls (*) have been stained with PTA. The contrast to the surrounding wax (w) is high, however, small blood vessels can not be immediately differentiated.	69
4.5	Slices for each distance at the propagation distance trial at the TOM-CAT beamline. Four sample-to-detector distances were tested for their resulting image contrast and red blood cell visualisation. The marked quadratic region in 4.5(d) show the region in which S_2 for the contrast-to-noise ratio (Equation (4.4)) was determined. The line profile used for comparison of edge-enhancement in Figure 4.6 is also marked. S_1 and σ_1 for CNR and signal-to-noise ratio (Equation (4.3)) were determined in the wax in the a quadratic region of the same size as for S_2 (in the blackened region).	71
4.6	Intensity profile for phase comparison for different sample-to-detector distances for the propagation distance trial at TOMCAT. There is a large increase in fringe intensity between 30 and 40 mm distance, however, higher sample-to-detector distances show less differences.	73
4.7	Slice of the sample at 60mm sample-to-detector distance. The edge-enhancement enables the visualisation of the RBCs (white dots) within the capillaries visible (*), as well as muscle spindles (s), nerves (n), the individual muscle fibres (m) and fascia (f).	74
4.8	Comparison of edge enhacement and phase retrieval for red blood cell imaging using phase contrast-based synchrotron radiation computed tomography. a) shows a slice of the direct reconstruction, while b) shows a slice of the Paganin phase-retrieved and then reconstructed data. The white dots in-between muscle fibres are red blood cells. Empty capillaries (black circular spaces in-between muscle fibres) and larger blood vessels (*) can also clearly be distinguished, as well as intramuscular structures such as muscle spindles (<). Scale bars are 50 μm	75
4.9	Skew of the scintillator focus. The scintillator installed in front of the CCD camera at the SLS was skewed vertically, thus resulting in a skew of the focus settings along its height. This resulted in a loss of sharpness over the length of an image stack.	76
4.10	Difference in sharpness at beginning and end of image stacks. 4.10(a) is taken at the end of one dataset and 4.10(b) is from the overlapping region at the beginning of the following image stack. The skew of the scintillator clearly resulted in a significant loss of sharpness which was circumvented by increasing the overlapping region and setting the focus in the middle region of the scintillator. The scale bars represent 50 μm	77
4.11	Slice of binary image stack. The binary image stack was obtained after region growing segmentation a Microfil-perfused muscle. The image stack is used for feature quantification.	78
4.12	Thickness map created by BoneJ plugin thickness 4.12(a) on a segmented blood vessel network. The colours correspond to the different thicknesses, see the legend 4.12(b). The mapped dataset allows thresholding for capillaries by greyscale thresholding.	81

5.1	3D renderings of blood vessel networks of all samples perfused with Microfil. The quality of the different networks is visible, i.e. ideally the blood vessels are continuous with as few breaks as possible. The capillary tree should be a dense network.	86
5.2	Morphological parameters of the capillary network of the Microfil-perfused muscles. The means (\pm standard deviation) of the structural parameters capillary density, tortuosity, fractal dimension, length density and volume fraction have been determined for the four dietary groups. N=3 for CC and CHF and n=2 for HFC and HFHF.	87
5.3	Means of morphological parameters of the capillary network (red circle) compared to the whole microvascular network (black square) of the Microfil-perfused muscles. The means of the structural parameters capillary density, tortuosity, fractal dimension, length density and volume fraction have been determined for the four dietary groups. N=3 for CC and CHF and n=2 for HFC and HFHF.	88
5.4	3D rendering of segmented blood vessels in PTA sample. Larger blood vessels were visible but only few blood vessels smaller than 10 μm in diameter could be segmented.	89
5.5	Zoom-in on medial region of unperfused sample imaged using propagation-based phase contrast SR CT. Larger blood vessels (*) are seen entering the muscle and dividing into smaller vessels, before giving way to the dense capillary network.	90
5.6	Means of structural measures per dietary group based on table 5.1 for unperfused samples imaged using phase contrast-based SR CT. * statistical significance ($p < 0.05$).	93
5.7	Comparison of corresponding histological (left) and SR CT (right) images of muscle spindles in transversal sections of mouse soleus muscle in control group. Nerves in (a,c) were stained with PGP9.5 antibody (see Chapter 6) and are visualised in brown by DAB chromagen. The characteristic structure of both nerve tissue (<) and muscle spindles (*) is visible in the SR CT images. The external capsule (eca) and intrafusal fibres (if) can be distinguished. Scale bars in (a,b) and (c,d) are 50 μm and 30 μm , respectively.	95
5.8	3D volume rendering of a muscle spindle. The different intrafusal fibres (if) (red, blue, green) and the external capsule (eca, yellow) have been segmented as well as the lumen of small arteriole (a) running along the spindle (turquoise) and one of the supplying nerves (n, orange). The representation of the muscle spindle has been derived from SR CT data, assessed at a voxel size of 0.77 μm	96
5.9	3D volume rendering of muscle spindles and the neurovascular bundle in control muscle. Spindles (eca) are displayed in yellow, nerves (n) in red and lumen of the larger blood vessels (v) in blue. The representation of the muscle spindles and the neurovascular bundle has been derived from SR CT data (displayed as one slice), assessed at a voxel size of 0.77 μm	97

5.10	3D volume rendering of muscle spindles in whole muscles of each study group. The muscle tissue is visualised in red and muscler spindles in yellow. (a) is a control muscle with 12 spindles, muscles in (b)-(d) contain 11 spindles and are from CHF, HFC and HFHF groups, respectively. The spindle distribution varies between different study groups. The scale bar is 3mm.	98
5.11	Cross-sectional area fraction of muscle spindles in muscle tissue per CT slice. The spindle area fraction of all CC muscles is given as baseline (with standard deviation).	98
5.12	Intramuscular adipose tissue. Adipose tissue (red arrow) can be clearly distinguished from the rest of the muscle tissue and thus segmented. The scale bar represents 50 μ m.	99
5.13	Fat segmentation in HFHF muscle. The fat volume (orange) was segmented in a HFHF using Avizo Fire 9.0 and displayed within the muscle volume (white) as a volume rendering. The representation of the neuro-muscular spindle has been derived from SR CT data, assessed at a voxel size of 0.77 μ m. The scale bar represents 4mm.	100
5.14	Mean fat volume per dietary group (n=3). Offspring high-fat diet was the determining factor for fat volume ($p < 0.05$), and the additive effect of combined maternal and offspring diet is visible. * statistical significance ($p < 0.05$).	101
6.1	Schematic for order of staining of serial sections. Sections were stained such that subsequent sections were stained with different stains and each stain was repeated for three sections of the same muscle. Staining for Martius Yellow Scarlet Blue (MSB) was applied later for subsequently microtomed sections.	106
6.2	Workflow for comparison of nerve identification in SR CT and histology images. Nerves in SR CT images (bottom row) were immediately segmented whilst histology images (top row) were first split into different colour channels to isolate the brown channel associated with the DAB chromagen. Based on these images the nerves were then segmented. The area of the nerves was computed for both segmented images and compared.	108
6.3	Correlated SR CT and histology images (stained with CD31) for RBC validation. SR CT and histology images were visually correlated. To account for the thickness of the histological sections, a maximum intensity projection over 7 SR CT slices was performed. SR CT images were bandpass filtered to highlight red blood cells. Blind counting of red blood cells was then performed on both by two independent observers.	109
6.4	Comparison of identified and measured nerve area in corresponding μCT and histology images. After segmentation the nerve area was measured in the corresponding images of the two imaging techniques, see figure 6.2. A linear regression line was fitted using Origin 8.1.	110
6.5	Comparison of red blood cell counts identified in SR CT and histology images. Red blood cells were counted blindly in histological slices stained with MSB and CD31 and compared to SR CT images. Two independent observers counted RBCs in the CD31 images. Linear regression lines were fitted to the counts.	111

6.6	2D structural parameters (capillary density and capillary-to-fibre ratio) determined from histological images. Comparison between the parameters determined by counting capillaries only versus red blood cells. The histology slides were stained using CD31 and images using a Zeiss Axio-scope 100X lens. The dependence of RBC:F and C:F (subfigure 6.6(b)) on offspring dietary group was found to be statistically significant ($p < 0.01$ and $p < 0.05$, respectively).	113
7.1	Voronoi tessellations vs. trapping regions to mark regions of oxygenation. Voronoi polygons are marked black and streamlines in red flowing from capillaries. The trapping regions are defined as the limits of the streamlines. It can be seen that Voronoi polygons and trapping regions match well. Inspired by Al-Shammari <i>et al.</i> [2014].	118
7.2	Myoglobin and haemoglobin O₂ saturation curves. Hb is more likely to release oxygen than myoglobin, as indicated by the Hb curve lying below the Mb curve. The numbers given are for rat blood. Figure taken from Goldman [2008].	125
7.3	Image for ScanIP. After image processing, an image stack with three grey scale values was obtained, for background, tissue and vessels. Using the ScanIP software, these can be masked by simple thresholding and the repective masks of interest will be meshed with coinciding nodes of the different materials.	128
7.4	Preview of ScanIP meshing for the 3D volume.	129
7.5	Solution of equation (7.15) with BCs (7.9) and (7.10) at $t = 5s$ for the finest and coarsest mesh settings. Different mesh coarsenesses of ScanIP's Free Mesh module where compared to test the Comsol model for convergence. Figure 7.6 shows the corresponding convergence graph. Note that the equation was solved for glucose, not oxygen.	133
7.6	FEM convergence plot The graph suggests a trend of convergence for finer meshes (read graph from right to left). Wishing for an accuracy of < 0.01 , it is necessary to create meshes with ScanIP using a coarseness of at least -20.	134
7.7	Oxygen diffusion in whole tissue at $t = 1s$. The vessels were perfused with Microfil and the model solved using Comsol for $M(C) = 0$. Within 1 s the whole muscle tissue should be perfused, which is not the case for the present muscle due too the low perfusion.	135
7.8	Tissue oxygenation with Michaelis-Menten consumption for exemplary muscle of the CC and CHF group. The oxygen diffuses from the red blood cells, where it is at its highest concentration, to the tissue where it is consumed.	139
7.9	Tissue oxygenation with Michaelis-Menten consumption for exemplary muscle of the HFC and HFHF group. The oxygen diffuses from the red blood cells, where it is at its highest concentration, to the tissue where it is consumed.	140
7.10	Mean tissue oxygen concentration for non-linear Michaelis-Menten kinetics (red) and constant consumption (blue). The means (\pm standard deviation) are given for all groups. $N=5$ for CC and $n=3$ or $n=2$ for CHF, HFC and HFHF groups for constant or non-linear consumption, respectively. Due to non-physiological negative concentrations the variability is significantly larger in the case of constant consumption.	141

7.11	Tissue oxygen concentration dependence on structural measures for all muscles. The mean tissue oxygenation based on Michaelis-Menten kinetics has been plotted against the computed structural parameters. A linear regression line was fitted for each plot and the quality of the fit was determined as R^2 . The best fits exist for the measures of volume fraction and mean distance whilst capillary density, fractal dimension and capillary-to-fibre ratios are poor predictors of tissue oxygenation. . .	142
8.1	Implemented workflow of image-based modelling including times and requirements for each step.	144
C.1	Three-dimensional model geometry of the tortuous blood vessel in a hexagonal tissue segment, for $a = 3, c = 4$.	161
C.2	3D results for $t = 0$ and $t = 2$ for $c = 4$.	163
C.3	2D results for $t = 0$ and $t = 2$ for $c = 4$.	164
C.4	Model evaluation for $c = 1$ and $c = 4$. With increasing a and increasing c the difference between 3D and 2D case increases before both reach the steady state solution.	165
D.1	Slice of reconstructed volume of first phase contrast test using the Versa 510 system. The tissue contrast is very low. The only feature discernible is a muscle spindle. The scale bar represents $100 \mu\text{m}$	168
D.2	Slices of distance trial on the Xradia Versa 510 system. The phase-contrast visually increases with the further distance. However, some streak artifacts are visible in D.2(b) and D.2(c). This is probably due to photon starvation. Scale bars are $100 \mu\text{m}$	169
D.3	Intensity profile for comparison of edge-enhancement for different sample-to-detector distances. Clearly, the intensity of the edge-enhancement increases with propagation distance.	170
D.4	CNR of radiographs of teflon sheet as in experiment II in [Bidola <i>et al.</i>, 2015]. Whilst the CNR decreases starkly at constant exposure time for increasing source-to-sample and sample-to-detector distances it remains high if the exposure time is adjusted for the changing distances. This image was taken from the IP report submitted by Marie Wallis.	171
D.5	Comparison of correlated slices of phase contrast-based tomography obtained at the synchrotron (D.5(a)) and for different propagation distances on the Versa 510 system. Propagation distances were increasing from RI (D.5(b)) to RII (D.5(c)) and RIII (D.5(e)) as in Bidola <i>et al.</i> [2015], see table D.3. Subfigures D.5(d)) and D.5(f) are for distances RII and RIII, respectively, with adjusted exposure time. Scale bars represent $50 \mu\text{m}$. . .	172
D.6	Zoom onto nerve and muscle spindle in correlated slices in figure D.5 from SLS and Versa 510 systems. Soft tissue contrast is high in the SLS image, however, in the images obtained on the Versa 510 system it is only possible to differentiate muscle tissue, nerves and muscle spindles at distance RIII with adjusted exposure time (RIII_{adj}).	173

List of Tables

2.1	Structural parameters used for assessing the microvasculature. Capillary density, capillary-to-fibre ratio, tortuosity, length density and volume fraction are parameters often used to describe the structure of blood vessel.	33
3.1	Comparison of imaging techniques. Imaging techniques are compared in terms of excitation signals, spatial resolution, penetration depth, preparation for image contrast, image acquisition times, imaging dimensions and <i>in vivo</i> imaging capability. For references and discussion see appendix A.	37
4.1	Summary of all samples prepared. Sample names are given, as well as contrasting methods, imaging systems used and whether or not the sample was analysed and used for mathematical modelling. The samples chosen for validation of the phase contrast imaging are also marked.	65
4.2	Fresnel number, wax and tissue signals, noise and SNR and CNR for the SLS distance trial. Computed according to equations (4.3) and (4.4). The noise is given as percentage of number of greyscale values in the 16-bit range (65536). For all distances, as The highest values for SNR and CNR are apparent at a sample-to-detector distance of 60 mm.	72
5.1	Detailed results of microvascular structural parameter analysis for unperfused samples. Structural parameters have been computed based on the visualisation of red blood cells in the soleus muscle of mice of the animal model of developmental priming. * statistical significance ($p < 0.05$).	92
5.2	Quantitative morphometry of muscle and muscle spindles for the four dietary groups CC, CHF, HFC and HFHF. a significant difference compared to CC group ($p < 0.05$), b significant difference compared to CHF group ($p_D < 0.05$), c significant difference compared to HFC group ($p_B < 0.05$), + ($p < 0.05$), x significant difference between C and HF offspring ($p < 0.01$). Values are given as mean \pm standard deviation.	94
5.3	Segmented fat volume for the four dietary groups CC, CHF, HFC and HFHF (n=3). The fat volume was segmented for three muscles of each dietary group and the volume fraction with respect to overall muscle volume computed. Fat volume was found to be dependent on dietary group ($p < 0.05$), with means of CC and HFHF groups being significantly different for both fat volume and fat volume fraction ($p_D < 0.05$).	101

5.4	Comparison of methods for inducing soft tissue contrast for μCT imaging of the microvasculature in skeletal muscle. The structural parameters of the microcirculation for the control groups (CC) obtained from perfusion, staining and phase contrast methods are compared and the advantages and disadvantages of the methods summarised. The structural parameters are given for the whole vessel network for the PTA-stained sample due to the small number of capillaries present.	102
6.1	Histological staining. Five different staining techniques were chosen to display RBCs, blood vessels, nerves and muscle fibres.	107
6.2	Detailed results of 2D microvascular structural parameter analysis for unperfused samples. Structural parameters have been determined based on the visualisation of red blood cells and the microvascular endothelium using CD31 stained light micrographs in the soleus muscle of mice of the animal model of developmental priming.	112
7.1	Model parameters as described by Al-Shammari <i>et al.</i> [2012, 2014]. The parameters are given in terms of tissue PO_2 and are converted into oxygen concentration C for model implementation. The conversion parameter is $0,0016 \text{ [mol/(mmHg m}^3\text{)]}$	130
7.2	Results for mean tissue oxygen concentration and partial pressure for unperfused samples for constant consumption and Michaelis-Menten kinetics. The mathematical model was created based on the phase contrast-based SR CT images of red blood cells in the soleus muscle of mice of the animal model of developmental priming. The model was solved in OpenFOAM.	136
8.1	Tabulation of all processes in the workflow and limitations that may have arisen with ways of circumvention. The workflow from sample preparation over imaging and validation is error prone, but it was applied in a consistent manner. Therefore, the relationships determined for structural parameters and tissue oxygenation are valid.	145
C.1	Geometric parameters used in the modelling of the influence of tortuosity on tissue oxygenation. A cylindric capillary is created within a hexagonal tissue segment. Tortuosity in the vessel is induced in the form of sinusoidal oscillations.	161
D.1	Scan settings for Versa 510 distance trial. The corresponding Synchrotron distances were computed using Equation D.1.	168
D.2	SNR and CNR for the Versa distance trial. Computed according to Equations (4.3) and (4.4). The highest values are apparent at a sample-to-detector distance of 164 mm, which is the shortest distance studied.	169
D.3	Source-to-sample and sample-to-detector distances chosen for the experiments, as in experiment I from Bidola <i>et al.</i> [2015]. The exposure time was adjusted for the longer propagation distances RII and RIII to account for the decrease of photon counts on the detector.	171

Declaration of Authorship

I, Berit Zeller-Plumhoff, declare that the thesis entitled *An Image-Based Computation of Microvascular Dysfunction* and the work presented in the thesis are both my own, and have been generated by me as the result of my own original research. I confirm that:

- this work was done wholly or mainly while in candidature for a research degree at this University;
- where any part of this thesis has previously been submitted for a degree or any other qualification at this University or any other institution, this has been clearly stated;
- where I have consulted the published work of others, this is always clearly attributed;
- where I have quoted from the work of others, the source is always given. With the exception of such quotations, this thesis is entirely my own work;
- I have acknowledged all main sources of help;
- where the thesis is based on work done by myself jointly with others, I have made clear exactly what was done by others and what I have contributed myself;
- parts of this work have been published as:
 - Image-based modelling of skeletal muscle oxygenation. B. Zeller-Plumhoff, T. Roose, G. F. Clough and P. Schneider. *Journal of the Royal Society Interface*, accepted 01/2017
 - Validation of phase contrast synchrotron radiation computed tomography of muscle spindles in the mouse soleus muscle. B. Zeller-Plumhoff, T. Roose, O. Katsamenis, M. Mavrogordato, C. Torrens, P. Schneider, G. F. Clough. *Journal of Anatomy*, re-submitted 11/2016 as brief communication, rejected, now revising major corrections for re-submission
 - Investigation of microvascular structural parameters for skeletal muscle tissue oxygenation by image-based modelling. B. Zeller-Plumhoff, K. R. Daly, G. F. Clough, P. Schneider, T. Roose. *Mathematical Bulletin of Biology*, in progress
 - Using High Resolution X-ray Computed Tomography to Create an Image Based Model of a Lymph Node. L.J. Cooper, B. Zeller-Plumhoff, G.F. Clough, B. Ganapathi-subramani and T. Roose. *Mathematical Bulletin of Biology*, in progress

Signed:.....

Date:.....

Acknowledgements

First and foremost, I would like to thank my supervisors Prof. Tiina Roose, Prof. Geraldine Clough and Dr. Philipp Schneider who helped me to develop professionally and who found just the right balance between letting me develop my own ideas and guiding me towards achieving my research goals. I greatly appreciate all the time they spent commenting paper drafts, proposals and this thesis. I would also like to thank Prof. Ian Sinclair for the valuable discussions and for making so many things possible.

I acknowledge the μ -VIS X-ray Imaging Centre at the University of Southampton that provided the equipment and tools for μ CT imaging, image processing and meshing. In particular I want to thank Dr. Richard Boardman and Dr. Neil O'Brien for always keeping things running smoothly in the computing suite, for all the helpful and enlightening discussions and for sharing coffee in times of great tiredness. I also thank Dr. Orestis Katsamenis, Dr. Anna Scott and Dr. Mark Mavrogordato for their input and for training me to use the different μ CT machines.

I would further like to thank Dr. Keith Daly for his incredible help to get the OpenFOAM model set up and running and for answering the endless questions that arose. Furthermore, I greatly appreciate the help by Dr. Susan Wilson, Jenny Norman, Jon Ward and Jamila McRobb in embedding and microtoming the muscle samples and in training me in histological staining. I am grateful to Dr. Christopher Torrens for assisting with the animal handling and dissectioning. Thanks also to Dr. Laura Cooper for helping out in counting red blood cells for the validation of the SR CT imaging and always keeping up my spirits. Additionally, thanks to all those that assisted me during my beamtime at the Swiss Light Source and to all my colleagues for the fun times.

Furthermore, I would like to acknowledge funding by the Engineering and Physical Sciences Research Council (EPSRC) for the EPSRC doctoral training grant and the British Heart Foundation for grant PG/12/18/29453 which funded my PhD thesis. I further acknowledge the Paul Scherrer Institut, Villigen, Switzerland for provision of synchrotron radiation beamtime at the TOMCAT beamline of the Swiss Light Source and I would like to thank Pablo Villanueva and Alessandra Patera for their assistance. The trial of edge-enhancement imaging and propagation distances was performed in June 2014 at a beamtime of Dr. Sam Keyes, who kindly lent 2 hours of beamtime to me. I also acknowledge the use of the IRIDIS High Performance Computing Facility, and associated support services at the University of Southampton, in the completion of this work.

Finally, I thank my family and friends, in particular my parents without whom I would not be here and my husband for all his patience and support.

Für Großmutter und Großvater.

Chapter 1

Introduction

The number of overweight adults has risen to over one billion worldwide, of which 400 million are obese (body mass index (BMI) > 30 kg/m) [Vickers, 2011]. Furthermore, 32% of women of childbearing age have been classified as obese [Drake & Reynolds, 2010]. At the same time, the number of non-communicable diseases, including diabetes, heart disease, renal disease, hypertension and stroke, has increased dramatically worldwide, accounting for 60% of deaths worldwide [Hanson & Gluckman, 2011].

Clearly, lifestyle, diet and exercise in adult life play a key role for the risk of developing a cardio-metabolic disease and the earlier an intervention takes place the lower the risk will be with increasing age. This is illustrated in figure 1.1 from Gluckman *et al.* [2009]. The risk for chronic disease, such as diabetes, increases with increasing age, but early intervention may lower the risk to a yet unknown but significant extent [Gluckman *et al.*, 2009, Hanson *et al.*, 2011]. In order for an intervention to take place as early as possible, genetic and other influences at an early age on the risk of developing a cardio-metabolic disease need to be taken into account. Whilst some genetic links between obesity and cardio-metabolic disease have been found, a large proportion of the risk is thought to be linked to “developmental programming”, i.e., the maternal diet pre-pregnancy and the dietary environment *in utero* [Vickers, 2011, Rkhzay-Jaf *et al.*, 2012].

By studying a cohort that was exposed to famine during the “Dutch Hunger Winter” 1944-1945, Roseboom *et al.* [2000] showed that coronary heart disease could be associated with low birth weight, as well as an exposure to famine during early gestation. Exposure to famine and birth weight were not correlated. Many further investigations were conducted researching the effect of premature birth and birth weight on development of cardio-metabolic disease. These found that prematurely born children (which exhibited low birth weight) were at higher risk of developing insulin resistance, higher blood pressure, abnormal retinal vascular development and

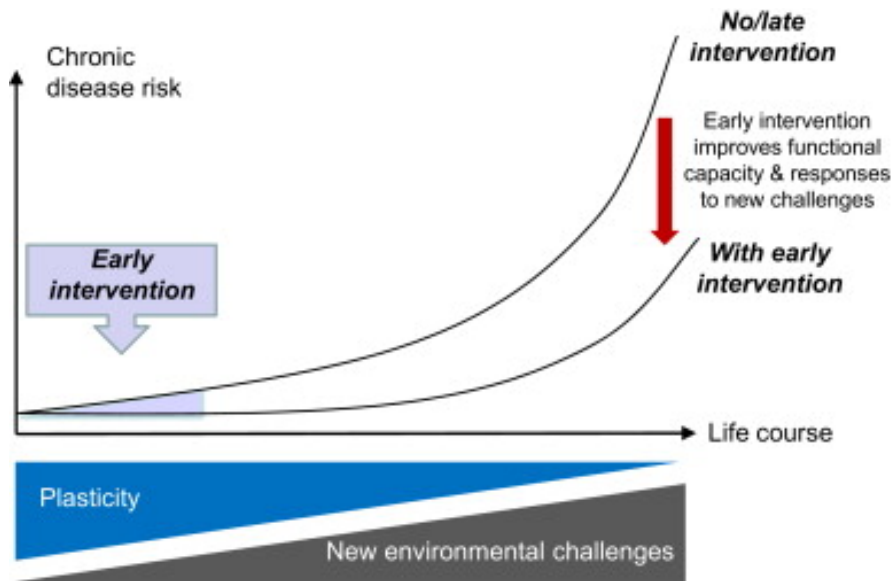


Figure 1.1: **Trajectory of the risk of chronic non-communicable disease** [Gluckman *et al.*, 2009]. The risk for chronic non-communicable disease, including cardio-metabolic disease, increases during lifetime. The higher the age, the steeper the risk curve becomes. Intervention in early life may significantly change the trajectory of the curve and lead to an improved risk over lifetime.

decreased peripheral skin blood flow [Bonamy *et al.*, 2005, Kistner *et al.*, 2002, 2005, Kerkhof *et al.*, 2012]. This has been reviewed extensively in Musa *et al.* [2014].

The development of cardio-metabolic disease is associated with changes in both macro- and microvascular networks in organs such as liver and heart and also in skeletal muscle. The microvasculature is defined as those vessels of diameter smaller than approximately 150 μm , whose primary function is the optimal delivery of nutrients and oxygen to the tissue [Pries & Secomb, 2009]. However, if the vascular structure changes, which can include reduced capillary density or enhanced vasoconstriction, the oxygen delivery is impaired due to longer diffusion distances from the capillaries to the tissue. Musa *et al.* [2014] highlight the need for further investigations into the origins and effects of structural changes of muscle microvasculature in particular, which would provide a link between the observed low birth weight and insulin resistance in later life, e.g., as muscle capillary density determines the supply of insulin to the tissue. The reduced capillary density has been previously reviewed [Clough & Norman, 2011] and observed in a number of models of maternal undernutrition [Pladys *et al.*, 2005, Costello *et al.*, 2008]. Similarly to low birth weight, a number of studies have shown the positive correlation between higher birth weight and obesity in adults, as reviewed in Sen *et al.* [2012], and the development of cardio-metabolic disease [Boney *et al.*, 2005, Samuelsson *et al.*, 2008, Elahi *et al.*, 2009, Tapp *et al.*, 2013], see review by Musa *et al.* [2014]. However, Musa *et al.* [2014] underlines the lack of data linking maternal overnutrition and microvascular structure of the offspring. The authors predict a clear association between maternal insulin

resistance resulting from maternal overnutrition and offspring microvascular structure due to changes in the placental development [Musa *et al.*, 2014].

One of the key tissues investigated in the origin and outcomes of cardio-metabolic disease is skeletal muscle, which makes up almost half of an (healthy) individual's body mass [Segovia *et al.*, 2014]. Skeletal muscle is one of the main tissues responsive to insulin, taking up glucose and fatty acids [Segovia *et al.*, 2014] and exhibiting reduced oxidative capacity as a result of obesity and diabetes [Denies *et al.*, 2014]. The environment *in utero* in particular plays a major role in the development of skeletal muscle as for example muscle fibre formation is mostly finished after birth [Segovia *et al.*, 2014].

This work is focussing on the visualization of the microvasculature such that the key structural parameters of the blood vessel network associated with microvascular delivery of oxygen to muscle can be investigated. The impact of maternal and offspring high-fat diet on these parameters is explored. To this end, an animal (mouse) model of developmental priming is employed. The oxygen supply capability of the individual microvascular networks is investigated using mathematical modelling based on the images obtained for the structural analysis of the networks.

1.1 Image-based modelling of skeletal muscle oxygenation

To assess the importance of morphological changes on the blood network's oxygen supply capability, the influence of a number of structural parameters, such as capillary density, vessel volume fraction and tortuosity, has been studied. Tumour networks in particular have been subject of such investigations [Jain *et al.*, 2013, Lang *et al.*, 2012]. For example, Lang *et al.* [2012] found that tumour networks and healthy/normal networks differ significantly in capillary diameter, i.e. $8.0 \pm 1.1 \mu\text{m}$ and $3.9 \pm 1.1 \mu\text{m}$, respectively. The effect of diabetes on the coronary microvasculature was studied by Jenkins *et al.* [2012]. In a rat model they found that compared to the microvasculature of healthy animals diabetes resulted in a microvasculature with smaller internal vessel diameters in the first to third branching order from the root arteries.

Generally, for all research where structural hallmarks of the vasculature are assessed to study structure-function links (e.g. through image-based modelling) it is important to capture the microvascular structure within the tissue in a state as close as possible to the *in vivo* situation. A number of different imaging techniques can be used to capture the vascular network morphology. These differ in many aspects, such as spatial resolution and tissue penetration depth that can be achieved. Since the length scales of the relevant anatomical features of microvascular systems range from a few micrometres in two dimensions (e.g. vessel cross-section) to several hundred micrometres in the third dimension (vessel length), high spatial resolution of the

employed imaging technique is required as well as the ability to cover a relatively large field of view. An additional challenge in imaging the (micro)vasculature is that image contrast for biological soft tissues is usually very low and/or homogenous in extended regions of interest for various imaging techniques. Thus, contrast agents are often applied to distinguish between features of interest [Pauwels *et al.*, 2013]. Whilst capturing and analysing the vascular morphology *ex vivo* may give good indication of changes in microvascular anatomy, it provides little information of the resulting changes in vascular function, in particular capillary oxygen delivery capability, which is crucial for maintaining the tissue in a healthy state. However, studying these structure-function links experimentally *in vivo* introduces another layer of complexity. Depending on the imaging technique employed different limitations may arise, such as the X-ray radiation dose entailed [Zhang *et al.*, 2014], the accessibility of imaging facilities [Jenkins *et al.*, 2012], a soft tissue image contrast medium that can be applied for *in vivo* experiments [Vakoc *et al.*, 2012], the accessible field of view (and hence the required tissue preparation) [Jain *et al.*, 2013, Kamoun *et al.*, 2010] or limitations in spatial resolution due to animal movements. Due to these complexities mathematical modelling is often used to inform how observed structural changes might lead to functional differences and it has frequently been employed to study blood flow and oxygen delivery to tissue. However, image-based and thus realistic modelling on actual morphological data from experiments is relatively novel and has only been made possible by the recent advances in high-resolution imaging techniques and the broad availability of high-performance computing.

Image-based mathematical modelling of biological processes poses a number of challenges because various requirements have to be satisfied - at least partially - at the same time, as summarised in figure 1.2. In order to analyse the structure of a microvascular system, an imaging system should offer spatial resolutions and field of views that allow a meaningful or relevant part of the tissue to be captured at sufficient detail. Specimen size, spatial resolution and field of view are three factors that are important in imaging. However, for most imaging techniques, there exists an intrinsic trade-off between those factors, which cannot always be optimised independently. Another challenge is the typically low image contrast between different soft tissues (e.g. vasculature versus muscle fibres) so that identification of the different tissues and individual segmentation thereof can become difficult. Therefore, it is often necessary to draw on contrast agents, which are specific for certain tissue types in the ideal case. Finally, tissue contrasting and imaging result in certain costs, both time-wise and financially. On the other hand, the major challenge for a mathematical model to describe the biological processes taking place is essentially to be as simple as possible whilst still having sufficient validity to provide meaningful results. The biological processes need to be modelled correctly, but too much unnecessary detail may lead to long computing times to find a numerical solution or even make the mathematical system too complex to be solved at all. Most importantly, the results provided by the

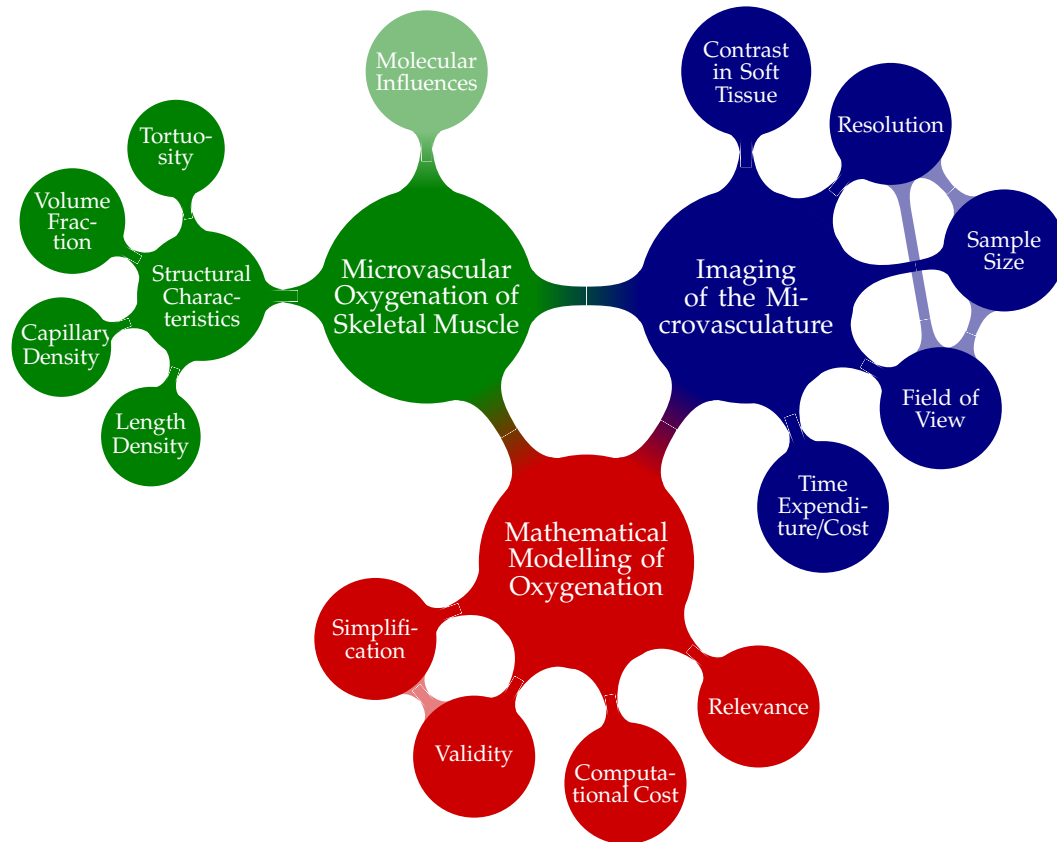


Figure 1.2: **Challenges and requirements in image-based modelling of biological processes.** The example shown applies namely for the oxygenation in skeletal muscle.

mathematical model ought to be validated experimentally, which in some cases can be used to provide (refined) parameters for mathematical modelling.

When considering the problem of microvascular function different scales can be investigated, e.g. cellular and whole organ scale [Walpole *et al.*, 2013]. The focus of this work is on the whole-organ scale by reviewing mathematical models of oxygen delivery in skeletal muscle based on *ex vivo* and *in vivo* imaging of the microvasculature to inform the association between anatomical characteristics and disease or in other words, to identify and characterise structure-function links that are important for microvascular systems. More specifically, this thesis discusses the different steps within the workflow for developing an image-based model of skeletal muscle oxygenation. Such a workflow has been adopted for example by Cooper *et al.* [2015] who created an image-based model of fluid flow in the lymph node (see figure 1.3 for a generic workflow). Following the image acquisition (here by micro-computed tomography or μ CT), the features of interest need to be segmented, either by hand or (semi-)automatically. For mathematical modelling of oxygen delivery in skeletal muscle, skeletal muscle tissue and blood vessels need to be segmented. The different features can subsequently be characterised through quantitative morphometry and

discretised for numerical modelling. The quantitative measures characterising the morphology and the outcomes of the mathematical model can be correlated and an optimal structural measure for the description of the muscle oxygenation identified. The resulting numbers may then have to be validated against those that can be obtained from gold standard imaging techniques, if non-standard imaging approaches have been used, and against biological experiments.

1.1.1 Aims of this thesis

The aim of this thesis was to enable the visualisation of the microvasculature in skeletal muscle using μ CT, such that structural parameters characterising the skeletal muscle oxygenation can be determined and their prediction capability of tissue oxygenation can be validated. This was done with particular regard to the influence of maternal and offspring high-fat diet.

To reach this aim it was necessary to:

- enable the non-invasive, three-dimensional imaging of the microvasculature,
- identify structural differences in the microvasculature in mice from the animal model of developmental priming,
- develop an image-based model of oxygenation based on the obtained images, and finally
- characterise the relationship between structural parameters and tissue oxygenation in skeletal muscle.

The first of these milestones has proven to be the most challenging, because of the difficulty to obtain sufficient soft tissue contrast for visualisation of the microvasculature. Therefore, the majority of this thesis is dedicated to the development of a workflow for imaging the microvasculature in skeletal muscle, whilst keeping in mind that modelling will need to be performed on the images.

1.1.2 Thesis structure

Chapter 2 introduces the biological background necessary to understand the role of the microvasculature for oxygen delivery to the tissue and the animal model of developmental priming used to study the maternal impact. The morphological parameters that are commonly used to describe vascular networks are presented. Chapter 3 (with appendix A) then compares different imaging systems and explains the basic theory and methodology behind micro-computed tomography. In chapter 4

methodologies used in imaging the microvasculature in skeletal muscle are described and compared. The results and comparisons for the dietary groups are presented in chapter 5, with section 5.4 presenting analysis performed on other muscular features, i.e., muscle spindles and intramuscular fat tissue, and variations due to dietary fat intake. The validation of the most promising imaging method is presented in chapter 6. Chapter 7 presents mathematical models of nutrient uptake and blood flow and the employed image-based model. Furthermore, the results from mathematical modelling and the structural analysis are linked and discussed. Finally, chapter 8 discusses limitations that occurred in the workflow of image-based modelling and gives conclusions from this work, which leads to a discussion on future work. Some of the work that has been undertaken in the course of this PhD project but does not directly add to the story of this thesis can be found in the appendices C and D.

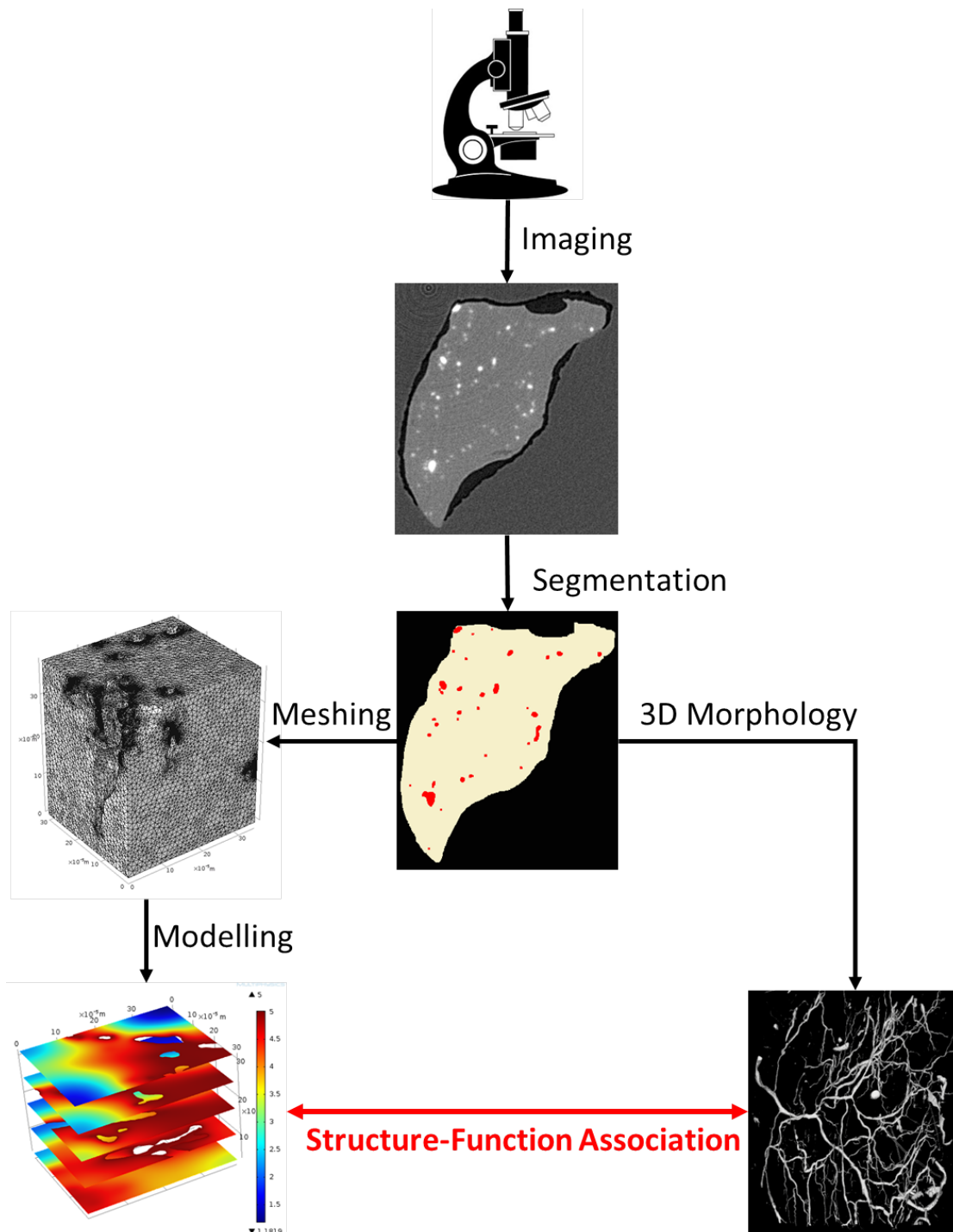


Figure 1.3: **Generic workflow for image-based modelling.** Images are acquired by a specific imaging technique. From the resulting images, blood vessels and muscle tissue can be segmented from the background material (here air). The blood vessels can now be analysed for their 3D structure by quantitative morphometry. At the same time, the segmented tissues can be meshed for finite element modelling. The mesh is then imported into a partial differential equation (PDE) solver, which will solve equations describing the biological process at hand. Given the results of the quantitative morphometry and the solved mathematical model, an association between 3D vascular structure and function can be derived, for instance in terms of fluid flow or tissue oxygenation. Microscope clipart from ClipartPanda.com.

Chapter 2

Clinical and biological background

In order to assess the impact of an exposure to a disadvantageous developmental environment (maternal high fat diet consumption) on later microvascular morphology in the adult offspring, it is necessary to gain an understanding of the structure of blood vessels and muscle fibres and oxygen transport in skeletal muscle. The next section serves to give a brief introduction of the main units of skeletal muscle. The influence of fat intake on body, organ and muscle development previously studied in models of developmental priming are presented and discussed.

2.1 Anatomy of skeletal muscle

Skeletal muscle consists of muscle fibres that are arranged in bundles. The muscle fibres are differentiated into two types. Fibre type I is the slow oxidative type, type IIa is fast oxidative and IIb is fast glycolytic. The ratio of these fibre types is different for each muscle and depends on its function. It was found by Soukup *et al.* [2002] that the soleus muscle in female inbred Lewis rats, which is a slow twitching muscle, contained mainly type I fibres, with a few IIa fibres adding up to the total number of fibres. Type I fibres contain a large number of mitochondria, intramyocellular fat droplets and the protein myoglobin, whose red colour pigments are responsible for the muscles with largely type I fibres being called red muscles [Despopoulos *et al.*, 2009]. The muscle fibres are long thin cells, that consist of a number of myofibrils, which are the contractile units of the fibre [Alberts, 2002]. Myofibrils are cylindrical with a diameter of 1-2 μm and are as long as the muscle fibre. They in turn consist of a chain of sarcomeres that are smaller contractile units of 2.2 μm length [Alberts, 2002]. In the sarcomere, thick (myosin) and thin (actin) filaments are aligned in parallel and partly overlapping. The thin filaments are at one end attached to a so-called Z-disk and on the other end overlap with the thick filament. During contraction the area of overlap increases and the sarcomere is shortened. Figure 2.1 shows an electron

microscopy micrograph of mouse soleus muscle. Its striated appearance can clearly be seen as well as the Z-disks and the overlapping actin and myosin filaments.

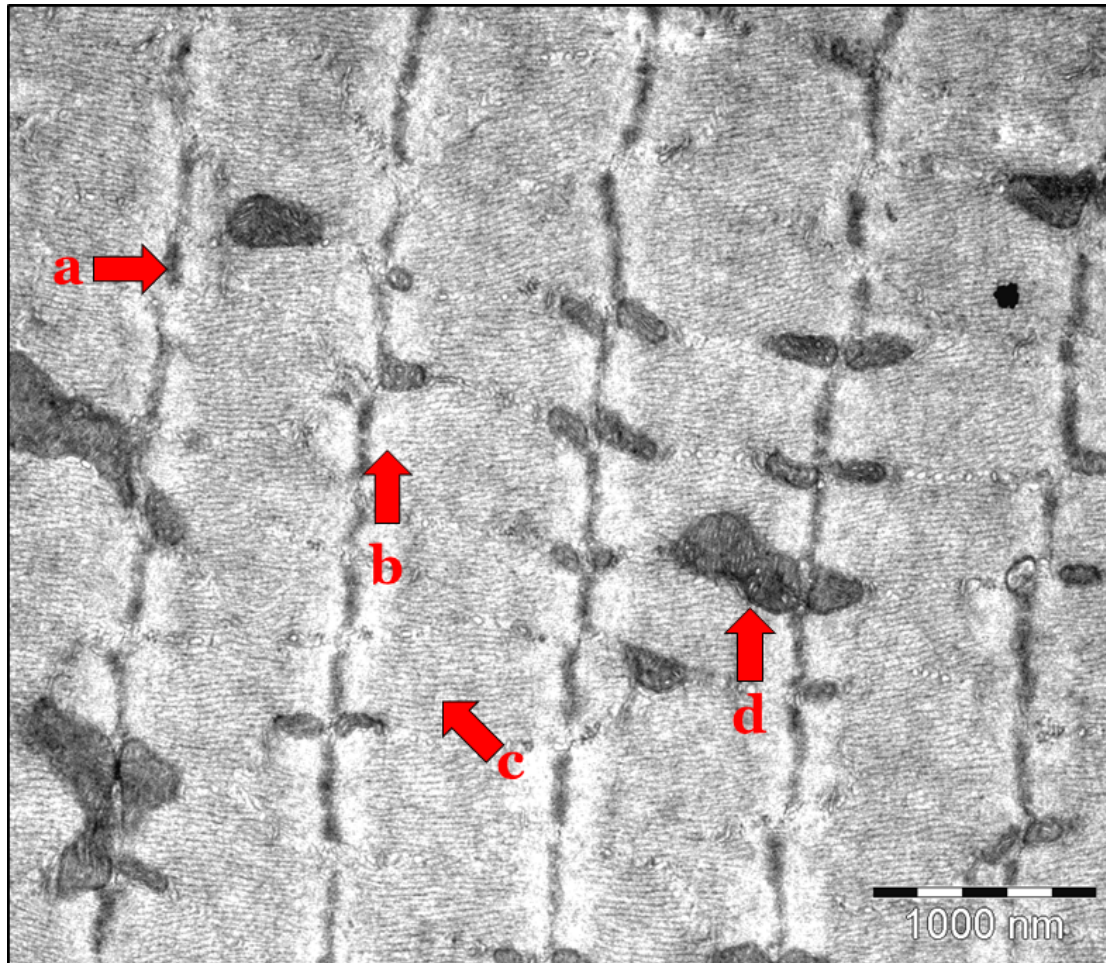


Figure 2.1: Transmission electron micrograph of mouse soleus muscle taken at 15000X magnification. The Z-disks (a) are visible, as well as the thin actin filaments (b) and the region of overlapping thick and thin filaments (c). Mitochondria are also visible (d). This image was taken during a training course on transmission electron microscopy at the Biomedical Imaging Unit (BIU) at Southampton General Hospital (SGH).

In this thesis, the soleus muscle was used to investigate the microvascular structure of the developmentally primed mice. The soleus is a muscle of the calf, located beneath the gastrocnemius, see figure 2.2. This muscle was selected as it is nearly homogeneous, containing mainly type I fibres.

2.1.1 The microvasculature in skeletal muscle

The microvasculature can be distinguished into three types of vessels, i.e., arterioles, capillaries and venules. The arterioles can again be distinguished into first-order arterioles that are fed by the arteries and the terminal arterioles that supply the capillaries [Levick, 2003]. The capillaries are about 500-1000 μm long and have a

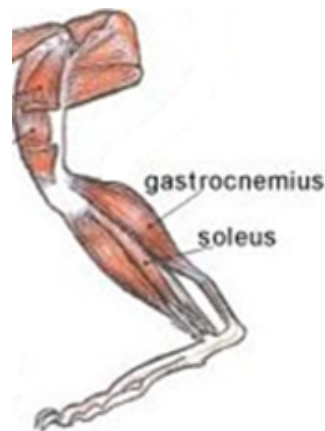


Figure 2.2: **Location of murine soleus muscle.** The soleus muscle is a muscle located below the gastrocnemius in the calf of an animal. Image taken and adapted from [Faulkes, 2016].

diameter of $5\text{--}10\ \mu\text{m}$. The terminal arterioles and pericytic venules have a diameter of about $15\text{--}20\ \mu\text{m}$. The biggest arterioles and venules have diameters in the range of $50\text{--}100\ \mu\text{m}$ [Caro *et al.*, 2012]. Venules and arterioles can also be linked via so-called arteriovenous anastomoses, which are about $20\text{--}130\ \mu\text{m}$ wide. However, they are usually found only in superficial tissues and therefore need not be considered in the muscle microvasculature [Levick, 2003]. Figure 2.3 from Levick [2003] shows a schematic of the microvasculature.

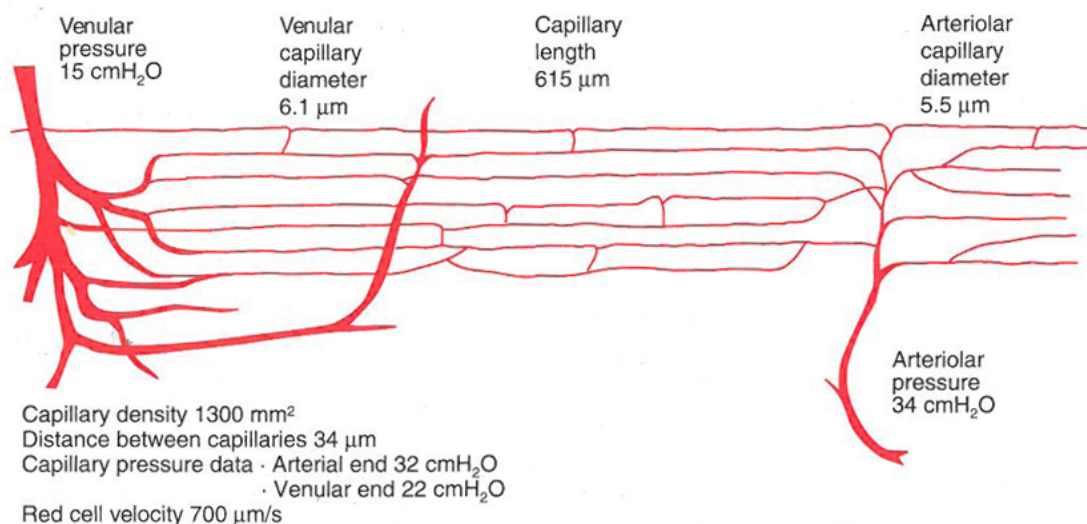


Figure 2.3: **Schematic of the microvasculature, taken from Levick [2003].** The vessels denoted by the term microvasculature are the arterioles, capillaries and venules, which have a diameter of $5\text{--}150\ \mu\text{m}$.

The main function of the microvasculature is the delivery of oxygen and nutrients to tissue. This delivery depends partly on the endothelial cells, which form the most inner part of the vessel wall [Alberts, 2002]. For larger vessels, such as arteries and

vein, the wall consists of connective tissue (i.e., collagen fibres) and smooth muscle cells which are separated from the endothelial cells (endothelium) by a basal lamina. See figure 2.4 for a schematic of the vessel wall. As vessel diameter decreases

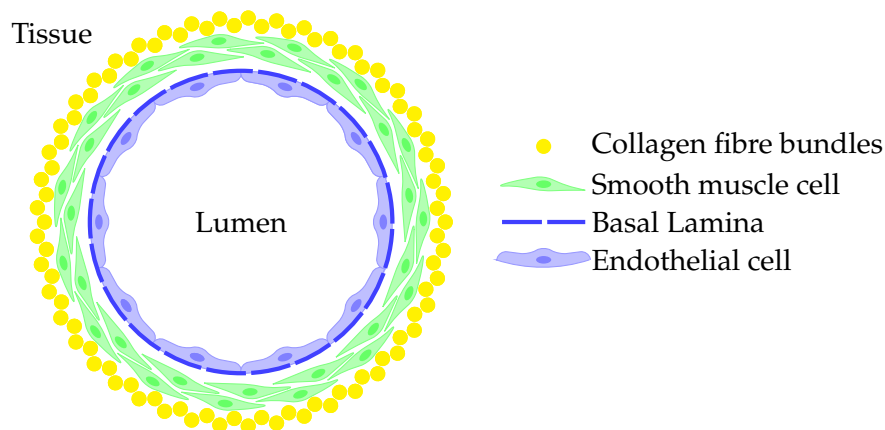


Figure 2.4: **Schematic of the vascular wall.** The vascular wall consists of connective tissue and smooth muscle cells which are separated from the endothelium by a basal lamina. Not to scale. This image is courtesy of L. Cooper.

connective tissue and smooth muscle cells are lost and the capillary wall consists only of the endothelium and the basal lamina. This can be seen in an electron micrograph in figure 2.5.

Another important function of the arterioles in particular is the regulation of peripheral resistance to reduce the variations in capillary pressure that are transferred from the systemic arterial pressure and to thereby regulate blood pressure [DeLano *et al.*, 1991]. This is done by regulating the vascular tone via vasoconstrictors and vasodilators, which may be impaired in the case of cardio-metabolic disease [Musa *et al.*, 2014]. However, this project is not concerned with this latter function of the microvasculature but focusses instead on its oxygen delivery capability. For further reading see e.g. Musa *et al.* [2014].

In skeletal muscle, the microvasculature is organised such that the muscle fibres, which are aligned longitudinally, are surrounded by a few vessels, which are mostly aligned in the same way. Depending on the kind of skeletal muscle, i.e., slow or fast twitching, the fibre type composition and consequently the capillarisation vary. In general, about 1.2-1.3 capillaries per muscle fibre should be apparent in mouse soleus muscle. Figure 2.6 shows histological sections of mouse soleus muscle, where the parallel alignment of muscle fibres and capillaries in cross-section is visible. In subfigure 2.6(b) a fluorescent marker was used to visualise the capillaries.

2.1.2 Nervous tissue in skeletal muscle

Nervous tissue is one of the four basic tissues in the human body. It is also present in the muscle, as information on motion coming from the brain needs to be transferred to

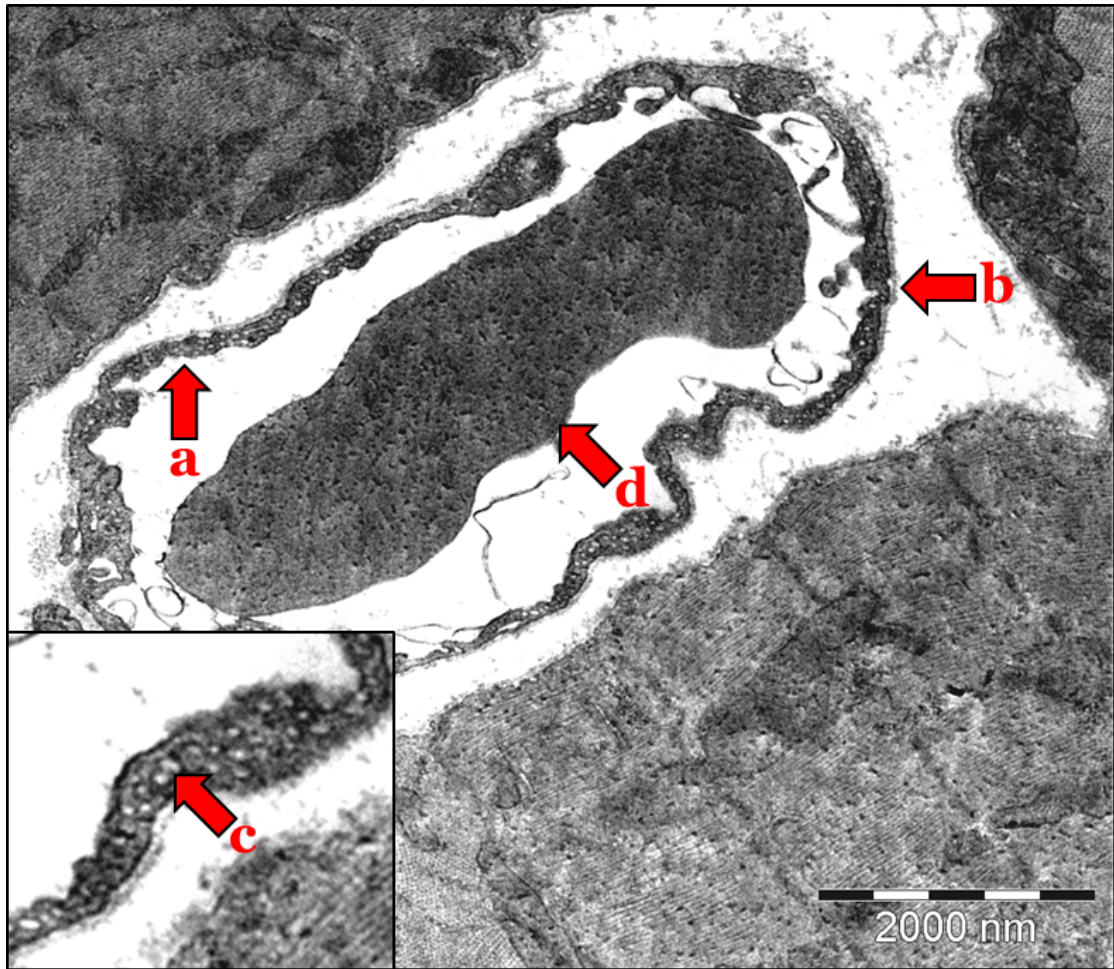
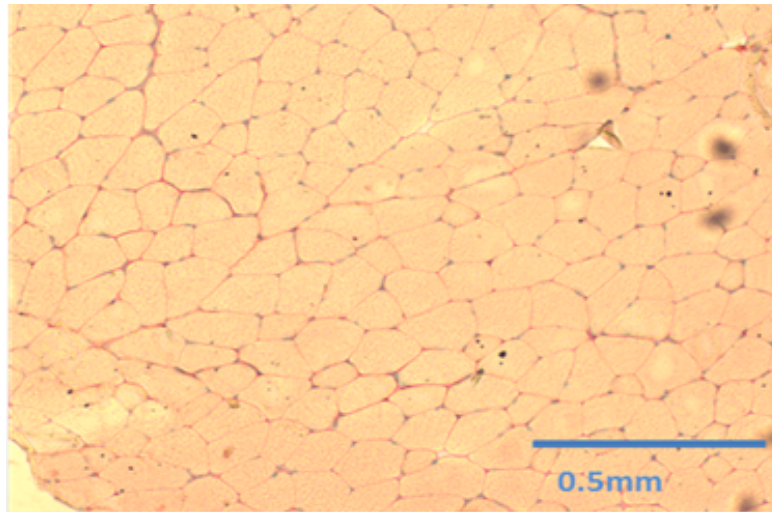


Figure 2.5: **Transmission electron micrograph of a capillary in mouse soleus muscle at 9000X magnification.** The capillary wall consists only of endothelium (a) and basal lamina (b). Vesicles are visible inside the endothelial cells (c). A red blood cell can be seen inside the capillary (d). This image was taken during a training course on transmission electron microscopy at the BIU at SGH.

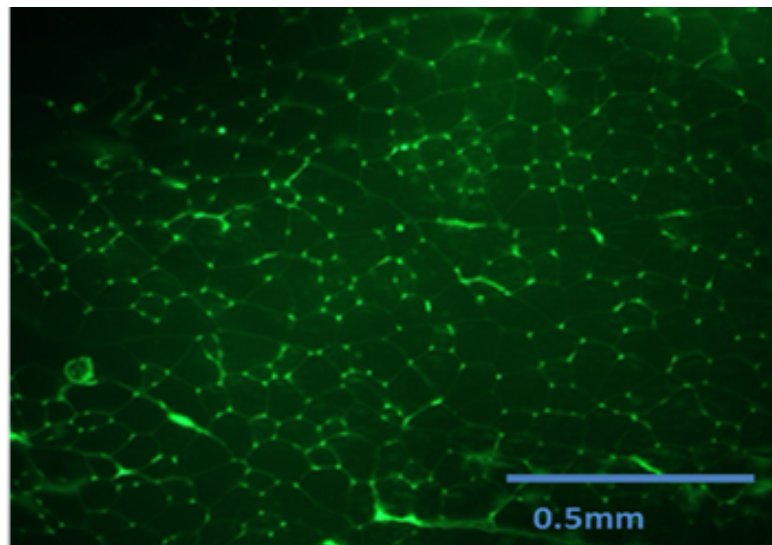
the muscle tissues. Information from the brain and the spinal cord (which is the central nervous system (CNS)) is received by the so-called peripheral nervous system (PNS). The transmission to the muscle is performed by the motor component of the PNS [Craigmyle, 1986].

Similar to muscles, the peripheral nerves consist of nerve fibres that are bundled together in fascicles, which are surrounded by a connective tissue sheath, the epineurium [Craigmyle, 1986].

The soleus muscle is innervated by the tibial nerve that branches of into smaller nerves, which then in turn transmit information to the contractile units of the muscle via the muscle spindles [Craigmyle, 1986].



(a) Light micrograph



(b) Fluorescent micrograph

Figure 2.6: **Light micrographs of histological slices of mouse soleus muscle in transversal section, courtesy of Katy Gould.** The muscle fibres are aligned parallel to each other, see subfigure 2.6(a). The capillaries between them are aligned in the same way, on average there are around 1.2-1.3 capillaries per muscle fibre. A fluorescent marker was used to visualise these (subfigure 2.6(b)).

2.1.2.1 Muscle spindles

Muscle spindles are mechanoreceptors located in skeletal muscles and are involved in the detection of position and movement [Kokkorogiannis, 2004]. Muscle spindles consist of a varying number of intrafusal muscle fibres that are surrounded by a capsule of connective tissue (ICA) [Craigmyle, 1986]. An external capsule (ECA) surrounds the internal capsule. Figure 2.7 from Diaz-Flores *et al.* [2013] displays a micrograph depicting ECA and ICA and figure 2.8 a schematic of the muscle spindle.

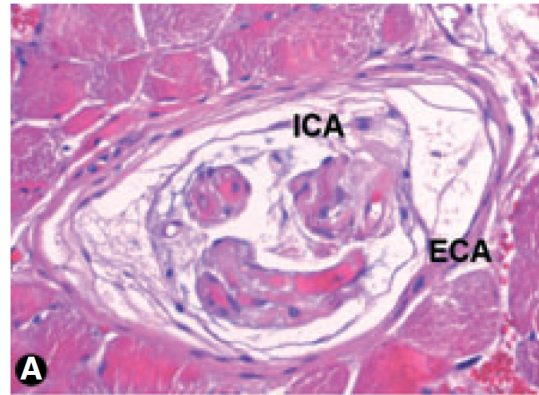


Figure 2.7: **Light micrograph of a muscle spindle.** ICA and ECA mark internal and external capsule, respectively. Three intrafuscal muscle fibres are visible within the ICA. The ECA can be significantly larger than the ICA, as can be seen in the image. Taken from Diaz-Flores *et al.* [2013]

The intrafuscal fibres are much shorter and smaller than the regular contractile muscle fibres. The diameters of the intrafuscal muscle fibres depend on their type, i.e., either chain or bag type, with the bag type fibres being considerably larger [Thornell *et al.*, 2015]. The number of muscle spindles can vary between different muscles [McComas, 1996] and between different strains of the same type of mammal [Lionikas *et al.*, 2013]. The number of intrafuscal fibres may also vary, but is reported to be between two and eight in mouse soleus muscle [Lionikas *et al.*, 2013].

2.2 Biology of oxygen uptake in skeletal muscle

Blood is a suspension of red blood cells (RBCs), which are deformable particles, and liquid particles, the so-called chylomicrons, in an aqueous solution called plasma [Caro *et al.*, 2012]. The chylomicrons are very small droplets with diameters of $0.2 - 0.5\mu\text{m}$ and have the primary function of facilitating fat transport in the circulation. However, due to their low concentration they have no significant effect on viscosity or osmotic pressure of the plasma [Caro *et al.*, 2012] and can therefore be neglected in the further discussion.

The RBCs are present in a high concentration of approximately $5 \times 10^6 \text{mm}^{-3}$ which represents about 45% of the plasma volume in larger blood vessels. RBCs are deformable, bi-concave discs with a diameter of about $8\mu\text{m}$ and a width of $2 - 3\mu\text{m}$ on the widest part at the outer side of the particle and $1\mu\text{m}$ in the centre of the RBC. When flowing through the capillaries, the RBCs will deform in different ways [Caro *et al.*, 2012]. The ratio of red blood cell volume to the whole blood volume is defined as the haematocrit. In the microvasculature the haematocrit decreases due to plasma skimming, which leads to a reduced viscosity and thus allows blood flow in the

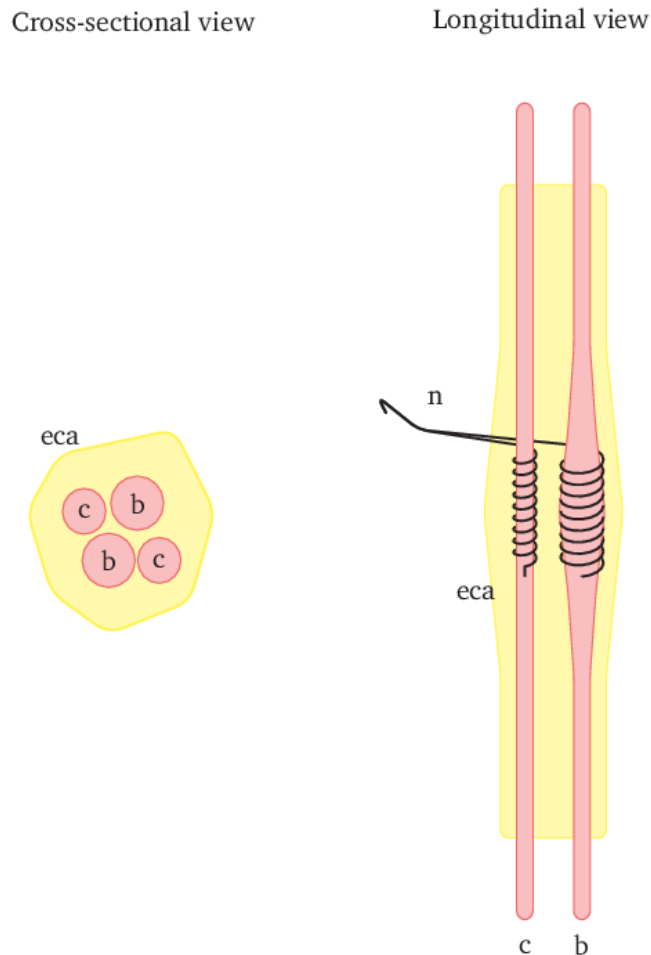
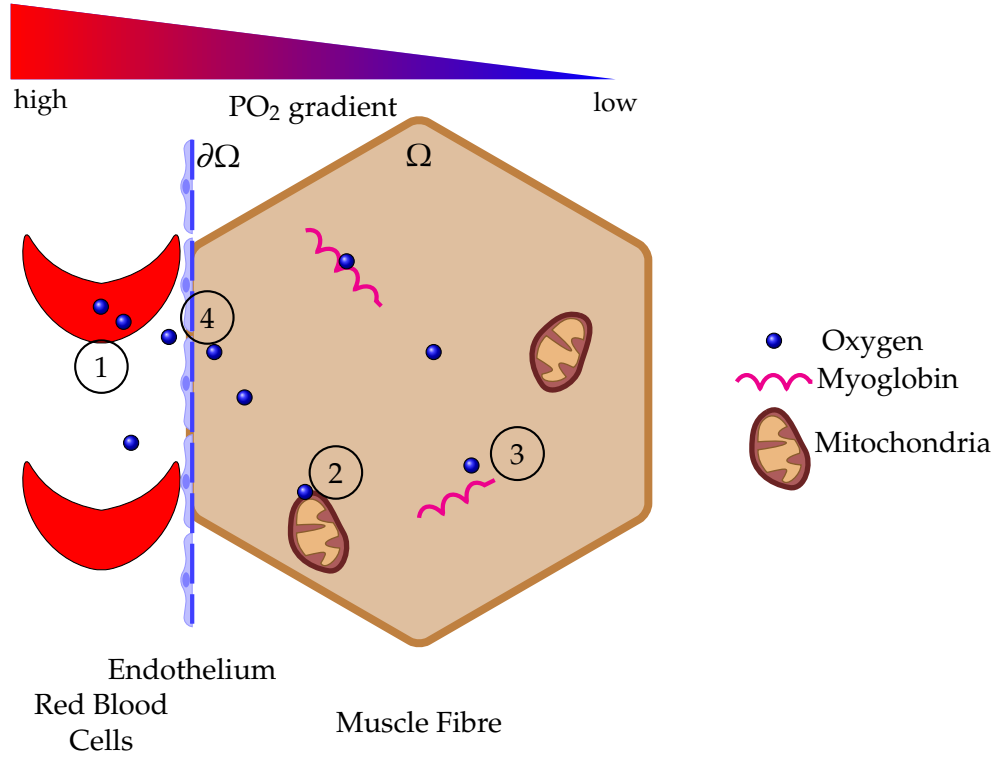


Figure 2.8: **Schematic of a muscle spindle.** The muscle spindle consists of an external capsule (eca) that surrounds the intrafusal fibres, which can be distinguished as chain (c) and bag fibres (b). The sensory innervation (n) of the intrafusal fibres lies in the middle the fibre.

capillaries. Oxygen is bound to the red blood cells by the protein haemoglobin and one haemoglobin molecule can bind up to four oxygen molecules [Mozzarelli & Bettati, 2011].

Oxygen will be released by the haemoglobin and diffuses down its partial pressure (PO_2) gradient toward the muscle tissue. How well a solute is transferred through the capillary wall is described by the permeability of the wall to the solute, which in a capillary comprises a single layer of endothelium and its basement membrane, and the characteristics of the diffusing substrate (e.g., size, charge or lipophilicity). This process of diffusion is illustrated in figure 2.9. O_2 exchange is very high due to the small molecular radius and because O_2 is lipophilic [Levick, 2003], and it occurs across both arteriolar and capillary parts of the vascular tree [Ellsworth & Pittman, 1990, Nair *et al.*, 1990, Secomb & Hsu, 1994]. In skeletal muscle cells the oxygen is utilised by the mitochondria (see figure 2.9) for adenosine triphosphate (ATP) generation to generate energy used for locomotion or exercise [Pittman, 2013]. Additionally, the released



Governing Equation of Conservation

$$\frac{\partial \alpha P}{\partial t} = \nabla \cdot [\alpha D \nabla P] + D_{Mb} C_{Mb} \nabla \cdot \left(\frac{dS_{Mb}}{dP} \nabla P \right) - M(P) \quad \text{in } \Omega$$

$$(1) \quad SO_2(P) = \frac{P^n}{P^n + P_{Hb,50}^n} \quad \text{in } \Omega$$

$$(2) \quad M(P) = \frac{M_0 P}{P + P_{50}} \quad \text{in } \Omega$$

$$(3) \quad S_{Mb}(P) = \frac{P}{P + P_{Mb,50}} \quad \text{in } \Omega$$

$$(4) \quad -n_v \cdot (D \alpha \nabla P) = k \alpha (P_0 - P) \quad \text{on } \partial \Omega$$

Figure 2.9: **Schematic of oxygen delivery in muscle tissue through diffusion.** Up to four oxygen molecules can be bound by one of the haemoglobin molecules present in the red blood cells (1). The partial pressure of oxygen is very high in the blood vessels, but low in the surrounding tissue. Therefore, the oxygen is released by the haemoglobin and diffuses along the gradient towards the surrounding tissue. It permeates the capillary wall (4), which consists only of the endothelium and its basement membrane. The released oxygen travels towards the mitochondria in the muscle tissue by which it will be consumed for adenosine triphosphate (ATP) generation (2). The protein myoglobin, which stores up to one oxygen molecule and releases this if the oxygen demand is very high (3), is also present in muscle tissue. Schematic is not to scale. Source code for mitochondria adapted from [Medina, 2015].

oxygen is bound and stored by the protein myoglobin, which is present in the sarcoplasm of skeletal muscle [Levick, 2003]. Myoglobin can facilitate the oxygen supply, especially in the case of high demand, by freeing the stored oxygen into the muscle fibre for ATP generation. Each myoglobin molecule can bind one oxygen molecule [Goldman & Popel, 2000].

Blood flow has a significant effect on oxygen exchange between blood and muscle tissue in cases where the rate of diffusion of oxygen is significantly higher than the blood flow rate [Geiger *et al.*, 1984]. There are two regimes in mass transfer, one being flow limited, the other diffusion limited. In the flow limited case, when the diffusion capacity of the capillary is higher than five times the blood flow, the solute concentration decays very quickly and the amount of nutrient delivery is limited by the blood flow rate. However, when the blood is flowing faster, an increase of blood flow has very little effect on the mass transfer and the delivery is dependent on the diffusion of the molecules over the capillary wall [Levick, 2003]. In mathematical modelling this fact is often used to assume a diffusion limited mass transfer regime, i.e., blood flow is high and tissue oxygenation is not limited by the supply of new (O_2 saturated) red blood cells [Al-Shammari *et al.*, 2012].

2.3 Association of cardio-metabolic disease and microvascular structure

A considerable number of studies have been performed, linking cardio-metabolic disease to structural changes in the microvasculature. Benedict *et al.* [2011] found that Zucker diabetic fatty rats suffer a decrease in branching points of the microvasculature per volume of muscle and in microvascular length density. They also found that the capillary flow per muscle volume decreased by almost one half. Diabetes type 2 was also linked to an imbalance between oxygen uptake and delivery during exercise [Bauer *et al.*, 2007].

Wiernsperger *et al.* [2007], Caton *et al.* [2009], Clough *et al.* [2009] and Clark [2008] further affirmed the link between microvascular dysfunction and insulin resistance and the positive effect that regular exercise may have. Similar results were obtained by Georgi *et al.* [2011], who also observed shunting (preferential flow pathways) of erythrocytes to specific terminal arteriolar branches in both diabetic and obese mice. Furthermore, obesity was linked to an alteration in blood flow both in skeletal and coronary capillaries [Wu *et al.*, 2011, Quercioli *et al.*, 2012] and was shown to worsen functional microvascular dilator capacity [Clough *et al.*, 2011]. Greene *et al.* [1989] found a maximum increase in vascular resistance of about 20% for a reduction in vessel number of approximately 40%, which also resulted in a considerable change in blood flow distribution. A mathematical model additionally showed that peripheral

resistance increased if the vessel network was rarefied with a critical vessel diameter or by a certain density threshold, thus changing the response to hypertension and possibly leading to further reduction in vessel number [Jacobsen *et al.*, 2003], [Jacobsen *et al.*, 2011].

Frisbee [2005] found that changes, in this case reduction of the microvessel density, in the microvasculature of obese Zucker rats (OZR) in skeletal muscle can be observed before the onset of macrovasculature disease, i.e., elevated mean arterial pressure. Furthermore, treatment to prevent elevated blood pressure did not result in positive changes to the microvessel density [Frisbee, 2005]. This suggests that early changes in structure and function of the microvasculature may precede the onset of overt macro or micro vascular disease. Lowered capillary density in high-fat fed (post-weaning) mice was confirmed by Thomas *et al.* [2014]. It was further shown that consumption of a high-fat diet leads to changes in muscle fibre types. Thomas *et al.* [2014] cited and found a shift towards more oxidative types, i.e., an increase in IIa and a decrease in type IIb fibres and an increase in fatty acid oxidation [Trajcevski *et al.*, 2013]. The authors argued that the decrease in capillary density in combination with the shift towards more oxidative fibres may be to counteract any functional disadvantages that would arise from either change occurring alone. Furthermore, Thomas *et al.* [2014] reviewed that intramuscular lipids built up in the muscle due to a high-fat diet. The intramuscular fat was associated with the increased insulin resistance [Sinha *et al.*, 2002]. Thus, obesity was linked to changes in muscle oxidative function Thomas *et al.* [2014].

Denies *et al.* [2014] reported a different shift in high-fat fed (post-weaning) male C57 BLK/6J mice; in particular they found that type I fibres appeared to transform into type I/IIA hybrid fibers, with the reduction of type I fibres depending on the relative fatness of the mouse ($p < 0.003$; $R^2 = 0.65$) [Denies *et al.*, 2014]. Denies *et al.* [2014] therefore argue that obesity has the largest impact on type I fibres. It was further found that the reported changes were sex dependent. Clark *et al.* [2011] found in miniature swine that a high-fat (and high cholesterol/fructose) diet led to an increase in muscle cross-sectional areas in both type I and II fibres and cited the association between weight loss and decrease of the same fibre cross-sectional areas. This relationship could be linked to the accumulation of intramuscular fat (in particular intramyocellular lipids), which was higher in type I than type II fibres [Clark *et al.*, 2011].

Frisbee *et al.* [2011] studied the influence of spatial perfusion heterogeneity on oxygen supply to skeletal muscle tissue in obese Zucker rats *in vivo*. The distribution of parent arteriolar blood flow into daughter arterioles was measured at bifurcations. It was found that this distribution was significantly different in OZR compared to lean Zucker rats (LZR), where the distribution was approximately equal between both daughter arterioles. Therefore, Frisbee *et al.* [2011] predicted a significantly broader perfusion profile in a simulated dichotomous branching network.

Numerical simulation by Butcher *et al.* [2014] showed that the blood flow distribution in skeletal muscle arteriolar bifurcations was less variable for OZR than LZR, thus implying a loss of system flexibility. Frisbee *et al.* [2016] concludes that this loss of flexibility, which results in a constant perfusion and perfusion distribution of the microcirculation, means that adaptation to different metabolic demands (e.g. in exercise) can no longer be ensured, thus leading to early muscle fatigue [Frisbee *et al.*, 2016] as it was previously observed by Frisbee [2003].

In summary it becomes clear that fibre type composition in skeletal muscle is not fixed and responds strongly to signals such as body fat and body morphology/size [Maltin, 2008]. The overall number of muscle fibres is set *in utero* and related to birth weight [Maltin, 2008].

It has also been shown in the literature that the maternal diet can have an influence on blood vessel numbers, complexity and surface in the placenta and other key tissues in the gestational stages and young age of the offspring [Rutland *et al.*, 2007, Ma *et al.*, 2010, Linderman & Boegehold, 1996a,b, Culver & Dickinson, 2010]. In order to study this effect of maternal diet on the microvasculature, models of developmental priming are being used.

2.3.1 Animal models of developmental priming

A number of different approaches exist for animal models of developmental priming through diet. Maternal undernutrition, e.g., restriction of nutrient requirements or low protein diets, has been studied [Pladys *et al.*, 2005], [Costello *et al.*, 2008], [Samuelsson *et al.*, 2008], [Torrens *et al.*, 2009], [Rutland *et al.*, 2007], as well as the effect of maternal overnutrition, e.g., high fat intake, [Bruce *et al.*, 2009], [Torrens *et al.*, 2012], [Ma *et al.*, 2010]. The animals used in these models are primarily rodents or sheep [Torrens *et al.*, 2009], [Ma *et al.*, 2010], [Rutland *et al.*, 2007].

The model used by the group at the University of Southampton to study overnutrition by increased fat intake is built up as following [Bruce *et al.*, 2009, Torrens *et al.*, 2012, Stead *et al.*, 2016, Ainge *et al.*, 2011]: dams are fed either a normal chow diet (C) or a high-fat diet (HF) for at least 35 days prior to mating, during pregnancy and lactation. Their respective offspring is then again divided into two groups that are being fed the respective diets. Thus, the offspring can be divided into four groups: CC, CHF, HFC and HFHF. This is displayed in figure 2.10.

In this model, the different groups display different phenotypes at 15 weeks of age [Bruce *et al.*, 2009, Torrens *et al.*, 2012, Stead *et al.*, 2016]. CHF and HFHF mice have a significantly higher body weight than the other groups, which is associated with a higher percentage of fat to lean tissue in the body, see figures 2.11(a) and 2.11(b)

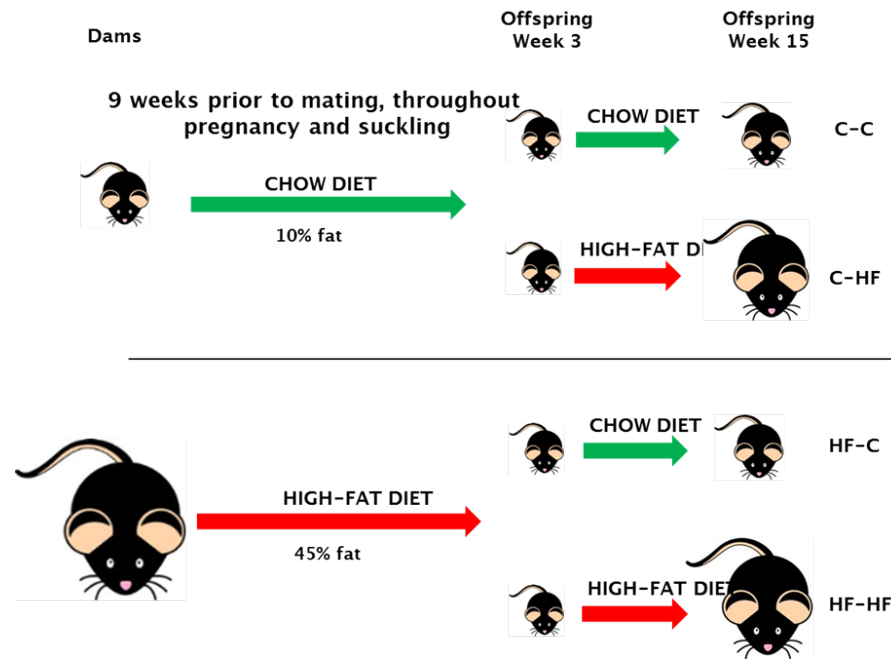


Figure 2.10: **Maternal high fat mouse model of developmental priming of the microvasculature.** Dams are fed either a normal chow diet (C) or a high-fat diet (HF) for 9 weeks prior to mating, during pregnancy and lactation. Their respective offspring is then again divided into two groups that are being fed the respective diets. Thus, the offspring can be divided into four groups: CC, CHF, HFC and HFHF. This schematic is courtesy of Moji Musa.

[Torrens *et al.*, 2012, Stead *et al.*, 2016]. The blood pressure is also significantly higher in the HFHF group, both for systolic and diastolic pressure, as shown in figure 2.11(c) [Torrens *et al.*, 2012, Stead *et al.*, 2016]. Additionally, the glucose level is higher in HFHF and in particular in the CHF group, see figure 2.11(d) [Stead *et al.*, 2016]. The same was found for offspring of overnourished dams by Samuelsson *et al.* [2008] and Elahi *et al.* [2009], which again exhibited an increase in body mass, high blood pressure and reduced insulin sensitivity.

Figure 2.12 shows that the skeletal muscle oxidative stress (accumulation of reactive oxygen species to a damaging level) is significantly higher in all groups compared to the control CC group [Torrens *et al.*, 2012], which lead to impaired vasorelaxation.

The impact of maternal fat intake on the development of disease such as non-alcoholic fatty liver disease (NAFLD) [Bruce *et al.*, 2009] in offspring has been studied previously. Bruce *et al.* [2009] found that HFHF mice develop non-alcoholic steatohepatitis (NASH) and CHF and HFC display advanced steatosis.

Switching to a healthier post-natal diet does not necessarily guarantee a bettering of the symptoms, yet a continuation of overnutrition will likely worsen the symptoms [Torrens *et al.*, 2012], as reviewed by Ainge *et al.* [2011] and Musa *et al.* [2014]

Bayol *et al.* [2005, 2009] used a cafeteria (high-fat and high-sugar) diet and showed that offspring of the cafeteria diet-fed mice experienced a 25% reduction in muscle

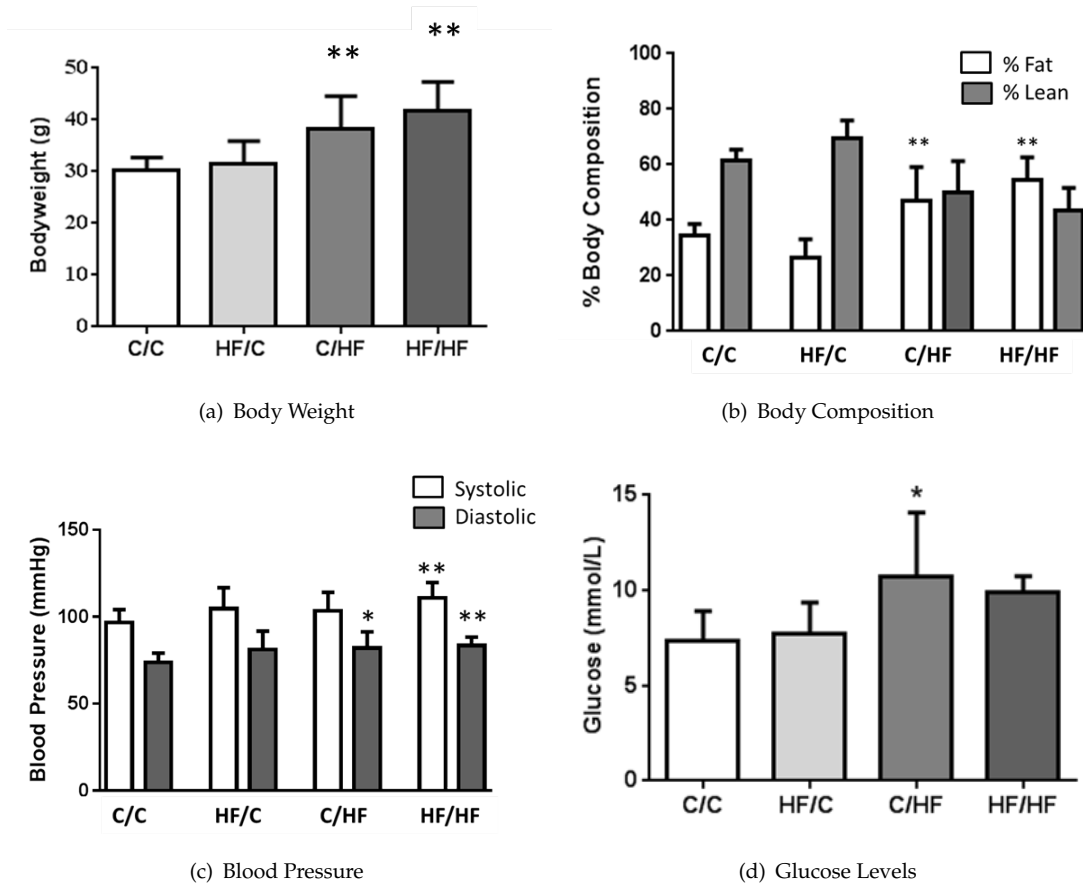


Figure 2.11: **Phenotype of offspring groups of the animal model of developmental priming at 15 weeks of age.** Animals of the HFHF group show a significantly worsened phenotype in body weight, fat percentage and blood pressure. Similarly, the CHF group shows elevated bodyweight, diastolic pressure, fat percentage and elevated glucose levels. Data published in Stead *et al.* [2016].

cross-sectional area and a decrease of 20% in muscle fibre number in comparison to control animals. Intramuscular fat was higher in offspring of the high-fat fed dams that was further fed a cafeteria diet during lactation compared to offspring then fed a standard chow diet. Furthermore, both of these groups showed pre-stages of reduced insulin sensitivity [Bayol *et al.*, 2005].

It has further been shown that a maternal high-fat diet leads to a decrease in exercise performance and training efficiency in male offspring, which were fed a low fat diet (10% energy from fat) [Walter & Klaus, 2014]. This was linked to a perturbation in lipid and glucose metabolism in the skeletal muscle of this offspring [Walter & Klaus, 2014]. Rodriguez-Porcel *et al.* [2000] performed a similar study to test the impact of a high cholesterol diet on cholesterol levels in pigs, which also showed that an early high cholesterol uptake could be associated with augmented vascularisation in the cardiac muscle.

Similarly, the effect of paternal fat intake was studied in mice, which suggested that

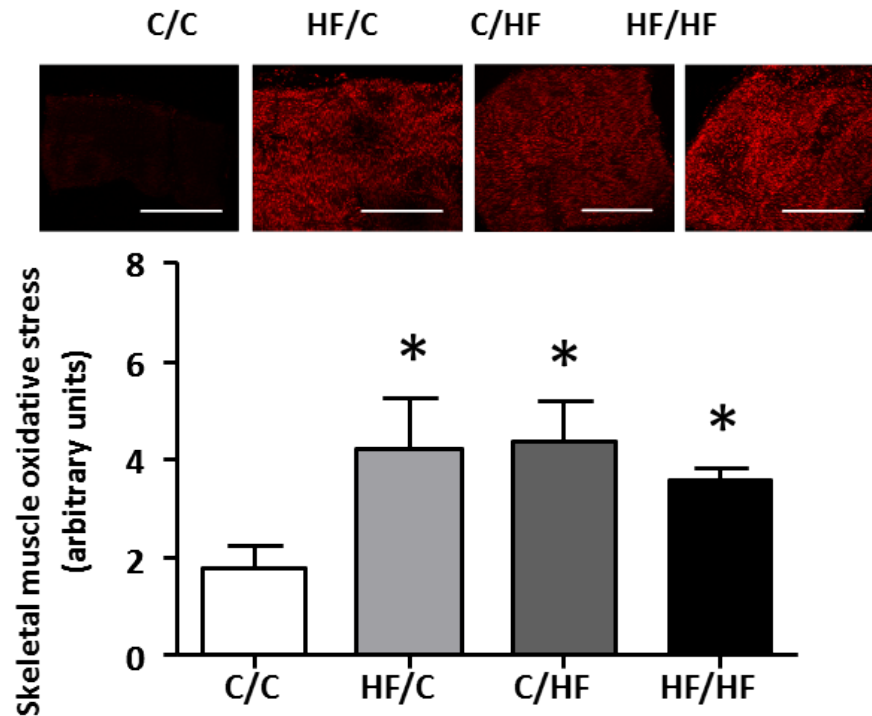


Figure 2.12: **Oxidative stress in offspring groups of the animal model of developmental priming at 15 weeks of age.** A high-fat diet (both maternal and post weaning) leads to an increase of muscle oxidative stress. Data published in Torrens *et al.* [2012].

the paternal obesity retards the embryonic development [Binder *et al.*, 2012].

For a more detailed review of studies linking cardio-metabolic disease and developmental programming, including also the assessment of endothelial function, see Drake & Reynolds [2010], Ainge *et al.* [2011], Clough & Norman [2011] and Musa *et al.* [2014].

2.3.2 Human models

Similar effects of dietary programming have been found in humans, as reviewed e.g. by Nuyt [2008] and Freeman [2010]. As mentioned in chapter 1, low birth weight is associated with development of cardio-metabolic disease, i.e., glucose intolerance, high blood pressure *etc.* The same holds for the other extreme of birth weight [Nuyt, 2008]. Birth weight has been challenged as the single determining marker for risk of cardio-metabolic disease [Nuyt, 2008], but it remains one of the main parameters studied in this context, as well as gestational age at birth. Studies have further shown however, that the negative effects associated with the extremes of birth weight can be counteracted or enhanced in postnatal life by adjustment of diet and lifestyle [Nuyt, 2008]. However, the link between birth weight/gestational age and maternal diet and

other influences in pregnancy needs to be further explored in human studies, to better identify the cause of the development of cardio-metabolic disease.

Freeman [2010] reviewed how maternal diabetes at pregnancy leads to an increase of type 2 diabetes in offspring and increased maternal weight correlated with heightened offspring percentage of body fat. Maternal obesity was further reported to lead to insulin resistance in the offspring.

In addition to the effect of birth weight on cardio-metabolic disease in offspring, the effect on muscle strength and bone development has been studied extensively, e.g., in the Hertfordshire Cohort Study [Patel *et al.*, 2010, Edwards *et al.*, 2013]. In particular, the association of muscle size and strength and bone structure was studied, determining a strong relationship between muscle size (measured as muscle cross-sectional area) and bone size and strength [Edwards *et al.*, 2013]. Kuh *et al.* [2002] found that increased birth weight was associated with an increase in grip strength, which was defined as the marker for muscle function. Accordingly, Sayer & Cooper [2005] found that low birth weight in humans and prenatal undernutrition (studied in animal models) were linked to reduced muscle mass and strength and low bone mineral content.

Also studied in the Hertfordshire Cohort Study was the effect of sarcopenia, i.e., the loss of muscle mass and function with age. It was found that sarcopenia was more likely to occur in people with lower birth weight [Sayer *et al.*, 2008]. However, muscle fibre density (fibres per square millimeter) was not significantly influenced by birth weight, in contrast to muscle fibre score (fibres kilograms per square millimeter) which was [Patel *et al.*, 2010]. Patel *et al.* [2015] further found that sarcopenia was not significantly related to capillary density or capillary-to-fibre ratio, but that it was related to satellite cell density. Satellite cells are thought to play a key role in postnatal muscle growth and repair [Sayer *et al.*, 2008]. It appears that muscle strength is less dependent on muscle oxygenation but rather on growth and repair of muscle fibres.

Whilst the cited studies provide evidence linking birth weight and cardiovascular disease, there has also been research challenging the published results. In particular the strength of associations with regard to study sample/participant numbers has been shown to decrease [Huxley *et al.*, 2002, Huxley & Neil, 2004]. Huxley *et al.* [2002] presented evidence that many studies exhibited bias in the interpretation and adjustment of results towards the hypothesis of developmental programming. Huxley & Neil [2004] themselves found no correlation between birth weight and markers for cardio-metabolic disease in a cohort of offspring of working-class women first recruited for the study towards the end of World War II. However, this study itself suffered from low offspring participation (137 compared to 400 women initially recruited), thus limiting its statistical power. The limitation of low sample numbers and resulting low statistical power is also prevalent in animal studies. Groups are often between 10 and 30 animals.

Studying the effect of maternal diet and resulting birth weight on offspring health, especially in post-natal life, in humans is difficult due to many confounding factors and the long times required [Segovia *et al.*, 2014], thus making animal studies the preferable choice. However, the translation of findings from animal models to humans regarding programming-induced alterations and intervention mechanisms is described as difficult, due to gender-specificity or adverse responses [Vickers, 2011] and due to inaccuracies in the description of diseases [Armitage *et al.*, 2004]. Furthermore, the major limitation of rodent models is the differing development in comparison to humans, with the majority of the maturation process occurring during weaning [Armitage *et al.*, 2004]. Some of these limitations are lifted in guinea-pig and primate models [Armitage *et al.*, 2004]. Another limitation in the comparability of the animal models themselves is the large variability of dietary composition studying the same effects, e.g., the carbohydrates can be supplied in the form of starch or glucose and the profile of fatty acids can vary considerably [Armitage *et al.*, 2004]. Overall however, the observed outcomes from developmental priming through diet in animals are similar and in agreement with those seen in humans [Armitage *et al.*, 2004]. For an in-depth comparison of the different compositions and resulting effects see Armitage *et al.* [2004]. Whilst animal models can clearly give initial indications on effects of maternal dietary programming, long-term studies in humans eventually need to follow.

In this work I am concentrating on the influence of maternal and offspring high fat intake on the structural development of skeletal muscle microvasculature. To this end, the mouse model that has been well established in our group [Bruce *et al.*, 2009, Torrens *et al.*, 2012, Stead *et al.*, 2016] is used. The dietary influence on the function of resistance arteries Torrens *et al.* [2012] and arterioles Stead *et al.* [2016] has been shown in particular for this model. Due to the development of muscles and organs in late gestation and early life it is possible that dietary stress impacts the growth, numbers and organisation of the muscle fibres and the microvessels within, as suggested by Bayol *et al.* [2005]. This body of knowledge is aimed to be expanded through the non-invasive three-dimensional imaging of the microcirculation performed in the course of this work.

Secondary reasons for making a mouse model the preferable choice for this project are the relatively small costs as litter size in mice is relatively high and the times for breeding relatively small. The mouse muscles are inherently smaller than those of other mammals commonly studied, which makes the process of imaging the muscles easier, as the muscle will fit more easily into the field of view when imaging at a certain resolution.

In the following I will review the structural parameters typically used to assess the microvasculature in skeletal muscle and report changes in these that have previously been observed due to dietary influences.

2.4 Assessment of microvascular oxygen exchange capability

Traditionally, the oxygen exchange capability of microvascular networks in skeletal muscle in terms of their anatomy is assessed using stereological measures on transverse and longitudinal cross-sections of the muscle tissue. The most frequently used measures are given in table 1. Differences in the resulting numbers of those measures between healthy and diseased animals are investigated and assumed to be related to the disease (see examples in table 1). Morphometric analysis looks at the shape and size of structures using statistical measures. This is possible in two or three dimensions. Stereology in turn looks at three-dimensional parameters that define a structure and can be translated into two-dimensional measurements that can be obtained on planar sections of the structure Skalak & Chien [1987]. I will next describe a number of different morphometric measures that are usually used to describe vascular networks. Some of these are often used in stereology but can be extended to a 3D network analysis. The 3D approach has the advantage of enabling an unbiased analysis of these measures, whereas there is always a bias when determining in which direction to section the sample under investigation. Erzen *et al.* [2011] showed that the 2D approach can for example lead to an underestimation of capillary length of up to 75%.

2.4.1 Capillary density

The capillary density (CD) is the number of capillaries per mm^2 . This number is assumed to give a good estimate of the oxygen supply capability and hence aerobic metabolism of a muscle [Hudlicka, 1985]. However, this is only the case if all capillaries are indeed perfused. The capillary density depends strongly on the diameter of muscle fibres, i.e., a muscle with larger fibres has a lower CD [Murakami *et al.*, 2010]. Dapp *et al.* [2004] found a CD of $1199 \pm 681 \text{ mm}^{-2}$ for mouse soleus muscle. Similarly, Audet *et al.* [2013] found an average CD of 1300 mm^{-2} . Davidson *et al.* [1999] determined a lower value of $867 \pm 100 \text{ mm}^{-2}$ in young mice, which increased to $1013 \pm 133 \text{ mm}^{-2}$ in older mice. Frisbee [2005] reported a decrease in capillary density from $\approx 890 \text{ mm}^{-2}$ in 15-17 week old lean Zucker rats to $< 700 \text{ mm}^{-2}$ in age-matched obese Zucker rats, which was a reduction by $\approx 23\%$.

2.4.2 Capillary-to-fibre ratio

The capillary-to-fibre ratio is the mean number of capillaries that are adjacent to a particular muscle fibre. Similar to the capillary density, this value gives information on the metabolic activity of the muscle. For mouse soleus muscle Poole *et al.* [1989] found a capillary-to-fibre ratio of 2.17 ± 0.06 and Hudlicka [1985] found 2.3 ± 0.03 .

Dapp *et al.* [2004] reported a capillary-to-fibre ratio of 1.83 ± 0.04 . This shows that the capillary-to-fibre ratio yields relatively consistent results. As the capillary-to-fibre ratio does not depend on muscle fibre area it may not immediately yield information about oxygen supply capability, although it does depend on fibre type.

2.4.3 Tortuosity in Skeletal Muscle

Tortuosity is a metric that is often studied when looking at the vasculature of organs and muscles, as it is assumed that higher tortuosity of vessels, through increase of surface area and reduction of oxygen diffusion distances, can be associated with an increased oxygen supply [Gaudio *et al.*, 1984]. There are a number of different metrics used for the determination of tortuosity, for comparability to other literature, I will use the most common distance metric:

$$T = \frac{1}{N} \sum_{i=1}^N \frac{\text{Vessel segment length}}{\text{Euclidian distance between the segment's end points}}. \quad (2.1)$$

Another metric, the sum-of-angle metric, was defined by Bullitt *et al.* [2003], and also used in [Lang *et al.*, 2012]:

$$SOAM = \frac{\sum_{k=2}^{n-2} \left(\sqrt{\gamma_1^2 + \gamma_2^2} \right)}{L}, \quad (2.2)$$

where γ_1 is the in-plane angle and γ_2 the tortuos angle.

However, there is also discussion that tortuosity has do less with the oxygen demand and supply but is rather simply related to the contractile state of the muscle and therefore the sarcomere length [Poole *et al.*, 1992, Mathieu-Costello, 1987, Mathieu-Costello *et al.*, 1989], see figure 2.13 for a schematic.

Poole *et al.* [1992] found that tortuosity in capillaries increases when the sarcomere length is reduced below $2.0 - 2.4 \mu\text{m}$. Furthermore, it was found that the length of the capillary network depends to 24-38% on the tortuosity Mathieu-Costello *et al.* [1988]. Moreover, Mathieu-Costello *et al.* [1989] and Poole *et al.* [1989] found no significant link between capillary tortuosity and body size, training, athletic ability or aerobic capacity. Mathieu-Costello [1987] also found that the error made when estimating tortuosity using transverse sections instead of a mixture of transverse and longitudinal sections can be up to 56%.

As we are using a 3D imaging technique, the issues related to sectioning to not apply. However, it should be ensured that the mouse leg is pinned at always the same angle for dissection so that the same soleus contractile state is comparable.

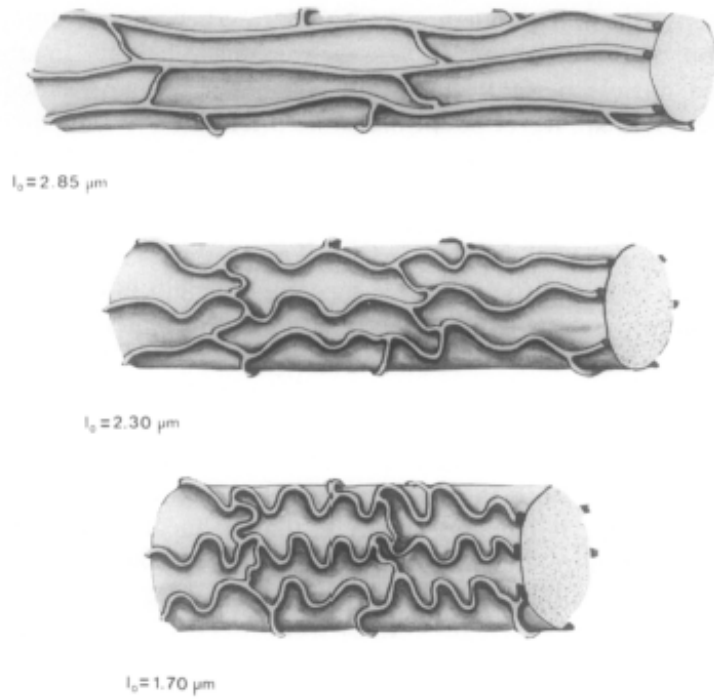


Figure 2.13: **Dependence of tortuosity on sarcomere length.** Taken without permission from Mathieu-Costello *et al.* [1989].

2.4.4 Length Density

The three-dimensional vascular length density is defined as [Safaeian *et al.*, 2010]:

$$L_D = \frac{1}{V_{tissue}} \sum_i^N L_i, \quad (2.3)$$

where L_i is the length of vessel segment i and there is a total number of vessel segments N .

This measure of length density is different to the standard stereological length density J_V , which is a two-dimensional measure and is defined as

$$J_V(a, c) = 2Q(a)/A(c), \quad (2.4)$$

with a the anisotropic structure being looked at, c the containing specimen, $Q(a)$ the point count of a on c and $A(c)$ the area of c Skalak & Chien [1987]. This needs to be considered when comparing measured values with the literature. Also, this form of length density depends on the angle and thickness of sectioning and on the degree of orientation of the objects. Poole *et al.* [1989] found a length density of $1886 \pm 73 \text{ mm}^{-2}$ in rat soleus. Dapp *et al.* [2004] found a total capillary length of $12056 \pm 901 \text{ mm}$ in mouse soleus. Georgi *et al.* [2011] reported an increase in mean total network length of 60% in the cremaster muscle of obese mice compared to age-matched C57/BL6 mice.

Diabetes on the other hand led to a 49% decrease in network length. Benedict *et al.* [2011] found a decrease of 19% in length density in 10-11 week-old Zucker diabetic fatty rats (ZDF) ($293 \pm 51.9 \text{ mm}^{-2}$ in control *vs.* $239 \pm 19 \text{ mm}^{-2}$ in ZDF). The capillary diameter was found not to have changed, thus the volume fraction would be affected accordingly.

2.4.5 Volume Fraction

Vascular volume fraction is defined as

$$V_F = \frac{V_{\text{vessels}}}{V_{\text{tissue}}}, \quad (2.5)$$

where V_{vessels} is the volume of vessels and V_{tissue} the tissue volume.

Kondo *et al.* [2011] showed that rats with type 2 diabetes displayed a difference in capillary volume in the soleus muscle though not necessarily in capillary number, which would be picked up by our measure of volume fraction. A distribution of capillary diameter showed a skew to the smaller diameters, i.e., 3 and 4 μm with a mean of $3.1 \pm 0.2 \mu\text{m}$, in the diabetic rats, whereas capillary diameter for the control rats was centered around 5 and 6 μm with a mean of $5.1 \pm 0.3 \mu\text{m}$. The capillary volume was 47% lower in the diabetic rats than in the control group. It may therefore be expected volume fraction to be an important measure to assess in our animal model.

2.4.6 Fractal Analysis

Another measure that is often used to group and characterise blood vessel networks is the fractal dimension. The idea for this comes from so-called self-similar structures. These are structures that *can be broken down into arbitrarily small pieces, each of which is a small replica of the entire structure* [Peitgen *et al.*, 1992]. The self-similarity dimension is then defined as [Peitgen *et al.*, 1992] follows:

Given a self-similar structure, there is a relation between the reduction factor s and the number of pieces a into which the structure can be divided

$$a = \frac{1}{s^D}, \quad (2.6)$$

where D is called the self-similarity dimension. However, blood vessel networks are not strictly self-similar, as there is a smallest dimension to them. For these *quasi self-similar* structures there is an analogue dimension, which is the *box-counting dimension* [Peitgen *et al.*, 1992]. This dimension is obtained by setting a regular mesh with mesh size s on top of the structure and counting the number of boxes $N(s)$ that cover some of the structure. s is progressively changed and with the corresponding $N(s)$ a log diagram $\log(N(s))/\log(1/s)$ can be obtained, where the slope D_b of a linear

fit to the diagram is then the box-counting dimension [Peitgen *et al.*, 1992].

The computation of D_b is very fast, yet the disadvantage of the method lies in the fact that the fractal dimension appears to have no obvious physiological meaning. It can still be used for grouping of samples.

For example, fractal box counting has often been used for the grouping of normal and tumour/diseased vascular networks Gazit *et al.* [1995], Lorthois & Cassot [2010]. The normal networks can clearly be distinguished into arteriovenous networks and capillary networks, which differ in their compactivity. Gazit *et al.* [1995] determined a fractal dimension of $d = 1.70 \pm 0.03$ for normal arteriovenous subcutaneous vascular networks, $d = 1.99 \pm 0.01$ for the capillary network and 1.88 ± 0.04 for tumour networks, so a grouping was clearly possible. It may be possible that such a grouping capability is also feasible for microvascular networks differing by dietary conditions. Gould *et al.* [2011] found a fractal dimension of 1.70 ± 0.05 in mouse muscle. Similarly, the fractal dimension for retinal vascular networks was found to be approximately 1.70 by Masters [2004], which is in general the fractal dimension for two-dimensional diffusion-limited growth processes, to which also the arteriovenous network belongs [Gazit *et al.*, 1995, Masters, 2004]. For three-dimensional diffusion-limited growth processes the fractal dimension lies between 2.4 and 2.5, as has been determined from diffusion limited aggregation (DLA) simulations [Peitgen *et al.*, 1992], also known as Laplacian fractals. However, the dimension determined from such simulations depends largely on modelling parameters chosen, e.g., the probability for particles sticking to one another.

2.4.7 Other measures

Other measures that have been studied extensively by Janacek *et al.* [2009], Cebasek *et al.* [2006], Cebasek *et al.* [2010], Erzen *et al.* [2011] are capillary length adjacent to individual muscle fibre per fibre length (L_{cap}/L_{fib}), fibre surface area (L_{cap}/S_{fib}) or fibre volume (L_{cap}/V_{fib}). Janacek *et al.* [2009] and Cebasek *et al.* [2010] found clear differences for these measures between soleus and extensor digitorum longus muscles. However, they have used confocal microscopy for imaging, which gives a very limited depth of fibres and capillaries.

The fibre volume measure L_{cap}/V_{fib} is very similar to the above measure of length density if taking only the capillaries into account, so we may compare our values to their findings, which however show high variability, i.e., $2029 \pm 170 \text{ mm}^{-2}$ [Cebasek *et al.*, 2006].

All the above measures take into account only the blood vessels that have been visualised by a specific imaging technique. Differences in numbers of these measures between healthy and diseased subjects are then used to associate the disease with the capillary oxygen exchange capability. Poole *et al.* [2013] oppose this approach to

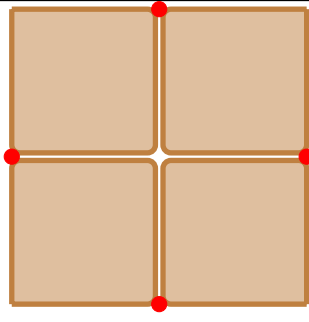
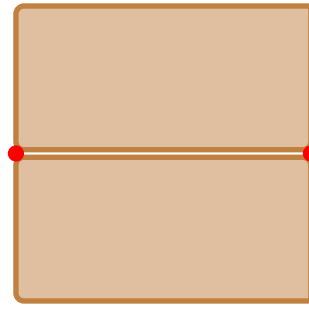
examine O₂ supply and reviewed the literature to show that impairment of vessel function has to do with differences in flux, i.e., RBC flux, blood-myocyte oxygen flux, and haematocrit, rather than number and volume of perfused capillaries. RBC flux is present in most capillaries at rest and increases with exercise to fulfil the muscle demand [Poole *et al.*, 2013]. In agreement with this, Maeda *et al.* [2015] reported that the number of capillaries exchanging oxygen was $93.0 \pm 5.5\%$ of all blood perfused capillaries in rat soleus muscle. A higher difference in these numbers was found by Fraser *et al.* [2015] in rat extensor digitorum longus muscle (EDL), i.e., around 12% of visible capillaries stayed unperfused during observation periods of 60 seconds. Overall, it remains inconclusive whether or not structural measures of muscle capillarisation can be used as explicit indicators of oxygen exchange capability. Mathematical modelling can help clarify this question. An association between metabolic syndrome and skeletal muscle microvascular haematocrit has also been found [Fraser *et al.*, 2013], thus suggesting that for investigating the impairment of microvascular oxygen exchange capability, not only the morphology of the blood vessels has to be taken in to account, but also the distribution of red blood cells within the vessels. Therefore, in order to assess microvascular oxygen exchange capacity meaningfully, the imaging technique adopted should be able to resolve the microvascular network structure, and simultaneously the distribution of RBCs within the blood vessels, and if possible, record changes of the network structure and the RBC distribution over time. By using mathematical modelling it is possible to study the muscle tissue oxygenation of different capillary networks (i.e., vascular function) and to link the results to the structural measures of those networks (i.e., vascular structure). This will increase the understanding of structure-function relationships for (micro)vascular systems.

2.5 Summary

The biological and clinical background to muscle anatomy and nutrient delivery in skeletal muscle have now been presented. The biological process of oxygen diffusion out of the blood vessels into the muscle tissue has been introduced.

The association of changes in the microvascular structure and disease was discussed and the influence of maternal and/or offspring diets on microvascular structure and skeletal muscle development. Typical structural parameters used for assessment of the microvasculature have been introduced.

Following this chapter it has become clear that length scales between 5 μm (the capillary diameter) and 8 mm (the average length of a murine soleus muscle) need to be resolved in order to non-invasively image the three-dimensional microvascular structure in skeletal muscle. This inherently determines the imaging system to address the research question.

Parameter	Definition	Example	Advantages	Disadvantages	Reference
Capillary density (CD)	# capillaries per muscle area	 <p>1 mm CD=4/mm² C:F=2</p>	<ul style="list-style-type: none"> • Easy to compute • Easy to automate 	<ul style="list-style-type: none"> • Dependent on fibre size and type • 2D measure 	<ul style="list-style-type: none"> • 1199 ± 681 mm⁻² mouse soleus [Dapp <i>et al.</i>, 2004] • 1300 mm⁻² mouse soleus [Audet <i>et al.</i>, 2013] • 867 ± 100 mm⁻² in young (6 month) mouse soleus
Capillary-to-fibre ratio (C:F)	# capillaries per muscle fibre	 <p>1 mm CD=2/mm² C:F=2</p>	<ul style="list-style-type: none"> • Gives information on metabolic activity • Independent of fibre size • Dependent of fibre type • Easy to compute • Easy to automate 	<ul style="list-style-type: none"> • 2D measure 	<ul style="list-style-type: none"> • 2.30 ± 0.03 mouse soleus [Hudlicka, 1985] • 2.17 ± 0.06 mouse soleus [Poole <i>et al.</i>, 1989] • 1.83 ± 0.04 mouse soleus [Dapp <i>et al.</i>, 2004]

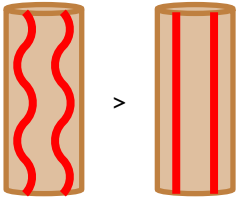
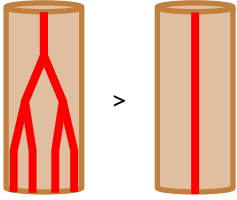
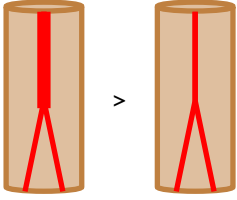
Tortuosity	$\frac{\text{Vessel segment length}}{\text{Euclidian distance}}$		<ul style="list-style-type: none"> • Easy to automate 	<ul style="list-style-type: none"> • Not related to oxygen demand but sarcomere length • Different definitions available • Connected vessel network required 	<ul style="list-style-type: none"> • 1.86 ± 0.06 in healthy rat soleus vs. 1.19 ± 0.10 in diabetic rat [Kondo <i>et al.</i>, 2011]
Length density	$\frac{\text{Vessel segment length}}{\text{Tissue volume}}$		<ul style="list-style-type: none"> • Indication for available oxygen exchange length 	<ul style="list-style-type: none"> • No information on exchange volume • May differ to original stereological definition • Depends on tortuosity 	<ul style="list-style-type: none"> • $1.88 \pm 0.07 \cdot 10^3 \text{ mm}^{-2}$ mouse soleus [Poole <i>et al.</i>, 1989] • $12.06 \pm 0.90 \cdot 10^3 \text{ mm}$ mouse soleus total capillary length [Dapp <i>et al.</i>, 2004]
Volume fraction	$\frac{\text{Vessel volume}}{\text{Tissue volume}}$		<ul style="list-style-type: none"> • Indication for available oxygen exchange volume 	<ul style="list-style-type: none"> • No information on exchange length • Computationally difficult 	<ul style="list-style-type: none"> • 0.07 ± 0.01 in healthy rat soleus vs. 0.03 ± 0.01 in diabetic rat [Kondo <i>et al.</i>, 2011]

Table 2.1: **Structural parameters used for assessing the microvasculature.** Capillary density, capillary-to-fibre ratio, tortuosity, length density and volume fraction are parameters often used to describe the structure of blood vessel.

Chapter 3

Literature review on soft tissue imaging

A range of techniques exists to image biological soft tissues, ranging from 2D to 3D methods with resolutions from several hundred micrometres down to a tenth of a nanometer. As the smallest vessels in the microvascular structure have a diameter of only 5-10 μm , it is desired to have instruments that are capable of imaging at such spatial resolutions and preferably below that.

In the following an overview of different techniques for imaging the microcirculation will be presented and compared with respect to resolution, depth of field, scanning times etc. Micro-computed tomography (μCT) and synchrotron radiation computed tomography (SR CT) will turn out to be best fitted to image the microvasculature for structural analysis. Thus, methods to induce soft tissue contrast for these imaging techniques will be presented and the principles of μCT and SR CT will be introduced.

3.1 Overview of imaging methods

Different imaging techniques consist of the same two fundamental components: a source and a detector. The source generates an excitation signal. This signal interacts with the sample lying in the signal path. The interaction of the signal with the sample either changes the original signal and/or generates a new signal emitted by the sample. The detector captures this changed and/or new signal. Excitation signals include visible light, electron beams, X-rays, magnetic pulses, positrons or acoustic waves [Rochow & Tucker, 1994]. Different imaging techniques can be distinguished by their different characteristics, such as 2D or 3D readouts, excitation mechanism, capability to penetrate tissue and compatibility for imaging *in vivo* or *ex vivo*. Imaging systems for the visualisation of vascular networks have been reviewed extensively, e.g., in the context of blood flow modelling by Kim *et al.* [2012], angiogenesis by

Kiessling *et al.* [2010] and systems biology by Kherlopian *et al.* [2008].

Table 3.1 gives an overview of contemporary imaging methods, with respect to their capabilities. A discussion of these can be found in appendix A.

3.1.1 Methods for *ex vivo* imaging of murine skeletal muscle

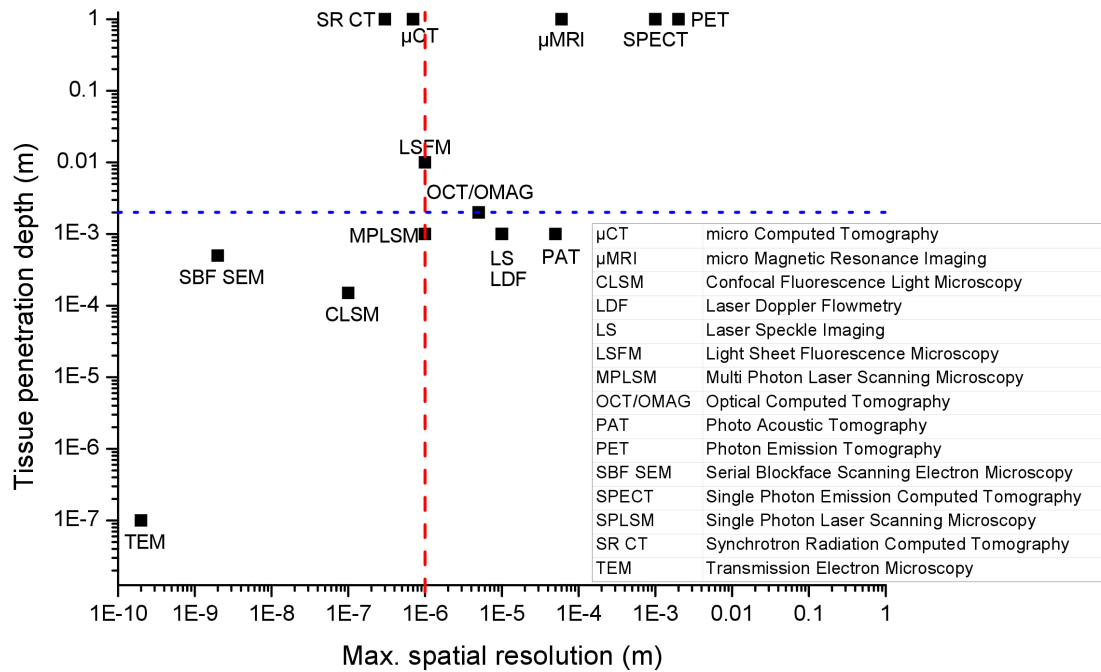


Figure 3.1: **Comparison of different imaging techniques with regard to maximum spatial resolution and tissue penetration depth.** The dashed red line marks $1\ \mu\text{m}$, which is the spatial resolution required to resolve the capillaries. The dotted blue line indicates the minimal tissue penetration required, based on murine muscle dimensions of $\sim 0.2 \times 0.2 \times 0.8\ \text{cm}^3$. The top left quadrant covers high-resolution 3D imaging techniques that are appropriate to assess the (muscle) microvasculature and includes micro-computed tomography (μCT), synchrotron-based CT (SR CT) and light sheet fluorescence microscopy (LSFM).

The scatter graph in figure 3.1 was created based on the information about the different imaging systems and compares their maximum spatial resolution and tissue penetration depth. For the three-dimensional (3D) imaging of the microvasculature, only techniques with a spatial resolution of about $1\text{--}1.5\ \mu\text{m}$ can be considered. By that, the finest capillaries of $5\ \mu\text{m}$ diameter will be represented by 3-5 voxels. The dashed red line in Figure 3.1 marks this limit. Furthermore, in order to non-destructively image the whole microvasculature within a murine soleus muscle of dimensions $\sim 0.2 \times 0.2 \times 0.8\ \text{cm}^3$ it is necessary to apply a technique that provides sufficient depth of field, i.e., about $0.2\ \text{cm}$. The only techniques providing this are μCT , SR CT and lightsheet fluorescence microscopy (LSFM). The resolution of μCT is sufficient to image the microvasculature, hence the usage of higher resolution μCT is not necessary as the imaging volume per scan would be very small and the imaging time for the

Technique	Excitation signal	Maximum spatial resolution	2D/ 3D	Penetration depth	Tissue preparation	Acquisition time	<i>in vivo</i> / <i>ex vivo</i>
Light microscopy (LM)	Light	0.2 μm	2D	-	staining	seconds	<i>ex vivo</i>
Confocal laser scanning microscopy (CLSM)	Light laser	0.1 μm	2D	150 μm	fluorescent staining	minutes	<i>ex vivo</i>
Lightsheet fluorescence microscopy (LSFM)	Light laser	0.2 μm	2D	1 cm	fluorescent staining	hours	<i>ex vivo</i>
Single Photon Laser Scanning Microscopy (SPLSM)	Light laser	0.2 μm	2D	-	fluorescent staining	minutes	<i>in vivo</i>
Multi photon laser scanning microscopy (MPLSM)	Light laser	0.2 μm	2D	1 mm	fluorescent staining	minutes	<i>in vivo</i>
Optical coherence tomography (OCT)	Light laser	5 μm	3D	2 mm	-	minutes	<i>in vivo</i>
Laser speckle contrast imaging (LS)	Light laser	10 μm	2D	1 mm	-	minutes	<i>in vivo</i>
Laser doppler flowmetry (LDF)	Light laser	10 μm	2D	1 mm	-	minutes	<i>in vivo</i>
Serial blockface scanning electron microscopy (SBF SEM)	Electron beam	2 nm	3D	500 μm	heavy metal staining	hours	<i>ex vivo</i>
Transmission electron microscopy (TEM)	Electron beam	0.2 nm	2D	100 nm	heavy metal staining	minutes	<i>ex vivo</i>
Micro-computed tomography (μCT)	X-rays	0.7 μm	3D	1 m	staining or perfusion	hours	<i>ex vivo</i>
Synchrotron radiation-based computed tomography (SR CT)	X-rays	0.3 μm	3D	1 m	staining or perfusion	minutes	<i>ex vivo</i>
Micro-magnetic resonance imaging (μMRI)	Magnetic pulse	60 μm	3D	1 m	contrast agent perfusion	hours	<i>in vivo</i>
Positron emission tomography (PET/SPECT)	Positrons	1-2 mm	3D	1 m	contrast agent perfusion	hours	<i>in vivo</i>
Photoacoustic tomography (PAT)	Acoustic waves	50 μm	3D	1 mm		hours	<i>in vivo</i>

Table 3.1: **Comparison of imaging techniques.** Imaging techniques are compared in terms of excitation signals, spatial resolution, penetration depth, preparation for image contrast, image acquisition times, imaging dimensions and *in vivo* imaging capability. For references and discussion see appendix A.

whole muscle would be too long. Therefore, μ CT and SR CT were used to obtain the three-dimensional vascular architecture in the murine soleus muscle. Furthermore, as transversal and longitudinal sectioning is still the gold standard for the assessment of muscle vasculature, light microscopy (LM) of histological sections obtained after scanning has been performed (see chapter 6). Additionally, LSFM should be considered to compare results in the future and will thus be shortly introduced.

3.1.1.1 Light sheet fluorescent microscopy

LSFM is a relatively recent development of light microscopy, where a laser is used to create a light sheet, which excites a several μ m thick plane within the sample. The fluorescence response of the sample is then detected [Santi, 2011]. In contrast to confocal laser scanning microscopy it has the advantage of little photobleaching (fading of the fluorescent dye due to non-specific illumination), as the fluorescent response is activated only as each plane is illuminated selectively [Huisken & Stainier, 2009]. LSFM can be employed to capture sample volumes of up to 1 cm³, without the need for any physical sectioning. The in-plane resolution of LSFM is about 1 μ m [Santi, 2011]. However, the technique requires the tissue to be cleared chemically for the laser sheet to be able to penetrate it and depends on the diffusion capability of fluorescent stains to permeate the tissue. Due to these limitations and the size of the imaging chamber, LSFM has had little application in imaging organs of larger animals. Most studies investigated zebrafish and fruit fly [Huisken & Stainier, 2009], few looked at brain neuronal activity in the mouse [Li *et al.*, 2014, Pampaloni *et al.*, 2015] and Mayer *et al.* [2012] used it to study high-endothelial venules in mouse lymph node. However, to the best of knowledge of the author, LSFM has yet to be trialled in mouse skeletal muscle for visualisation of vascularisation. Combined with μ CT, LSFM has the potential to yield more conclusive results as it can visualise features not normally observed using μ CT only, e.g., the lymphatic network, nerves and different cellular structures.

To induce image contrast Janacek *et al.* [2009] and Cebasek *et al.* [2010] have reported use of the primary mouse anti-rat cluster of differentiation 31 (CD31), also known as PECAM-1, antibody to label the capillary endothelial cells and secondary goat anti-mouse antibodies Alexa Fluor 488 (green) for the capillaries. The basal lamina was visualised in red by using secondary goat anti-mouse antibody Alexa Fluor 546. The oxidative metabolism of the muscle fibres was visualised by immersion of the sample into NADH-tetrazolium(TR) anenzyme. Alexa Fluor dyes are resistant to fading, which makes them recommendable for staining.

3.2 The principles of computed tomography

Computed tomography (CT) first became available for clinical use in 1971, after Godfrey N. Hounsfield had developed an algebraic reconstruction algorithm to analyse X-ray images of the brain [Hounsfield, 1973]. Previously Allen M. Cormack had used an inversion formula to determine radiation absorption within the body [Leahy, 2012]. The image reconstruction algorithms are based on a transform developed by Johann Radon in 1917 that allows reconstruction of an object with n -components from its $(n - 1)$ -dimensional projections [Radon, 1917]. Since the clinical implementation of CT scanners, the technology has quickly developed and is now extending to the diffraction limit of visible light.

3.2.1 X-ray generation

In the following, both the setup of lab-based and synchrotron based μ CT are presented, as both have been used in the course of this project.

3.2.1.1 X-ray generation in lab-based computed tomography

The setup of μ CT scanners in their current generation is such that in an electron gun an electron beam is generated from a filament (generally tungsten, but other materials, e.g. iridium, are also possible) which is a cathode and emitted towards the anode, the *target* [Hsieh, 2015], which is usually made of tungsten (W), molybdenum (Mo) or silver (S) [Landis & Keane, 2010]. On its way the electron beam is focussed by coils to strike the target in as small a focal spot as possible. As the electron beam hits the target, X-rays are emitted as a cone beam. See figure 3.2 for a sketch of the cross-section of a microfocus X-ray tube from [Xra, 2016].

The emitted X-ray spectrum is continuous, consisting of *Bremsstrahlung* resulting from the slowing down of the electrons by the target material's nuclei and of characteristic X-rays resulting from electrons in the K-M shells of the target material being ejected by the high-speed electrons. These X-rays are characteristic for each target material. Because of the spread of the resulting X-ray spectrum, lab-based X-ray sources are called *polychromatic*. Figure 3.3 depicts an exemplary X-ray spectrum taken from chapter 2 in Hsieh [2015].

3.2.1.2 X-ray generation in synchrotron radiation computed tomography

Similar to laboratory CT scanners, a synchrotron involves an electron gun where the electron beam is created. In a linear accelerator this electron beam is accelerated to

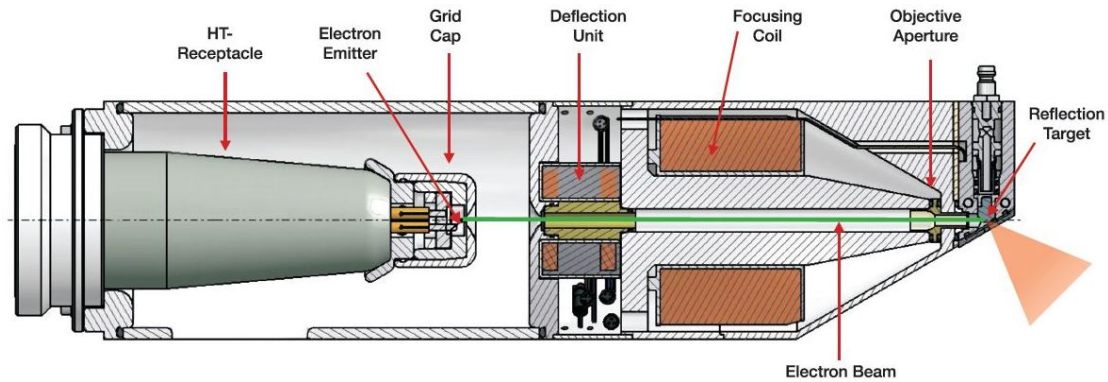


Figure 3.2: **Sketch of the cross-section of a microfocus X-ray tube from [Xra, 2016].** A filament, the cathode, is used to generate an electron beam which travels towards the anode, the so-called target. Focus coils are used to focus the electrons to achieve as small a focal spot on the target as possible. As the electron beam hits the target, X-rays are emitted as a cone beam.

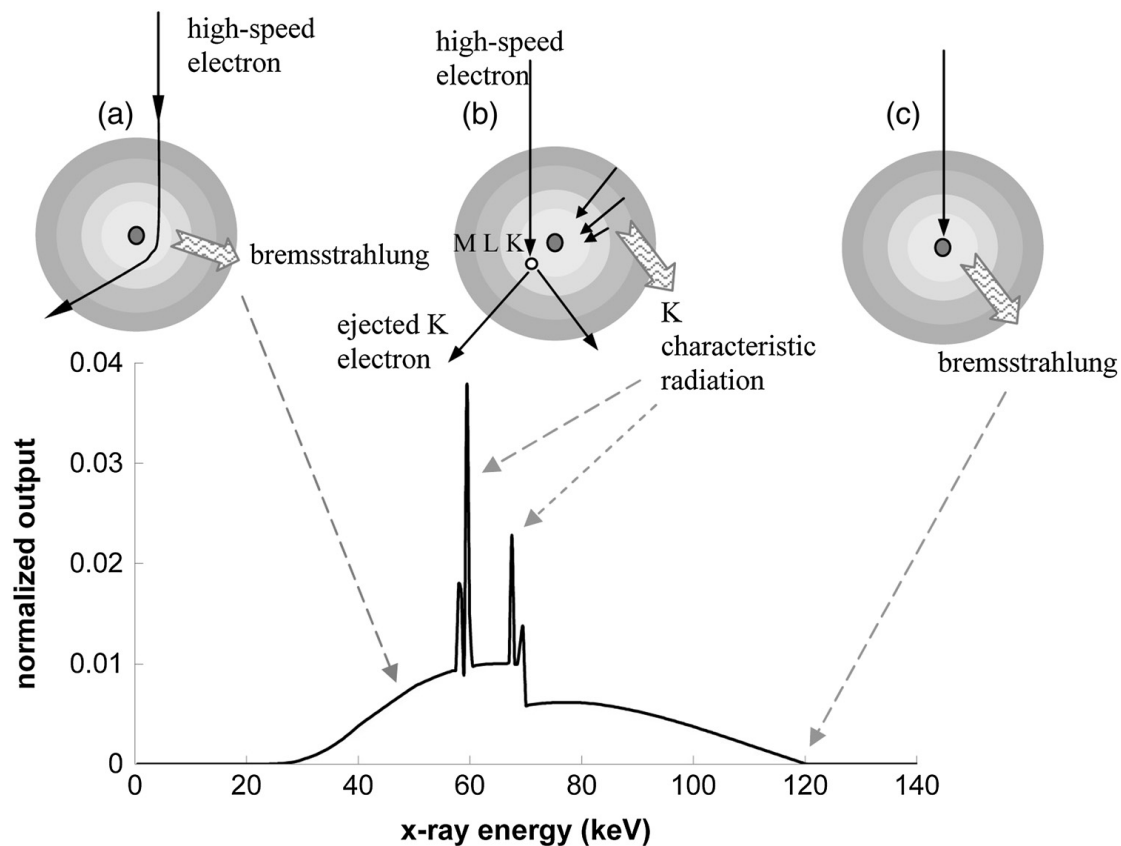


Figure 3.3: **Exemplary X-ray spectrum of a (microfocus) X-ray tube.** The X-ray spectrum emitted by the target is continuous, consisting of Bremsstrahlung and characteristic X-rays. Bremsstrahlung results from the slowing down of the electrons by the target material's nuclei. The characteristic X-rays are peaks which result from electrons in the K-M shells of the target material being ejected by the high-speed electrons and they are characteristic for each target material. Taken from chapter 2 in Hsieh [2015].

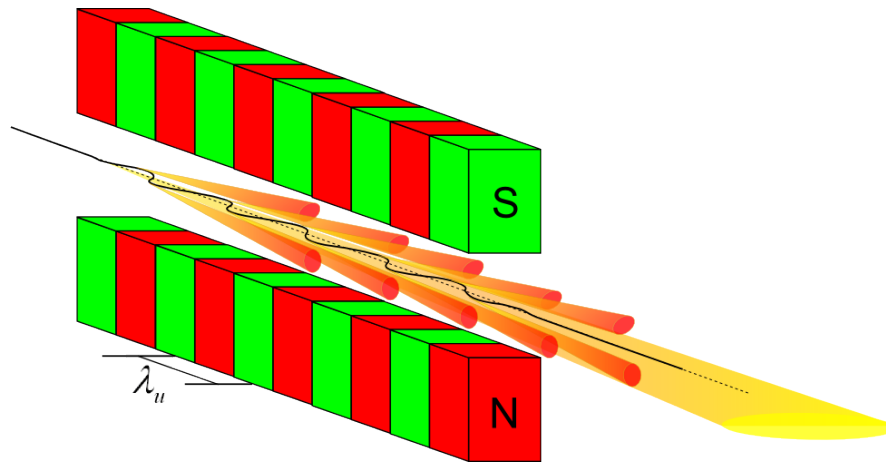


Figure 3.4: **Sketch of an undulator array.** A periodic array of magnets generates a sinusoidal oscillation of the electron beam which leads to emission of X-rays. The setup of a wiggler looks much the same in general, with longer period lengths of the dipole arrangements. This results in the angles of the emitted radiation to be much larger for the wiggler devices. The shorter period lengths in the undulator result in the X-rays being created due to relativistic effects with significantly higher brilliance than in the wiggler, where the X-rays are created by the deflection of the X-ray beam only. Image taken from [Elektronensynchrotron, 2016]

high energies (typically MeV levels). The electron beam then enters a booster synchrotron where it is further accelerated to GeV levels. Once the electrons have reached this energy, they enter the storage ring where they are kept at this energy under ultrahigh vacuum (pressure under 10^{-13} atmospheres) [Margaritondo, 2002]. *Bending magnets* in the curved sections of the ring keep the electron beam on its path. Bending of the electron beam emits X-rays. In up to 2nd generation synchrotrons this was the only method to generate X-rays, 3rd generation synchrotrons then went on to use *wigglers* and *undulators*. These are periodic arrays of magnets inserted in the straight section of the storage ring (they are thus also called insertion devices). The array of magnets with different orientations leads the electron beam to oscillate and emit X-rays of different wavelengths, depending on the strength of the magnetic field [Margaritondo, 2002], see figure 3.4 for a sketch of an undulator array from [Elektronensynchrotron, 2016]. The setup of a wiggler looks much the same in general, with longer period lengths of the dipole arrangements. This results in the angles of the emitted radiation to be much larger for the wiggler devices. The shorter period lengths in the undulator results in coherent interference of the X-rays, thus leading to a significantly more brilliant X-ray spectrum. However, as a result the spectrum of an undulator is not continuous, whilst it is continuous (but with lower brilliance) if generated by wiggler devices.

The emitted X-ray radiation is lead to the respective beamlines that are tangential to the storage ring. The beam passes through an optics hutch, where the beam is

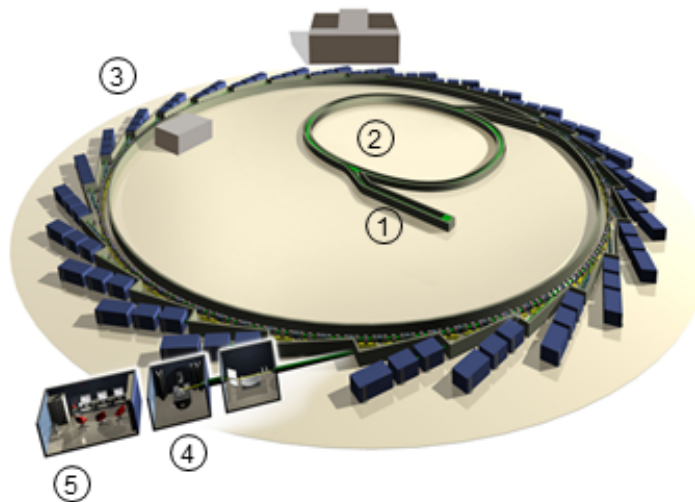


Figure 3.5: **Setup of a synchrotron [dia, 2013]:** An electron beam is created by an electron gun and accelerated in the linear accelerator (1). Here it reaches an energy of hundreds MeV. It is then further accelerated to several GeV inside the booster synchrotron (2). In the storage ring (3) it is kept at this energy. Emitted radiation reaches the experimental hutch (4), where the sample is staged and controlled via the control cabin (5).

conditioned (e.g. filtered, attenuated, shuttered, focused) and an energy band for the X-ray beam is chosen by application of the monochromator crystal. The beam then reaches the experimental hutch where sample stage and detector are located. The setup of the Diamond synchrotron is depicted in figure 3.5 [dia, 2013].

The advantage of synchrotron radiation includes the fact that the X-ray beam is coherent and spatially homogenous with high photon flux. This enables imaging modes other than conventional absorption computed tomography, i.e., phase contrast SR CT in particular and imaging can be performed at fast speeds due to smaller exposure times necessary for high photon flux.

3.2.2 Data acquisition

X-rays that have been generated by a source are emitted and hit the sample which is located somewhere along their path. The X-rays interact with the matter of the sample depending on their energy, the sample material density, and the atomic number Z of the sample material. As the X-rays interact they can lose energy, be (partly) absorbed or diverted and subsequently the X-ray beam which emerges behind the sample has lost intensity. Typically they then hit a scintillator which is excited by the beam energy and re-emits this energy in form of visible light. This light in turn is captured by a charge-coupled device (CCD), i.e., an electronic light sensor. The entity of scintillator and CCD is usually known as detector. During the scan, the sample rotates on a stage, so that the detector takes images for at least 180° . The process is depicted in figure 3.6.

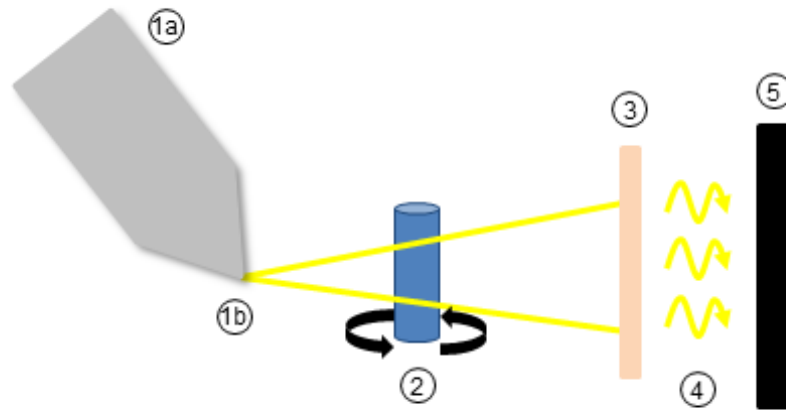


Figure 3.6: **Schematic of a typical modern μ CT scanner.** An electron beam generated by a filament at the top of the electron gun (1a) hits a metal target (1b), e.g. tungsten or molybdenum, thereby creating X-rays. The X-rays are emitted in the form of a cone beam and hit a sample located behind the source (2). When passing through the sample, the X-rays lose intensity, due to different interaction processes with the sample material. The beam then hits a scintillator (3) which emits visible light (4) that can be detected by a charge-coupled device camera (5). The sample stage can rotate, so that projections of the sample for at least 180° can be recorded.

In some cases, for example in the Zeiss Xradia Versa 510 system, the detector further includes a light microscope lens, which is built in between scintillator and camera and enables imaging at higher magnification without a change of sample-to-source or sample-to-detector distance. The lens being used is the same as in standard light microscopes, with varying magnifications being available.

The absorption of monochromatic X-rays by the sample can be described using the Beer-Lambert law, which for a homogeneous material is

$$I(x, y) = I_0(x, y)e^{-\mu\Delta z}, \quad (3.1)$$

where (x, y) are the coordinates of the imaging plane (detector), $I(x, y)$ denotes the current X-ray intensity, $I_0(x, y)$ the initial intensity before the beam hits the sample, μ is the attenuation coefficient of the material and Δz is the distance the X-ray beam has travelled through the sample. Note that μ depends on the incident photon energy and the material's Z-number, typically being controlled by photoelectric absorption or Compton scattering [Hsieh, 2009].

As most samples usually consist of more than one material, the Beer-Lambert law for monochromatic imaging in reality takes a more complex form

$$I(x, y) = I_0(x, y)e^{-\int_{z_1}^{z_2} \mu(x, y, z) dz}. \quad (3.2)$$

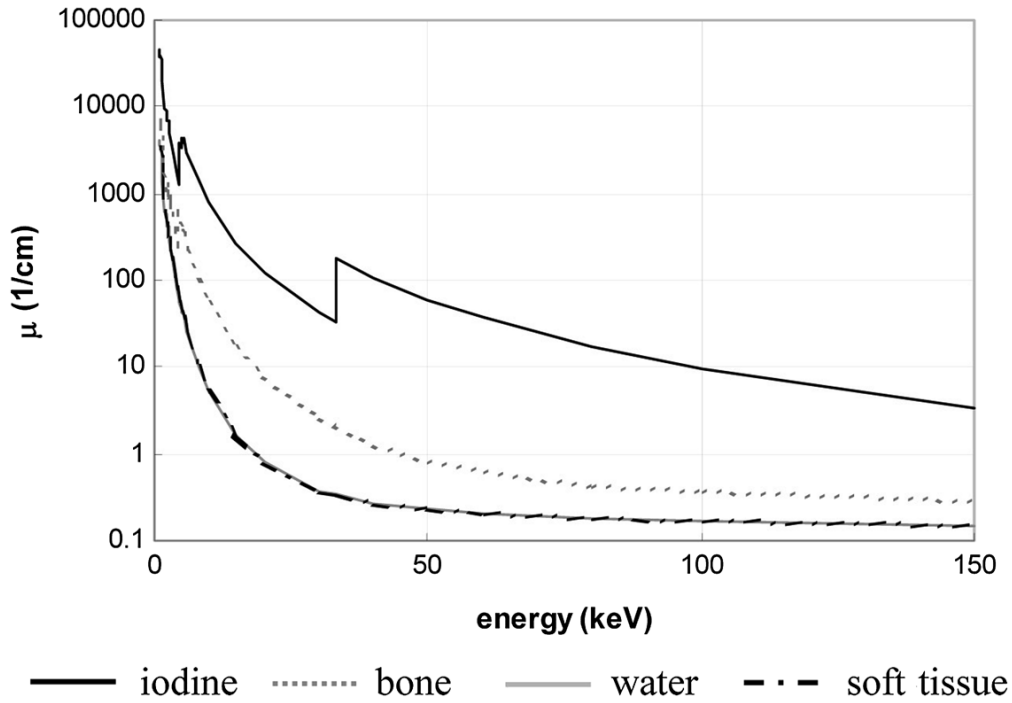


Figure 3.7: **X-ray energy-attenuation curves for exemplary materials.** Depending on the material the attenuation coefficient μ will be overall higher or lower, i.e., iodine attenuates X-rays the strongest, followed by bone which contains as a main component calcium and finally water and soft tissue. It holds that the higher the X-ray energy, the lower the X-ray attenuation and generally the worse the contrast. Iodine is an exception with the step change at around 33 keV arising from the characteristic K-edge of iodine, i.e., the binding energy of K-shell electrons [Hsieh, 2015]. Taken from Chapter 2 in Hsieh [2015].

Furthermore, for laboratory X-ray sources the polychromaticity of the beam needs to be taken into account, i.e.,

$$I(x, y, E_{max}) = \int_{E=0}^{E=E_{max}} I_0(x, y, E) e^{-\int_{z_1}^{z_2} \mu(x, y, z, E) dz} dE, \quad (3.3)$$

with E the X-ray energy and E_{max} the tube voltage of the X-ray source.

When optimising scan settings, different factors have to be taken into account, such as sample size and field of view, desired contrast and scanning time. The lower the kV settings, the better the contrast will be, as the relative difference in absorption between different materials is higher. However, this is only true until a minimum threshold of ~ 10 - 15 keV. See for example the X-ray energy-attenuation curves for different materials, depicted in figure 3.7 from chapter 2 in Hsieh [2015]. Depending on the material the attenuation coefficient μ will be overall higher or lower, i.e., iodine attenuates X-rays the strongest, followed by bone which contains as a main component calcium and finally water and soft tissue. The step change in the iodine curve at around 33 keV arises from the characteristic K-edge of iodine, i.e., the binding energy of K-shell electrons [Hsieh, 2015]. For higher energy, the attenuation of X-rays

decreases and tissue penetration increases leading to a higher signal-to-noise ratio. High flux helps to achieve shorter scan times, but can for laboratory sources lead to target erosion. Therefore, laboratory systems are usually either not allowing the user to operate the machine in this regime or automatically defocus the spot, which results in lower resolution images. Increasing exposure time will increase signal-to-noise ratio, however, this can significantly increase the scan time. If possible, a frame per projection, i.e., imaging the sample at the same angle several times and average the resulting radiographs, rate higher than 1 should be used in order to increase the signal to noise ratio, though again the scan time will be increased.

3.2.3 Image reconstruction

Following image acquisition the three-dimensional image of the sample can be reconstructed from the two-dimensional projections by using a reconstruction algorithm. In general the *Nyquist sampling criterion* should be fulfilled [Nixon & Aguado, 2008] for the reconstruction:

“In order to reconstruct a signal from its samples, the sampling frequency must be at least twice the highest frequency of the sampled signal.”

For CT imaging, this is the case if [Kak & Slaney, 1988]:

$$P_{proj} = \frac{\pi}{2} \times N_{ray} \quad (3.4)$$

holds. N_{ray} is the number of pixels the area of interest covers as the sample rotates and P_{proj} number of projections uniformly distributed over the chosen rotation range.

The most common reconstruction algorithms are Filtered Back Projection (FBP) and the Algebraic Reconstruction Technique (ART). ART is computationally considerably more intensive as it is iterative, but it results in a less noisy image than FBP [Hsieh, 2009]. In the following only FBP and derivations will be considered, as more elaborate reconstruction algorithms were not required for the methods presented in the following chapters.

3.2.3.1 Filtered backprojection

In the following the coordinate system is set as follows: z is the direction of propagation of the X-rays, (x, y) is the tuple describing the perpendicular imaging plane to z , with x being the horizontal coordinate and y the vertical coordinate in an actual imaging setup (see Figure 3.8). The rotated axis x around an angle θ is described as t . $f(x, z)$ is the object being reconstructed (at fixed height y) and $p(t, \theta)$ its projection onto the detector plane at angle θ .

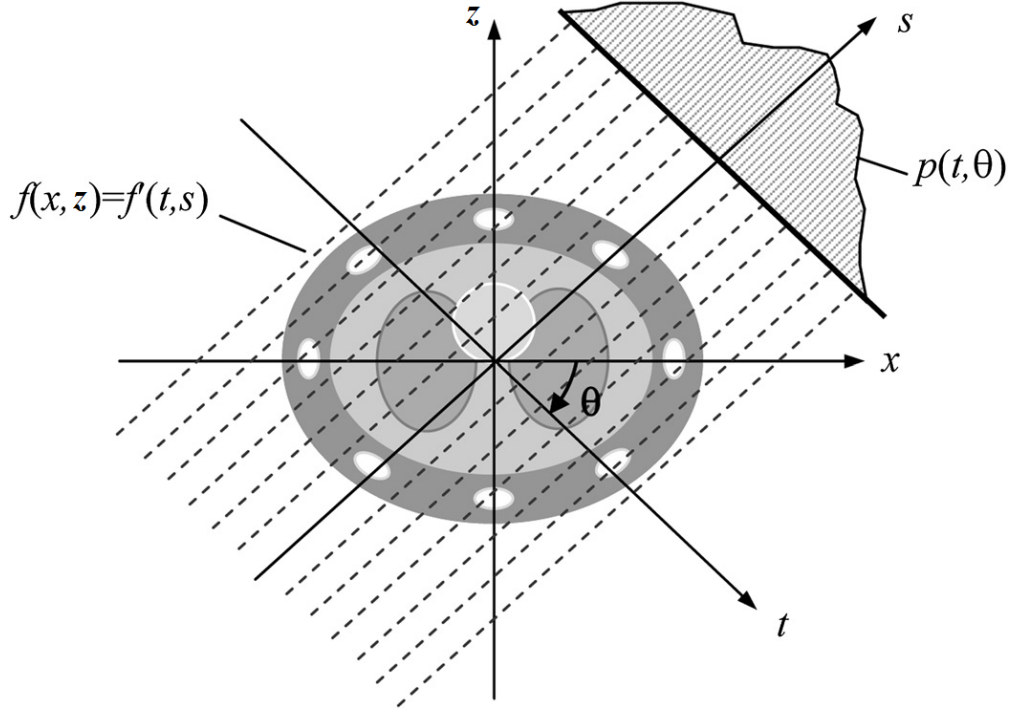


Figure 3.8: **Original and rotated coordinate system in an imaging system.** z is the direction of propagation of the X-rays, (x, y) is the tuple describing the perpendicular imaging plane to z , with x being the horizontal coordinate and y the vertical coordinate in an actual imaging setup. The rotated axis x around an angle θ is described as t . Adapted from Hsieh [2015], chapter 3.

The Filtered Backprojection (FBP) makes use of the Fourier slice theorem to obtain the three-dimensional reconstruction from two-dimensional (2D) projection images. The Fourier slice theorem states that for a projection $p(t, \theta)$ taken at angle θ of the object function $f(x, z)$ the one-dimensional (1D) Fourier transform of p , $P(\omega, \theta)$, equals the two-dimensional Fourier transform of f [Hsieh, 2009]:

$$P(\omega, \theta) = \int_{-\infty}^{\infty} p(t, \theta) e^{-2\pi i t \omega} dt = \int_{-\infty}^{\infty} \int_{-\infty}^{\infty} f(x, z) e^{-2\pi i (xu + zw)} dx dz. \quad (3.5)$$

Thus, $f(x, z)$ can be obtained by rewriting the left hand side using $P(\omega, \theta)$ and applying an inverse Fourier transform [Hsieh, 2009]:

$$f(x, z) = \int_0^{\pi} \int_{-\infty}^{\infty} P(\omega, \theta) |\omega| e^{2\pi i \omega t} d\omega d\theta. \quad (3.6)$$

$|\omega|$ in this case is the filter of the “filtered” backprojection and results from the inverse Fourier transform when spatial coordinates (x, z) are converted into polar coordinates (ω, θ) and the restriction onto the interval $[0, \pi]$. The implementation of the filter is often as a bandpass filter, such as a window function, Hanning, Butterworth or Ram-Lak filter [Hsieh, 2015]. The choice of filter can influence the reconstruction quality significantly. For a projection taken at angle $\theta \in [0, 180]$ in a μ CT imaging setup

equation (3.6) relates a horizontal line in the image captured by the detector to the slice through the sample at this fixed (but arbitrary) height y . For fixed y and varying θ a 2D stack of these projection lines is called *sinogram* [Hsieh, 2009]. Applying equation (3.6) to all sinograms, the three-dimensional image of f can be reconstructed. The implementation of this theory is usually performed using fast Fourier transforms (FFT) and their inverse, which are computationally efficient [Hsieh, 2009].

In the μ CT imaging setup the projection data $p(t, \theta)$ is the projected exponential of the linear attenuation coefficient $e^{\int_{z_1}^{z_2} \mu(t, \theta) dz}$ at fixed height y . Thus, the reconstructed 3D image gives information on the three-dimensional attenuation properties of the sample. This can in some cases be directly related to other properties of the sample, e.g., in the case of bone samples it relates to the bone mineral density [Bouxsein *et al.*, 2010].

3.2.3.2 *gridrec* algorithm

Due to fast imaging times and large datasets, it can become a struggle to keep up with reconstructing images using the FBP whilst performing high-throughput experiments at synchrotron sites. To this end, Dowd *et al.* [1999] developed a fast reconstruction algorithm called *gridrec* which is based on the concept of the FBP and found implementation, e.g., by F. Marone and M. Stampanoni [Marone & Stampanoni, 2012]. The difference of the *gridrec* algorithm to traditional FBP implementations lies in gridding the data from polar coordinates onto Cartesian coordinates before applying the inverse 2D Fourier transform. To this end, a convolution kernel $W(u, w)$ is applied to the data in polar coordinates and the output is evaluated in Cartesian coordinates [Marone & Stampanoni, 2012], i.e., for $F(u, w)$ the 2D Fourier transform of the object function $f(x, z)$ (note that (u, w) are Cartesian coordinates of the Fourier space):

$$H(u, w) = F(u, w) * W(u, w) = \int_0^{2\pi} \int_{-\infty}^{\infty} F(\omega \cos \phi, \omega \sin \phi) W(u - \omega \cos \phi, w - \omega \sin \phi) |\omega| d\omega d\phi. \quad (3.7)$$

Equation (3.7) is discretized for implementation and after application of the inverse Fourier transform to H , the contribution of $W(u, w)$ would be removed by division. Marone & Stampanoni [2012] have shown that the difference in the reconstructed image between FBP and *gridrec* is negligible if 0.5 zero-padding is applied to the sinograms during *gridrec* whilst the reconstruction time was 20 times faster than that of FBP. Zero-padding is the process of elongating a signal/image by adding zeros to the sides of it and it is used to avoid artefacts from the application of the convolution kernel [Marone & Stampanoni, 2012]. The parameter of the zero-padding means that each sinogram is extended by 0.5 times the original field of view [Marone & Stampanoni, 2012].

3.2.4 Imaging Artefacts

CT imaging is prone to different types of artefacts, including aliasing, beam hardening and ring artefacts. Especially for materials with high Z-number, beam hardening is often apparent. Most reconstruction software therefore includes beam hardening correction algorithms. Undersampling, which leads to aliasing, can be prevented by ensuring that the number of projections fulfils the Nyquist sampling criterion (see equation (3.4)) [Nixon & Aguado, 2008]. However, aliasing artefacts will always be present for samples containing step edges, as the support of the Fourier spectrum of a step function is infinity [Vidal *et al.*, 2005].

Ring artefacts are due to defective or badly corrected pixels [Vidal *et al.*, 2005]. They can be circumvented in the scanning process by applying shuttling. This is a process whereby the sample is periodically shifted during a scan to ensure that individual angular paths through the sample are represented by an average of several pixels on the detector, rather than a single one. This can have a limiting effect on the image resolution. Software corrections for ring artefacts are also available in many image reconstruction software.

Other artefacts can be introduced by sample and camera misalignment, sample drift, a limited field of view and the discrete nature of the detector, which results in partial volume effects, i.e., a continuous object is imaged by a number of discrete voxels, thus resulting in averaged (blurred) information at the recorded edges of the object. Blurring of edges due to a non-perfect X-ray focal spot and the detector can be accounted for by determining the point spread function, which is the response of the system to an ideal point. Similarly, an edge spread function can be obtained [Vidal *et al.*, 2005]. These functions are then used to describe the sharpness of the system.

3.3 Sample preparation methods

As X-ray absorption contrast of organic soft tissue is typically limited for μ CT and SR CT, it is conventionally considered necessary to prepare tissues with staining agents. The choice of staining agent strongly depends on the imaging technique to be used and the feature of interest. It is necessary to consider several aspects, such as costs, toxicity, possible tissue shrinkage and perfusion range.

The methods to enhance vascular contrast for μ CT imaging can be differentiated into methods that stain vessel walls (*Staining Methods*) and those that fill the lumen of the vessel (*Perfusion Methods*).

Staining Methods: Osmium tetroxide (OsO_4) gives very good imaging contrast and has low tissue shrinkage but is very toxic and therefore also requires specific disposal, which results in high disposal costs [Metscher, 2009], [Pai *et al.*, 2012]. Lugol's solution

(I₄K) on the other hand has low toxicity and low tissue shrinkage and is easy to prepare [Metscher, 2009], [Degenhardt *et al.*, 2010]. However, Lugol's solution is prone to leakage into the tissue system. Metscher [2009] also tested phosphotungstic acid (PTA) against the former two, which gave high contrast and stability. Pauwels *et al.* [2013] compared another 27 staining agents, amongst others Mercury(II)chloride (HgCl₂), phosphomolybdic acid (PMA), PTA and ammonium orthomolybdate ((NH₄)₂MoO₄), concluding that most of these were similarly suitable for the visualisation of soft tissue. However, depending on the agent, sample size or staining times need to be adjusted [Pauwels *et al.*, 2013]. These methods have also partly been reviewed for soft tissue staining in Mizutani & Suzuki [2012]. Overall staining methods are rather unsuitable for imaging the microvasculature in skeletal muscle, as they are largely non-specific, leaving only the vessel lumen unstained. Thus, even at high spatial resolutions segmentation of capillaries becomes difficult as the vessel lumen is small and the vessels may easily collapse, making them difficult or even impossible to detect.

Perfusion Methods: Two different sets of perfusion methods exist, firstly perfusion with polymers for corrosion casting and secondly perfusion with nanoparticles. Corrosion casting is a technique often applied to study the microvasculature using scanning electron microscopy (SEM). After perfusion of the blood vessels with the polymer and the time necessary for curing the polymer, the surrounding organic tissue is macerated [Lametschwandtner *et al.*, 1984, 1990, Folarin *et al.*, 2010] and can be prepared for SEM. The most commonly used polymer for corrosion casting for μ CT is Mercor, commercially available in its non-hazardous form Mercor II (Ladd Research, Williston, Vermont, USA). Mercor polymerizes quickly, which means that perfusion times and volumes must be relatively small [Gregor *et al.*, 2012]. Mercor has good penetration properties within the entire vascular network and shows minimal shrinkage [Gregor *et al.*, 2012]. However, one of its drawbacks is its low X-ray absorption and its brittleness [Krucker *et al.*, 2006]. In order to enhance X-ray absorption, it can be coated with a material of high atomic number, such as osmium tetroxide [Mondy *et al.*, 2009b]. Microfil ®(Flow Tech Inc., US) is another frequently used silicone rubber; a polymer that is fluid during perfusion and hardens within 30 minutes [Garcia-Sanz *et al.*, 1998], [Zhu *et al.*, 2004], [Vasquez *et al.*, 2011], [Downey *et al.*, 2012], [Xie *et al.*, 2012], [Xu *et al.*, 2013], [Razavi *et al.*, 2012]. It has often been used for corrosion casting [Atwood *et al.*, 2010], [van der Merwe & Kidson, 2010]. However, Microfil perfusion complicates histological sectioning and a problem often encountered with this agent is that it does not always perfuse all of the microvasculature as reported by Downey *et al.* [2012]. Ghanavati *et al.* [2013] on the other hand reported a very uniform filling of the cerebrovasculature using Microfil. Apart from Microfil, other casting agents can be used, such as the polyurethane-based resin PU4ii (vasQtec, Zurich, Switzerland), for which good perfusion of the cerebral and the murine hind limb microvasculature was reported [Schneider *et al.*, 2009],

[Krucker *et al.*, 2006], [Meyer *et al.*, 2007], [Nebuloni *et al.*, 2014].

It is also possible to perfuse the vasculature with nanoparticles, which are small particles of a high atomic number material with dimensions of about 100 nm. This can be, for example, a suspension of gold nanoparticles [Clark *et al.*, 2013, Moding *et al.*, 2013], liposomal iodine nanoparticles [Ghaghada *et al.*, 2011] or bismuth sulphide (Bi_2S_3) nanoparticles. Nanoparticles can also be used for in vivo μCT imaging [Nebuloni *et al.*, 2014]. The size of the nanoparticles used can be varied depending on the vasculature investigated. For example, as tumour vasculature is leaky, larger particles may be beneficial or in contrast, smaller particles can be used in order to determine tumour permeability [Clark *et al.*, 2013].

Due to the difficulty of visualising capillaries using staining methods perfusion methods should be the method of choice for absorption-based μCT of the microvasculature in skeletal muscle. However, as results from perfusion with polymers are largely variable in terms of filling quality and depend strongly on user proficiency, nanoparticles can be a viable alternative as blood vessel perfusion is ensured due to the delivery of the nanoparticles by the blood itself from the location of injection [Ashton *et al.*, 2015].

3.3.1 Applications of μCT

μCT has been used extensively for imaging of soft tissues and the microvasculature; some examples include the imaging of corrosion casts of the ocular and renal microvasculature [Atwood *et al.*, 2010], [van der Merwe & Kidson, 2010], [Xu *et al.*, 2013], phenotyping of cardiovascular development in mouse embryos [Degenhardt *et al.*, 2010], functional imaging in rat hearts [Umetani & Fukushima, 2013], studying cavernous haemangioma of the liver [Duan *et al.*, 2013], studying neovascularisation in tissue engineered bone constructs [Bolland *et al.*, 2008] and computer-aided design of microvasculature [Mondy *et al.*, 2009a], [Mondy *et al.*, 2009b]. Heinzer *et al.* [2006] used a combination of both μCT and SR CT to perform a multiscale analysis of vascular networks, similarly, Schneider *et al.* [2009] studied the murine hind limb using corrosion casts with both μCT and SR CT. Razavi *et al.* [2012] imaged the pulmonary and cardiac circulation using μCT .

3.3.2 μCT imaging modes

The most common μCT scanning mode is by far attenuation-based scanning, which has so far been presented. For attenuation-based μCT the X-ray beam is not required to meet any requirements. Phase contrast-based imaging however can only take place using X-rays with high coherence. This will be discussed in more detail in the next section. Another modification of μCT is the usage of dual energy μCT as used by

Badea *et al.* [2008], Clark *et al.* [2013] and Moding *et al.* [2013]. For this modality two X-ray sources are applied with different energies. The two sources are arranged such that the centreline beams are perpendicular to each other. Dual energy μ CT results in better contrast between materials [Badea *et al.*, 2008]. The technique can also be implemented using two scans with the same X-ray source at different energy settings.

3.3.3 Phase contrast-based micro-computed tomography

Phase contrast-based micro-computed tomography is dependent on the lateral spatial coherence of the beam. This coherence may be estimated as [Mayo *et al.*, 2012]:

$$l_c = \lambda \frac{R_1}{2\pi\sigma} \quad (3.8)$$

with σ denoting the X-ray source size, R_1 the source-to-sample distance and λ the wavelength. High spatial coherence can be achieved either through long source-to-sample distances or very small source sizes, i.e., about $10\mu\text{m}$ or smaller [Mayo *et al.*, 2012]. When passing through a sample, the X-rays are not only attenuated but also refracted, as they are electromagnetic waves. The *refractive index* n for such an interaction is defined as

$$n = 1 - \delta + i\beta \quad (3.9)$$

with β being related to μ (the absorption coefficient from the Beer-Lambert law in equation (3.1)) via

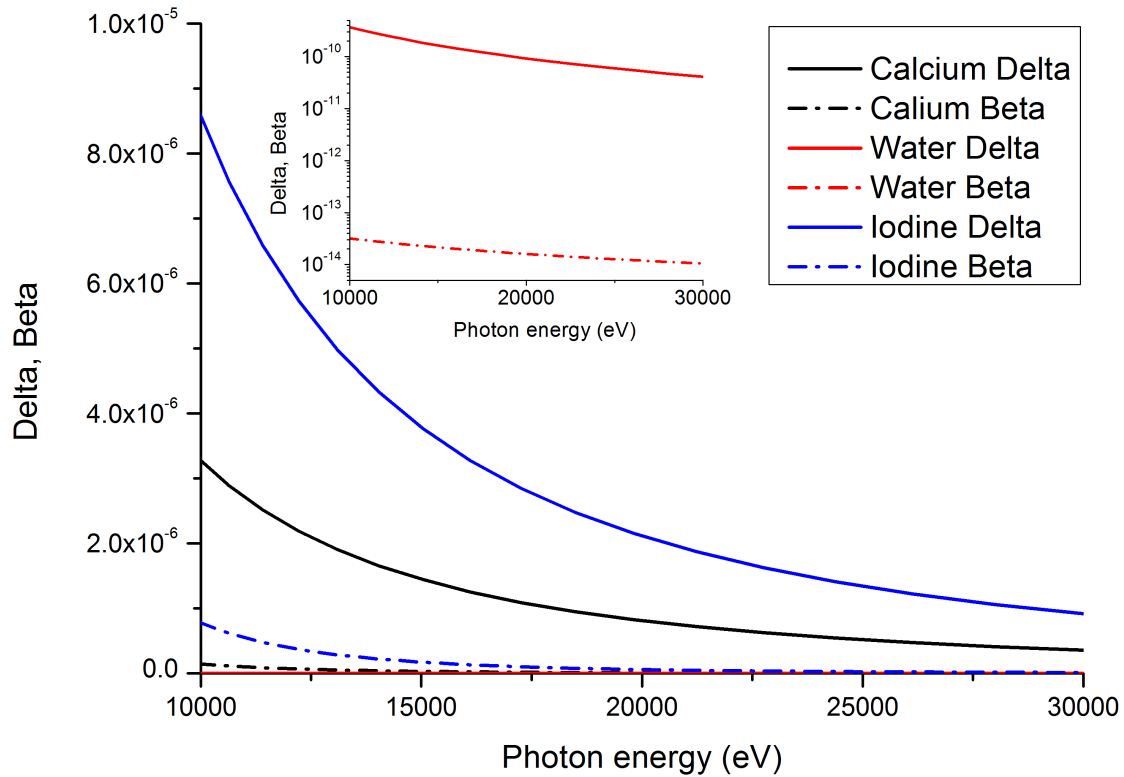
$$\mu = \frac{4\pi}{\lambda}\beta,$$

λ being the wavelength and $i = \sqrt{-1}$ [Margaritondo, 2002]. δ in the above equation relates to the phase shift Φ that is introduced as the X-rays interact with the sample:

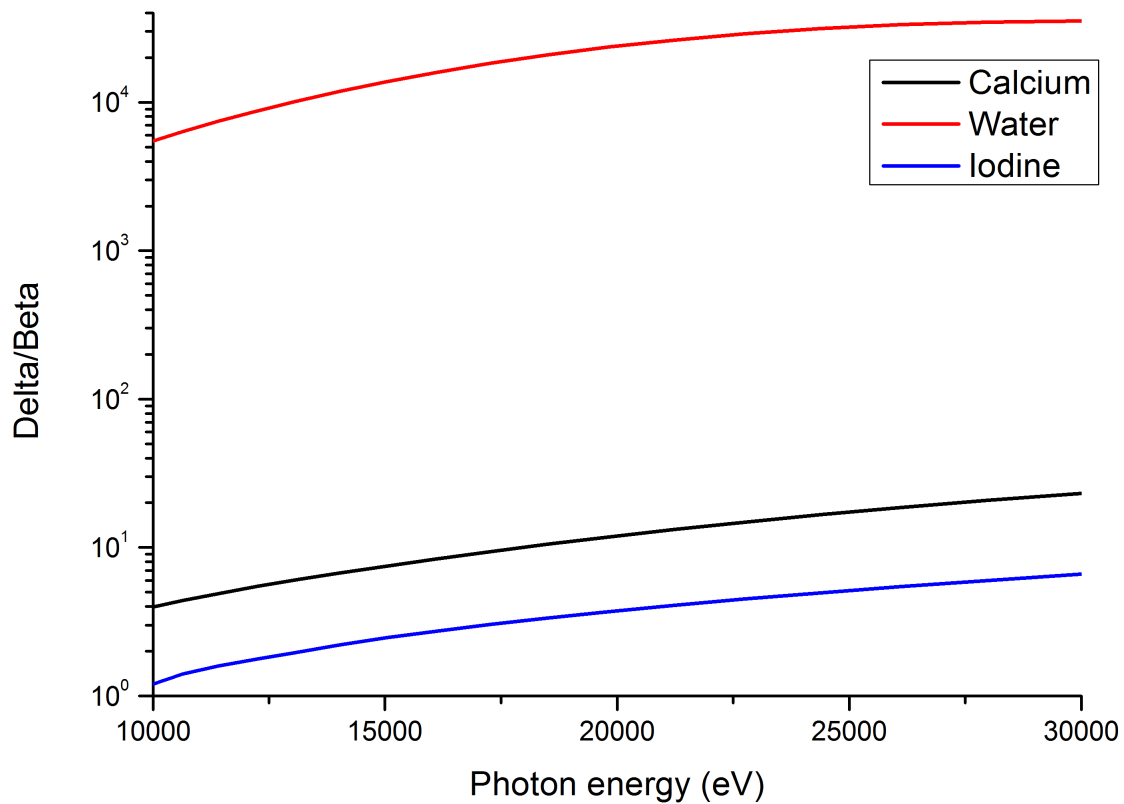
$$\Phi(x, y, z = 0) = -\frac{2\pi}{\lambda} \int \delta(x, y, z) dz, \quad (3.10)$$

where λ is the wavelength of the X-ray beam (for simplicity assumed to be constant in this description) and $\delta = \frac{r_c \lambda^2 \rho_e}{2\pi}$, with $r_c = 2.8 \text{ fm}$ the classical electron radius and ρ_e the electron density of the material [Cloetens *et al.*, 1999]. Note that for a homogeneous sample ($\delta = \text{const.}$) it holds that $\Phi(x, y, z = 0) = -\frac{2\pi}{\lambda} \delta T(x, y)$ for an object of projected thickness $T(x, y)$ in the contact plane ($z = 0$, when the X-rays have just passed through the sample).

δ can be two to three orders of magnitude larger than β , thereby making phase-contrast imaging an important alternative to classical absorption-based imaging, especially if absorption contrast between different components of a sample is low, as is usually the case for soft-tissue samples, see comparisons of δ and β for iodine, calcium and water in figure 3.9. A number of different techniques have been



(a) Delta and beta



(b) Delta/beta ratio

Figure 3.9: δ (solid line) and β (dashed line) of the refractive index for iodine (blue), calcium (black) and water (red). δ and β curves are given in 3.9(a) and their ratio in 3.9(b). They depend on the material density and its interaction with X-rays. Values obtained from hen [2016], Henke *et al.* [1993].

developed to make use of the phase shift for CT imaging; these include simple propagation-based methods, interferometric methods, diffraction enhanced imaging methods and crystal analyser methods. They all vary in the complexity of the experimental setup and the physical signal that is recorded [Pfeiffer *et al.*, 2006].

3.3.3.1 Free space propagation

The simplest phase contrast CT technique in terms of implementation is free space propagation, where the X-rays are allowed to propagate towards the detector without alteration. This makes use of the Fresnel edge diffraction of different rays of the beam when it is hitting edges between different materials. The rays that are diffracted can interfere in a destructive or constructive manner, resulting in dark and bright fringes around the edges of the detected object, see figure 3.10. The manner in which they interfere depends on the X-rays' differences in path length [Margaritondo, 2002]. One requirement for the detection of the fringes is sufficient resolution of the detector. This parameter, however, can be varied through an increase of the sample-to-detector distance [Margaritondo, 2002]. Free space propagation is both used for edge-enhancement, i.e., for increasing the visibility of edges through interference fringes, and phase retrieval or holotomography [Cloetens *et al.*, 1999], where the sample is imaged for a number of different sample-to-detector distances and phase images are then reconstructed based on the radiographs of all images. Propagation-based phase contrast is especially useful for high-resolution imaging, as most other phase-contrast techniques do not reach a spatial resolution below a few micrometers [Pfeiffer *et al.*, 2006].

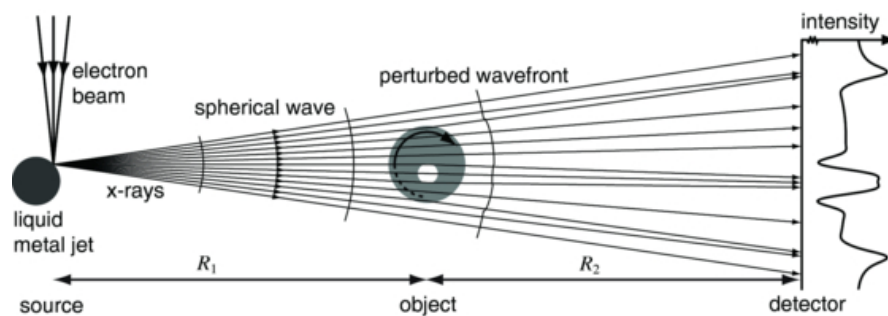


Figure 3.10: **Principles of Fresnel fringes through X-ray interference.** Taken from [Lundstrom *et al.*, 2012]. The X-rays hitting the interfaces between different materials within the sample are refracted and if being allowed to propagate for a longer distance behind the sample they will interfere. This results in dark and light fringes around the material interfaces.

Like most other phase contrasting techniques free phase propagation is mainly used at synchrotron sources, because most lab-based X-ray CT sources cannot provide sufficient beam coherence. Coherence of the X-ray beam is important for the interference and hence for the phase information to be extracted correctly [Als-Nielsen

& McMorrow, 2011]. Another advantages of synchrotron radiation includes the fact that the X-ray beam can be filtered to be (quasi-)monochromatic whilst still being delivered at high flux, both of which are not essential for propagation-based phase contrast [Wilkins *et al.*, 1996], but avoid beam hardening effects and reduce scanning time significantly, respectively.

Propagation-based phase contrast SR CT has successfully been used to image sub-micrometer particles in unstained lung tissue with a voxel size of 370nm side length [Schittny *et al.*, 2011]. However, the technique has been used relatively little to image the vasculature. Lang *et al.* [2012] have been able to identify tumour vasculature and only recently it was reported that phase contrast imaging in conjunction with phase retrieval at synchrotron facilities enabled simultaneous visualisation of blood vessels and nerve fibres in the spinal cord without the need for contrast agents [Fratini *et al.*, 2015]. Using state-of-the-art lab-based μ CT systems Walton *et al.* [2015] demonstrated that phase contrast can also be exploited to some extent using commercial μ CT scanners. Namely, Walton *et al.* [2015] visualised sub-micrometer structures within skin and rat artery walls using μ CT and they reported that subsequent histological and immunohistochemical staining was compatible with prior X-ray exposure.

3.3.3.2 Grating interferometry

Phase contrast imaging using a grating interferometer was first introduced in 2005 by Weitkamp *et al.* Two gratings, a phase grating G_1 and an absorption grating G_2 , are placed in between sample and detector, as can be seen in figure 3.11 from Weitkamp *et al.* [2005]. The phase grating divides the incoming beamfront into the first two diffractions orders and the angle between these two diffracted beams is very small. The waves interfere with the interference pattern depending only on the period of G_1 and the phase shift introduced by the grating. Additionally, the sample placed in front of the grating displaces the interference pattern and by detecting the displacement of the fringes, the shape of the wavefront, and hence the shape of the sample can be detected. To this end, the second grating is placed directly in front of the detector and transforms the fringe location into a signal intensity variation. Moreover, in order to cancel out this information from any noise, the absorption grating will be displaced in transverse direction (x_g in figure 3.11) over one period of the grating. By this, the phase profile of the sample can be retrieved (see Weitkamp *et al.* [2005] for more detail). The distance between G_1 and G_2 is given by the m th Talbot distance

$$d_m = \left(m - \frac{1}{2}\right) \frac{g_1^2}{4\lambda}, \quad (3.11)$$

with g_1 being the pitch of the phase grating and λ the beam wavelength [Weitkamp *et al.*, 2005].

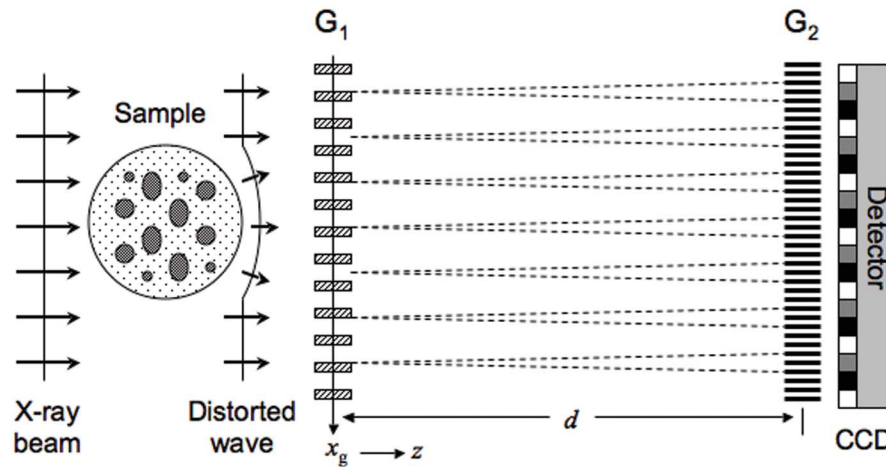


Figure 3.11: **Principle of grating interferometry.** By use of two gratings, G_1 and G_2 , which are placed between sample and detector, the first two diffraction orders of the refracted X-rays are extracted (G_1) and interference patterns are transformed into intensity variations (G_2). Taken from [Weitkamp *et al.*, 2005].

The technique requires monochromaticity and spatial coherence of the beam. It is very sensitive to small phase gradients, which is especially useful for soft tissue imaging [Pfeiffer *et al.*, 2006, McDonald *et al.*, 2009]. However, the resolution of the technique is limited by the grating size, and lies currently at $3.7 \mu\text{m}$ [Weitkamp *et al.*, 2005, Pfeiffer *et al.*, 2006, McDonald *et al.*, 2009].

The current technology allows a full volume of 1024×1024 pixels with 1000 projections and 9 phase steps, i.e., 9000 projections in total and a pixel size of $7.4 \mu\text{m}$ to be obtained within 20 minutes [Pfeiffer *et al.*, 2006], which is about 3-4 times longer than a scan using propagation based phase contrast at even higher resolution. Grating interferometry at synchrotron sources has successfully been used to image rat testicles [Zanette *et al.*, 2013] metastatic lymph nodes [Jensen *et al.*, 2013], microcalcifications in X-ray mammography [Wang *et al.*, 2014], as well as rat brain tissue [McDonald *et al.*, 2009, Pinzer *et al.*, 2012]. The technique is implemented at the European Synchrotron Radiation Facility (ESRF), as well as at the Swiss Light Source (SLS). Grating interferometry can also be used with conventional X-ray tubes by placing a third transmission grating G_0 between source and sample, which creates a sufficiently coherent line source [Pfeiffer *et al.*, 2006]. Lang *et al.* [2014] performed an experimental comparison between grating interferometry and propagation-based phase contrast at the ESRF, in Grenoble, France. They found that the propagation-based method yielded higher spatial resolution, but lower contrast-to-noise ratio than the grating-based method. Furthermore, Lang *et al.* [2014] found grating interferometry to be more exact for the measurement of material densities and more robust against low-frequency artefacts. Overall, the authors concluded that both methods could be seen as complementary and should be chosen based on the application.

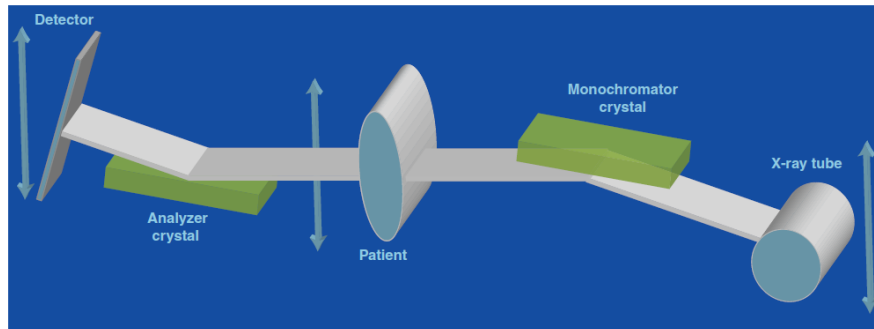


Figure 3.12: **Principle of diffraction enhanced imaging.** An analyser crystal is inserted between sample and detector to convert the X-ray diffraction into intensity changes in the projections. Taken without permission from Connor & Zhong [2014].

3.3.3.3 Diffraction enhanced imaging

Diffraction enhanced imaging (DEI) using an X-ray source was developed in the mid-1990s by Chapman *et al.* [1997]. In this experimental setup, an additional crystal, similar to the monochromator that is used to select the energy band from the synchrotron, is used to diffract the X-rays that have been transmitted through the object. See figure 3.12 from [Connor & Zhong, 2014] for a schematic of this setup. This crystal is called an analyser crystal, or also Bragg-diffraction crystal.

The crystal converts the diffraction into intensity changes in the detected image and additionally removes scattered photons [Connor & Zhong, 2014]. The resulting images can be reconstructed using standard filtered backprojection. The technique has been used for various applications, such as mammography, joint and lung imaging and analysis of the bone microarchitecture. Compared to grating interferometry, DEI has a higher signal-to-noise ratio when higher energies are used [Connor & Zhong, 2014]. The resolution of DEI is currently in the range of about $30\mu\text{m}$ [Hu *et al.*, 2014]. A disadvantage of the technique is the requirement of a monochromatic beam, which makes it difficult to implement as a lab-based system [Connor & Zhong, 2014]. However, Nesch *et al.* [2009] have made use of a two-crystal monochromator placed behind a tube X-ray source and have thereby been able to create a stable 22 keV beam for DEI imaging. The spatial resolution of the lab-based system however is limited to $160 \pm 7\mu\text{m}$ horizontally and $153 \pm 7\mu\text{m}$ vertically [Nesch *et al.*, 2009]. An ideal contrast agent for DEI was found to be air, although all standard contrast agents can also be used [Connor & Zhong, 2014].

One important application of the technique in terms of imaging the microvasculature involved research by Hu *et al.* [2014] and Duan *et al.* [2013] to identify the microvascular architecture in stages of liver cirrhosis. Liver samples were fixed and then scanned using DEI at the Beijing Synchrotron Radiation Facility, China. It was

found that vascular density decreased whereas intercapillary distance increased in fibrotic rats as compared to cirrhotic rats. Immunohistochemical analysis was used for validation of the findings. However, as the imaging resolution was limited to $30\mu\text{m}$, it is unlikely that the authors were able to detect capillaries and may have missed out on a large number of blood vessels.

Other phase contrast-based imaging methods that will not be mentioned in further detail are crystal interferometry, Zernike phase contrast and coherent diffraction imaging. All of the mentioned experiments have been carried out *ex vivo*. Other experimental setups for grating-based interferometry and other phase contrast imaging techniques have been reviewed by Bravin *et al.* [2013].

For *ex vivo* imaging with the purpose of providing image data sets for mathematical modelling of oxygen supply to tissue on the whole organ scale, propagation-based phase contrast SR CT and μCT are the only phase contrast-based techniques operating under high enough spatial image resolution so that the finest capillaries can be resolved. Phase contrast-based SR CT has the advantage of fast scanning times due to the high photon flux, yet access to synchrotron facilities is limited. Lab-based μCT however requires significantly longer scanning times yet access is easily obtained.

3.3.4 Phase retrieval algorithms

With the phase contrast-based SR CT methods explained above, e.g., propagation-based phase contrast SR CT etc., one captures the information on both phase and attenuation of the given object in the projections (and thus the reconstruction). However, whilst the attenuation information is directly available in the way it is related to the image brightness *via* the Beer-Lambert law (equation (3.1)), the phase information can not be immediately read out. Thus, there are two possibilities to determine the phase information: Firstly, Bronnikov [1999] proposed an approach for a pure phase object with which δ can immediately be reconstructed; secondly, other algorithms take an intermediate step between acquisition of radiographs and reconstruction called phase retrieval. One of the phase retrieval methods implemented at synchrotron facilities is the algorithm proposed by Paganin *et al.* [2002] for a homogeneous sample which determines the phase shift $\Phi(x, y, z)$ for a δ assumed constant.

Both the Bronnikov and Paganin algorithm are based on the transport-of-intensity equation (TIE) [Paganin *et al.*, 2002]:

$$\nabla_{\perp} [I(x, y, z) \nabla_{\perp} \Phi(x, y, z)] = -k \frac{\partial I(x, y, z)}{\partial z} \quad (3.12)$$

where \perp represents the restriction of the operator to coordinates of the imaging plane and with $k = \frac{2\pi}{\lambda}$ the wavenumber and λ the wavelength. The TIE can be derived from propagating a monochromatic paraxial electromagnetic wave ψ in the Fresnel regime (small propagation distance z) [Paganin *et al.*, 2002], where $\psi(x, y, z = 0)$ in the contact plane can be described by

$$\psi(x, y, z = 0) = \sqrt{I(x, y, z = 0)} \exp(i\Phi(x, y, z = 0)) \quad (3.13)$$

with I the wave amplitude, or intensity, for which the Beer-Lambert law (3.2) holds if the Laplacian of the wave in the imaging plane can be neglected, $\nabla_{\perp}^2 \psi(x, y, z = 0) \simeq 0$ and Φ is the phase of the wave described in equation (3.10).

In the following R_2 will denote the sample-to-detector distance.

3.3.4.1 (Modified) Bronnikov algorithm

For his algorithm, Bronnikov [1999] assumed that the sample is not attenuating X-rays, i.e., $\mu \simeq 0$. δ in this case is unknown and needs to be determined. Starting from the TIE in the form of a finite difference equation for the right hand side between the contact plane and the imaging plane at $z = R_2$, one obtains

$$\nabla_{\perp}^2 \Phi(x, y) = -\frac{2\pi}{\lambda R_2} g_{\theta}(x, y) \quad (3.14)$$

with θ the projection angle and $g_{\theta}(x, y) = \frac{I(x, y, z=R_2)}{I_{in}} - 1$ is called the data function.

Application of a 3D radon transform in combination with a second derivative along the object coordinate system (x', y', z') results in a relationship between 2D radon transform of g and 3D radon transform of δ is established, for which the solution is given as the convolution

$$\delta(x', y', z') = \frac{1}{4\pi^2 R_2} \int_0^{\pi} q * g_{\theta} d\theta, \quad (3.15)$$

with a filter $q = \frac{|y|}{x^2 + y^2}$. The filter is in practice applied in the Fourier domain, as the convolution becomes a simple multiplication in this case.

In order to accomodate for samples that are only slightly attenuating, Groso *et al.* [2006] suggested a correction parameter α for the filter, which then takes the form (in the Fourier space)

$$Q(\xi, \eta) = \frac{|\xi|}{\xi^2 + \eta^2 + \alpha}. \quad (3.16)$$

3.3.4.2 Paganin algorithm

For the Paganin algorithm the following assumptions need to be made: the sample is homogeneous, β and δ are known, the TIE holds and the Fresnel number is large ($N_F \gg 1$) [Paganin *et al.*, 2002]. The Fresnel number is $N_F = a^2 / \lambda R_2$, with sample-to-detector distance R_2 , λ the wavelength and a the smallest sample feature to be resolved [Als-Nielsen & McMorro, 2011].

To obtain the phase Φ of a sample in a projection image at position (x, y) the projected thickness $T(x, y)$ needs to be determined. Using the assumption of a homogeneous sample, the thickness is related to the intensity $I(x, y, z)$ *via* the Beer-Lambert law (3.1) and to the phase *via* equation (3.10). If these are inserted into the TIE and the right hand side is approximated by a finite difference between contact plane ($z = 0$) and imaging plane at $z = R_2$, one obtains

$$\left(-\frac{R_2 \delta}{\mu} \nabla_{\perp}^2 + 1 \right) e^{(-\mu T(x, y))} = \frac{I(x, y, z = R_2)}{I_{in}}.$$

With representation as Fourier integrals this leads to

$$\mathcal{F}\{\exp(-\mu T(x, y))\} = \mu \frac{\mathcal{F}\{I(x, y, z = R_2)\} / I_{in}}{R_2 \delta |\omega_{\perp}|^2 + \mu}.$$

ω_{\perp} denotes the Fourier frequencies related the coordinates of the imaging plane. With inverse Fourier transform and solving for $T(x, y)$, this gives

$$T(x, y) = -\frac{1}{\mu} \ln \left(\mathcal{F}^{-1} \left\{ \mu \frac{\mathcal{F}\{I(x, y, z = R_2)\} / I_{in}}{R_2 \delta |\omega_{\perp}|^2 + \mu} \right\} \right). \quad (3.17)$$

T relates to the phase shift Φ *via* equation (3.10). The algorithm is implemented to employ fast Fourier transforms and to return phase retrieved radiographs that contain the information $e^{-\mu T(x, y)}$ for all angles.

3.3.4.3 Reconstruction post Paganin phase retrieval

After the phase retrieval step the normal FBP (or *gridrec*) reconstruction algorithm is applied to the phase retrieved projections. The intensity in the projection images now depends on the projected thickness $I(x, y) = \exp(-\mu T(x, y))$. Following equation (3.10) this is the same as $I(x, y) = \exp(\mu \frac{\lambda}{2\pi\delta} \Phi(x, y))$ and thus the phase shift Φ is being backprojected with a linear scale of $\mu \frac{\lambda}{2\pi\delta}$. Consequently, the greyscales in the reconstructed volume are giving information about the phase shift in each point.

3.3.4.4 Other algorithms

A number of other phase retrieval algorithms exist, all of which are subject to different assumptions, as reviewed in Burvall *et al.* [2011]. As no other phase retrieval algorithm was implemented at the SLS and good quality of the results obtained with the Paganin algorithm (see next chapter), it was decided to not apply a different phase retrieval algorithm to our data and are thus referring the reader to Burvall *et al.* [2011] for further information.

3.3.5 μ CT for *in vivo* imaging

The main advantages of μ CT are its non-destructive nature and the relatively high spatial resolution that can be obtained in comparison to other three-dimensional imaging techniques [Kiessling *et al.*, 2010], as shown in table 3.1 and figure 3.1. Typical maximal spatial resolutions of commercial μ CT systems are just below 1 μ m, whilst synchrotron-based CT setups normally operate down to the diffraction limit of visible light, which is around a few 100 nm. One general drawback of μ CT is that at high spatial resolutions the exposure to significant levels of X-ray radiation is a crucial factor to consider. Hence, the maximal pixel size is typically limited to around 5 μ m for *in vivo* applications, resulting in actual spatial resolutions in 3D of around 10 μ m. Moreover, animal or sample movement during scanning detrimentally affects image quality of the reconstructed CT data, which becomes critical when high spatial resolutions are targeted. Commercial scanners exist for small animals such as mice, rats or rabbits, where the heart rate can be monitored for respiratory gating under anaesthetic, which is used in order to avoid or at least minimise movement artefacts. Badea *et al.* [2008] and more recently Clark & Badea [2014] have reviewed the suitability of μ CT for *in vivo* imaging of small animals. A lethal dose for mice (50% of the population die within 30 days) is estimated to be 5-7.6 Gy [Taschereau *et al.*, 2006]. For low-resolution μ CT scans (e.g., 135 μ m pixel size) this is a lesser problem as the reported dose at this level is around 0.25 Gy. In contrast, for high-resolution scans required to assess microvasculature (5 μ m pixel size) the lethal dose can easily be reached [Ford *et al.*, 2003]. However, rodents can repair damages induced by X-ray radiation of up to 0.3 Gy [Parkins *et al.*, 1985]. This is a threshold six times higher than the accumulated 5 Gy after a 6 week *in vivo* imaging study for which no radiation damage of tissue was observed [Detombe *et al.*, 2013]. Furthermore, modern detector technology provides more sensitive scintillators and thus higher photon flux that is recorded by the detector, which results in shorter scanning times. This way, it may be possible to reduce the X-ray radiation dose if the detector pixel size can be further reduced for high-resolution imaging [Osborne *et al.*, 2012]. Also, further work on optimising tube current and voltage may help to decrease dose [Kalender, 2011]. In

conclusion, μ CT has reached a point where it is commonly used for *in vivo* imaging of small rodents.

Chapter 4

Methodology for micro-computed tomography of the microvasculature in skeletal muscle

4.1 Animal model of developmental priming

The animal model used in this project is the high-fat model introduced in figure 2.10 in chapter 2. All animal procedures were in accordance with the regulations of the United Kingdom Animals (Scientific Procedures) Act 1986 and were conducted under Home Office Licence number 70-6457. The study received institutional approval from the University of Southampton Biomedical Research Facility Research Ethics Committee. Supervision of the animals and handling until killing was kindly undertaken by Dr. Christopher Torrens, associate professor in physiology at the University of Southampton.

Female C57/BL6 mice were maintained under controlled conditions and assigned to either a high-fat diet (HF; 45% kcal fat, 18% kcal protein, 35% kcal carbohydrate; TestDiet, St. Louis, Missouri, USA) or standard chow diet (C; 10% kcal fat, 18% kcal protein, 72% kcal carbohydrate; RM1, Special Diet Services, Witham, UK). Dams were fed six weeks prior to conception and during gestation and lactation. At weaning, the male offspring were assigned either a HF or C diet, generating four experimental groups: HFHF (n=5), HFC (n=5), CHF (n=5), CC (n=5), which represent prenatal (first letter code) and postnatal dietary exposure (second letter code), respectively [Stead *et al.*, 2016]. At 15 weeks of age the mice were killed by cervical dislocation. The mean weight (g) for each group at the time of killing was determined in litter mates to be CC 31.7 ± 1.1 ; HFC 31.5 ± 2.1 ; CHF 40.9 ± 1.4 ; HFHF 40.2 ± 3.7 , n=5 per group.

4.2 Sample preparation

Three different sample preparation techniques to induce soft tissue contrast for μ CT imaging were employed and compared. In the first case blood vessels were perfused with a radio-opaque agent to obtain image contrast. In the second case soft tissue contrast was induced by staining of the tissue surrounding the blood vessels. The third method was leaving the samples unstained and using propagation-based phase contrast SR CT to obtain tissue contrast. In all cases the mice were sacrificed by cervical dislocation.

Table 4.1 contains a list of the samples that have been prepared, their preparation method, the respective imaging settings and information on whether or not they were segmented and analysed. The experiments were conducted in two rounds, in each of which 20 mice were killed. In the first round in November 2013 mice were prepared for imaging using perfusion and staining methods, with 10 muscles being prepared for each stain group. In the second round in April 2015 mice were prepared for phase contrast imaging, after a trial run of edge-enhancement imaging in June 2014.

4.2.1 Contrast by perfusion method

N=3 CC and CHF and n=2 HFC and HFHF mice were prepared using a perfusion technique. After killing of the offspring at 15 weeks of age, the abdominal aorta was cannulated and perfused with warmed, heparinised saline to flush out the blood. This was performed using a syringe pump at a perfusion rate of 0.25 ml/min. The syringe was then replaced with a syringe filled with Microfil®MV122 (Flow Tech Inc., US). The vasculature was perfused with Microfil at a rate of 0.25 ml/min. The perfusion was performed until the Microfil became visible in the leg vein. Figure 4.1 shows an image of Microfil-perfused leg arteries and veins taken under the light microscope.

The whole leg was then dissected and the Microfil allowed to cure overnight at 4°C. The next day, the soleus muscle was dissected and fixed in 10% formaldehyde at 4°C overnight. Subsequently, the muscle was dehydrated in a graded series of methylated spirit and embedded in a coffin mould in paraffin wax. For imaging the wax block was trimmed using an industrial razor blade and glued onto a SEM stub that can be clamped into any standard pin chuck. This is depicted in figure 4.2.

4.2.2 Contrast by staining method

For this method, n=10 muscles were prepared. However, only one muscle of the control group CC was finally imaged and analysed as explained in the next chapter.

Sample name	Contrasting method	Imaging system	Analysed	Validation
CIIC8-L	Microfil	Zeiss Versa 510	✓	✗
CIIC3-R	Microfil	Zeiss Versa 510	✓	✗
CIIC3-L	Microfil	Zeiss Versa 510	✓	✗
6CHF1-L	Microfil	Zeiss Versa 510	✓	✗
9HFC2-R	Microfil	Zeiss Versa 510	✓	✗
6CHF1-L	Microfil	Zeiss Versa 510	✓	✗
5CHF1-L	Microfil	Zeiss Versa 510	✓	✗
10HFC1-L	Microfil	Zeiss Versa 510	✓	✗
8HFHF1-R	Microfil	Zeiss Versa 510	✓	✗
10HFHF1-L	Microfil	Zeiss Versa 510	✓	✗
10HFHF1-R	PTA	Zeiss Versa 510	✗	✗
10HFHF2-R	PTA	Zeiss Versa 510	✗	✗
10HFC1-R	PTA	Zeiss Versa 51	✗	✗
9HFC2-R	PTA	Zeiss Versa 510	✗	✗
8HFC1-L	PTA	Zeiss Versa 510	✗	✗
8HFC1-R	PTA	Zeiss Versa 510	✗	✗
8HFHF1-L	PTA	Zeiss Versa 510	✗	✗
CIIC8-R	PTA	Zeiss Versa 510	✓	✗
CC1	Unperfused	TOMCAT, Swiss Light Source	✓	✓
CC2	Unperfused	TOMCAT, Swiss Light Source	✓	✓
CC3	Unperfused	TOMCAT, Swiss Light Source	✓	✓
CC4	Unperfused	TOMCAT, Swiss Light Source	✓	✗
CC5	Unperfused	TOMCAT, Swiss Light Source	✓	✗
CHF1	Unperfused	TOMCAT, Swiss Light Source	✓	✓
CHF2	Unperfused	TOMCAT, Swiss Light Source	✗	✗
CHF3	Unperfused	TOMCAT, Swiss Light Source	✓	✓
CHF4	Unperfused	TOMCAT, Swiss Light Source	✓	✓
CHF5	Unperfused	TOMCAT, Swiss Light Source	✗	✗
HFC1	Unperfused	TOMCAT, Swiss Light Source	✓	✓
HFC2	Unperfused	TOMCAT, Swiss Light Source	✓	✓
HFC3	Unperfused	TOMCAT, Swiss Light Source	✗	✓
HFC4	Unperfused	TOMCAT, Swiss Light Source	✓	✗
HFC5	Unperfused	TOMCAT, Swiss Light Source	✗	✗
HFHF1	Unperfused	TOMCAT, Swiss Light Source	✗	✗
HFHF2	Unperfused	TOMCAT, Swiss Light Source	✓	✓
HFHF3	Unperfused	TOMCAT, Swiss Light Source	✓	✗
HFHF4	Unperfused	TOMCAT, Swiss Light Source	✓	✓
HFHF5	Unperfused	TOMCAT, Swiss Light Source	✗	✓

Table 4.1: **Summary of all samples prepared.** Sample names are given, as well as contrasting methods, imaging systems used and whether or not the sample was analysed and used for mathematical modelling. The samples chosen for validation of the phase contrast imaging are also marked.

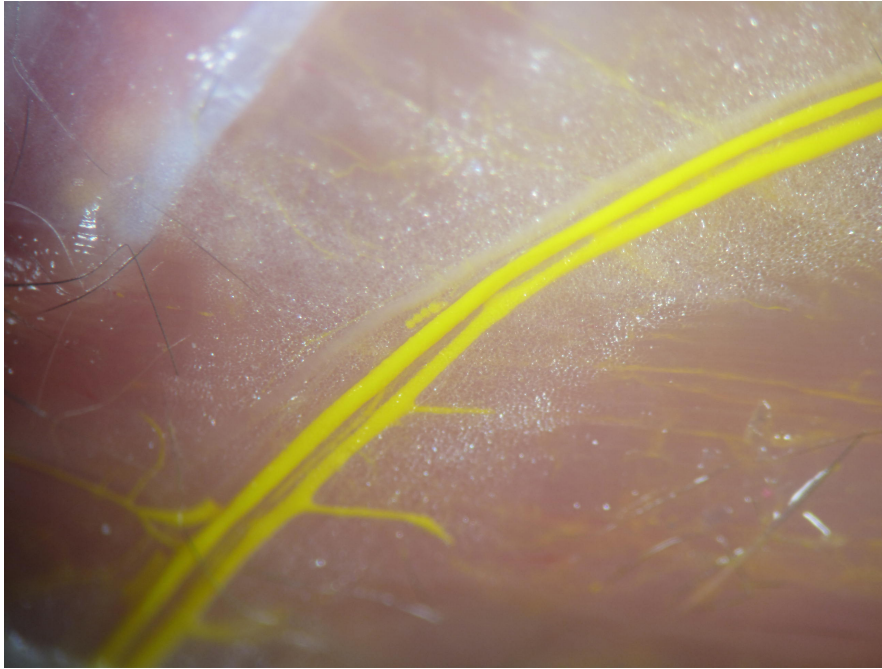


Figure 4.1: **Microfil-perfused vessels.** In order to enhance imaging contrast, the vascular network is perfused with the radio-opaque silicone rubber Microfil®MV122 (Flow Tech Inc., US), which has a yellow colour. When the perfusion is complete, both arteries and veins can be clearly seen in yellow.

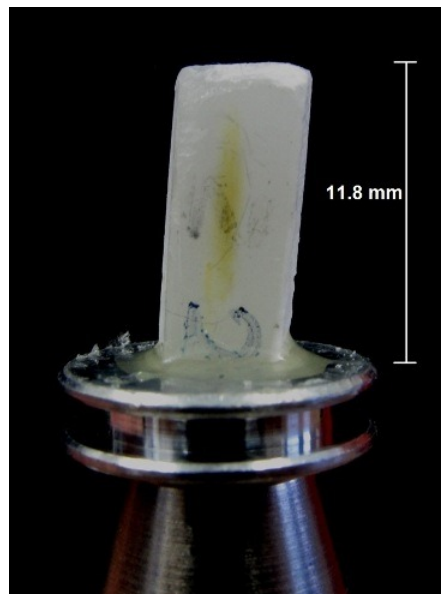


Figure 4.2: **Sample mounting for μ CT and SR CT imaging.** For imaging, the wax block containing the muscle was trimmed and glued onto a SEM stub. The mounting of the muscle was such that the longitudinal direction of the muscle was perpendicular to the X-ray path.

After killing, the abdominal aorta was cannulated and perfused with warmed, heparinised saline to flush out the blood. This was performed using a syringe pump at a perfusion rate of 0.25 ml/min. For staining with phosphotungstic acid (PTA) the

muscle was then dissected and immersed in 1% PTA overnight. Subsequently, fixation, embedding and mounting were performed as explained above for the Microfil-perfused samples.

4.2.3 Propagation-based phase contrast

As a third technique muscles were prepared that have not had the blood flushed out and were left unstained and thus only fixed and embedded in wax blocks. The hypothesis was that phase contrast alone enables the visualisation of red blood cells. 5 offspring mice of each dietary group were selected. The soleus muscle of the right leg was dissected directly after killing, thus leaving the blood within the blood vessels, and fixed in 10% formaldehyde at 4°C overnight. Dehydration, embedding and mounting are performed as explained above for the Microfil-perfused samples.

4.3 Imaging of samples

4.3.1 Imaging of the Microfil-perfused samples

The scans of the Microfil-perfused samples were performed using the Zeiss/Xradia Versa 510 system at the μ VIS X-ray Imaging Centre at the University of Southampton because of its small spot size and high resolution capability.

On the Zeiss/Xradia Versa 510 tungsten is used as the target metal. Instead of moving the sample stage, source and detector can move towards and away from the sample. There is a choice of microscope lenses with individual scintillators linked to a high performance digital CCD camera (Andor iKon-L), with which CT image resolutions in the order of 700 nm can be achieved.

For scanning the Microfil-perfused muscles the 4X lense was used at 80kV and 7W and at a pixel size of 1.4 μ m. Exposure time was between 2 and 3.5 seconds, depending on transmission values, a minimum of 2001 projections was taken and a detector bin 2 was used. Reconstruction of the datasets was performed with the in-built reconstruction software.

A slice of the reconstructed data can be seen in figure 4.3. The resolution was sufficient to detect capillaries. However, the perfusion of the vascular network appears insufficient as the distribution of the microvasculature would be expected to be much denser (see figure 2.6(b)). Furthermore, shrinkage of the Microfil appears visible in a number of blood vessels. The muscle tissue is visible against the surrounding wax, but individual muscle fibres or other soft tissue structures can not be distinguished.

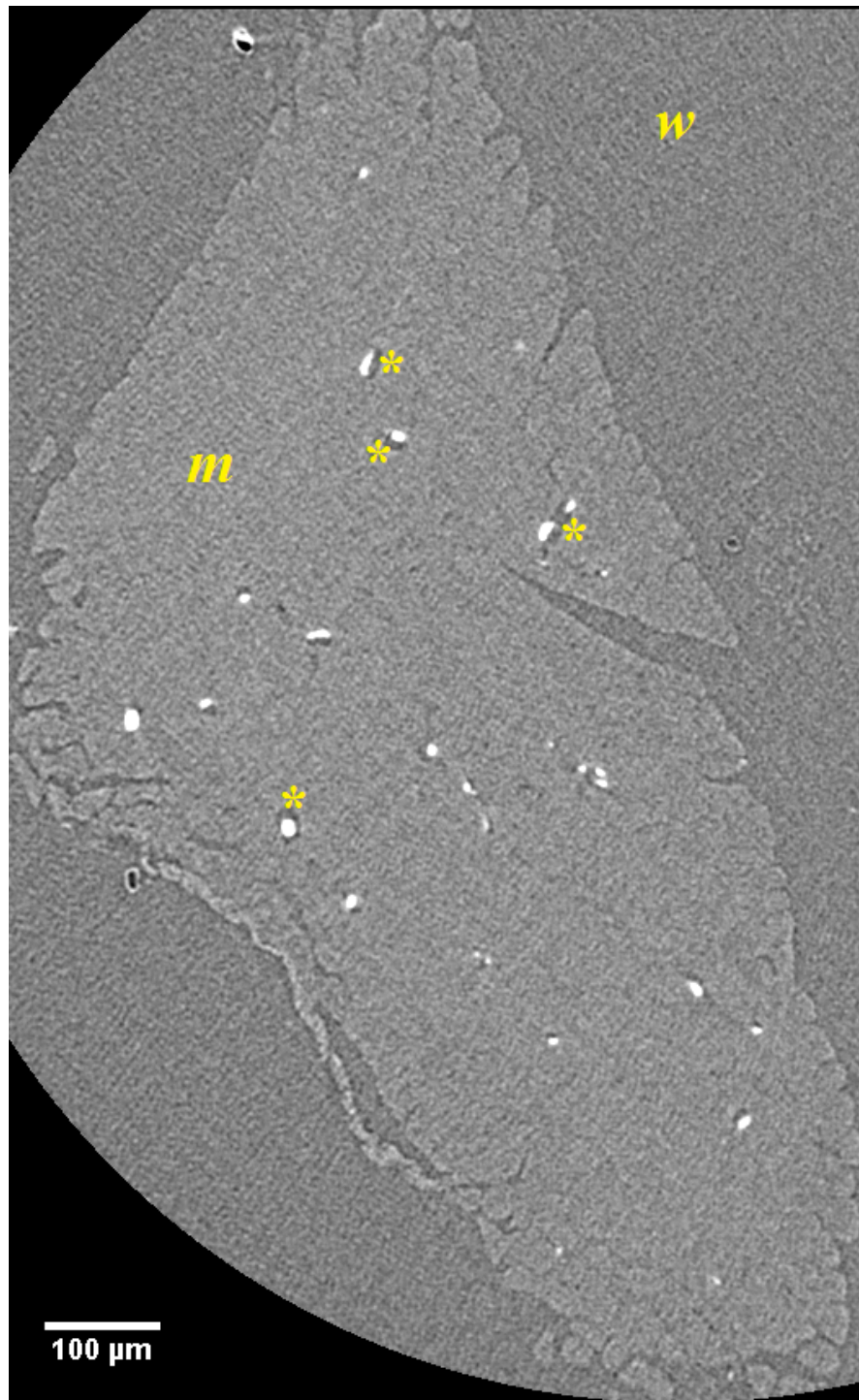


Figure 4.3: **Zeiss/Versa 510 scan of CC mouse soleus perfused with Microfil.** Imaging was performed on the 4X lense at 80kV/7W, at 1.4 μm pixel size, detector bin 2. Exposure time was between 2 and 3.5 seconds and a minimum of 2001 projections was used. Microfil appears bright in the reconstructed image. The muscle tissue (m) is visible against the surrounding wax (w). The Microfil appears to have shrunk in a number of blood vessels (*).

4.3.2 Imaging of the PTA-stained sample

PTA-stained samples were scanned on the Zeiss/Xradia Versa 510 using the 20X lense at 100kV and 9 W, detector binning 2 and with an exposure time of 3 seconds. 2001 projections were obtained. The difference in scanning settings compared to the Microfil samples is due to the high Z number of PTA, i.e., higher flux was necessary to reach a sufficient photon count on the detector.

Figure 4.4 shows a slice of this scan. All muscle fibres are stained as well as the vessel wall. However, the voxel resolution ($0.8\ \mu\text{m}$) appears not to be high enough to immediately differentiate between the different features and enable segmentation of the capillaries.

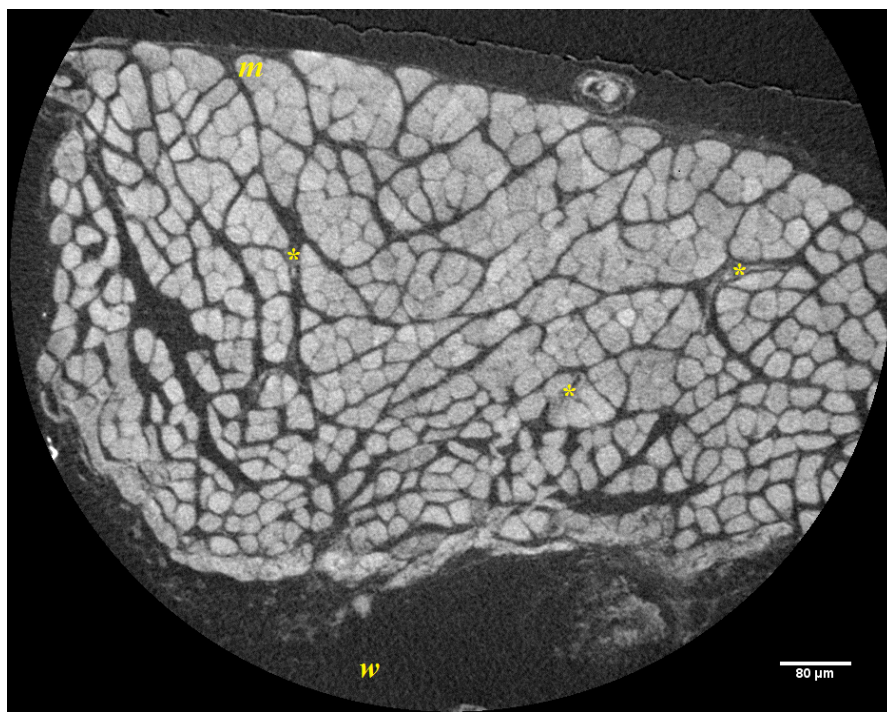


Figure 4.4: Zeiss/Versa 510 scan of CC mouse soleus stained with PTA. Imaging was performed on the 20X lense at 100kV/9W, at $0.8\ \mu\text{m}$ pixel size, detector bin 2. Exposure time was 3 seconds and 2001 projections were obtained. All muscle fibres (m) and vessel walls (*) have been stained with PTA. The contrast to the surrounding wax (w) is high, however, small blood vessels can not be immediately differentiated.

4.3.3 Phase contrast-based imaging at the Swiss Light Source

The imaging of the unstained samples was carried out at the Swiss Light Source, located at the Paul Scherrer Institut in Villigen, Switzerland. The experiments were conducted at the beamline for TOMographic Microscopy and Coherent rAdiology experimenTs (TOMCAT).

At TOMCAT it is possible to image using an energy between 8-45 keV and a voxel size from 0.16 up to 14.8 μm . Propagation-based phase contrast was used to visualise the red blood cells within the microvasculature and thereby gain information on the microvascular structure within the context of the animal model of developmental priming. To this end, two sets of scans were performed at TOMCAT; firstly, one control muscle was imaged at different sample-to-detector distances to be able to decide which propagation distance yielded the best image contrast and detectability of red blood cells. Secondly, scans at the chosen propagation distance of 60 mm were taken of all ($n=20$) muscle samples, which consisted of individual batch scans of 5-7 scans per muscle.

All scans at the SLS were performed at 14 keV, an exposure time of 180 ms and 1501 projections over an angle range of 0 – 180 deg. For each scan 32 dark field and 160 flat field images were initially taken to correct perturbations of the X-ray beam. In the cases where the muscle was too wide for the field of view a wide-field scan was performed with 3001 projections overall. The voxel size was 0.77 μm . The Fresnel number for each trialled propagation distance is given in table 4.2. It was computed as

$$N_F = \frac{a^2}{R_2 \lambda},$$

with $a = 0.77 \mu\text{m}$ the image voxel size, R_2 the sample-to-detector distance and λ the wavelength of the X-rays. At the finally chosen propagation distance of 60 mm it follows that $N_F = 1.12$.

4.3.3.1 Choice of propagation distance

An unperfused control muscle (group CC) was scanned at four different sample-to-detector distances, i.e., 30mm, 40mm, 50mm and 60mm, to study which distance provided the highest image contrast and best enabled the visualisation of red blood cells for further segmentation.

To the eye the difference in the phase contrast seems low for the different distances, see figure 4.5.

To assess the qualitative differences of the tomographies regarding image contrast, noise and feature identification the greyscale values of all image stacks were calibrated prior to analysis. This was done by determining the average greyscale value of the muscle tissue S_2 and the wax S_1 for two scans (S and \tilde{S}) that were to be calibrated against each other. A system of linear equations was set up to convert $\tilde{S}_{1,2}$ into $S_{1,2}$,

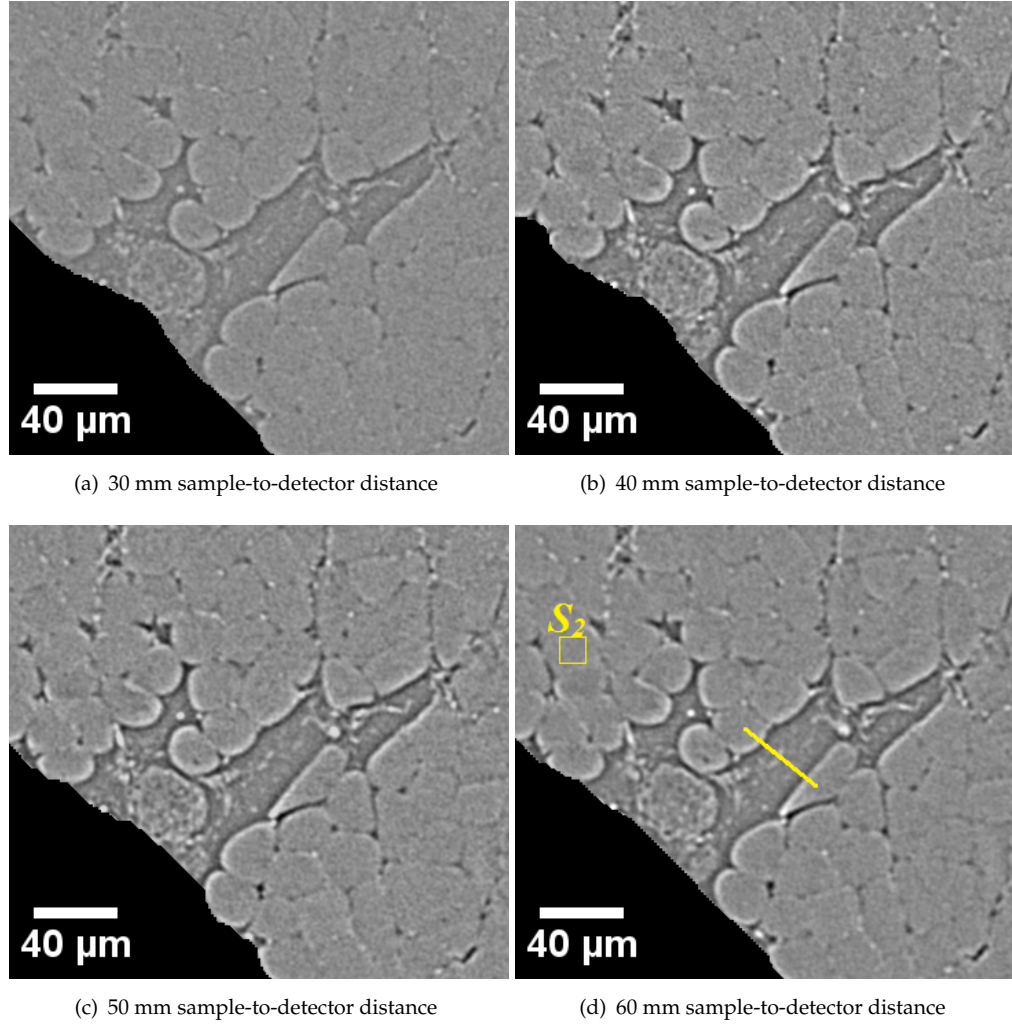


Figure 4.5: **Slices for each distance at the propagation distance trial at the TOMCAT beamline.** Four sample-to-detector distances were tested for their resulting image contrast and red blood cell visualisation. The marked quadratic region in 4.5(d) show the region in which S_2 for the contrast-to-noise ratio (Equation (4.4)) was determined. The line profile used for comparison of edge-enhancement in Figure 4.6 is also marked. S_1 and σ_1 for CNR and signal-to-noise ratio (Equation (4.3)) were determined in the wax in the a quadratic region of the same size as for S_2 (in the blackened region).

respectively. This took the form

$$S_1 = m * \tilde{S}_1 + n \quad (4.1)$$

$$S_2 = m * \tilde{S}_2 + n \quad (4.2)$$

and was solved for m and n . The greyscales \tilde{S} in the image to be calibrated were then updated to the calibrated values $\tilde{S}_{new} = m * \tilde{S} + n$. This was performed in ImageJ Fiji [Schindelin *et al.*, 2012].

After calibration the signal-to-noise ratio (SNR) and the contrast to noise ratio (CNR)

were computed for each propagation distance. The SNR is defined as

$$SNR = \frac{S_2}{\sigma_1}, \quad (4.3)$$

where S_2 is the mean grey value of the material in question (muscle tissue, see subfigure 4.5 and σ_1 is the standard variation of the background, in this case wax, signal (noise).

The CNR of these scans was computed according to

$$CNR = \frac{S_2 - S_1}{\sigma_1}, \quad (4.4)$$

where S_1 is the mean grey values of a second material which is compared to the first. Wax was chosen here to determine the soft tissue contrast against the background material. Generally, the higher the values of SNR and CNR, the better is the contrast between muscle and wax tissue and the lower is the noise in relation to the image signal. However, with increasing propagation distance a decrease in image noise is likely as the finite spot size (and thus finite coherence length) can be associated with increasing blurring of features for increasing propagation distances. This can be derived from the van Cittert-Zernike theorem [Wolf, 2007].

Detector distance [mm]	Fresnel number N_F	Wax S_1 [a.u.]	Tissue S_2 [a.u.]	Noise σ_1 [%]	SNR	CNR
30	2.23	35091	37480	3.68	15.53	0.99
40	1.67	37007	38936	2.73	21.74	1.08
50	1.34	39576	41263	2.98	21.12	0.86
60	1.12	33982	35482	1.98	27.39	1.16

Table 4.2: **Fresnel number, wax and tissue signals, noise and SNR and CNR for the SLS distance trial.** Computed according to equations (4.3) and (4.4). The noise is given as percentage of number of greyscale values in the 16-bit range (65536). For all distances, as The highest values for SNR and CNR are apparent at a sample-to-detector distance of 60 mm.

The results are given in table 4.2. Clearly, the scan at 60mm detector distance has the highest SNR and CNR of the propagation distances investigated. The intensity profiles along edges for the different distances were also compared, as shown in figure 4.6. Note that in the figure, the greyscale values were adjusted for the differing mean value between different sample-to-detector distances. There was a large increase in fringe intensity between 40 and 50 mm distance, however, higher sample-to-detector distances show less differences. Due to the high SNR and CNR and the large fringe intensity, the sample-to-detector distance of 60 mm was chosen. See Figure 4.7 for a whole slice of the tomographic reconstruction of a scan at this distance. It needs to be noted, however, that the large increase in SNR and CNR for 60 mm will partly stem

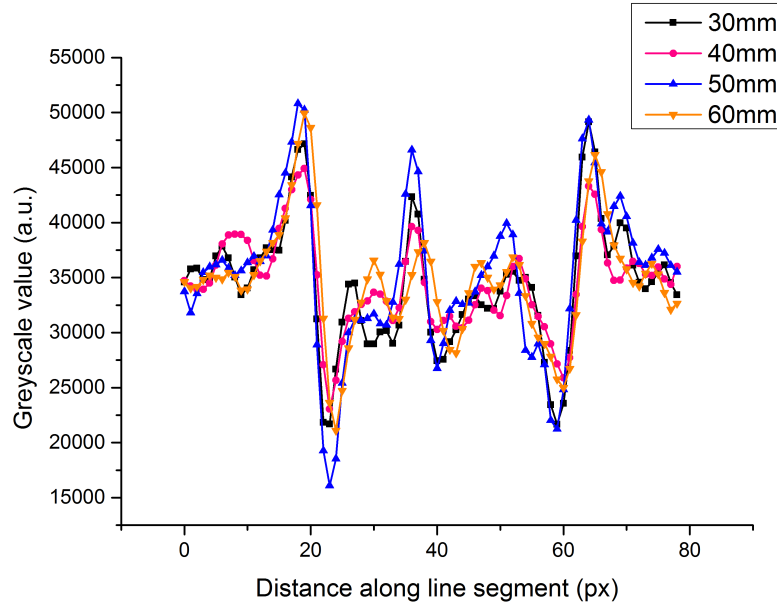


Figure 4.6: **Intensity profile for phase comparison for different sample-to-detector distances for the propagation distance trial at TOMCAT.** There is a large increase in fringe intensity between 30 and 40 mm distance, however, higher sample-to-detector distances show less differences.

from the fact that blurring of the features (thus leading to a decrease in noise) occurs due to the finite spot size. Furthermore, at 60 mm sample-to-detector distance, the condition for near-field imaging, i.e., $N_F \gg 1$ has almost diminished. Technically, this is of consequence for the validity of the chosen phase retrieval algorithm (in this case Paganin), as the assumptions by which the algorithm was derived no longer hold. This was ignored as phase retrieval was used only to enhance image contrast of different soft tissue features.

4.3.3.2 Phase retrieval

With propagation-based phase contrast SR CT it is possible to either reconstruct the three-dimensional tomography directly from the projections or to phase retrieve the projections prior to reconstruction. The phase of the projections obtained at TOMCAT was retrieved using an in-house implementation of the Paganin single-distance non-iterative phase retrieval algorithm [Paganin *et al.*, 2002]. $\beta = 3.49 \cdot 10^{-8}$ and $\delta = 1.66 \cdot 10^{-6}$ were chosen as parameters for phase retrieval (as in the definition of the refractive index (3.9)). These were experimentally determined by researchers at the SLS to be the values working best for biological (soft tissue) specimen. A number of different parameters were tested, but the above values proved optimal. Interestingly, these values are incident with those for Calcium at an energy of 14keV, whilst values for e.g. glucose and paraffin wax have a β/δ ratio different by two orders of magnitude at the same energy due to lower β values [hen, 2016, Henke *et al.*, 1993].

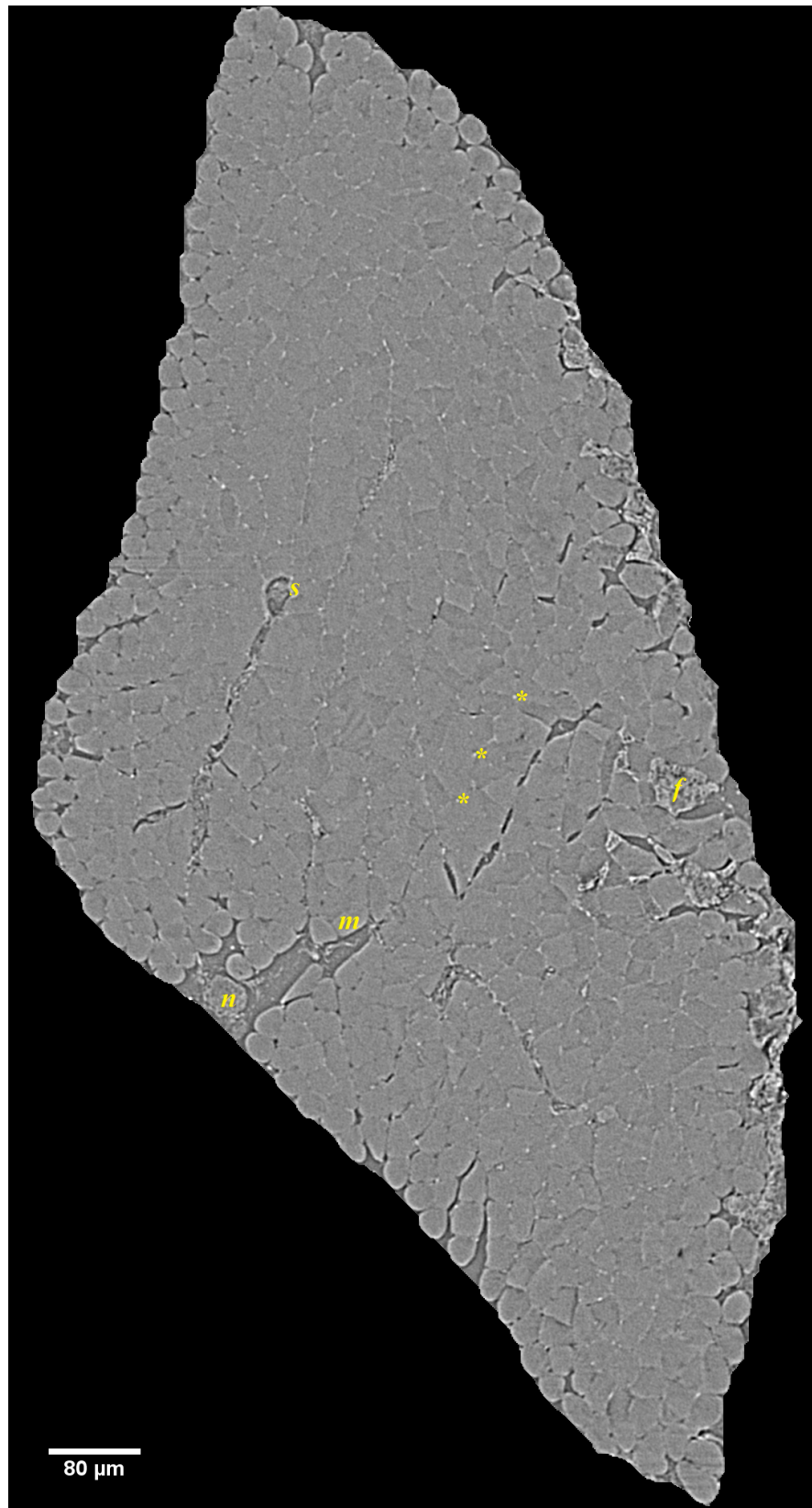


Figure 4.7: **Slice of the sample at 60mm sample-to-detector distance.** The edge-enhancement enables the visualisation of the RBCs (white dots) within the capillaries visible (*), as well as muscle spindles (s), nerves (n), the individual muscle fibres (m) and fascia (f).

Subsequently, the 3D dataset were reconstructed using an in-house implementation [Marone & Stampanoni, 2012] of the *gridrec* algorithm [Dowd *et al.*, 1999] at TOMCAT. At the same time the *gridrec* algorithm was used by itself to derive edge enhanced reconstructions. Figure 4.8 shows resulting slices using both methods. In the directly reconstructed image the red blood cells appear clearer due to the high contrast with the surrounding muscle fibres, whilst muscle spindles (<) and vessel walls (*) of larger blood vessels are clearer in the image that was Paganin phase-retrieved prior to reconstruction as no fringes impair the visualisation.

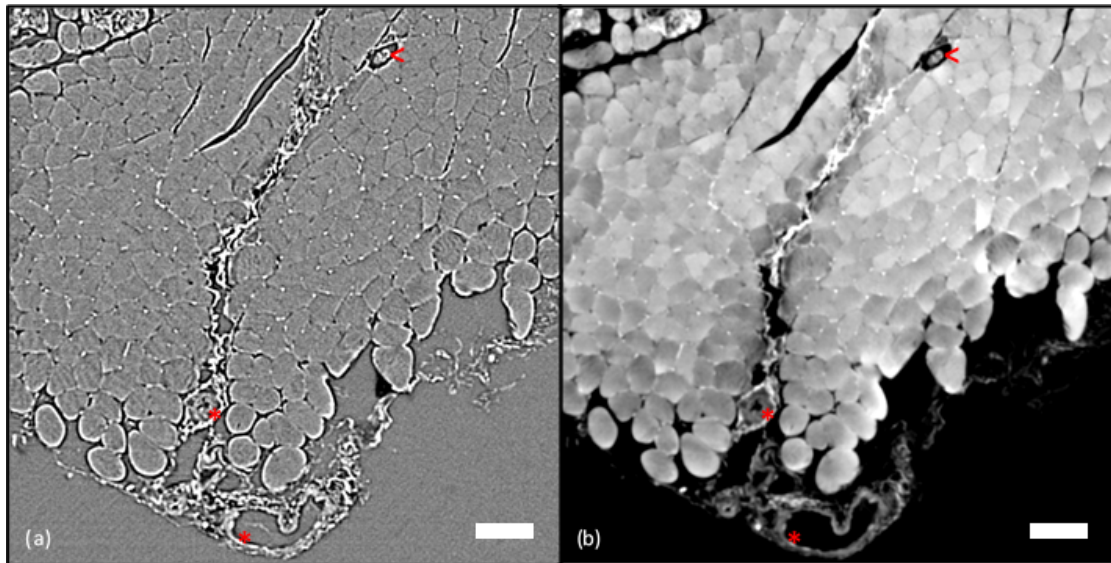


Figure 4.8: Comparison of edge enhancement and phase retrieval for red blood cell imaging using phase contrast-based synchrotron radiation computed tomography. a) shows a slice of the direct reconstruction, while b) shows a slice of the Paganin phase-retrieved and then reconstructed data. The white dots in-between muscle fibres are red blood cells. Empty capillaries (black circular spaces in-between muscle fibres) and larger blood vessels (*) can also clearly be distinguished, as well as intramuscular structures such as muscle spindles (<). Scale bars are 50 μm .

4.3.3.3 Limitation by scintillator setup

Whilst imaging at TOMCAT one major technical limitation occurred: the scintillator installed in front of the CCD camera appeared to be slightly distorted, thus leading to a skew in the focus settings over its length. This is shown in figure 4.9. In particular towards the lower end of each image stack the data would appear slightly out of focus and greyscales would change slightly (figure 4.10). Therefore, larger overlapping regions were created between every two datasets to have a larger amount of sharp data when stitching the overall muscle dataset together. As segmentation would eventually be performed manually, this was thought to reduce the error in resulting

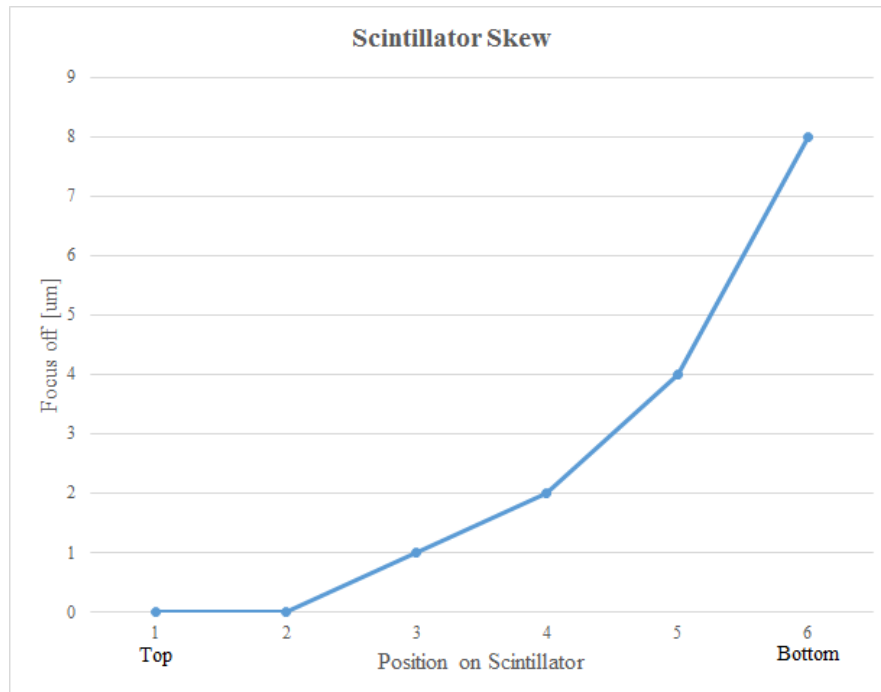


Figure 4.9: **Skew of the scintillator focus.** The scintillator installed in front of the CCD camera at the SLS was skewed vertically, thus resulting in a skew of the focus settings along its height. This resulted in a loss of sharpness over the length of an image stack.

RBC numbers as much as possible. Swapping the scintillator for a non-distorted one was not possible as no replacements were available.

4.4 Image segmentation

In the following the process of stitching together the datasets of each muscle and the segmentation of blood vessel and red blood cells is explained.

4.4.1 Data stitching

As the muscles were considerably (~ 8 mm) longer than wide (~ 2 mm) and the field of view in imaging both on the Versa 510 and at TOMCAT covered only 2×2 mm², it was necessary to take a number of scans along the length of the muscle in order to be able to image the whole muscle. Depending on the straightness of the muscle and its total length, this resulted in 5-7 scans per muscle (including overlapping regions). After reconstruction, the images of the scans of each muscle were calibrated, so that the greyscales of RBCs/Microfil and muscle fibres for all datasets matched. The calibration was conducted as described in section 4.3.3.1, with S_2 being the average RBC/Microfil greyscale value. The data obtained after reconstruction was given as 16-bit unsigned

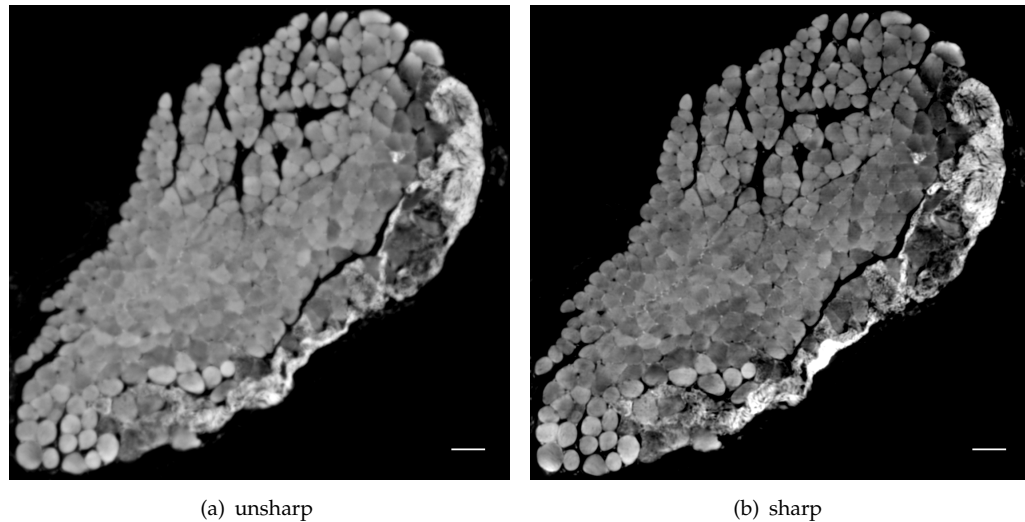


Figure 4.10: **Difference in sharpness at beginning and end of image stacks.** 4.10(a) is taken at the end of one dataset and 4.10(b) is from the overlapping region at the beginning of the following image stack. The skew of the scintillator clearly resulted in a significant loss of sharpness which was circumvented by increasing the overlapping region and setting the focus in the middle region of the scintillator. The scale bars represent $50\ \mu\text{m}$.

data and converted to 8-bit datasets after calibration and prior to concatenation, to be able to process all datasets. Concatenation of scans obtained at TOMCAT required up to 250 GB memory, thus almost exhausting the maximum memory of computing machines available in the μVIS X-ray Imaging Centre. The process of concatenation of the 8-bit datasets required up to 6 hours for a whole muscle and result in datasets of up to 90 GB size. Due to this effort and them showing better soft tissue contrast, only the phase-retrieved tomographies obtained at TOMCAT were concatenated.

4.4.2 Microfil samples

For the $n=10$ Microfil perfused sample the segmentation of the blood vessels was performed by applying a region growing tool, such as the “magic wand” tool in Avizo®Fire 7.0 (Visualization Sciences Group, US). This tool selects all voxels connected to a user-defined seed point within a certain grey level range. A faster, but less exact tool would be simple absolute thresholding by greyscale. By applying the region growing tool a binary image stack containing the blood vessel voxels against a black background was obtained. An example can be seen in figure 4.11.

The muscle tissue was segmented manually using the “edge tracing” tool in Avizo to segment the muscle in every 50th slice and then interpolate over all remaining slices. The interpolation is linear and thus not “intelligent” and cannot account for sudden

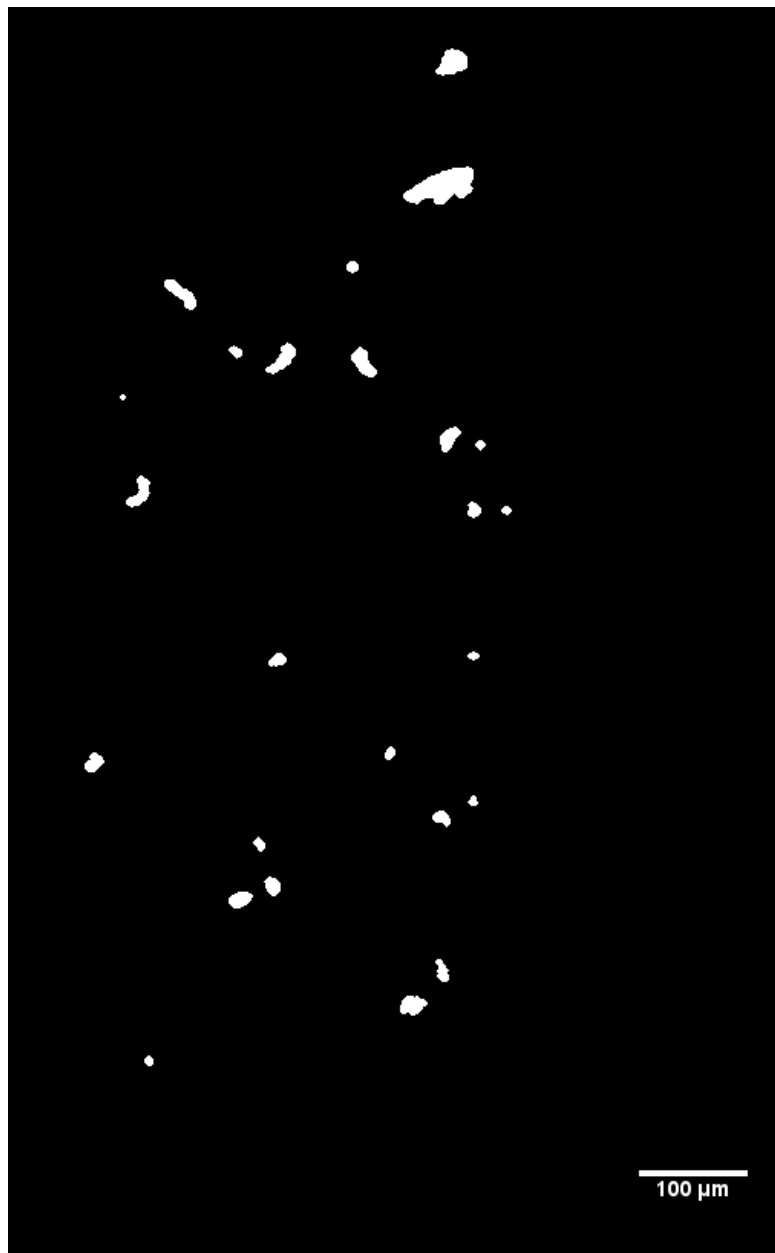


Figure 4.11: **Slice of binary image stack.** The binary image stack was obtained after region growing segmentation a Microfil-perfused muscle. The image stack is used for feature quantification.

changes in the segmentation. Thus, such occurrences were corrected for manually afterwards. The muscle tissue volume was exported as a binary image stack.

The binary datasets were then used for quantification of the microvascular as will be explained in section 4.5 and for computational modelling (see section 7.3.1).

4.4.3 PTA samples

For the PTA-stained control sample it was not possible to segment the vessel structure in such a straightforward fashion. The vessel lumen was dark against the bright muscle tissue, but other dark features were also visible in the image, e.g., spaces between muscle fibres. Thus, any identification of these features as capillaries was difficult and could not be automated. Therefore, the segmentation of the blood vessel lumen had to be undertaken manually. To this end Avizo Fire 7.0 was used. The “brush tool” enables segmentation of the feature of interest in a specific slice of the μ CT stack and the interpolation tool was used to expand the segmentation into the intermediate slices. The muscle tissue was again segmented by combination of edge tracing and interpolation, as explained above. The segmented blood vessel network and muscle tissue were saved as respective binary datasets for the subsequent image analysis.

4.4.4 Unperfused samples

Due to the computational load of processing the segmented dataset for computational modelling (see chapter 7) and time requirements, the segmentation of each muscle was limited to a $(1.5\text{mm})^3$ cube from the medial muscle region. As the oxygen supply to the tissue is from the capillaries mainly only the red blood cells in the capillaries were segmented and not those in larger blood vessels.

Whilst the phase retrieved image showed good contrast between different soft tissues (figure 4.8), it was difficult to segment the red blood cells from the image using an automated method as greyscales of RBCs and surrounding muscle fibres were often not significantly different enough. To enhance the contrast between RBCs and muscle fibres a “bandpass filter” was applied in ImageJ [Schindelin *et al.*, 2012] with an upper and lower threshold of 3 px and 1 px, respectively. This resulted in highlighting all spatially fast-changing features, such as the RBCs and muscle fibre edges. However, imaging artefacts, in particular ring artefacts (resulting from bad detector pixels, see section 3.2.4) were also enhanced. To facilitate segmentation and reduce the ring artefact enhancement a 2x2x2 binning filter in ImageJ [Schindelin *et al.*, 2012] was subsequently applied. This binning filter averages the greyscales of every 2x2x2 voxel block into one new voxel, thus halving the image resolution to $1.54\text{ }\mu\text{m}$, which is the upper limit for capillary detection as introduced in section 3.1.1.

The resulting image was then thresholded by greyscale to segment bright features,

i.e., the RBCs and muscle fibre edges. This was performed in Avizo Fire 9.0 (FEI, Hillsboro, OR, USA). The chosen threshold was determined using a short parametric study of the influence of the threshold on the resulting number of detected red blood cells. The edges resulting from fringes were manually selected using the magic wand tool in Avizo (as explained in 4.4.2) to subtract them from the segmentation. The region growing over all slices allowed for fast selection of the edges.

Overall, this process of segmentation was very time intensive, requiring at least 2-3 days per muscle cube. Therefore, the analysis was limited to $n=3$ muscles for the dietary groups CHF, HFC and HFHF, instead of all $n=5$ dissected muscles (yet $n=5$ for CC).

The muscle tissue was segmented as explained above and binary images of muscle tissue and RBCs were saved for analysis.

As phase contrast-based imaging with subsequent phase retrieval also enabled the visualisation of intramuscular soft tissues other than blood vessels, muscle spindles and adipose tissue in the obtained datasets of the whole muscle have also been segmented (without application of a bandpass filter). The segmentation was performed in Avizo Fire 9.0 in the same way the muscle tissue was segmented, i.e., edges of the objects were traced over in a number of slices and connected by linear interpolation between the slices. The results concerning muscle spindles and fat are presented separately in section 5.4.

4.5 Feature quantification

In section 2.4 the morphological parameters used for assessing the microvascular structure and its oxygen exchange capability have been introduced. These measures were computed for the blood vessel networks obtained from Microfil-perfused samples, the PTA-stained sample and for the unstained samples imaged using propagation-based phase contrast.

4.5.1 Identification of capillaries

For the identification of capillaries within the blood vessel network the software ImageJ [Schindelin *et al.*, 2012] and its plugin BoneJ [Doubé *et al.*, 2010] were used. The diameters were determined using the BoneJ plugin thickness, which is based on a method developed by Hildebrand and Rüeggsegger [Hildebrand & Rüeggsegger, 1997]. This method computes a local thickness measure of the structure being inspected. For each point within the structure, the diameter of the largest sphere containing this point is computed. This diameter is the local thickness of the respective point. The result is then saved as a three-dimensional local thickness map by changing the greyscale values of each of structure to its local thickness, see figure 4.12. Maximum thickness,

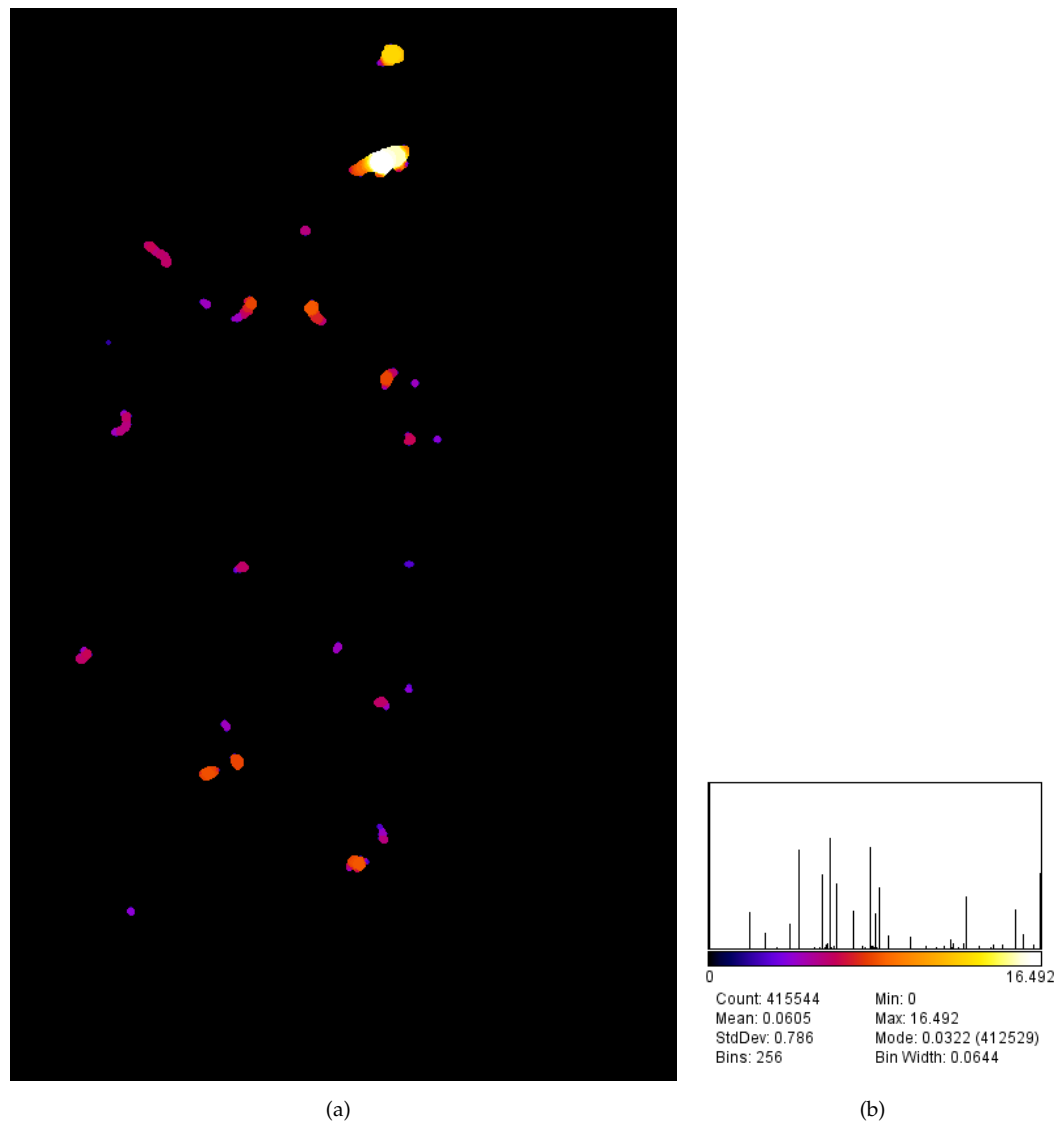


Figure 4.12: Thickness map created by BoneJ plugin thickness 4.12(a) on a segmented blood vessel network. The colours correspond to the different thicknesses, see the legend 4.12(b). The mapped dataset allows thresholding for capillaries by greyscale thresholding.

mean thickness and thickness distribution are calculated. The method was previously successfully applied to derive bone morphometric measures [Hildebrand & Rüegsegger, 1997].

By greyscale thresholding on the thickness map the capillaries of the network can then be distinguished and the structural analysis can be conducted for these. $10\text{ }\mu\text{m}$, the largest diameter of a capillary, was chosen for thresholding, which corresponded in the image to a greyscale value of $10/1.4(\text{resolution}) \approx 7$ (pixels).

Avizo®Fire 7.0 can also be used to compute vessel diameter. The diameter distribution can be given applying the “Autoskeleton” module and subsequently applying the “Radius Histogram” module [Burrell *et al.*, 2012]. However, as the

algorithm averages over a vessel of varying diameters and thereby skews the results, this module was not employed.

4.5.2 Volumes and volume fraction

Muscle volume and vessel volume are computed using the BoneJ plugin “Volume Fraction” Doube *et al.* [2010]. The plugin is applied to the binary images of the muscle and the vessel network respectively. The plugin counts the number of black and white voxels in a binary image. To determine the actual volume in mm^3 the counts are corrected for the voxel resolution. Division of both volumes gives the volume fraction of the microvasculature.

4.5.3 Tortuosity

In order to determine the network’s tortuosity the ImageJ plugin “Skeletonization” Schindelin *et al.* [2012] is used on the original binary image of the structure. This plugin determines the (geometric) centerlines of the vascular tree, i.e. each vessel segment is thinned to its centerline. Using the “Analyse Skeleton” plugin, total vessel segment length as well as the Euclidian distance for the end points of each segment are given. Following the equation given in section 2.4 the tortuosity can be determined. Tortuosity was not computed for the unperfused samples, as the visualisation of the red blood cells results in a disconnected network thus rendering the value of tortuosity meaningless.

4.5.4 Length density

The length density of the capillary network was computed by applying the volume fraction plugin to the skeletonized image, which essentially computes the total length of the vessel network. The value needs to be corrected for the voxel size of the dataset. Division by the previously computed muscle volume gives the length density.

4.5.5 Capillary density

The number of capillaries/red blood cells per slice was computed by counting the number of white voxels per slice in the skeletonised blood vessel image, using the volume fraction plugin. The count was divided by the muscle tissue area from the corresponding slice, which was obtained using the volume fraction plugin on the slice of the binary muscle volume dataset and correction for the voxel size. The counting

was performed for three slices in the medial region of the muscle and the final number was obtained by averaging over these.

4.5.6 Capillary-to-fibre ratio

After determining the capillary density, the corresponding three slices were selected in the original muscle dataset. The number of muscle fibres in the slices were counted manually. Division of the capillary/red blood cell number from above by the number of muscle fibres gave the capillary/red blood cell to fibre ratio and the average of the three slices was determined.

4.5.7 Fractal dimension

Fractal dimension was given by applying the BoneJ plugin “Fractal Dimension” Doube *et al.* [2010], which uses the box-counting algorithm to determine the dimension, as described in section 2.4.6. The plugin returns fractal dimension as well as the error of the fit.

4.5.8 Mean distance to next red blood cell (RBC spacing)

For the SR CT imaged sample the mean distance to the next red blood cell (in 3D) for each point in the muscle tissue was computed using the “3D distance map” plugin in ImageJ Schindelin *et al.* [2012]. The plugin was applied to the binary red blood cell image stack and multiplied with the binary muscle volume image stack to limit the distance map to the muscle tissue. The arithmetic mean of greyscales in the resulting dataset was taken as the mean RBC spacing.

4.6 Statistical analysis

The analysis of statistical significance was performed using IBM SPSS 21.0/22.0 (IBM Corp., NY, USA), which is a comprehensive data analysis package Kirkpatrick & Feeney [2013]. A group sample size $n = 3$ is normally necessary Berkman & Reise [2012], but with a sample size of $n = 2$ the analysis can still be performed, however, the results are less meaningful.

Data from offspring from the four dietary groups (CC, HFC, CHF and HFHF) were analysed with maternal diet and offspring diet as between-subject factors. Specific comparisons between HF-fed offspring groups and their respective controls were made using a generalised linear model with posthoc Bonferroni and Dunnett’s tests

where appropriate, indicated as p_B and p_D , respectively [Everitt, 2002]. Relationships between measures were assessed by linear regression. All data are expressed as mean \pm standard deviation (SD). Results were considered statistically significant for $p < 0.05$.

4.7 Summary

In this chapter the animal model of developmental priming used in this PhD project was introduced and the three different techniques of inducing soft tissue contrast for visualisation of the microvasculature in high-resolution computed tomography imaging were presented. In particular, a perfusion technique (with the polymer Microfil) and a staining technique (with phosphotungstic acid) in combination with lab-based μ CT imaging were utilised, as well as propagation-based phase contrast SR CT on unstained samples. The methodology of imaging, image segmentation and morphometric analysis for all three methods was presented.

Chapter 5

Results of micro-computed tomography of the microvasculature in skeletal muscle

The results of the structural analysis of the microvascular networks in the applied animal model of developmental priming are presented in this chapter. The reader be reminded that four dietary groups, i.e., CC, CHF, HFC and HFHF (C - chow diet, HF - high fat diet) were investigated using three methods to induce soft tissue contrast for μ CT imaging: Microfil perfusion of the vasculature, staining of the muscle tissue with phosphotungstic acid (PTA) for soft tissue contrast and phase contrast-based SR CT imaging of red blood cells within the vasculature.

5.1 Microfil-perfused samples

Figure 5.1 shows the 3D renderings of all samples perfused with Microfil, as described in table 4.1 in the previous chapter. As described in section 4.5, five characteristic measures for all Microfil samples have been determined, these were capillary density, tortuosity, fractal dimension, volume fraction and length density. The mean values for each group for the capillary networks are shown in figure 5.2 and figure 5.3 shows the results for the capillary network versus the whole network.

As can be seen in figure 5.2, the difference in means for all measures is very low while the variance within groups is high. The only difference is in the fractal dimension were at least CC and CHF group can be clearly differentiated from each other and all other groups. The tortuosity was found to be lower when looking at the capillary network only instead of the whole blood vessel network for most samples. This suggests that the larger blood vessels are more tortuous in these networks. Sample 10HFHF2-L

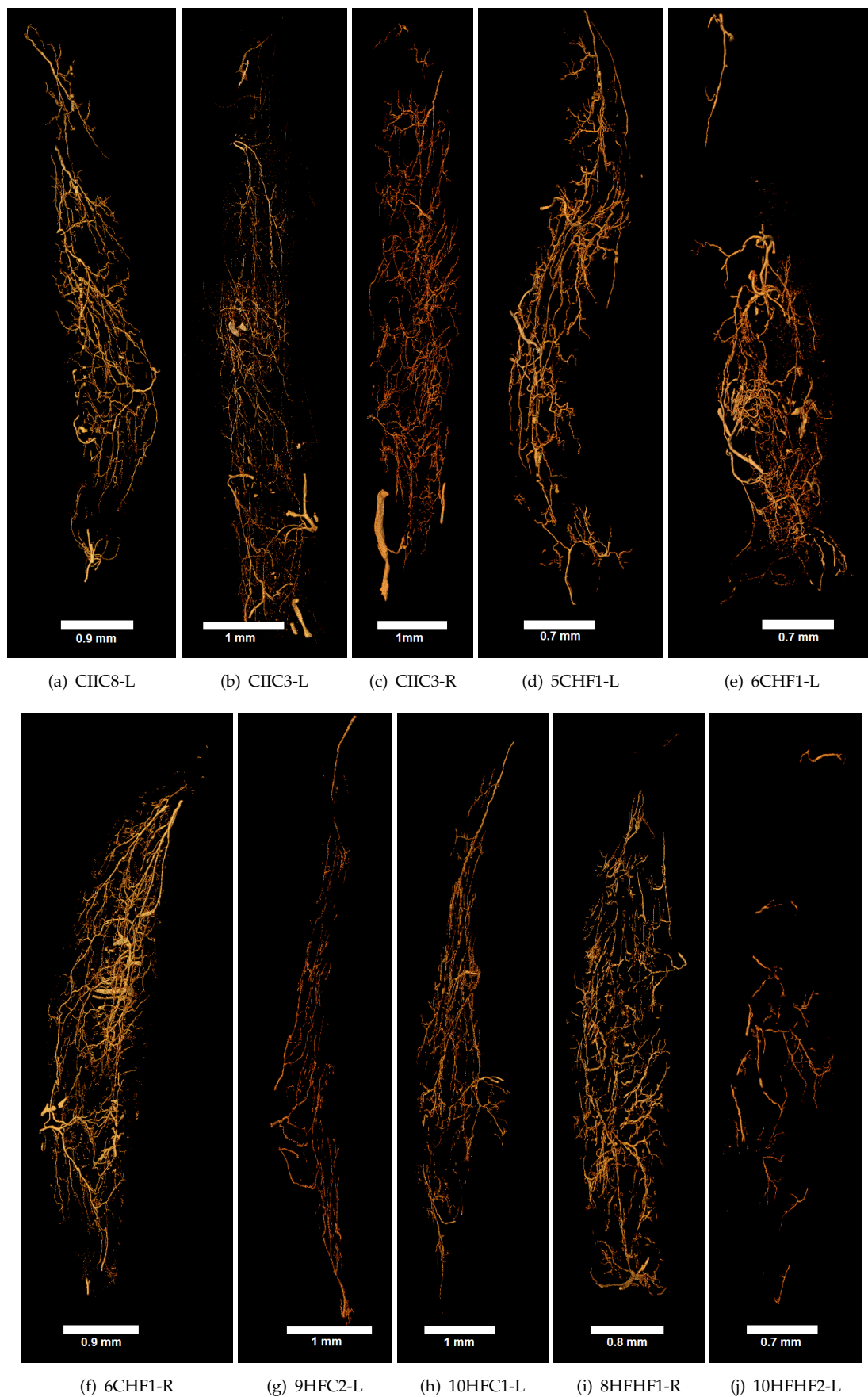


Figure 5.1: **3D renderings of blood vessel networks of all samples perfused with Microfil.** The quality of the different networks is visible, i.e. ideally the blood vessels are continuous with as few breaks as possible. The capillary tree should be a dense network.

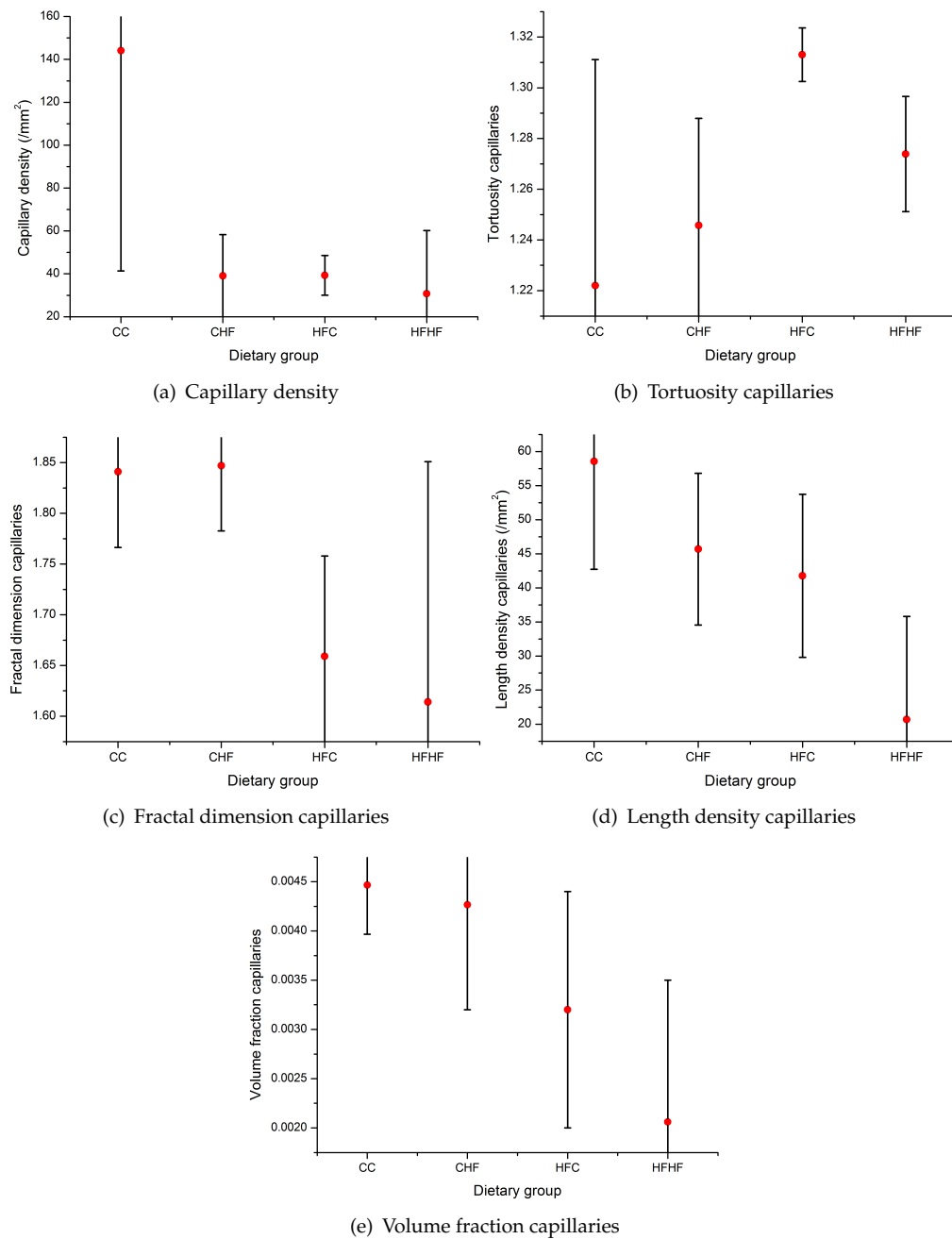


Figure 5.2: **Morphological parameters of the capillary network of the Microfil-perfused muscles.** The means (\pm standard deviation) of the structural parameters capillary density, tortuosity, fractal dimension, length density and volume fraction have been determined for the four dietary groups. $N=3$ for CC and CHF and $n=2$ for HFC and HFHF.

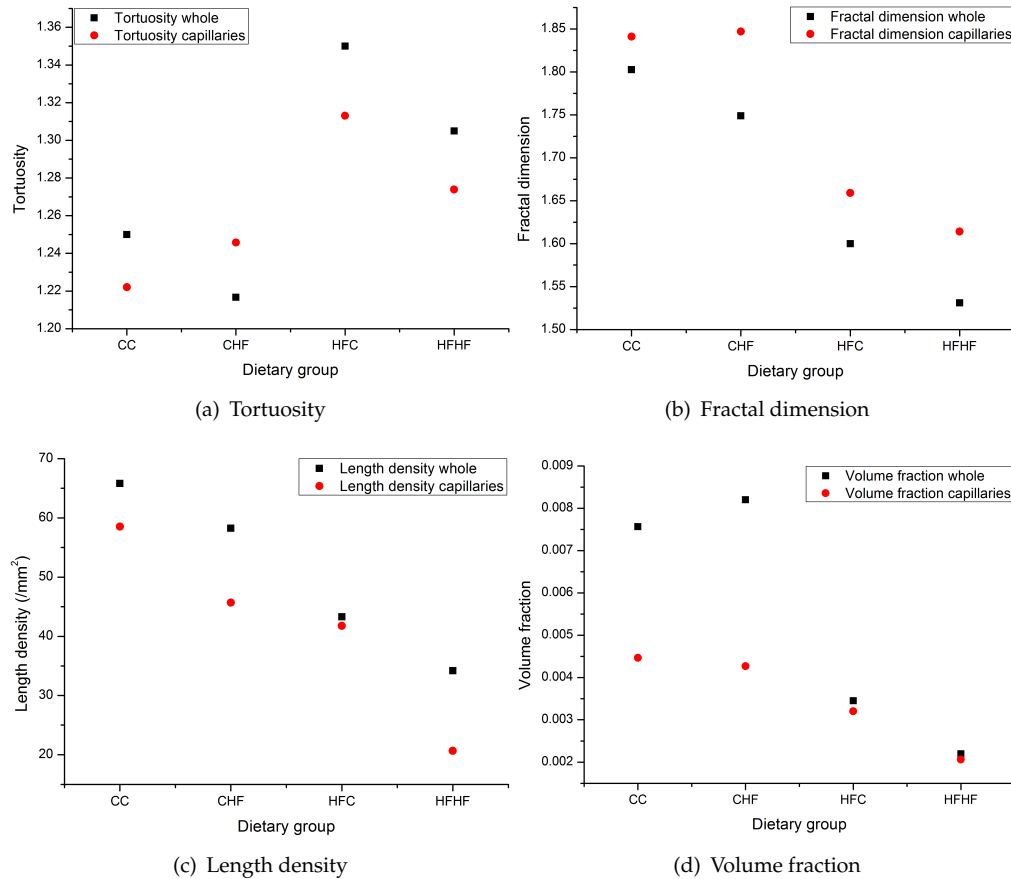


Figure 5.3: Means of morphological parameters of the capillary network (red circle) compared to the whole microvascular network (black square) of the Microfil-perfused muscles. The means of the structural parameters capillary density, tortuosity, fractal dimension, length density and volume fraction have been determined for the four dietary groups. $N=3$ for CC and CHF and $n=2$ for HFC and HFHF.

shows poor perfusion in comparison with the other samples. This is likely to have resulted in skewed results for the morphometric analysis.

Overall, the difference between dietary groups for all measures was found to not be statistically significant.

Maternal diet was found to have an effect on whole network volume fraction ($p < 0.05$) and whole network fractal dimension ($p < 0.05$) across the four offspring groups. Volume fraction of capillaries ($p = 0.064$) and whole network tortuosity ($p = 0.078$) approached but did not reach the threshold for significance.



Figure 5.4: **3D rendering of segmented blood vessels in PTA sample.** Larger blood vessels were visible but only few blood vessels smaller than $10\ \mu\text{m}$ in diameter could be segmented.

5.2 PTA-stained samples

Figure 4.4 shows a slice of a CC muscle stained with PTA. It was difficult to segment the smaller blood vessels in the PTA-stained samples, as the capillaries could not be distinguished from surrounding muscle tissue. However, the PTA stain helped in identifying other soft tissue structures, such as muscle spindles and it was possible to segment all larger vessels. Figure 5.4 shows a 3D rendering of the blood vessels segmented in the PTA-stained CC sample. As capillaries could not be differentiated further segmentation was discontinued.

The capillary density was determined to be $22 \pm 5\ \text{mm}^{-2}$. Capillary-to-fibre ratio was not determined, as not all muscle fibres could be distinguished. Whole network volume fraction was determined as 0.0042, length density as $23\ \text{mm}^{-2}$, fractal dimension as 1.59 and tortuosity as 1.18.



Figure 5.5: **Zoom-in on medial region of unperfused sample imaged using propagation-based phase contrast SR CT.** Larger blood vessels (*) are seen entering the muscle and dividing into smaller vessels, before giving way to the dense capillary network.

5.3 Phase contrast-based imaging

Figure 5.5 displays a segmented blood vessel network of an unstained CC muscle scanned using propagation-based phase contrast SR CT. The image is immediately visually much richer in blood vessels than those of the previous methods. In the depicted belly region of the muscle the larger blood vessels are entering the muscle and branching into smaller vessels. This indicates that with this method of inducing soft tissue contrast it is possible to visualise the smallest of blood vessels, in a way not possible beforehand.

As only red blood cells were segmented for the analysis (see section 4.4.4), the vessel diameter for unperfused samples was not computed. The results of all computed structural measures for the segmented unperfused samples are given in table 5.1. Due to the naturally variable perfusion of capillaries with red blood cells the standard deviation of the different structural parameters per muscle group is large. See figure 5.6 for the display of mean values per group with standard deviation. Mean distance of each point in the muscle tissue to the next capillary (RBC spacing) was dependent

on dietary group ($p < 0.05$), in particular the means of CC and HFC group were significantly different ($p_D < 0.05$). Length density missed the threshold of significance closely (LD $p = 0.087$).

The observed power was 28% (effect size $\eta=0.305$) for capillary density, 11% for capillary-to-fibre ratio ($\eta=0.108$), 51% for length density ($\eta=0.466$), 48% for volume fraction ($\eta=0.446$), 32% for fractal dimension ($\eta=0.343$) and 64% for the mean distance measure ($\eta=0.534$). This suggests that sample numbers should be increased to obtain better confidence in the results.

5.4 3D visualisation of other intramuscular structures using phase contrast-based SR CT

Intramuscular soft tissues other than blood vessels and red blood cells were visualised using propagation-based phase contrast SR CT with Paganin phase retrieval. Namely it was possible to visualise muscle spindles in 3D, as well as intramuscular adipose tissue and nerves for the first time. Muscle spindles and adipose tissue were analysed in the context of the animal model of developmental priming to assess the effect of maternal and offspring diet on the development on these soft tissues.

In chapter 2, section 2.3.1 the negative influence of maternal and offspring high-fat diet on skeletal muscle development was presented. For muscle spindles in particular it has been shown that diabetes (which can result from a high-fat diet) gives rise to changes in the innervation of muscle spindles [Muller *et al.*, 2008]. As the development of skeletal muscle and of muscle spindles mainly occurs *in utero* and is completed by postnatal day 4 in mice [Milburn, 1973], it may be hypothesised that an adverse developmental environment could influence the number and/or distribution of muscle spindles. Furthermore, an increase in bodyweight and body fat percentage has been observed in the HF offspring and using phase contrast-based SR CT we can determine if this can be linked to an increase in adipose tissue in skeletal muscle.

5.4.1 Muscle spindles

Figure 5.7 shows examples of muscle spindles observed in a reconstructed slice of the acquired SR CT data, together with corresponding slides from histology stained with PGP9.5 antibody (see Chapter 6). The different structures of nerves, spindles and intrafusal fibres can clearly be distinguished in the SR CT images.

Due to the non-invasive 3D nature of SR CT imaging it was possible to follow the intrafusal fibres along not only within the ECA, as shown in figure 5.8, but throughout the whole muscle until they merge into the muscle fascia (not shown). The dedicated

Muscle ID	Capillary density mm^{-2}	Capillary-to-fibre ratio	Length density mm^{-2}	Volume fraction E-02	Fractal dimension	Mean distance to next capillary* μm
CC1	810	0.95	781	0.59	2.54	10.99 \pm 3.50
CC2	1078	1.25	1083	0.78	2.59	9.50 \pm 2.80
CC3	783	0.75	825	0.54	2.48	11.31 \pm 3.33
CC4	817	0.94	920	0.77	2.55	10.24 \pm 3.23
CC5	652	0.62	768	0.58	2.50	11.30 \pm 3.60
CHF1	1414	1.32	1539	1.07	2.62	8.54 \pm 3.10
CHF3	729	0.64	914	0.61	2.54	10.43 \pm 3.18
CHF4	1077	1.05	1215	0.90	2.58	9.20 \pm 2.85
HFC1	1362	1.24	1499	1.14	2.62	8.37 \pm 2.31
HFC2	1091	0.85	1279	0.89	2.56	9.00 \pm 2.43
HFC4	851	1.05	977	0.82	2.58	9.69 \pm 3.95
HFHF2	800	0.79	895	0.64	2.54	10.29 \pm 2.71
HFHF3	768	0.74	862	0.61	2.57	10.18 \pm 3.97
HFHF4	995	1.05	1130	0.86	2.60	9.72 \pm 6.63

Table 5.1: **Detailed results of microvascular structural parameter analysis for unperfused samples.** Structural parameters have been computed based on the visualisation of red blood cells in the soleus muscle of mice of the animal model of developmental priming. * statistical significance ($p < 0.05$).

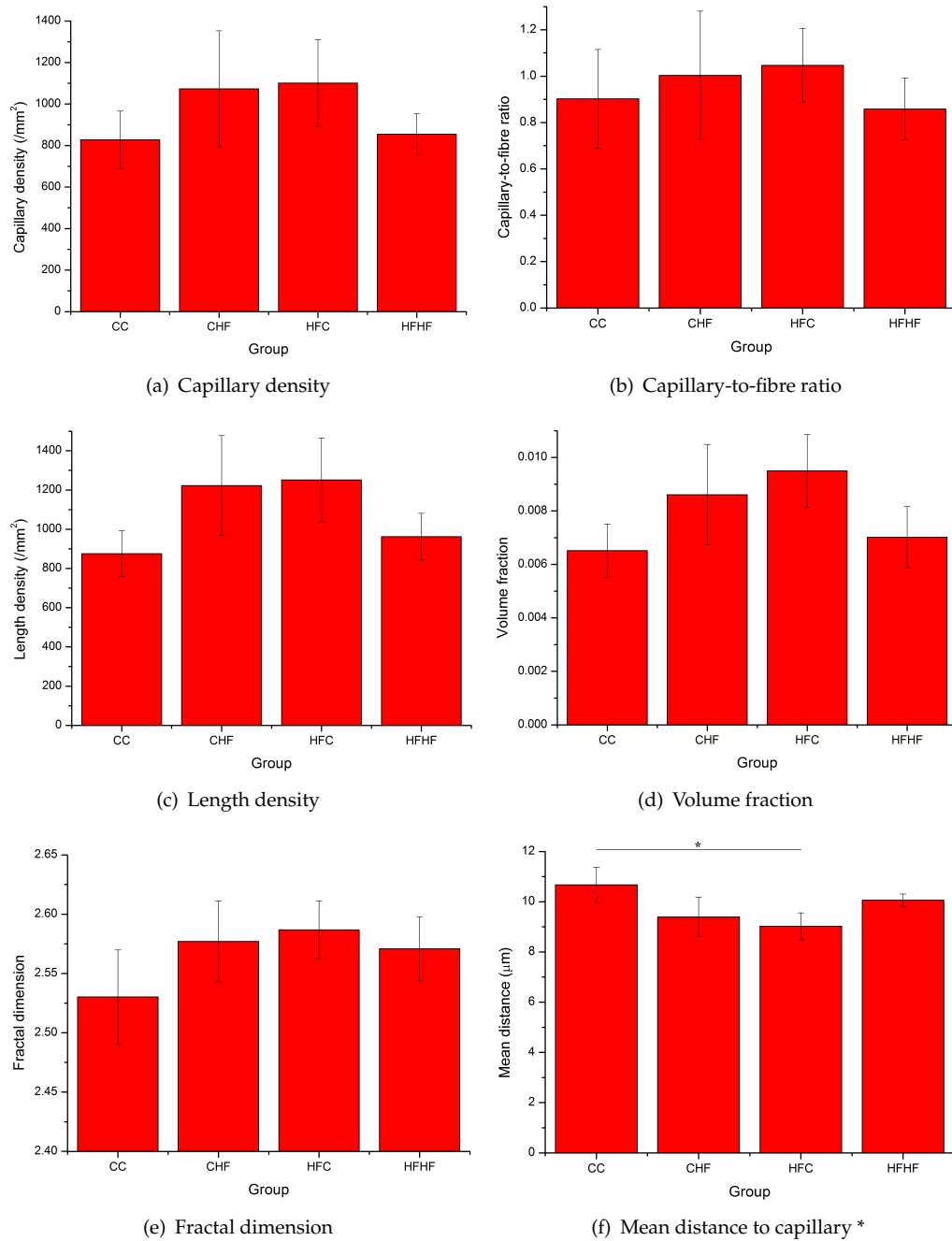


Figure 5.6: Means of structural measures per dietary group based on table 5.1 for unperfused samples imaged using phase contrast-based SR CT. * statistical significance ($p < 0.05$).

	CC (n=5)	CHF (n=4)	HFC (n=5)	HFHF (n=4)
Muscle volume [mm ³]	5.21±0.40	5.91±0.72 ^a	5.07±0.15 ^{b+}	6.38±0.37 ^{a+,c+}
Number of muscle spindles	11.40±0.80	11.50±1.50	12.20±2.48	12.50±1.12
Number of muscle fibres per cross-section	1012.90±45.34	1033.67±42.69	971.73±51.58	1008.08±48.62
Number of intrafusal fibres	3.70±0.09	3.85±0.11 ^a	3.88±0.31	3.73±0.17
Intra-muscle variability of number of intrafusal fibres	0.68±0.15	0.63±0.17	0.73±0.17	0.73±0.02
Number of spindles per unit muscle volume [mm ³]	2.20±0.22	1.88±0.23 ^a	2.41±0.47 ^b	1.97±0.25
Number of muscle fibres per muscle spindle	89.31±7.53	91.31±11.92	81.86±11.13	85.85±10.35
Number of muscle fibres per unit muscle volume [mm ³] ^x	195.55±18.10	167.89±16.61 ^a	191.74±4.90	158.98±15.54 ^{a,c+}

Table 5.2: **Quantitative morphometry of muscle and muscle spindles for the four dietary groups CC, CHF, HFC and HFHF.** a significant difference compared to CC group ($p < 0.05$), b significant difference compared to CHF group ($p_D < 0.05$), c significant difference compared to HFC group ($p_B < 0.05$), + ($p < 0.05$), x significant difference between C and HF offspring ($p < 0.01$). Values are given as mean±standard deviation.

arterioles that supply the muscle spindles and run along them could be observed in 3D; this morphology was as anticipated by Kokkorogiannis [2004]. However, not every muscle spindle was accompanied by such an arteriole.

Figure 5.9 shows all muscle spindles as well as the neurovascular bundle in a control muscle. In chow-fed control animals (CC) the mean volume of the soleus muscle was $5.21 \pm 0.40 \text{ mm}^3$ (mean±SD). The number of muscle fibres per SR CT cross-section in the medial region of the muscle was 1013 ± 45 (table 5.2).

A significant influence of offspring diet on muscle volume in adult offspring was observed (maternal diet $p = 0.960$ $F=0.1$; offspring diet $p < 0.0001$, $F=28.7$), with animals fed a post weaning fat-rich diet having a greater muscle volume compared with their dietary controls ($p_D < 0.05$ CHF vs. CC and $p_D < 0.01$ HFHF vs. HFC) (table 5.2). While there was no significant difference in numbers of muscle fibres in the medial cross section across the four dietary groups, a significant influence of offspring diet on the number of muscle fibres per unit volume of muscle (maternal diet $p = 0.431$ $F=0.7$; offspring diet $p = 0.02$, $F=14.8$) was identified. The number of muscle fibres per unit volume was lower in animals exposed to a post-natal fat-rich diet (table 5.2). An average of 11.8 ± 0.7 neuromuscular spindles per muscle from CC mice with a mean of 3.7 ± 0.1 intrafusal fibres per muscle spindle (table 5.2) was derived. The number of

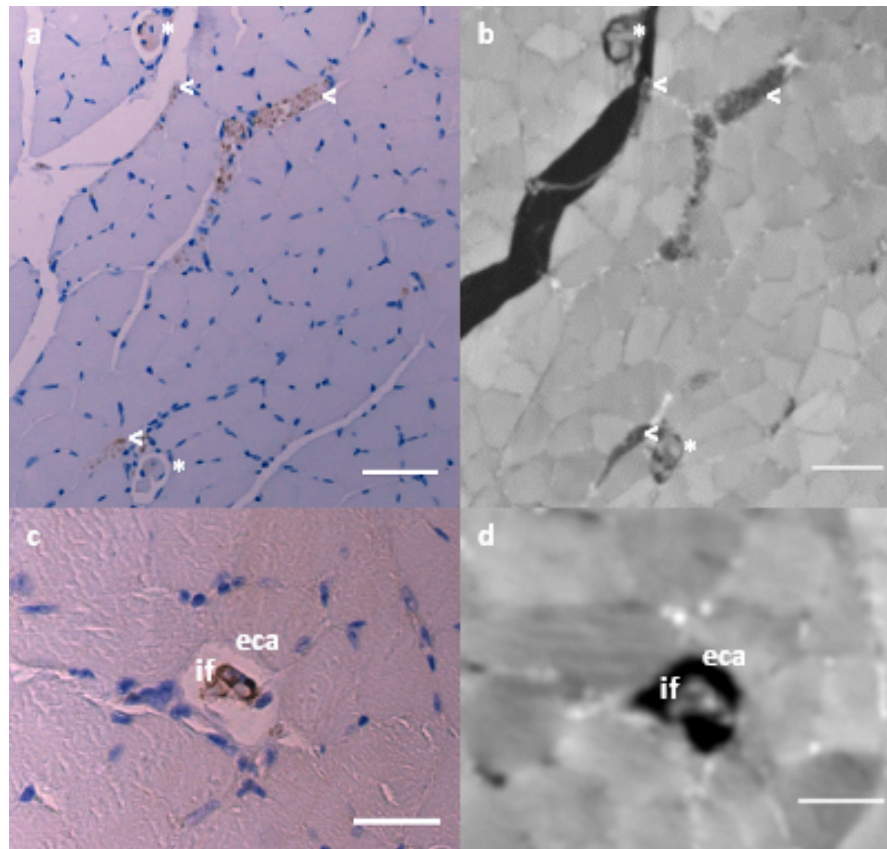


Figure 5.7: **Comparison of corresponding histological (left) and SR CT (right) images of muscle spindles in transversal sections of mouse soleus muscle in control group.** Nerves in (a,c) were stained with PGP9.5 antibody (see Chapter 6) and are visualised in brown by DAB chromagen. The characteristic structure of both nerve tissue (<) and muscle spindles (*) is visible in the SR CT images. The external capsule (eca) and intrafusal fibres (if) can be distinguished. Scale bars in (a,b) and (c,d) are 50 μm and 30 μm , respectively.

spindles was greatest in the belly of the muscle (figure 5.10). In the post-weaning high fat fed mice, the number of spindles per unit volume of muscle decreased with increasing muscle volume (maternal diet $p = 0.493$ $F=0.5$; offspring diet $p = 0.025$ $F=6.3$). A significant difference in the number of intrafusal fibres between the CC and CHF groups ($p_D < 0.05$) was noted. Figure 5.10 shows 3D volume renderings of soleus muscles and the muscle spindles from each dietary group, based on SR CT data. It can be seen that the spindle distribution between the groups appears different in the muscles. Figure 5.11 shows the area fraction of muscle spindles in muscle tissue per SR CT slice for the control group (CC) (including standard deviation). The mean spacing distance between muscle spindles and the muscle border is $0.28 \pm 0.15 \mu\text{m}$ (maximum $0.51 \mu\text{m}$) in the control group.

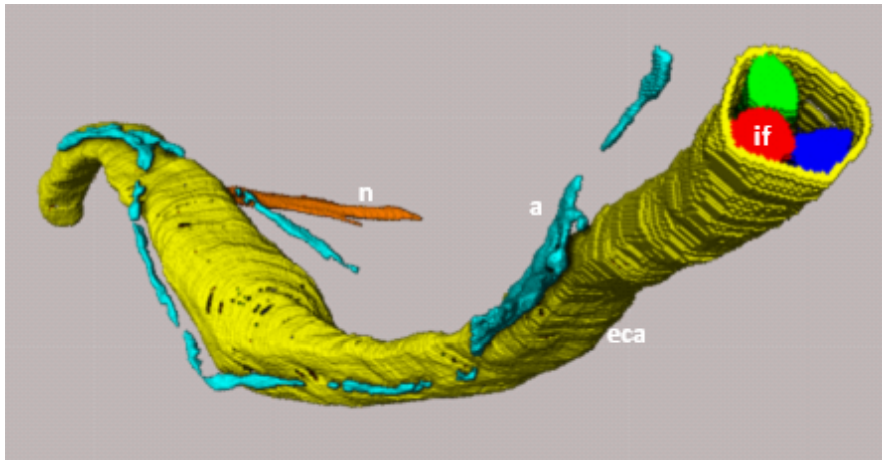


Figure 5.8: **3D volume rendering of a muscle spindle.** The different intrafusal fibres (if) (red, blue, green) and the external capsule (eca, yellow) have been segmented as well as the lumen of small arteriole (a) running along the spindle (turquoise) and one of the supplying nerves (n, orange). The representation of the muscle spindle has been derived from SR CT data, assessed at a voxel size of $0.77 \mu\text{m}$.

5.4.2 Fat volume

In order to assess how much the increased muscle volume in high-fat offspring depends on increased intramuscular fat depots adipose tissue within the muscle of $n=3$ mice per dietary group was segmented. The adipose tissue could be clearly distinguished from the rest of the muscle tissue and is characterised by its morphology, as seen in figure 5.12.

A volume rendering of the segmented volume within the muscle is displayed in figure 5.13.

Table 5.3 displays the segmented fat and muscle volume of the investigated muscles, as well as the resulting fat-to-muscle volume fraction. For each group, the mean \pm SD fat volume is displayed in figure 5.14. The difference of the fat volume per group is statistically significant ($p < 0.05$). The significance is lost when correcting for muscle volume ($p_D = 0.065$). The means of CC and HFHF groups remained significantly different for both fat volume and fat volume fraction ($p < 0.05$ for both), suggesting the additive negative effect of offspring high-fat diet in addition to maternal high-fat diet. In the post-weaning high fat fed mice the fat volume increased significantly (maternal diet $p = 0.209$ $F=1.8$; offspring diet $p = 0.030$ $F=6.4$). The same held for the fat volume fraction (maternal diet $p = 0.219$ $F=1.7$; offspring diet $p = 0.033$ $F=6.1$)

This suggests that the increase in muscle volume in the high-fat fed offspring is linked to increase in intramuscular fat volume. Furthermore, this matches the increase in body weight and body fat percentage observed in these animals [Stead *et al.*, 2016].

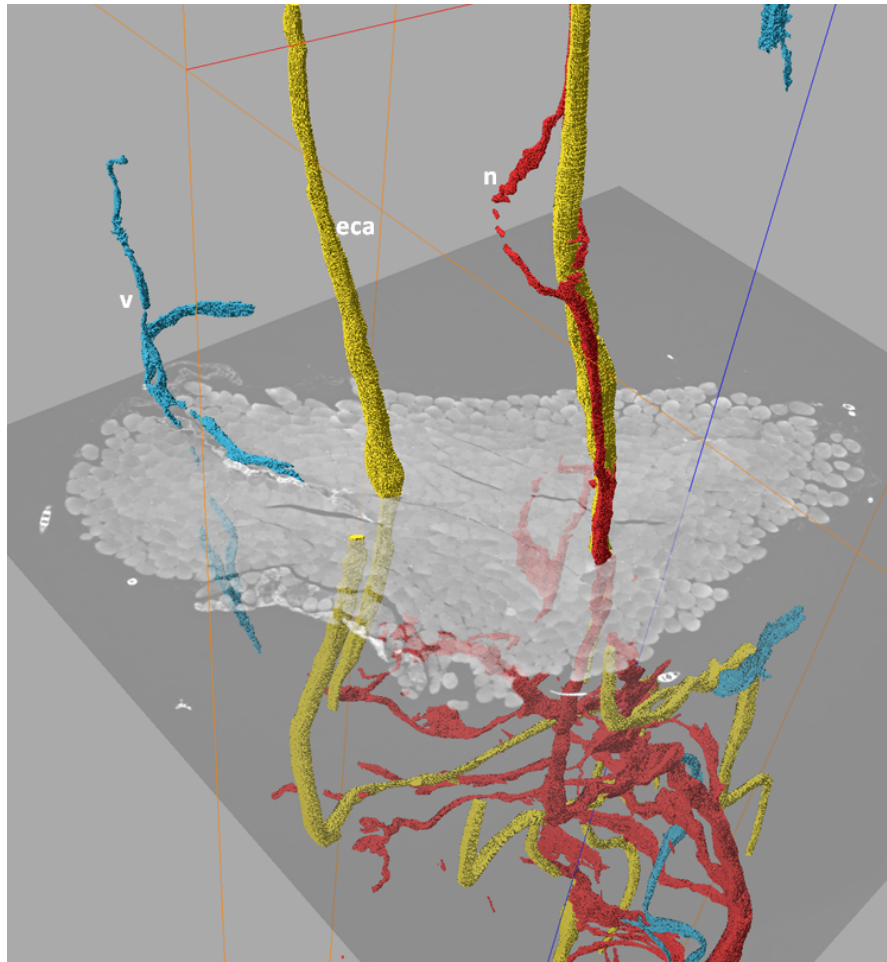


Figure 5.9: **3D volume rendering of muscle spindles and the neurovascular bundle in control muscle.** Spindles (eca) are displayed in yellow, nerves (n) in red and lumen of the larger blood vessels (v) in blue. The representation of the muscle spindles and the neurovascular bundle has been derived from SR CT data (displayed as one slice), assessed at a voxel size of $0.77 \mu\text{m}$.

5.5 Discussion

The structural parameters of the blood vessel and capillary networks obtained for Microfil-perfused datasets, a control PTA-stained dataset and for the uncontrasted samples imaged using phase contrast-based SR CT have been presented. A comparison of the means for the control group (CC) for the three methods is given in table 5.4 with a listing of methodological advantages and disadvantages.

The numbers of capillaries imaged in the Microfil-perfused samples and the PTA-stained sample was very low, i.e. capillary density for control muscles was $286 \pm 66 \text{ mm}^{-2}$ and $22 \pm 5 \text{ mm}^{-2}$, respectively, compared to the phase contrasted samples ($828 \pm 139 \text{ mm}^{-2}$) and the literature ($860 - 1300 \text{ mm}^{-2}$, see section 2.4.1, chapter 2). Therefore, the resulting structural measures from Microfil-perfused and the PTA-stained datasets have little meaning other than indicating a trend for the

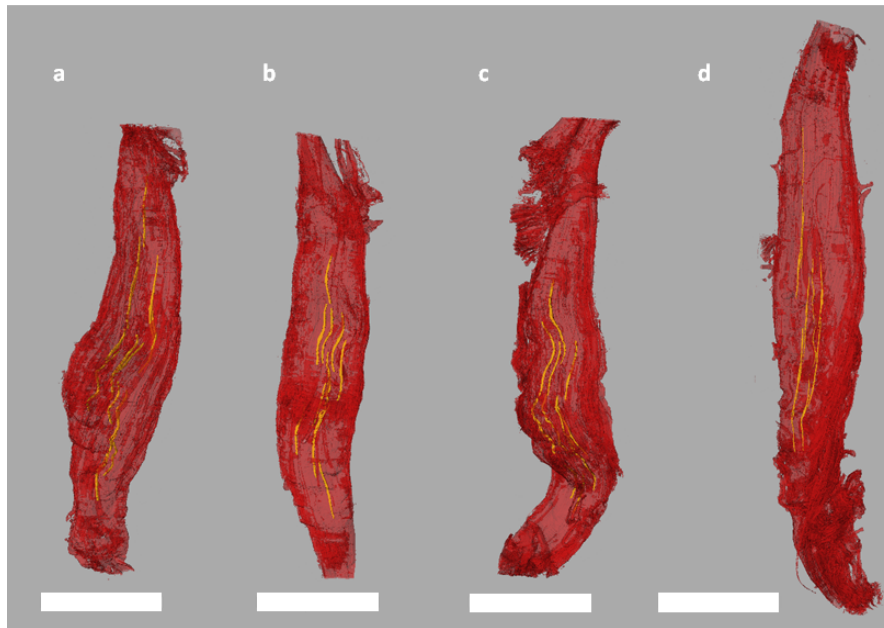


Figure 5.10: **3D volume rendering of muscle spindles in whole muscles of each study group.** The muscle tissue is visualised in red and muscler spindles in yellow. (a) is a control muscle with 12 spindles, muscles in (b)-(d) contain 11 spindles and are from CHF, HFC and HFHF groups, respectively. The spindle distribution varies between different study groups. The scale bar is 3mm.

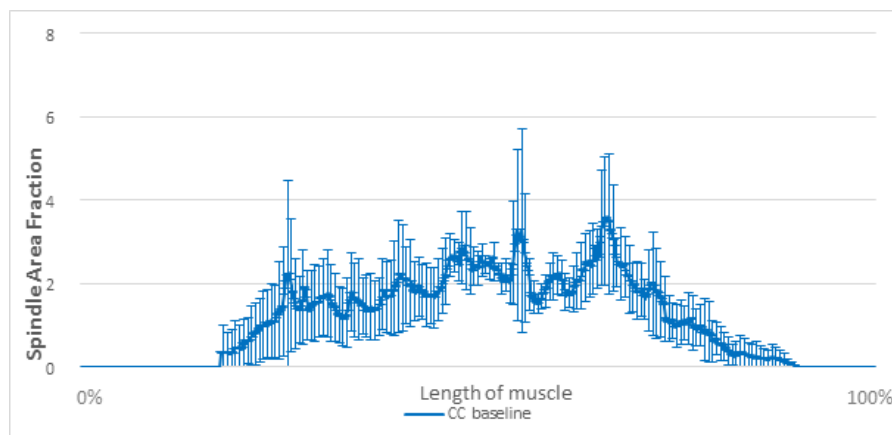


Figure 5.11: **Cross-sectional area fraction of muscle spindles in muscle tissue per CT slice.** The spindle area fraction of all CC muscles is given as baseline (with standard deviation).

relationships between dietary groups. Moreover, the sample number was too low for at least two of the groups (HFC and HFHF) in the Microfil study for meaningful comparison.

For the unperfused samples imaged using phase contrast-based SR CT an average red blood cell density of $828 \pm 139 \text{ mm}^2$ was determined for the control group CC, which is in agreement with values found in the literature, especially for young mice (CD $867 \pm 100 \text{ mm}^2$ [Davidson *et al.*, 1999]) as presented in section 2.4.1.

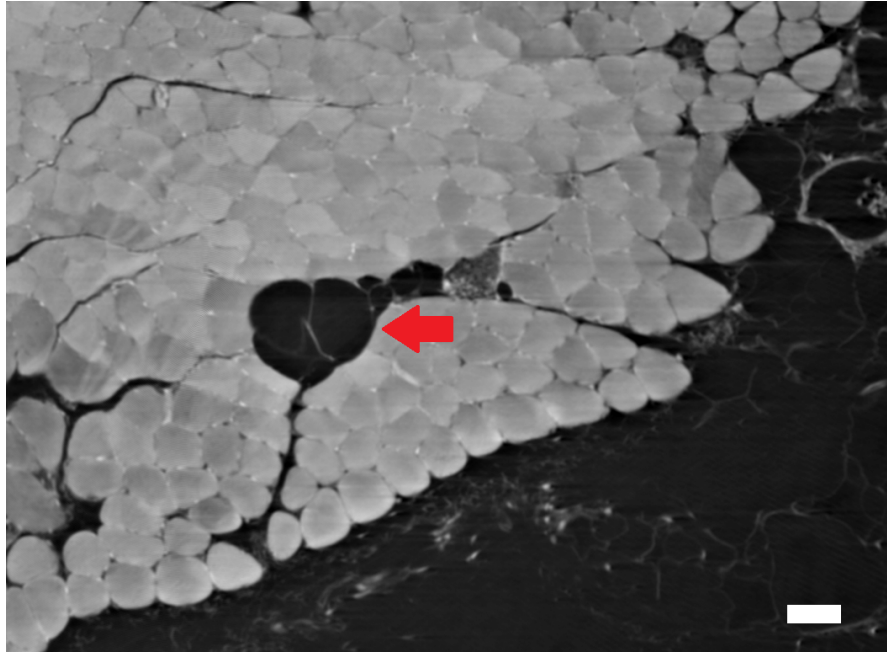


Figure 5.12: **Intramuscular adipose tissue.** Adipose tissue (red arrow) can be clearly distinguished from the rest of the muscle tissue and thus segmented. The scale bar represents 50 μm .

The red blood cell-to-fibre ratio of the control group CC was determined as 0.90 ± 0.21 which is significantly lower than values found in the literature (> 1.8 , see section 2.4.2). However, histological counting performed in an independent PhD project in our research group found an average capillary-to-fibre ratio of 0.90 ± 0.11 . This suggests that the value obtained by SR CT is representative of the capillary-to-fibre ratio in this breed of mouse.

The average fractal dimension of the control group CC was 2.53 ± 0.04 which is slightly higher than fractal dimension reported in the literature (see section 2.4.6). A problem with the comparison to the literature is that most authors do not describe the overall volume used to determine the fractal dimension, which influences the results in fractal box counting (the bigger the volume compared to the structure studied, the smaller the fractal dimension). Furthermore, the value of 2.53 ± 0.04 is in agreement with the values obtained by Peitgen *et al.* [1992] for 3D diffusion-limited growth processes ($2.4 - 2.5$), which suggests that the determined values are meaningful. The trend in increase of fractal dimension with maternal and/or offspring diet could indicate deviations of the growth processes of the microvascular trees from the diffusion-limited regime for these dietary groups.

The mean length density of the control group of $875 \pm 117 \text{ mm}^{-2}$ was significantly lower than values found in the literature. The reason for this is that by visualisation of RBCs in the blood vessels and not the blood vessels themselves and if the RBCs are not everywhere within the vessels, the length of the blood vessel network is underestimated. Moreover, the comparison with the literature is difficult if the

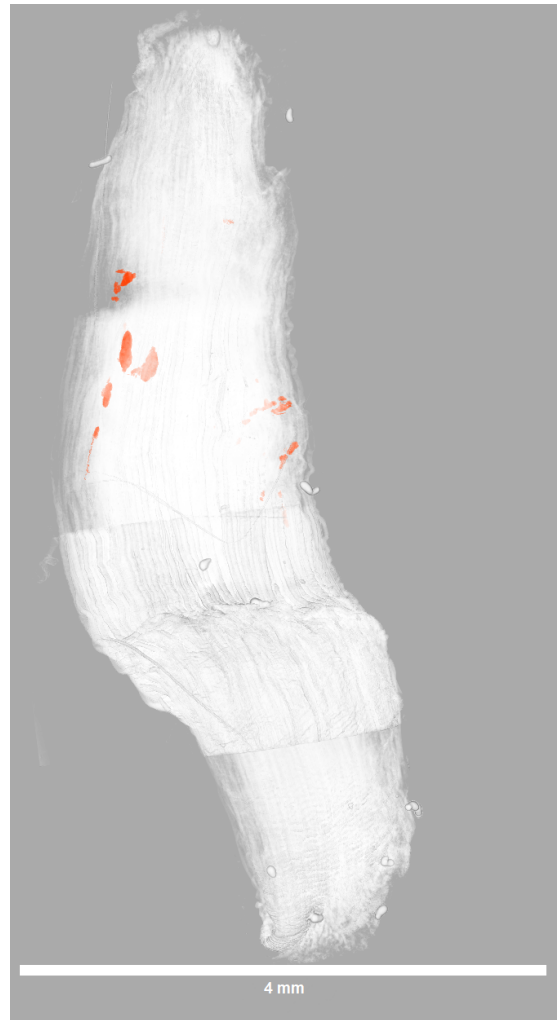


Figure 5.13: **Fat segmentation in HFHF muscle.** The fat volume (orange) was segmented in a HFHF using Avizo Fire 9.0 and displayed within the muscle volume (white) as a volume rendering. The representation of the neuromuscular spindle has been derived from SR CT data, assessed at a voxel size of $0.77 \mu\text{m}$. The scale bar represents 4mm.

standard stereological definition of length density was used rather than an adapted definition.

Finally, the mean volume fraction of $6.51 \pm 1.00 \cdot 10^{-3}$ in the control group is lower than that obtained for the rat soleus muscle by one order of magnitude [Kondo *et al.*, 2011]. This, however, may be due to the difference between animals. No findings regarding volume fraction in mouse soleus muscle were published in the literature.

The values presented for mean number of muscle spindles per muscle and intrafusal fibres per spindle in the mouse soleus muscle, based on SR CT data, are consistent with those reported by Lionikas *et al.* [2013] using light microscopy. The number of spindles per muscle reported by Lionikas *et al.* [2013] for the C57/BL6 mouse strain was between 10 and 11 with a mean number of intrafusal fibres of 3.9. Using phase contrast SR CT imaging 11.8 ± 0.7 neuromuscular spindles were observed per muscle

Muscle ID	Fat Volume [mm ³]	Muscle Volume [mm ³]	Fat volume Fraction
CC1	6.58E-05	4.81	1.37E-05
CC2	1.20E-04	5.77	2.08E-05
CC5	1.47E-04	4.97	2.97E-05
CHF1	1.72E-03	5.55	3.10E-04
CHF4	1.20E-03	6.57	1.83E-04
CHF5	1.98E-04	5.74	3.45E-05
HFC1	3.35E-04	5.10	6.57E-05
HFC2	8.88E-04	5.34	1.66E-04
HFC3	1.17E-04	4.92	2.38E-05
HFHF2	3.88E-03	6.50	5.97E-04
HFHF4	3.44E-03	6.42	5.36E-04
HFHF5	7.03E-04	6.80	1.03E-04

Table 5.3: **Segmented fat volume for the four dietary groups CC, CHF, HFC and HFHF (n=3).** The fat volume was segmented for three muscles of each dietary group and the volume fraction with respect to overall muscle volume computed. Fat volume was found to be dependent on dietary group ($p < 0.05$), with means of CC and HFHF groups being significantly different for both fat volume and fat volume fraction ($p_D < 0.05$).

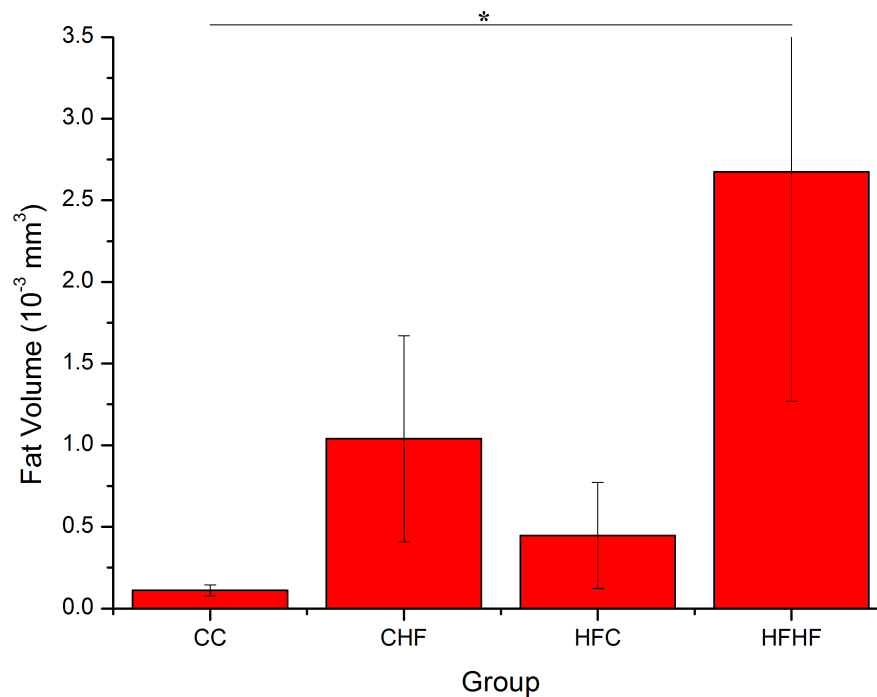


Figure 5.14: **Mean fat volume per dietary group (n=3).** Offspring high-fat diet was the determining factor for fat volume ($p < 0.05$), and the additive effect of combined maternal and offspring diet is visible. * statistical significance ($p < 0.05$).

and 3.7 ± 0.1 intrafusal fibres per spindle for the CC mice. Banks [2006] counted 14 neuromuscular spindles per mouse soleus muscle using serial sectioning for light microscopy, but the mouse strain remained unnamed in the experiment. In our study

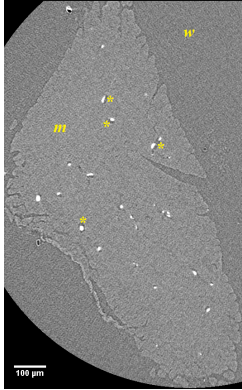

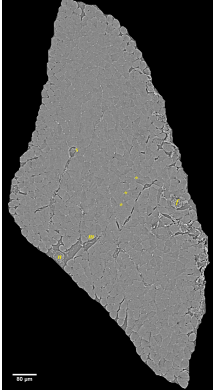
	Microfil perfusion (n=3)	PTA staining (n=1)	Phase contrast-based SR CT (n=5)
Representative slice			
Capillary density [mm ⁻²]	144 ± 103	22 ± 5	828 ± 139
Capillary-to-fibre ratio	-	-	0.90 ± 0.21
Tortuosity	1.22 ± 0.09	1.18	-
Length density [mm ⁻²]	58 ± 16	23	875 ± 117
Volume fraction [E ⁻²]	0.45 ± 0.04	0.42	0.65 ± 0.10
Fractal dimension	1.84 ± 0.07	1.59	2.53 ± 0.04
Mean distance to next RBC [μm]	-	-	10.7 ± 0.7
Advantages	<ul style="list-style-type: none"> • high absorption contrast • fast scan times 		
Disadvantages	<ul style="list-style-type: none"> • cumbersome preparation • expensive • insufficient perfusion in vessels of diameter <10μm • incomplete filling of vessel lumen 		

Table 5.4: Comparison of methods for inducing soft tissue contrast for μ CT imaging of the microvasculature in skeletal muscle. The structural parameters of the microcirculation for the control groups (CC) obtained from perfusion, staining and phase contrast methods are compared and the advantages and disadvantages of the methods summarised. The structural parameters are given for the whole vessel network for the PTA-stained sample due to the small number of capillaries present.

in male C57/BL6 mice, the CC muscles had a lower percentage of spindles with four intrafusal fibres, accounting for 68.5% of all spindles, compared to 87.5% reported by Lionikas *et al.* [2013]. Furthermore, the mean muscle extrafusal fibre count in the medial region of the soleus muscle of the CC mice did not differ significantly from that reported by Lionikas *et al.* [2013], i.e., 1012 ± 45.34 vs. 949 ± 61 , respectively.

A difficulty with the datasets obtained at the SLS was the high computational effort required for segmentation and morphometric analysis. The stitched datasets of the whole muscle have a size of about 80 GB and when opened for segmentation in Avizo require double that memory. For morphometric analysis of the fractal dimension the required memory increased further. Therefore, and because of the considerable amount of time needed for segmentation, the limitation of segmentation and morphometric analysis to a smaller cubic volume was straightforward. This is a complication inherent in handling large datasets and needs to be dealt with on the hardware side by provision of sufficiently powerful computing machines.

A limitation of the current study in terms of sample preparation is the possible shortening of the muscle during fixation and embedding [Bancroft & Gamble, 2008], as the muscles, while fixed initially *in situ* before excision, were not pinned to a fixed length. This would distort any 2D and 3D measurement of distribution or separation of red blood cells or muscle spindles within the muscle volume and the distortion of measurements may vary between different dietary groups due to differing fat content. This is not a matter that can currently be resolved.

Furthermore, the quality of the morphological analysis of the structure of the microvasculature by visualisation of red blood cells depends on there being RBCs present in the capillaries. The number of capillaries that contain RBCs will vary with perfusion and haematocrit. Therefore, light microscopy was used to validate the method and image the muscles and it was possible to compute the haematocrit for most muscles to give an indication of how the parameters determined on the visualisation of RBCs may differ from the actual structural parameters of the microvasculature. This is presented in the next chapter.

The consistency of the presented counts of muscle spindles, intrafusal fibres and microvascular morphometric parameters with published material shows that phase contrast SR CT is well suited to identify and quantitatively characterise the structure of intramuscular features. Furthermore, it has the advantage that scanning times are short, i.e., each scan was completed within 6 minutes, with 5-6 scans necessary to cover the whole length of a muscle. Phase retrieval and CT reconstruction could be performed simultaneously to subsequent scanning, leading to a maximum of 45-60 minutes processing time for creating the 3D dataset of the whole muscle. Data segmentation in this case was the bottleneck, with the segmentation of all muscle spindles in one muscle taking about 5-6 hours and the segmentation of the RBCs in

one cubic volume taking 2-3 days. Morphometric analysis on the other hand was fast, with the ImageJ plugins running between a few seconds for volume fraction counting and minutes for the determination of space separations (performed on a computer with at least 16 CPU cores and 256 GB memory). The time and hardware requirements of the workflow post imaging are given in figure 8.1.

In contrast to this, serial sectioning of a whole muscle of about 1 cm length at 20 μm sectioning thickness would lead to 500 sections, for which the scanning time alone can be estimated as a minimum of 6 days for high-resolution imaging on an automated slide scanning microscope [Hannon-Fletcher & Maxwell, 2009]. Staining with e.g. PGP 9.5 requires another 1.5 days with feature segmentation and 3D alignment of the light micrographs having to be performed subsequently. Furthermore, phase contrast SR CT has left the muscle intact, thus enabling subsequent analysis with different methods, whilst histological sectioning is destructive. The skill of the scientist performing the sectioning plays a large role here as well, as physical sectioning can induce shearing and thus tissue distortion as well as overlapping artefacts. The main disadvantage of SR CT imaging is the availability of and access to the few SR sources worldwide (<http://www.lightsources.org/regions>), as allocation of scanning time is granted on a competitive base, where proposals need to be submitted typically half a year in advance. Lab-based micro-computed tomographic systems, which allow for (partially) coherent X-ray generation at high spatial resolutions and hence for phase contrast-based high-resolution CT are available [Bidola *et al.*, 2015] However, scanning times are considerably longer (several hours) due to the much lower flux provided by lab-based X-ray sources compared to SR light sources, and implementation of phase contrast-based SR CT calls for some expert (X-ray imaging and image processing) knowledge.

5.6 Summary

In this chapter the results of the morphometric analysis of the microvasculature were presented for Microfil-perfused, PTA-stained and unstained samples imaged using propagation-based phase contrast SR CT. The capability of phase contrast-based SR CT was shown for visualisation of blood vessels and red blood cells inside as well as other soft tissues in skeletal muscle, such as nerves, muscle spindles and adipose tissue. Using the SR CT datasets the microvascular structure, muscle spindle anatomy and adipose tissue fraction were analysed in terms of maternal and/or offspring fat intake.

Chapter 6

Validation of phase contrast-based SR CT imaging

Standard histology of the previously imaged muscles was used to compare and validate the capillary numbers identified by the presence of RBCs and nerves within the phase contrast-based SR CT images.

6.1 Methods

Three muscles of each dietary group, depending on the quality of the SR CT scan, were stained. Muscles which displayed reconstruction artefacts due to being scanned in widefield mode were avoided. See table 4.1 to see which muscles were chosen. The muscles were serially sectioned by Jenny Norman in the histology research unit (HRU) of Southampton General Hospital. The thickness of serial sections was 4 μm and they were taken from the belly of the muscle. Staining was performed for red blood cells (twice), vascular endothelium and nerves. For each stain three slices per muscle were taken. The stains used are displayed in table 6.1. To stain for red blood cells the Lison-Dunn technique, H&E staining and Martius Yellow Scarlet Blue (MSB) were employed. For the vascular endothelium the cluster of differentiation (CD) 31 was used and for the nerve fibres protein gene product (PGP) 9.5. Furthermore, a negative control was taken for the CD31 and PGP 9.5 stains, to assess the validity of the antibody stain. See figure 6.1 for a schematic of how the serial sections were distributed on the microscopy slides for histological staining. The MSB stain was later added to the bulk as the Lison-Dunn technique proved ineffective. CD31 and PGP9.5 are primary antibodies that specifically stain vascular endothelium and motor neurons, respectively. For CD31 a polyclonal antibody (ab28364, Abcam) raised in rabbit was used at a dilution 1:150. The PGP9.5 antibody was a monoclonal rabbit antibody (ab108986, Abcam), used in dilution 1:750. Apart from applying a

different primary antibody the protocols for CD31 and PGP9.5 were identical, both using a goat biotinylated anti-rabbit secondary antibody (dilution 1:800, Vector) followed by a streptavidin biotin peroxidase complex (dilution 75:1:1, Vector) to which 3,3'-diaminobenzidine tetrahydrochloride (DAB) was bound as chromogen. The detailed protocols can be found in appendix B.

The application of each stain was done for all slides simultaneously. For CD31 and PGP9.5 staining a microwave pretreatment was performed for antigen retrieval. See appendix B.3 for the method. The Lison-Dunn stain did not stain the muscle samples, despite working for control mouse liver samples, as shown in table 6.1.

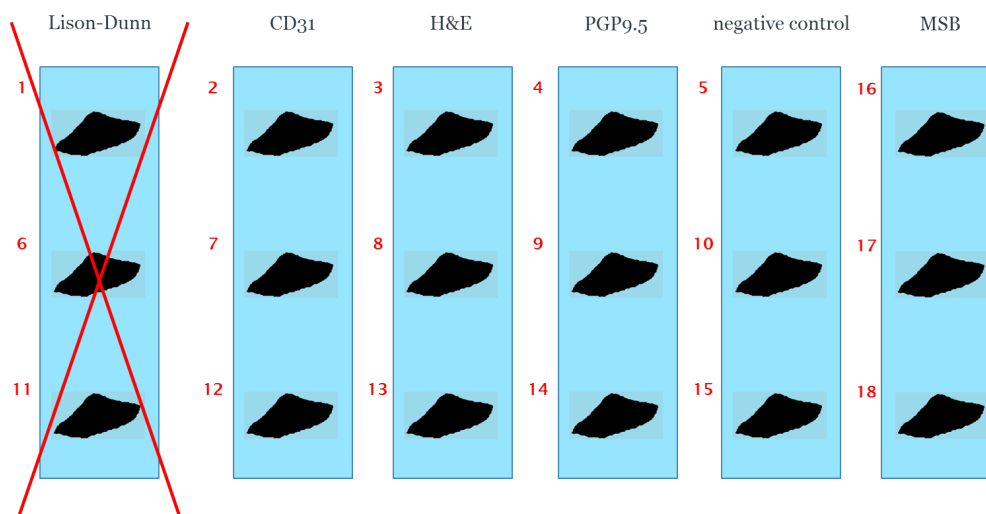


Figure 6.1: **Schematic for order of staining of serial sections.** Sections were stained such that subsequent sections were stained with different stains and each stain was repeated for three sections of the same muscle. Staining for Martius Yellow Scarlet Blue (MSB) was applied later for subsequently micro-tomed sections.

6.1.1 Image correlation between SR CT and histology slices

For the comparison between SR CT and histology data the SR CT volume was visually aligned in VGStudio Max 2.0 (Volume Graphics GmbH, Germany) to find slices corresponding to the histological sections. To this end both the 2D histological slide and the 3D SR CT volume were imported into VGStudio. With the “simple registration” software in VGStudio the 3D dataset was rotated around its axes until a good correlation with the 2D dataset was found. The “1-2-3 registration” tool was subsequently used to select three points in the 3D dataset that coincided with three points in the 2D slice. The software then automatically computed and executed the necessary rotations in order to align the 3D slice to the 2D slice to that the three chosen points were in a plane. The rotated 3D volume was exported. As the histological slide was thicker (4 μm) than the height of a voxel in the SR CT image (spatial resolution was 0.77 μm), it was necessary to account for the fact that more features would be

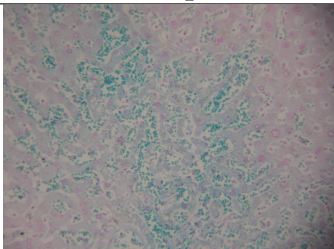
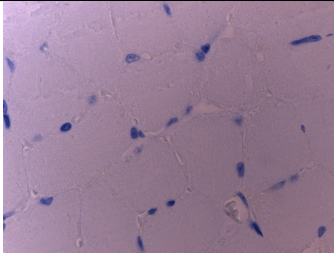
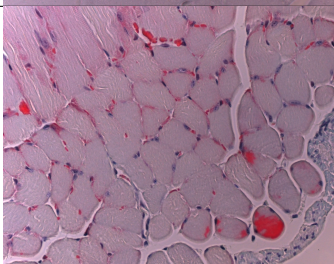
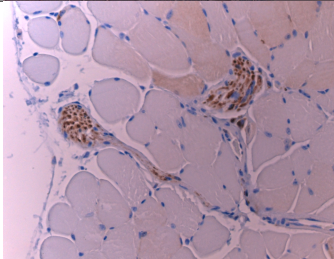
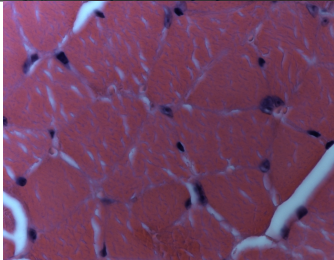
Stain	Corresponding Tissue	Stain Colour	Example
Lison-Dunn	Oxyhaemoglobin	Turquoise	
CD31	Vascular Endothelium	Brown	
MSB	Red Blood Cells	Orange/red	
PGP9.5	Motor Neurons	Brown	
H&E	Muscle Fibres and RBCs	Red	

Table 6.1: **Histological staining.** Five different staining techniques were chosen to display RBCs, blood vessels, nerves and muscle fibres.

visible in a micrograph than in one SR CT plane. To this end, the rotated 3D volume was imported into Fiji ImageJ and 7 consecutive slices with features displayed in the 2D slices were selected. A maximum intensity projection [Schindelin *et al.*, 2012] was applied over these slices, thus joining them into one slice with the greyscale at each point in the resulting slice being the maximum of all greyscales in that respective point over the 7 slices. This resulting slice was then compared with the slide imaged using histology. To this end, the red blood cells and nerve fibres were segmented for validation and comparison.

6.1.2 Segmentation of nerves and analysis

For the nerve segmentation on histology sections, images were first loaded into Fiji ImageJ and split up into three RGB colour bases, i.e. [0.65,0.70,0.29], [0.27,0.57,0.78] and [0.71,0.42,0.56] [Ruifrok & Johnston, 2001]. This was done in order to single out the brown colour of the DAB chromagen, which is the second colour base, so as to facilitate the segmentation. The images of this colour channel were then manually segmented using Avizo Fire 9.0 (FEI, Hillsboro, OR, USA); the same was done with the corresponding phase-retrieved SR CT images. See figure 6.2 for visualisation of this process. The nerve area was computed using the Avizo “volume fraction” tool to count the labelled voxels. A linear regression line was fitted to compare the nerve area counts from the histological slides to the nerve area counts from the SR CT data using Origin 8.1 (OriginLab Corp., Northampton, MA, USA). Origin uses a least-square method to determine the fitted function.

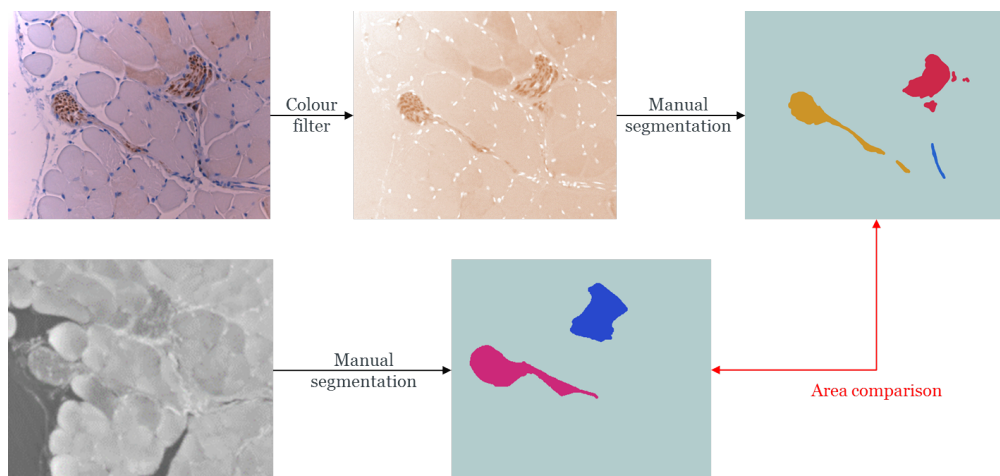


Figure 6.2: **Workflow for comparison of nerve identification in SR CT and histology images.** Nerves in SR CT images (bottom row) were immediately segmented whilst histology images (top row) were first split into different colour channels to isolate the brown channel associated with the DAB chromagen. Based on these images the nerves were then segmented. The area of the nerves was computed for both segmented images and compared.

6.1.3 Segmentation of red blood cells and analysis

The red blood cells were identified and counted manually in the MSB and CD31 images in Fiji ImageJ. For the phase retrieved SR CT images, a bandpass filter was applied in Fiji ImageJ (upper limit 3 pixel, lower limit 1 pixel, as explained in chapter 4, section 4.4.4) to highlight the red blood cells, which were then counted manually also. Two observers independently blindly counted RBCs in the slides stained with CD31 to avoid bias. See figure 6.3 for an example of two correlated SR CT and CD31 stained histology slices.

Linear regression lines were fitted for the counts for each observer and each stain to compare the red blood cell counts from the histological slides to the red blood cell counts from the SR CT data using Origin 8.1. The quality of the fit is determined by the adjusted R^2 value.

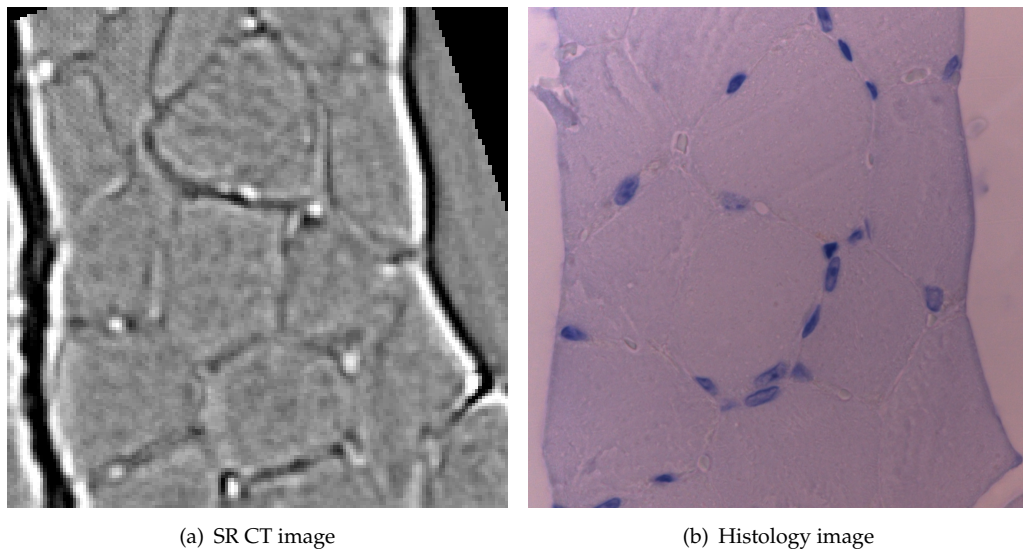


Figure 6.3: Correlated SR CT and histology images (stained with CD31) for RBC validation. SR CT and histology images were visually correlated. To account for the thickness of the histological sections, a maximum intensity projection over 7 SR CT slices was performed. SR CT images were bandpass filtered to highlight red blood cells. Blind counting of red blood cells was then performed on both by two independent observers.

After blind counting images of SR CT and histology were compared to count how many red blood cells had been misidentified, i.e., how many cells had been counted in one image but not the other and *vice versa*.

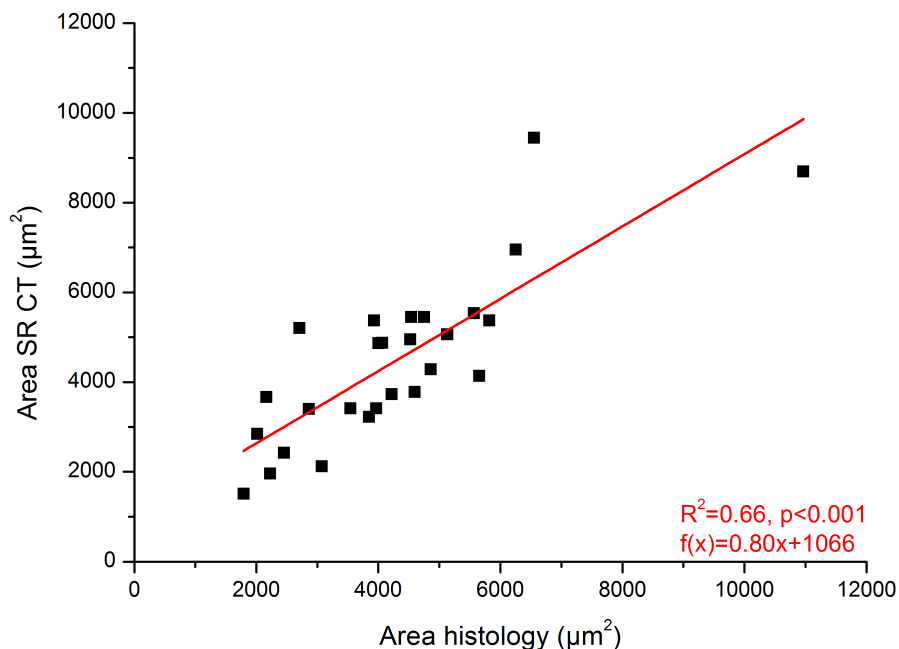


Figure 6.4: **Comparison of identified and measured nerve area in corresponding μ CT and histology images.** After segmentation the nerve area was measured in the corresponding images of the two imaging techniques, see figure 6.2. A linear regression line was fitted using Origin 8.1.

6.2 Results

6.2.1 Nerves

Figure 6.4 displays the result of the comparison of nerve identification between SR CT and histology images. The fitted linear regression line has a slope of 0.80 with $R^2 = 0.66, p < 0.001$. Thus, the identification of nerves was consistent, yet the area determined from SR CT images slightly underestimated the area determined from histological sections.

6.2.2 Red blood cells

Figure 6.5 displays the result of the comparison of red blood cell identification between SR CT and histology images. The linear regression line fitted for MSB red blood cell counts is $1.43x - 27.51$ with $R^2 = 0.98, p < 0.001$. The counting for CD31 by observer 1 is fitted by the line $0.91x + 0.58$ with $R^2 = 0.85, p < 0.001$ and is fitted by $1.04x - 0.01$ with $R^2 = 0.68, p < 0.001$ for observer 2. The counting between both observers was consistent as the counts were not significantly different. A linear fit to the combined counting of MSB and CD31 by observer 1 is given by $1.09x - 2.84$ with $R^2 = 0.98, p < 0.001$.

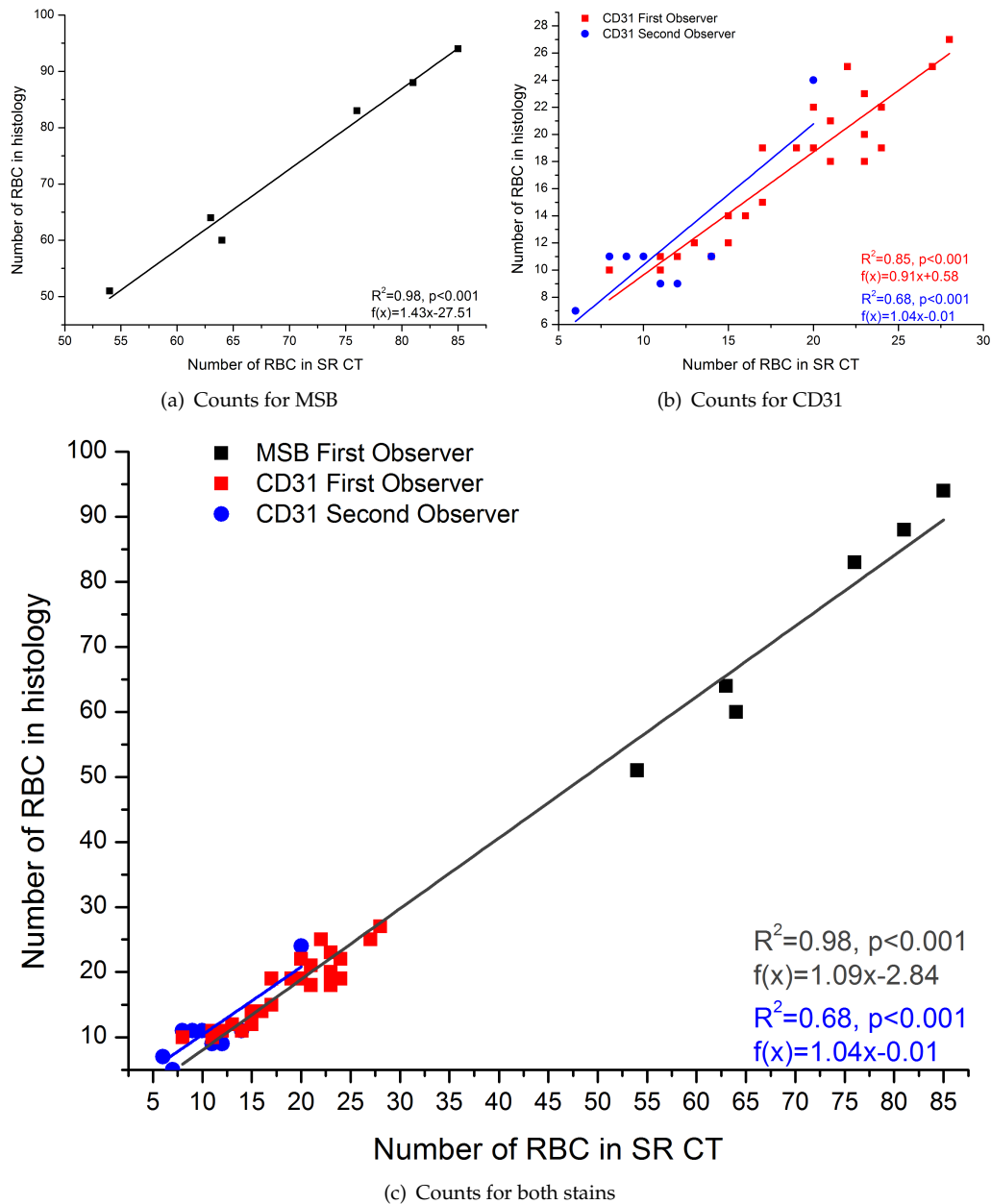


Figure 6.5: **Comparison of red blood cell counts identified in SR CT and histology images.** Red blood cells were counted blindly in histological slices stained with MSB and CD31 and compared to SR CT images. Two independent observers counted RBCs in the CD31 images. Linear regression lines were fitted to the counts.

It was found that the number of misidentified red blood cells was lower than 10% and the overall number of RBCs identical when derived via histology or SR CT.

Muscle ID	Red blood cell density mm ⁻²	Capillary density mm ⁻²	Red blood cell-to-fibre ratio	Capillary-to-fibre ratio	Haematocrit
CC1	949	1004	0.85	0.96	0.95
CC2	916	1389	0.65	0.83	0.92
CC3	540	770	0.40	0.48	0.70
CHF1	757	889	0.82	0.97	0.85
CHF3	1021	1159	0.90	1.03	0.88
CHF4	948	994	0.88	0.92	0.95
HFC1	665	744	0.63	0.70	0.89
HFC2	744	843	0.64	0.72	0.88
HFC3	698	797	0.55	0.63	0.88
HFHF2	698	790	0.67	0.76	0.88
HFHF4	902	988	1.01	1.10	0.91
HFHF5	994	1087	0.99	1.08	0.92

Table 6.2: **Detailed results of 2D microvascular structural parameter analysis for unperfused samples.** Structural parameters have been determined based on the visualisation of red blood cells and the microvascular endothelium using CD31 stained light micrographs in the soleus muscle of mice of the animal model of developmental priming.

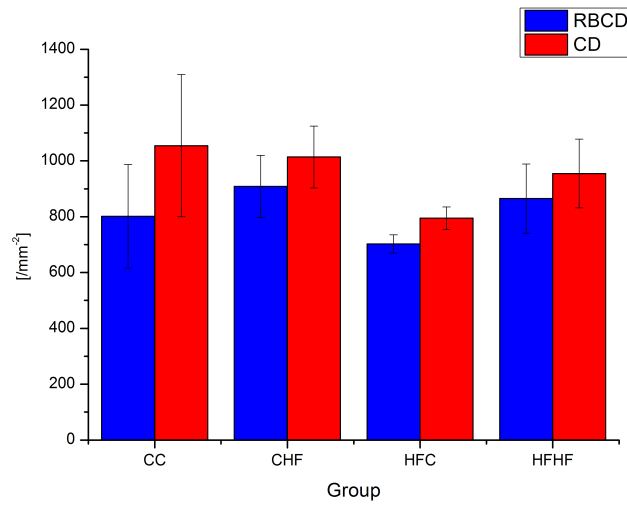
6.2.3 Structural Parameters from Histology

Using the slices stained with CD31 the capillary density (CD) and capillary-to-fibre ratio (C:F) using both RBC and capillary counts from the histological slides (counted by observer 1 only) were determined. In the following RBCD will denote the red blood cell density (number of red blood cells per mm² of muscle) and RBC:F the red blood cell-to-fibre ratio, as in similarity to CD and C:F.

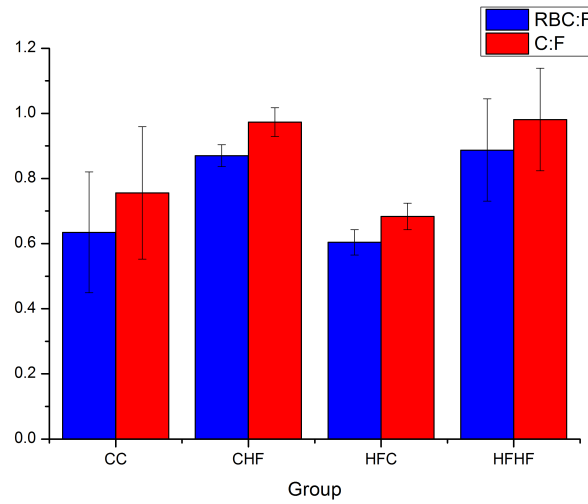
The haematocrit was determined by dividing the total number of RBCs by the total number of capillaries in all the images. The results are shown in Table 6.2. Figure 6.6 further shows a comparison between the numbers determined by counting RBCs vs. capillaries. Using one-way ANOVA in IBM SPSS the dependence of RBC:F and C:F on offspring dietary group (CC and HFC vs. CHF and HFHF) was found to be statistically significant ($p < 0.01$ and $p < 0.05$, respectively).

6.3 Discussion and conclusion

SR CT appears to be good enough to identify the location of blood vessels with the number of misidentified red blood cells being lower than 10%. This number may however be overestimated as the correlation between histological slides and SR CT images is error prone, considering the small size of the RBCs. It is important to find



(a) RBC and capillary density



(b) RBC and capillary-to-fibre ratio

Figure 6.6: 2D structural parameters (capillary density and capillary-to-fibre ratio) determined from histological images. Comparison between the parameters determined by counting capillaries only versus red blood cells. The histology slides were stained using CD31 and images using a Zeiss Axioscope 100X lens. The dependence of RBC:F and C:F (subfigure 6.6(b)) on offspring dietary group was found to be statistically significant ($p < 0.01$ and $p < 0.05$, respectively).

the optimal set of rotations to correlate the images, as well the right SR CT slices over which the maximum intensity projection was applied, in order to minimize the difference between correlated SR CT and histology images. In validating features between SR CT slices and histology slices, the optimal alignment of these is the main challenge and much time was therefore spent in this process.

The method of overlaying these slices may not be ideal, possibly a method averaging

the greyscales in each slice would achieve a more appropriate comparison than the maximum intensity projection. This averaging could be weighted depending on their position in the 7-slice stack to account for the focus of the light microscope. Finally, the application of the bandpass filter to the phase retrieved SR CT images not only highlights the RBCs but also all edges of muscle fibres and empty capillaries, which can lead to misidentification of some RBCs. This however is a minor complication as the misidentification can be expected to be consistent over all slices, thus the overall slope the linear regression would change, yet the consistency of results remains. Errors in the comparison may be induced during the processing of the samples for staining, e.g., microtoming the samples can result in shearing and ultimately tearing the tissue slices. Furthermore, it can not always be ensured that the thickness of the cut slices is constant. During dewaxing of the slices in a graded series of ethanol it is also possible that RBCs flow away if they were not properly bound to surrounding tissue. These errors in processing are intrinsic in the process of microtoming and histological staining and can not be entirely circumvented.

A haematocrit close to one was computed from the histology light micrographs for all muscles investigated. As by definition of the haematocrit the number of red blood cells is therefore representative of the number of capillaries. Thus, the established relationships between dietary groups regarding the structural measures (such as capillary density) remain the relatively the same, whether they are computed by counting red blood cells or capillaries themselves. This, and the fact that the number of misidentified red blood cells is low, suggests that the structural measures and their dependence on dietary group determined using SR CT imaging RBCs are representative of the same measures and dependencies determined by counting capillaries on histological slides.

However, the mean RBC:F and RBCD computed by counting in light micrographs are lower than those computed on the 3D SR CT datasets presented in the previous chapter. I.e., 0.63 *vs.* 0.98 and 802 *vs.* 890, respectively. This is likely to be due to the small field of view considered in histological counting. As a result the statistical significance observed for RBC:F observed in histological counting was lost when considering the 3D dataset.

6.4 Summary

It was shown that using phase contrast-based SR CT one can visualise red blood cells in the microvasculature, and thereby identify the location of the blood vessels. Furthermore, nerve tissue and adipose tissue can be differentiated, the first of which has been explicitly shown.

Chapter 7

Mathematical modelling of oxygen uptake in mouse skeletal muscle

Whilst enabling structural analysis, images of muscles and their microvasculature do not immediately reveal information of muscle functionality, in particular of the vasculature's ability to supply the muscle with sufficient oxygen throughout.

Morphological measures such as capillary density give a first insight into this, but only with mathematical modelling of oxygen perfusion is it possible to link such structural information to the actual ability of the microvascular network to fulfil the tissue oxygen demand. Furthermore, the results of mathematical modelling ought to be validated by *in vivo* measurements of tissue oxygenation.

Models of the oxygen supply to soft tissues with a particular focus on image-based models will be reviewed in the following. The equations and parameters needed for modelling of tissue oxygenation are given. Whilst the oxygen delivery to skeletal muscle does partly depend on blood flow, models of blood flow have been reviewed previously by Kim *et al.* [2012] and to some extent by Pittman [2013] in the context of oxygen transport and regulation. The main output of blood flow modelling used in modelling of tissue oxygen perfusion are the partial pressure of oxygen in blood and its oxygen saturation. Partial oxygen pressure and oxygen saturation are directly related to the blood haematocrit. Most models of molecule transport in and across blood vessels use parameters and equations reviewed in the Handbook of Physiology - Section 2, Volume IV [Geiger *et al.*, 1984]. The theory of oxygen transport to tissue was also presented and reviewed by Popel [1989]. Jain [1987b,a] reviewed the transport of molecules (including oxygen) in the tumour interstitium and across the tumour vasculature, while Goldman [2008] reviewed theoretical models of oxygen transport to tissue. In the review of Toma-Dasu & Dasu [2013] models of tumour oxygenation are discussed, which are similar to oxygenation of other soft tissues.

7.1 Literature review of image-based mathematical models

Many models of oxygen diffusion in soft tissue are implemented on artificial vascular networks, which are based on observations by imaging or theoretical approaches. The first model of oxygen transport from the capillaries to muscle tissue was developed nearly hundred years ago by Krogh in 1919. Krogh determined diffusion coefficients of oxygen through different tissues, e.g., the abdominal wall of the frog or the number and distribution of capillaries in the horse gastrocnemius. He also studied the contraction and opening of capillaries in resting and stimulated muscle [Krogh, 1919a,c,b].

As the capillaries appear to be hexagonally packed in skeletal muscle, Krogh assumed that for each capillary in a cross-section the region of oxygen supply could be described as a circular area [Krogh, 1919a], thus resulting in a so-called Krogh cylinder when viewed in 3D. The area of all circles in a cross-section was calculated by counting the number of capillaries within the total muscle area using light microscopy and division of the area by the count. For the geometric limitation imposed by the Krogh's model, i.e., a circular region with capillary radius r and cylinder radius R and with oxygen partial pressure $P(x)$ at a point x the diffusion equation can be solved analytically, under the following assumptions: The diffusion is in a steady state ($\frac{\partial P}{\partial t} = 0$), where diffusion in longitudinal direction (orthogonal to the capillary cross-section) is neglected and consumption is constant ($M_P(P) = p$). The relation between oxygen pressure difference in the capillary (P_0) and at a certain point with distance x in the circular region $P(x)$ is then described [Krogh, 1919a] as:

$$P_0 - P(x) = \frac{p}{D} \left(\frac{1}{2} R^2 \ln \frac{x}{r} - \frac{x^2 - r^2}{4} \right) \quad (7.1)$$

with the diffusion rate D . By setting $x = R$, the maximum pressure difference between capillary and tissue necessary to supply the whole muscle is calculated.

Krogh's model was a first useful approximation to the regions of oxygen supply of the capillaries, leading to investigations of the influence of relevant anatomical factors for tissue oxygenation, such as tortuosity and capillary distribution [Goldman & Popel, 2000, Fraser *et al.*, 2013, Goldman & Popel, 2001, Bos *et al.*, 1995]. However, studies have found the Krogh's cylinder model is insufficient to describe the process accurately as it results in unphysiological gaps or overlaps and large regions of unperfused tissue when capillary rarefaction is present [Ellsworth & Pittman, 1990]. Nevertheless, the Krogh model is still used as a simple approach to model oxygen supply to tissue, for instance recently by Jung *et al.* [2005]. Modification of the no-flux boundary condition at the outer border of the Krogh cylinder into an infinite-domain boundary condition (permitting flux with zero net exchange) leads to a decrease in axial tissue PO_2 gradient Secomb [2015]. Results of such altered models remain yet to be validated by experimental data. Thus, Krogh's model can be used for a first

assessment of tissue oxygenation, but for more complex geometries and questions, more complex models need to be considered, as presented in the following.

7.1.1 Image-based modelling

The advantage of image-based modelling in contrast to modelling using simplified and/or artificial geometries is that the model input represents the actual observed microvasculature. For microvascular networks that have a complex 3D structure it is difficult to obtain valid predictions about oxygenation from simple artificial networks. This is even more pronounced in pathological cases such as tumour networks.

To achieve a more physiological description of capillary oxygen supply in comparison to the Krogh cylinder, the concept of "domains of influence" has been introduced. In this case, the region of interest is tessellated, i.e., by using Voronoi polygons, which accounts for heterogeneity of the capillary spacing [Egginton & Ross, 1992, Degens *et al.*, 2006]. A Voronoi polygon V_i is defined as the set of points in an area/volume that are closest to a capillary with centre at point x_i and farther from any other capillary in the area/volume. I.e., mathematically:

Given a cross-section of tissue whose global domain is denoted by $D \in \mathbb{R}^2$. Let $x_i \in D$ denote the geometric centre of the i -th capillary, $i = 1, \dots, N_c$, where N_c denotes the number of capillaries. Then, the Voronoi polygon containing the i -th capillary is the set

$$V_i = \{x | x \in D; |x - x_i| \leq |x - x_k|, k \neq i\} \quad (7.2)$$

with the V_i tessellating D .

Figure 6 shows an example of the Voronoi tessellation (black lines) of a mouse soleus muscle. For tissue tessellated by such supply domains V_i with areas A_i , Hoofd [1995] has generalised the Krogh cylinder solution for the oxygen diffusion to determine tissue oxygen partial pressure at location r to

$$P = \frac{p}{4d} \left(\Phi(r) - \sum_{i=1}^N \frac{A_i}{\pi} \left(\frac{|r - r_i|^2}{r_{ci}^2} \right) \right) \quad (7.3)$$

with r_i the location of the i th capillary and r_{ci} the non-dimensionalisation distance, e.g., the capillary radius [Hoofd, 1995]. $\Phi(r)$ is a so-called background function, which depends on the geometry of the oxygen demand domain or domains of influence, such as the Voronoi polygons, and satisfies Green's theorem [Hoofd, 1995].

Intuitively, the description of the capillary oxygenation regions by Voronoi polygons seems straightforward; under the assumption of an isotropic/homogeneous muscle (diffusion and consumption equal everywhere) and equal and constant PO_2 in all capillaries. The oxygen would diffuse across the muscle at the same speed everywhere and at all times, thus supplying the regions closest to each capillary and no other, and

thus describing Voronoi polygons. Al-Shammari *et al.* [2012] showed that the description of supply domains using Voronoi polygons is indeed sufficient in most (2D) cases. An important exception are pathological cases, where the number of capillaries is greatly reduced (capillary rarefaction), which are not packed quasi-hexagonally within the muscle. By solving the diffusion equation for the 2D steady state case with constant consumption, Al-Shammari *et al.* [2012] proved that the areas enclosed by the Voronoi polygons matched the so-called trapping regions well. The trapping regions are defined as those regions where there is no oxygen partial

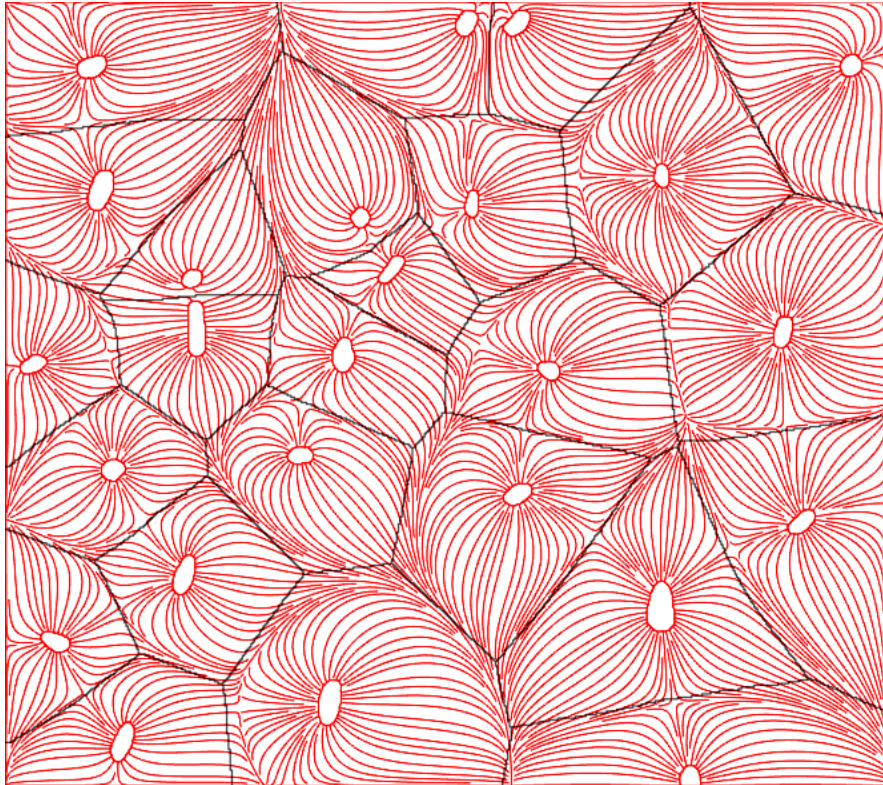


Figure 7.1: **Voronoi tessellations vs. trapping regions to mark regions of oxygenation.** Voronoi polygons are marked black and streamlines in red flowing from capillaries. The trapping regions are defined as the limits of the streamlines. It can be seen that Voronoi polygons and trapping regions match well. Inspired by Al-Shammari *et al.* [2014].

pressure difference across the region boundaries, i.e. the regions supplied with oxygen by a certain capillary, delimiting the streamlines initiating from each capillary. Figure 7.1 shows the comparison between streamlines (red) and Voronoi polygons (black). In the perfect case, where the Voronoi polygons match the trapping regions (Al-Shammari's hypothesis), no streamlines would cross over the lines of the Voronoi polygons. Al-Shammari's hypothesis was further supported by examining the difference between Voronoi and trapping regions when taking fibre type, size, distribution, and varying oxygen demand into account [Al-Shammari *et al.*, 2014]. It was found that the difference in Voronoi and trapping regions was small in most pathological cases, thus making Voronoi tessellations the best and most easily

computable representation of capillary oxygen supply regions. An extension of the model into three dimensions has not yet been presented.

Most image-based models of tissue oxygen perfusion are based on 2D image data, and namely on histological images [Gould & Linninger, 2015, Al-Shammari *et al.*, 2012, Lo *et al.*, 2003]. This is mainly due to the lack of relevant 3D data sets and/or efforts to reduce computing time. 2D models generally come along with the assumption that oxygen diffusion in the longitudinal direction (z -direction) of the muscle can be neglected, to simplify the diffusion process as a 2D problem [Al-Shammari *et al.*, 2012, 2014, Hoofd, 1995]. This is a valid assumption for straight vessels along the muscle's main axis in z -direction with parallel cross-sections in the xy -plane of the tissue, as the drop of capillary oxygen partial pressure is very low compared to the gradient perpendicular to the vessel. A 3D description can then be obtained by stacking the 2D solutions for all values of z [Hoofd, 1995]. However, if tortuosity of the vessel is high, i.e., the vessel direction is sometimes perpendicular to the muscle's main axis, diffusion in the z -direction takes place and can no longer be neglected. An example of this situation was analysed by Penta & Ambrosi [2015]. They created a multiscale model, i.e., capillary intersection ($40\ \mu\text{m}$) vs. whole network (1 cm), for the drug delivery in tortuous tumour networks, to investigate the influence of capillary tortuosity for drug delivery. Capillary tortuosity has been introduced by a sinusoid wave making up the centre line of the capillary, while frequency and amplitude of the wave were varied to increase tortuosity. Hydraulic conductivity and surface area were determined for a microscale cell and then fed into the macroscale problem, which has been solved assuming local periodicity of the microscale cell. In reality, this assumption may not apply, especially for irregular networks like tumour networks. However, the research performed by Penta and Ambrosi shows that tortuosity has a significant impact on drug concentration within the tissue. They showed that the drug concentration in the tortuous network was decreased by more than 50% in comparison to the straight network and that it was below 10% of the injected drug concentration, thus leaving only a small amount of the drug to reach the tumour. Whilst only an example case was presented in Penta & Ambrosi [2015], this research underlines the importance of treating a vascular network as the 3D structure, and the necessity to take into account the resulting complexity of molecular convection and diffusion. In Penta & Ambrosi [2015] the studied network was artificially created and in order to obtain realistic predictions of concentration distributions (here of the drug; in our case oxygen) the computation would ideally be performed on experimentally derived images of tumour vasculature, and the results would need to be validated against experimental data.

In a novel approach, Grimes *et al.* [2016] investigates tumour oxygenation by deriving an oxygenation kernel model, allowing straight vessel segments to diffuse oxygen in a spherical fashion as an array of discrete point sources. Two spherical, scalable kernels

are computed; one for a well perfused tumour network and one for a poorly perfused one, i.e. best and worst case scenarios. The model is inspired by other similar problems, e.g. traffic flow, and is applied to 3D images of tumour vasculature obtained using two-photon microscopy. Validation using fluorescence microscopy is attempted, staining for hypoxia in tumours of the same mouse model. The relative areas of hypoxia resulting from the two kernel models cover a broad range: $37.2 \pm 9.8\%$ for high vessel perfusion versus $53.5 \pm 13.2\%$ for low perfusion. Whilst the experimentally determined area lies within that range ($39.6 \pm 9.1\%$) it remains inconclusive how well the kernel model approximates tissue oxygenation as the vessel perfusion level is unknown. The authors argue that validation using 2D methods may be insufficient, but it is also the case that the resolution of the 3D imaging method is too low to capture all blood vessels and therefore tissue oxygenation may be underestimated. It will be interesting to test the presented approach on a more regular vessel network (e.g. in healthy muscle) captured at higher resolution and using a 3D imaging method, such as light sheet fluorescence microscopy, for validation. Furthermore, whilst some initial analysis is provided, additional analysis needs to be performed to examine the difference between the kernel method and a full computation of tissue oxygenation using a finite element model.

The works of Goldman and colleagues [Goldman & Popel, 1999, 2000, 2001, Goldman *et al.*, 2004, 2006] are based on histological images of the capillaries in hamster cheek pouch retractor muscle that were obtained, which was subsequently adapted to rat EDL muscle. To obtain a 3D network the 2D information was extrapolated into the third dimension. The effect of anastomoses and tortuosity was investigated by overlaying straight tissue segments with a sinusoidal wave and adding a physiological number of anastomoses in a random fashion [Goldman & Popel, 2000]. The authors argue that tortuosity with the addition of anastomoses significantly increased tissue oxygen heterogeneity, however, no tests of statistical significance were performed, thus leaving the results inconclusive.

In [Goldman *et al.*, 2006, 2004] tissue oxygenation during sepsis was investigated and it was predicted that pathological conditions were influenced by heterogeneous shunting of blood flow between capillaries. More recently, the same group also compared the oxygen delivery of a 3D reconstructed microvascular volume from intra-vital video microscopy against that of parallel capillary arrays and found significant differences in resulting tissue PO_2 [Goldman & Popel, 2001]. In the healthy and resting case the parallel network overestimated the PO_2 by around 7%, yet, this starkly increased to 18% in hypoxia and 37% during exercise. This demonstrates the importance and accuracy of realistic 3D microvascular networks over artificially created ones.

Overall, whilst the mathematics of oxygen diffusion in skeletal muscle tissue are well-established and frequently used as in the models presented above, to the best of our knowledge, no image-based studies exist where quantitative conclusions have

been drawn about links between modelling results and structural parameters of the imaged vasculature. Furthermore, most models include two major limitations: neglecting the influence of the haematocrit and lacking validation against experimental data.

7.1.1.1 Limitation 1: Role of the haematocrit

Many 2D image-based models of oxygen delivery in skeletal models do not take into account haematocrit distribution, because they are lacking the structural information of the network of the blood vessels present in the experimentally derived image data sets. Instead, a fixed tube haematocrit is assumed and the discharge haematocrit computed using an empirically derived formula [Goldman *et al.*, 2006]. In addition, the blood oxygen level is kept constant [Al-Shammari *et al.*, 2012], which is another constraint. Furthermore, it is common to neglect the fact that not all capillaries contain RBCs and thus, do not deliver oxygen to the tissue. In other words, the presence of a capillary is put on an equal footing with the presence of an oxygen-supplying RBC [Al-Shammari *et al.*, 2012], although the presence of a capillary is only a necessary but not a sufficient condition for oxygen supply. In theoretical mathematical modelling the important role of the RBCs has long been taken into account; some models consider RBCs as point-like oxygen sources [Bos *et al.*, 1995], while others assume separate homogeneous flowing regions of plasma and RBCs [Fedosov *et al.*, 2010]. Gould & Linninger [2015] reviewed such existing models against morphological data of vascular trees and as a result, presented a working model of haematocrit distribution.

For image-based modelling of oxygen supply in tissue, this leaves two alternatives: firstly, to image the blood vessel structure and to employ a haematocrit distribution model to correctly predict oxygen delivery; or secondly, in addition to imaging the vascular structure, using an imaging technique capable of identifying RBCs within the vasculature. Tateishi *et al.* [1997] have imaged the RBCs in an isolated mesenteric blood vessel using an inverted light microscope. They were able to simultaneously measure oxygen saturation and distribution of RBCs within the blood vessel. However, this approach was limited to 2D and to an isolated environment. For 3D imaging of RBCs *in vivo*, Kamoun *et al.* [2010] proposed the use of confocal laser scanning microscopy (CLSM) or multi photon laser scanning microscopy (a method similar to CLSM, however not using a pinhole aperture but the laser beam itself for optical sectioning of the sample) to capture fluorescently labelled RBCs. Using phase contrast-based SR CT it was shown to be possible to image the RBC distribution within a 3D tissue sample. However, the information will then still be intrinsically *ex vivo*, but closer to the *in vivo* case than in any existing image-based tissue oxygenation model.

7.1.1.2 Limitation 2: Validation of results

The validation of computational modelling results is often not properly addressed. The only mathematical model presented in this chapter that has been validated against experimental data was the tumour oxygenation model by Grimes *et al.* [2016].

Complexity of experiments and lack of available resources are most likely the reasons for this. The method employed by Grimes *et al.* [2016] stains for hypoxic regions in tumour, but for healthy soft tissue this can pose a problem as no hypoxic regions should theoretically be present. Alternatively, a tissue stain to mark oxygenation could be used. For the validation of a blood haemodynamics model Liu *et al.* [2011] perfused the muscle of the anesthetized rat with Tyrode's solution. Similarly, in an effort to validate computational modelling results for tissue oxygen supply, the vasculature could be perfused with fluorescent nanoparticles and their diffusion into the tissue could be recorded visually, similar to Kamoun *et al.* [2010].

Another, likely more robust, approach is to make use of *in vivo* imaging techniques that are capable to image oxygenation and blood vessel morphology. There are a number of *in vivo* imaging methods that are already widely used for blood flow and oxygenation imaging, such as laser Doppler flowmetry [Kuliga *et al.*, 2014] or laser speckle contrast imaging [Humeau-Heurtier *et al.*, 2015]. These imaging techniques generally suffer from their usage of arbitrary units, thus allowing comparison between measurements only, but not quantification of blood flow *per se*.

Japee *et al.* [2005] introduced a video imaging system for capturing RBC flow and oxygenation simultaneously for superficial imaging of excised muscles. It was applied in Ellis *et al.* [2010] and Fraser *et al.* [2013] for comparison with computational modelling results. Other works combined different imaging systems, such as optical coherence tomography (OCT) and fluorescence and hyperspectral imaging [Gagnon *et al.*, 2015] and two-photon microscopy combined with a PO₂ nanoprobe [Gagnon *et al.*, 2015]. Both OCT and two-photon (or multi-photon) laser scanning microscopy have been used extensively by the group of R.K. Jain in the characterisation of tumour vasculature, but are both limited to imaging only a superficial fraction of tissue within a small field of view [Jain *et al.*, 2013, Fukumura *et al.*, 2010, Fukumura & Jain, 2008]. They are however well established methods and could, with addition of an oxygenation sensing technique such as a PO₂ probe, be used to validate results of image-based modelling of muscle oxygenation as images of the vasculature could be cross-correlated. Thus, the combination of existing imaging and oxygen measurement methods can lead to further exciting results to understand the supply of oxygen to tissue in health and disease.

7.2 Mathematical description of oxygen exchange in skeletal muscle

In this section all equations generally used to describe the oxygen diffusion and uptake in skeletal muscle are presented.

7.2.1 Modelling oxygen diffusion

Diffusion is the process of molecules filling a space through random movement. This process can be described relating molecule flux to concentration. The relation of flux and concentration is described by Fick's first law

$$J = -D\nabla C, \quad (7.4)$$

with C the oxygen concentration, D its diffusion coefficient in muscle tissue and J the oxygen flux [Al-Shammari *et al.*, 2012]. The relation of concentration C and partial pressure P can then be described using Henry's law

$$C = \alpha P, \quad (7.5)$$

with α being the coefficient of tissue oxygen solubility [Al-Shammari *et al.*, 2012]. The conservation of oxygen can thus be described as

$$\frac{\partial C}{\partial t} = \nabla \cdot [D\nabla C] - M(C), \quad (7.6)$$

or in terms of the oxygen partial pressure [Al-Shammari *et al.*, 2012]:

$$\frac{\partial \alpha P}{\partial t} = \nabla \cdot [\alpha D \nabla P] - \tilde{M}(P), \quad (7.7)$$

where M and \tilde{M} are the respective oxygen consumption functions.

7.2.2 Oxygen tissue metabolism

The consumption of oxygen within tissue ((2) in figure 2.9) is usually described using Michaelis-Menten kinetics in equations (7.6)/(7.7):

$$M(P) = \frac{M_0 P}{P + P_{50}}, \quad (7.8)$$

where M_0 is the maximum oxygen consumption rate within the tissue and P_{50} the oxygen pressure at half-maximal consumption. P_{50} is usually found to be 0.5-1.0 mmHg [Goldman, 2008] and can be determined experimentally by methods described

in Pittman [2011]. For studying oxygen supply regions in skeletal muscle, Al-Shammari *et al.* [2014] took into account the fact that M_0 differs between different muscle fibre types (I, IIa, and IIb).

7.2.3 Boundary and initial conditions

In order to solve the above equations it is necessary to employ initial and boundary conditions.

In particular, two types of boundary conditions are required to solve equations (7.6) or (7.7): one that describes the oxygen flux at the vessel-tissue interface and one that describes the behaviour at the outer tissue surface.

The flux of oxygen from the capillaries into the tissue is described by a flow along a concentration or partial pressure gradient, respectively [Al-Shammari *et al.*, 2012], [Goldman & Popel, 2001], [Goldman & Popel, 2000], depending on the vessel permeability. The permeability can be described by a mass transfer coefficient k , which depends on the haematocrit and the type of vessel, i.e., capillary, arteriole or venule [Goldman, 2008]. This boundary condition is given by

$$-n_v \cdot (D\nabla C) = k(C_0 - C), \quad (7.9)$$

where n_v is the unit normal vector to the vessel surface (pointing into the vessel), C and C_0 are the molecular concentration in mol/m³ at time t and initially, respectively; and D the diffusion coefficient in m²/s.

The boundary condition usually imposed at the outer tissue surface is a no-flux boundary condition, i.e.,:

$$-n_o \cdot \nabla C = 0, \quad (7.10)$$

where n_o is the outer unit normal vector to the outer tissue surface. This means that all oxygen supplied by the blood vessels in one muscle stays within this muscle.

Finally, the initial condition for the model can be set to

$$C = C_{rest} \quad \text{at } t = 0. \quad (7.11)$$

7.2.4 Extensions of the simple diffusion model

Whilst the above equations are sufficient to set up a simple muscle tissue oxygenation model, a number of additional biological processes may be needed to be taken into account.

7.2.4.1 Myoglobin facilitated oxygen transport

The myoglobin (Mb) oxygen saturation is determined using the Hill equation ((3) in figure 2.9) [Goldman, 2008]:

$$S_{Mb}(P) = \frac{P}{P + P_{Mb,50}}, \quad (7.12)$$

with $P_{Mb,50}$ being the half-saturation value of myoglobin. The shape of the myoglobin oxygen saturation curve and of the corresponding haemoglobin (Hb) saturation curve is shown in figure 7.2. For the same partial oxygen pressure the haemoglobin O_2 saturation is lower than that of myoglobin, which indicates that haemoglobin is more likely to release oxygen. Myoglobin-facilitated transport reaches a plateau for a tissue oxygen partial pressure higher than $PO_2=2.5$ mmHg and can thus be neglected [Goldman & Popel, 2000].

When considering myoglobin facilitated transport of oxygen, the right hand side of

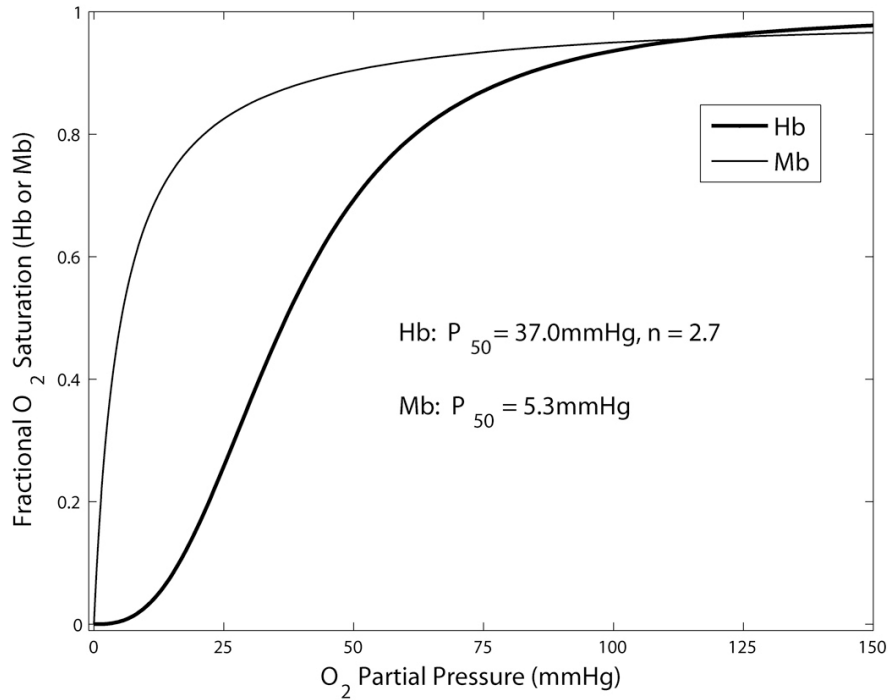


Figure 7.2: **Myoglobin and haemoglobin O_2 saturation curves.** Hb is more likely to release oxygen than myoglobin, as indicated by the Hb curve lying below the Mb curve. The numbers given are for rat blood. Figure taken from Goldman [2008].

equation 7.6 is extended by the term $D_{Mb}C_{Mb}\nabla \cdot \left(\frac{dS_{Mb}}{dC}\nabla C\right)$ Goldman & Popel [2000], with D_{Mb} , C_{Mb} and S_{Mb} being the myoglobin diffusivity, concentration and oxygen saturation. Equation 7.6 is thus transformed into

$$\frac{\partial C}{\partial t} = \nabla \cdot [D\nabla C] + D_{Mb}C_{Mb}\nabla \cdot \left(\frac{dS_{Mb}}{dC}\nabla C\right) - M(C). \quad (7.13)$$

7.2.4.2 Arteriolar oxygen supply

Although capillaries are acknowledged to play a major part in oxygen supply to the tissue, it is also known that other microvessels, especially the arterioles, are responsible for a considerable supply of oxygen. Whereas the previously cited models assume that oxygen diffuses only out of the capillaries into the tissue, it has been shown that oxygen also diffuses from the arterioles into both tissue and to neighbouring capillaries and venules within a vicinity of 100 μm of the arteriole [Ellsworth & Pittman, 1990], [Nair *et al.*, 1990], [Secomb & Hsu, 1994]. Moschandreou *et al.* [2011] developed a mathematical model based on Nair *et al.* [1989] to study the influence of arteriolar oxygen transport, considering also the effect of intraluminal variations in oxygen concentration. Moschandreou *et al.* [2011] found that oxygen tension decreases were larger in smaller vessels, as blood flow rates were higher in larger vessels. Secomb & Hsu [1994] showed that for higher flow and consumption rates, e.g., during exercise, less oxygen diffuses out of the arterioles. Bos *et al.* [1995] modelled RBCs as point-like oxygen sources, from which the oxygen was released into the tissue. This approach can provide further accuracy especially for larger blood vessels, in which the RBCs are not squeezed but may be distributed within the cross-section of the vessel. This approach also takes into account the influence of RBC haemoglobin saturation.

7.2.5 Modelling of blood flow

The flow in both interstitium and microvasculature can be assumed incompressible, as the compressibility of blood is similar to that of water and there is only a limited range of intravascular pressure Lee & Smith [2008a]. This hugely simplifies the Navier-Stokes equations, which describe the fluid flow within the vasculature. Furthermore, blood flow in the microvasculature depends only on the local pressure gradient and viscous forces. Inertial forces are negligible, as the Reynolds number of the flow is very low, i.e., 0.005-0.05 [Caro *et al.*, 2012]. In a large number of models, the flow rate in each vessel segment is assumed to follow Poiseuille's law, which describes the incompressible and unidirectional flow through a cylindrical tube of constant cross-section driven by a pressure gradient:

$$Q_{ij} = \frac{\pi R_{ij}^4 \Delta P_{ij}}{8\mu L_{ij}}, \quad (7.14)$$

where i, j are the nodes joint by a single vessel segment of radius R_{ij} and length L_{ij} , μ is the fluid viscosity and $\Delta P_{ij} = P_i - P_j$ the pressure drop across the vessel segment [Pries *et al.*, 1990], [McDougall *et al.*, 2002], [Secomb, 2011], [Secomb *et al.*, 2013], [Fry *et al.*, 2012].

7.3 Implementation of image-based modelling of muscle tissue oxygenation

In order to solve the equation (7.6) with corresponding boundary conditions (7.9) and (7.10) numerically, a method for discretisation of space and time is required.

One of such techniques is the finite element (FE) method. The spatial domain in this case is broken down into certain shapes (called element), e.g., triangles, tetrahedrons, cubes. The combination of all these elements forming the entire spatial domain is called a mesh. For each of the element shapes certain basis functions are defined [Zienkiewicz *et al.*, 2005]. The solution of the model is then calculated by minimizing the energy functional for the corners (nodes) of each shape and approximated via the basis functions for the rest of the element. In order to solve the model equations, it is converted into its weak form, for which a unique solution exists. The element size can either be uniform or adaptable to the complexity of the model domain, i.e., in our case it should be refined close to the blood vessels/red blood cells. It is important for the mesh to be fine enough so that the computed solution is a good approximation of the analytical solution [Zienkiewicz *et al.*, 2005]. Other geometry discretization techniques include finite difference (FD) methods. However, FD are less suited to handle complex geometries, also the approximation of the solution between nodes can be less accurate using FD instead of FE. For the time derivative in equation (7.6) and (7.7) however, a finite difference discretisation is usually used, e.g., forward or backward Euler scheme or Crank-Nicolson scheme.

7.3.1 Mesh Generation and Solver Choice

As explained in the previous chapter, binary images of the background vs. tissue and vessels/red blood cells, respectively, were generated for each muscle. These images were combined into one dataset with distinct greyscale values for each domain using Fiji ImageJ. This is shown in figure 7.3, with the domains and boundaries identified. Based on such datasets the software ScanIP (Simpleware Ltd, UK) was used to generate an FE mesh based on the images. Masks for each domain were created in ScanIP 3.0-4.4 using thresholding for the respective greyscale value. ScanIP creates tetrahedron meshes. Figure 7.4 shows a ScanIP preview of a 3D mesh created based on a Microfil dataset.

Depending on the dataset, different meshing workflows have been employed. For the Microfil datasets a volume mesh for import into COMSOL Multiphysics ®(COMSOL AB, Sweden) was created. However, creation of volume meshes in ScanIP is computationally time and memory intensive, even more so if the dataset contains very small features requiring to be meshed, as is the case with the red blood cells. Therefore, surface meshes were created for the unstained muscle datasets, of muscle

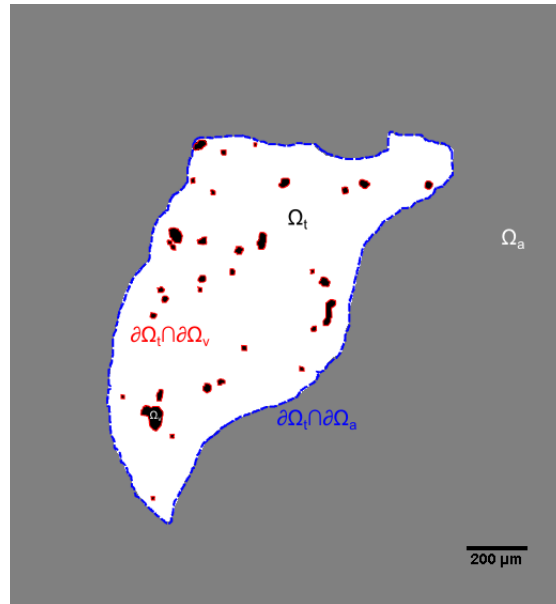


Figure 7.3: **Image for ScanIP.** After image processing, an image stack with three grey scale values was obtained, for background, tissue and vessels. Using the ScanIP software, these can be masked by simple thresholding and the respective masks of interest will be meshed with coinciding nodes of the different materials.

and red blood cell masks individually and exported the resulting files as .stl files.

These meshes were for import into OpenFOAM (OpenCFD Ltd, ESI Group), where the relatively coarse surface meshes would be further refined by an specialized algorithm and extended into volume meshes.

A disadvantage of ScanIP is that it is not an opensource software and therefore the algorithms used to generate the meshes are not visible to the user. Thus, many parameters had to be determined in a “trial and error” fashion. The dimensions of the resulting mesh files were exported in mm. This was accounted for by setting the geometry dimensions in COMSOL to mm and by adjusting units for the OpenFOAM model.

All resulting models were run on the IRIDIS High Performance Computing Facility.

COMSOL Multiphysics COMSOL Multiphysics is commercial software for solving computational fluid dynamics (CFD) problems. It allows the import of user-defined geometries and meshes or the creation of these within the software. A wide range of mathematical equations is already implemented in the software, making the description of many physical problems straightforward. However, the meshing and solving of any geometry and equation is fairly “black box”, with the user only being allowed to choose between a number of numerical solvers and adaptation of any codes is not possible. Furthermore, parallelization of codes, whilst possible, is not advantageous due to long communication times between processors. The main

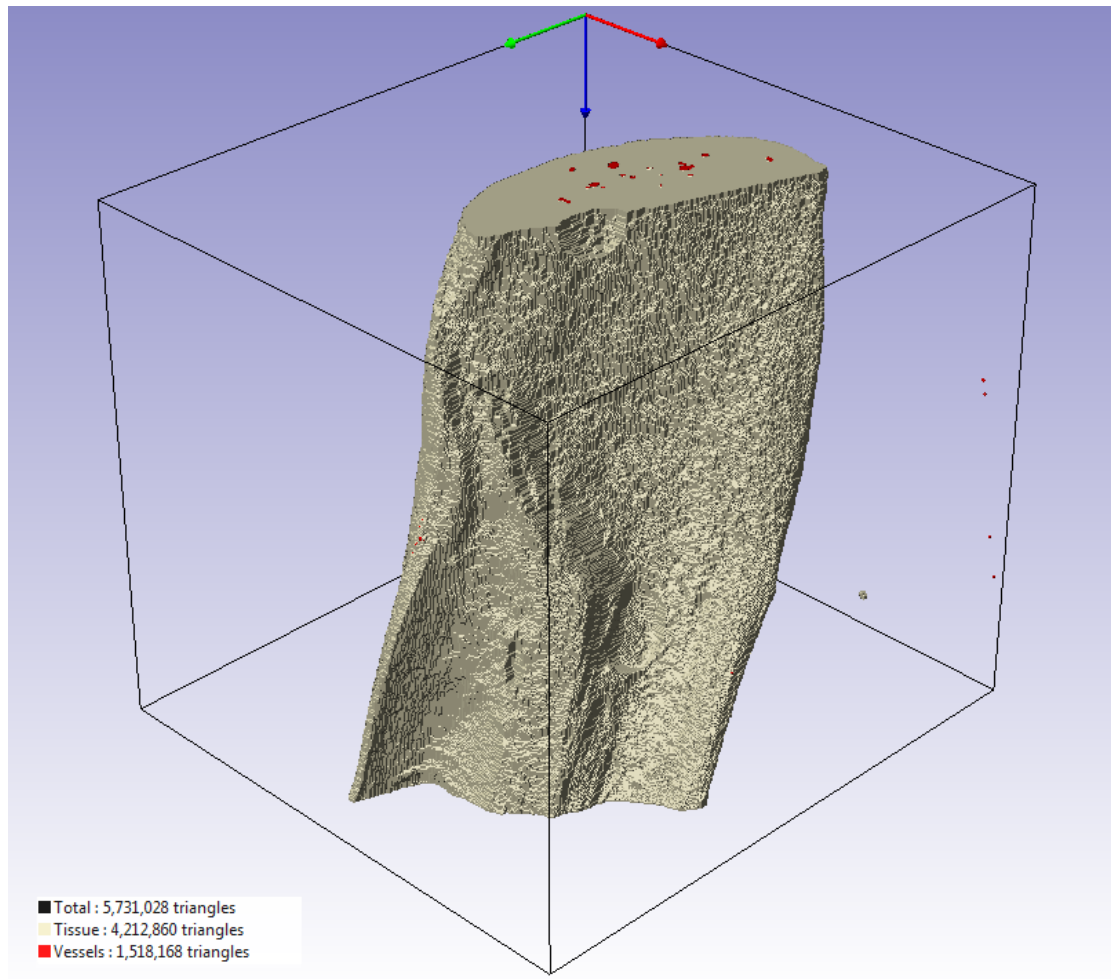


Figure 7.4: Preview of ScanIP meshing for the 3D volume.

advantage of COMSOL is the inclusion of all steps, i.e., creating a geometry, meshing, defining mathematical equations to be solved, solving and visualisation of results and its ease of use.

OpenFOAM OpenFOAM is a free, open source CFD based on the programming language C [ope, 2016]. It is created as a building block system of libraries, allowing users to add and delete modules as they choose. OpenFOAM is especially useful for solving large custom-built problems as parallelization is straightforward. Meshes are imported as surface meshes and will be refined by the *snappyhexmesh* library. The level of refinement is defined by the user. The solver schemes, i.e. time stepping, definition of gradients and interpolation schemes, are defined in *fvSchemes*. All schemes and tolerances can be defined by the user. This makes OpenFOAM a very adaptable solution that can be optimized for individual problems, however, it is clearly error prone depending on the experience of the user.

For import into OpenFOAM, two separate files for muscle tissue and red blood cells were created, so as to be able to define two separate boundaries, i.e., the muscle-RBC

Parameters defining the oxygen perfusion in muscle		Value	Source
O ₂ Diffusion coefficient (37°C) [10^{-9} m ² /s]		2.11	Levick [2003]
Consumption rate in muscle at rest [10^{-5} ml O ₂ /ml s], in muscle fibre type	I	15.7	Wust <i>et al.</i> [2009]
	IIa	13.82	
	IIb	7.85	
Myoglobin concentration [10^{-3} ml O ₂ /ml], in muscle fibre type	I	10.2	Meng <i>et al.</i> [1993]
	IIa	4.98	
	IIb	1.55	
Myoglobin PO ₂ saturation at half-maximum [mmHg]		5.3	Jurgens <i>et al.</i> [1994]
Myoglobin oxygen diffusion coefficient [10^{-11} m ² /s]		1.73	Jurgens <i>et al.</i> [1994]
Intracapillary PO ₂ [mmHg]		20	Eggleton <i>et al.</i> [2000]
O ₂ solubility [10^{-5} ml O ₂ / ml mmHg]		3.89	Goldman & Popel [1999]
O ₂ capillary wall permeability [m/s]		~ 10 ⁻³	Levick [2003]
Muscle PO ₂ at half demand [mmHg]		0.5	Honig & Gayeski [1982]
Muscle PO ₂ in resting muscle [mmHg]		20	Levick [2003]
Muscle PO ₂ in exercising muscle [mmHg]		< 5	Levick [2003]
End-capillary PO ₂ in resting muscle [mmHg]		40	Levick [2003]
End-capillary PO ₂ in exercising muscle [mmHg]		15	Levick [2003]

Table 7.1: **Model parameters as described by Al-Shammari *et al.* [2012, 2014].** The parameters are given in terms of tissue PO₂ and are converted into oxygen concentration *C* for model implementation. The conversion parameter is 0,0016 [mol/(mmHg m³)].

interface and the muscle-air interface.

Visualisation of simulation results however needs to be performed in a separate opensource kit called Paraview (Kitware Inc., US and Los Alamos National Laboratory, US).

7.3.2 Model Description and Solver Settings

The parameters used for modelling the diffusion and uptake of oxygen in muscle tissue have been summarised by Al-Shammari *et al.* [2012, 2014] and can be found in table 7.1. Before integration into the model, all values were converted into a description as oxygen concentration rather than PO₂, as the implementation of the diffusion equation in COMSOL was based on concentration.

7.3.2.1 Microfil datasets in COMSOL Multiphysics

Despite the small occurrence of capillaries in the Microfil perfused datasets, the mathematical model based on the images was implemented as a proof of concept. The generated FE mesh was imported into COMSOL Multiphysics, in order to solve the mathematical model describing the nutrient flow out of the vessels into the tissue. In the tissue domain Ω_t , a diffusion equation based on (7.6) was employed, with constant diffusion coefficient and no oxygen consumption, i.e.:

$$\frac{\partial C}{\partial t} = D \nabla^2 C \quad \text{in } \Omega_t, \quad (7.15)$$

where C is the molecule, i.e., glucose or oxygen, concentration in mol/m^3 , t the time in seconds, and D the diffusion coefficient in m^2/s .

The boundary conditions on the tissue-vessel interface is described by the vessel permeability boundary condition in equation (7.9):

$$-\mathbf{n}_v \cdot (D \nabla C) = k(C_0 - C) \quad \text{on } \partial\Omega_t \cap \partial\Omega_v, \quad (7.16)$$

and on the outer tissue surface the no-flux boundary condition was applied as in equation (7.10)

$$-\mathbf{n}_o \cdot \nabla C = 0 \quad \text{on } \partial\Omega_a \cap \partial\Omega_v. \quad (7.17)$$

Ω_a denotes the background/air domain surrounding the muscle tissue and Ω_v the vessel domain.

However, the boundary condition (7.9) is defined in Comsol as

$$-\mathbf{n} \cdot (D \nabla c) = g - qc. \quad (7.18)$$

It follows for equation (7.16) $q = k$ and $\frac{g}{q} = C_0$. $\frac{g}{q}$ can then be determined as follows: using the intercapillary PO_2 , $P_0 = 20\text{mmHg}$ and the O_2 solubility $\alpha = 3.89 \cdot 10^{-5} \text{ mlO}_2/\text{mlmmHg}$ the intercapillary oxygen concentration can be computed, i.e., $C_0 = \alpha \cdot P_0 = 7.78 \cdot 10^{-4} \text{ mlO}_2/\text{ml} = 3.2417 \cdot 10^{-2} \text{ mol/m}^3$. As $1 \text{ mlO}_2 = 4.16 \cdot 10^{-5} \text{ mol}$, it follows $\frac{g}{q} = 3.2417 \cdot 10^{-2} \text{ mol/m}^3$. Furthermore, the value for q given in the literature can be verified; $g = k \cdot P_0 = 3.328 \cdot 10^{-5} \text{ mol/m}^2\text{s}$ and it follows for $q = \frac{g}{C_0} = 1.03 \cdot 10^{-3} \text{ m/s}$, which is consistent with the permeability given in Levick [2003].

The initial conditions for the model are

$$C = 0 \quad \text{in } \Omega_t \text{ at } t = 0$$

and

$$\nabla C = 0 \quad \text{in } \Omega_t \text{ at } t = 0.$$

Convergence Test To validate the convergence of the FE model implemented in COMSOL depending on the mesh coarseness, equation (7.15) was solved for different mesh sizes, from coarse to fine and the convergence of the solution at a number of points in time was checked. With ScanIP Free Grid meshes of coarseness -50 to +10 were created, i.e., very coarse to fine meshes. Figure 7.5 shows the different solutions for the coarsenesses of -50 and +10 at $t = 5$ s.

Figure 7.6 shows the mean error of meshes with coarseness 0 to -50 compared to the solution obtained using a mesh of coarseness (fineness) +10 for 1000 data points. The graph suggests a trend of better convergence for the finer meshes. Thus, a mesh of coarseness -20 provided for sufficiently good results.

7.3.2.2 Unstained dataset in OpenFOAM

The original OpenFOAM model used in this thesis was based on a modified LaplacianFoam solver. The initial modifications and OpenFOAM implementation was created in the soil sciences context by Dr. Keith Daly, a postdoctoral research fellow in the Bioengineering Sciences research group at UoS. Adaptations to the model including implementation of the non-linear Michaelis-Menten kinetics, mesh refinement and adaptation of time stepping algorithm were made by Berit Zeller-Plumhoff after consultation with Dr. Daly.

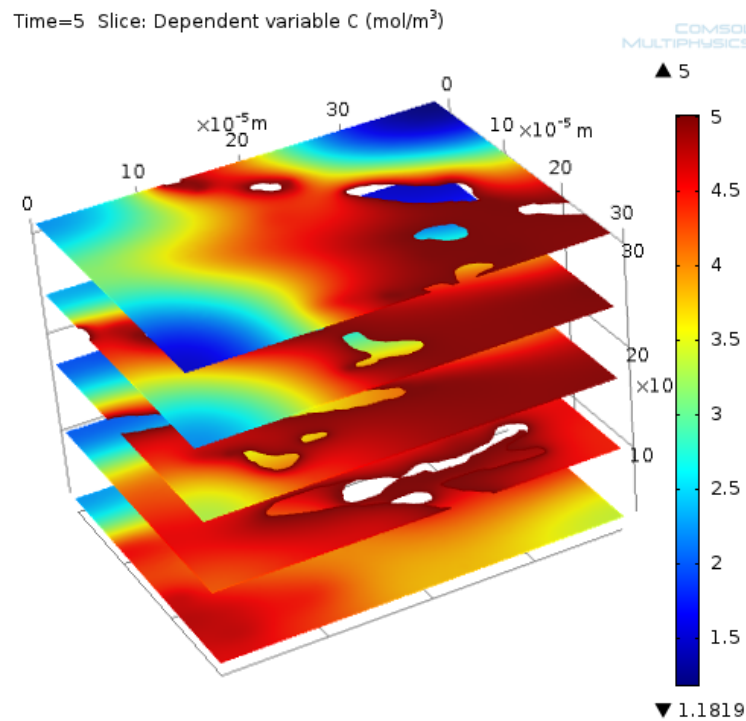
The equation

$$\frac{\partial C}{\partial t} = D\nabla^2 C - M(C) \quad \text{in } \Omega_t,$$

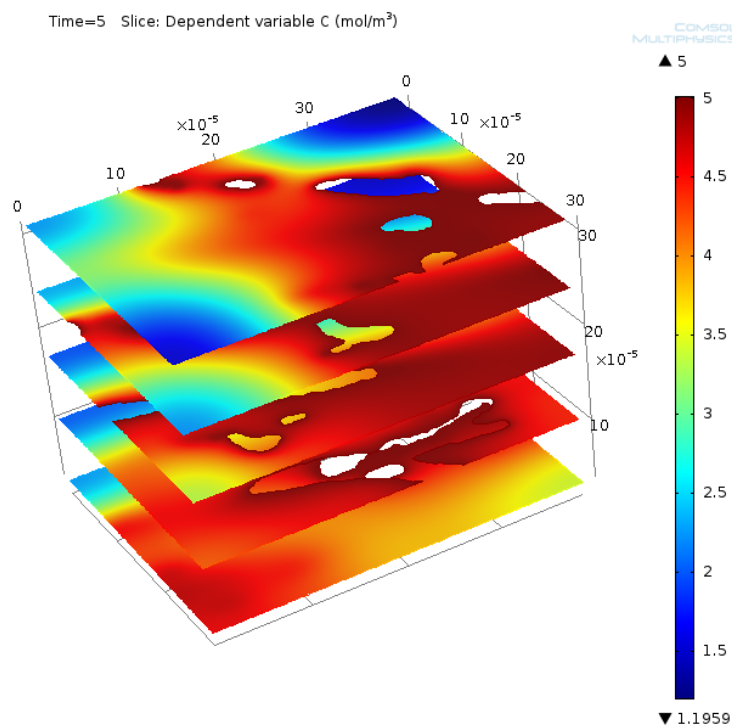
was solved for constant consumption $M(C) = M_0$ and Michaelis-Menten kinetics $M(C) = \frac{M_0 C}{C + C_{50}}$ with $C_{50} = 8.1 \cdot 10^{-4} \text{ mol/m}^3$ the muscle oxygen concentration at half demand (taken from table 7.1). The case of constant consumption is not physiological and results in negative oxygen concentrations but was solved because of the ease of obtaining a solution. For the non-linear Michaelis-Menten it was necessary to use a mixed Crank-Nicolson and implicit Euler scheme to be able to solve the equation numerically. The solver was defined to be CrankNicolson 0.9 in *fvSchemes*. The parameter $\phi = 0.9$ in this case defines the blending between both methods, with $\phi = 1$ being a pure Crank-Nicolson scheme and $\phi = 0$ a pure implicit Euler scheme ope [2016]. The default setting of $\phi = 0.9$ increases the stability of the otherwise possibly unstable Crank-Nicolson scheme. For constant consumption functions it was possible to employ the faster implicit Euler algorithm. In both cases all other solver schemes were to linear Gaussian interpolations.

In order to capture the very small red blood cells, it was necessary to refine the mesh around these by halving the size of all edges at least 5 times. No refinement of the muscle surface was performed.

For implementation, the model dimensions were changed into $[C] = \text{nmol/mm}^3$, such



(a) ScanIP Free Grid Coarseness -50



(b) ScanIP Free Grid Coarseness +10

Figure 7.5: **Solution of equation (7.15) with BCs (7.9) and (7.10) at $t = 5$ s for the finest and coarsest mesh settings.** Different mesh coarsenesses of ScanIP's Free Mesh module were compared to test the Comsol model for convergence. Figure 7.6 shows the corresponding convergence graph. Note that the equation was solved for glucose, not oxygen.

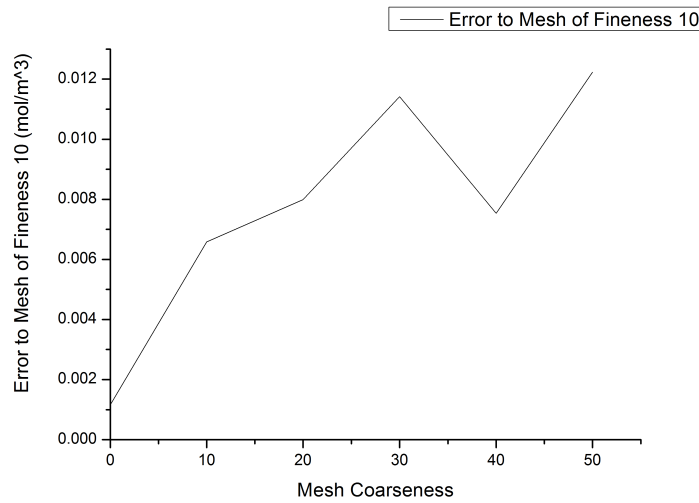


Figure 7.6: **FEM convergence plot** The graph suggests a trend of convergence for finer meshes (read graph from right to left). Wishing for an accuracy of < 0.01 , it is necessary to create meshes with ScanIP using a coarseness of at least -20.

that in equation (7.16) $k = 1\text{mm}$. Furthermore, as $D/k \ll 1$ the boundary condition (7.16) was approximated $C = C_0$. A no-flux boundary condition was implemented at the air-tissue interface. The initial condition was set to $C(0) = C_0$.

It was assumed that all red blood cells were fully saturated with oxygen and remained so over time.

Tissue oxygenation could not be solved for CHF4, HFC1 and HFHF4 muscles for the non-linear case as the geometry was too complicated.

7.4 Results

7.4.1 Results for Microfil sample oxygenation

Equation (7.15) was solved for the diffusion of oxygen within the whole tissue of a Microfil perfused muscle for $t = 0, \dots, 1$ s. Figure 7.7 shows the solution at $t = 1$ s. The insufficient perfusion due to few capillaries being present within the muscle tissue can be observed.

Therefore, no further modelling based on the Microfil samples was performed. Solving this model for the case of Michaelis-Menten kinetics was not possible, as memory requirements exceeded the available resources on the Iridis computing cluster.

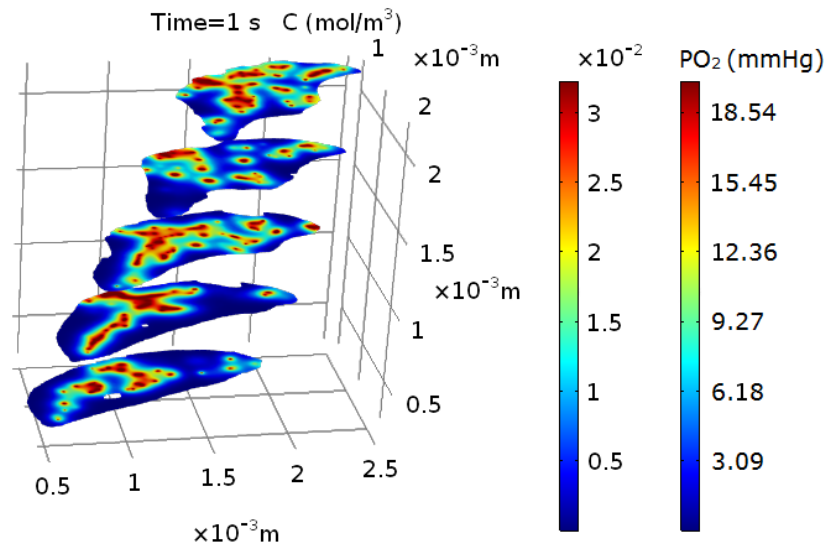


Figure 7.7: **Oxygen diffusion in whole tissue at $t = 1$ s.** The vessels were perfused with Microfil and the model solved using Comsol for $M(C) = 0$. Within 1 s the whole muscle tissue should be perfused, which is not the case for the present muscle due too the low perfusion.

7.4.2 Results for unperfused sample oxygenation

Figures 7.8 and 7.9 displays the results of the tissue oxygenation in the case of Michaelis-Menten kinetics for an exemplary muscles of each of the dietary groups. The results of both the constant and non-linear consumption cases are given in table 7.2 and the group means are displayed in figure 7.10.

In the constant case the muscle tissue oxygenation between groups was different but missed the threshold for statistical significance closely ($p=0.094$, $F=2.8$). Such a dependence on diet was not observed for Michaelis-Menten kinetics ($p=0.116$, $F=2.8$). However, the observed power in this case was only 44%, clearly suggesting that a larger groups ought to be investigated. Furthermore, as the relationships between values appear similar for constant and non-linear consumption, it is possible that the three missing solutions for Michaelis-Menten kinetics negatively affect the statistical significance.

7.4.2.1 Structural parameter - oxygenation relationship

For each muscle the mean oxygen concentration within the modelled cubic muscle volume was computed. The mean oxygen concentration *vs.* each structural parameter and the respective fitted linear regression lines are displayed in figure 7.11. The respective linear regression lines was computed in Origin8.1 (which uses the least squares method), returning also the adjusted R^2 that determines the quality of the

Muscle ID	Michaelis-Menten kinetics		Constant oxygen consumption	
	E-02 mol/m ³	mmHg	E-02 mol/m ³	mmHg
CC1	3.004 ± 0.251	18.56 ± 1.55	1.76 ± 0.88	10.88 ± 5.44
CC2	3.094 ± 0.144	19.12 ± 0.89	2.35 ± 0.50	14.52 ± 3.09
CC3	2.997 ± 0.253	18.52 ± 1.56	1.80 ± 0.86	11.12 ± 5.31
CC4	3.097 ± 0.15	19.14 ± 0.93	2.44 ± 0.49	15.08 ± 3.03
CC5	3.021 ± 0.255	18.67 ± 1.58	1.96 ± 0.88	12.11 ± 5.44
CHF1	3.086 ± 0.141	19.07 ± 0.87	2.85 ± 0.29	17.61 ± 1.79
CHF3	3.034 ± 0.22	18.75 ± 1.36	2.09 ± 0.70	12.92 ± 4.33
CHF4	-	-	2.64 ± 0.36	16.31 ± 2.22
HFC1	-	-	2.84 ± 0.22	17.55 ± 1.36
HFC2	3.132 ± 0.12	19.35 ± 0.74	2.62 ± 0.42	16.19 ± 2.60
HFC4	3.102 ± 0.139	19.17 ± 0.86	2.47 ± 0.49	15.26 ± 3.03
HFHF2	3.012 ± 0.214	18.61 ± 1.32	1.76 ± 0.76	10.88 ± 4.70
HFHF3	2.991 ± 0.268	18.48 ± 1.66	1.75 ± 0.90	10.81 ± 5.56
HFHF4	-	-	2.56 ± 0.46	15.82 ± 2.84

Table 7.2: **Results for mean tissue oxygen concentration and partial pressure for unperfused samples for constant consumption and Michaelis-Menten kinetics.** The mathematical model was created based on the phase contrast-based SR CT images of red blood cells in the soleus muscle of mice of the animal model of developmental priming. The model was solved in OpenFOAM.

fitting. R^2 was used to conclude which structural parameter best predicted the tissue oxygenation. For the relationship of RBC spacing and mean tissue oxygenation, a logarithmic (natural logarithm) regression line was also computed, as this was governing the relationship between diffusion distance and tissue PO_2 determined by Krogh (for constant $M(C)$ though), see equation (7.1).

The highest R^2 value was computed for the relationship between volume fraction and mean oxygen concentration with $R^2 = 0.63$ followed by that for the mean distance to the next RBC (RBC spacing) with $R^2 = 0.52$. The third highest $R^2 = 0.40$ is for length density followed by capillary density $R^2 = 0.30$. Finally, the lowest fit was computed for fractal dimension ($R^2 = 0.28$) and capillary-to-fibre ratio ($R^2 = 0.26$).

The logarithmic regression line for RBC spacing had the same fitting quality as the linear line, i.e., $R^2 = 0.52$, as the natural logarithm can be well approximated by a line in the small interval of diffusion distances that was investigated.

7.5 Discussion

From the computed R^2 values it follows that the best measures to predict muscle tissue oxygenation are indeed the 3D volume fraction, followed by the 3D mean distance measure from each point in the tissue to the next capillary (RBC spacing). Overall all 3D measures show a better fitting (except fractal dimension) than the 2D measures

capillary density and capillary-to-fibre ratio. This was to be expected, as the 2D measures fail to incorporate 3D variations in the microvascular structure. Furthermore, the capillary-to-fibre ratio does not take into account any area or volume of tissue oxygenation, thus performing poorly in predicting it. The capability of the capillary density to predict oxygen supply however is likely to increase if it were to be computed over a larger number of SR CT slices, as more variations would then be taken into account. However, it would still only take into account the number of oxygen exchange points in each slice and not the exchange surface, which is a better predictor for the overall oxygen exchange and thus tissue oxygenation. This fact is taken into account in the volume fraction measure, especially if it is assumed that the capillary diameter is (quasi-)constant, which then linearly links vessel volume to vessel surface. Finally, the mean distance to the next RBC (in 3D) expectedly emerged as one of the best predictors for tissue oxygenation, as the tissue oxygenation was governed by diffusion and thus mainly depending on the diffusion distance. A higher value R^2 might be computed if the mathematical model took into account the soft tissues present in the muscle other than muscle fibres.

Solving the model numerically was computationally very expensive. It required 8 computing nodes with 12 processors each and between 15 to 72 hours for the non-linear consumption function to be solved using the mixed Crank-Nicolson scheme.

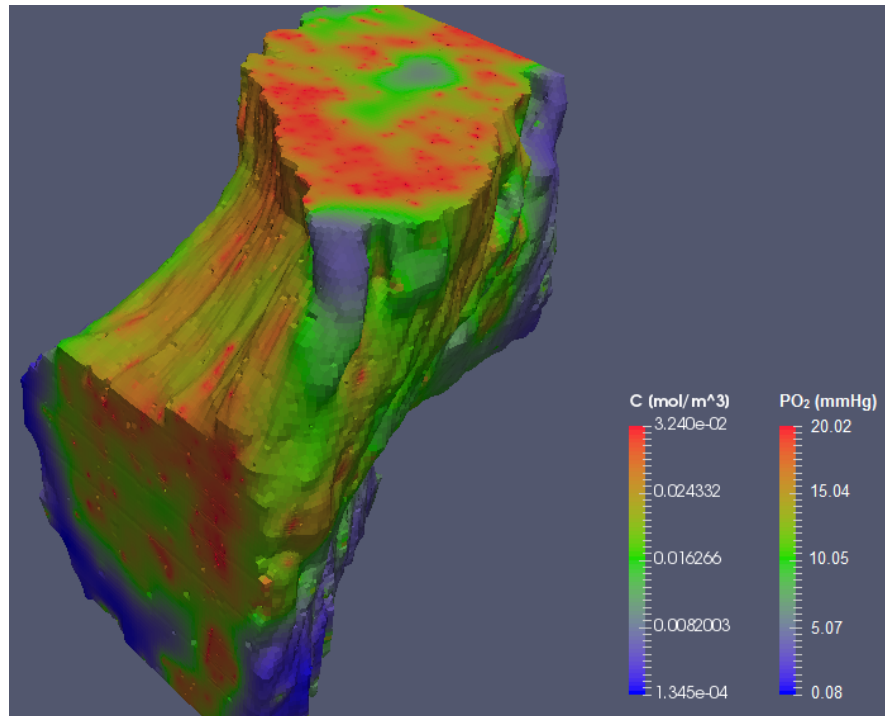
As a proof of concept, it was further shown that the image-based modelling based on images of the Microfil perfused datasets in COMSOL Multiphysics was possible, however, the perfusion was insufficient, i.e. within one second the whole muscle should be supplied with oxygen, especially as no oxygen consumption was applied. Furthermore, in this model, all blood vessels were assumed to be exchanging oxygen with the muscle tissue, a task which in reality would be limited to the microvasculature only. Thus, the resulting tissue oxygenation as presented above is still overestimating the actual oxygen supplied by the visualised dataset.

Clearly, the supply of oxygen to muscle tissue as modelled through the visualisation of red blood cells is more realistic and withstands the application of oxygen uptake. Whilst it is unrealistic for all red blood cells present in the muscle to be fully saturated with oxygen to be supplied to the tissue, it is a first approximation of the reality.

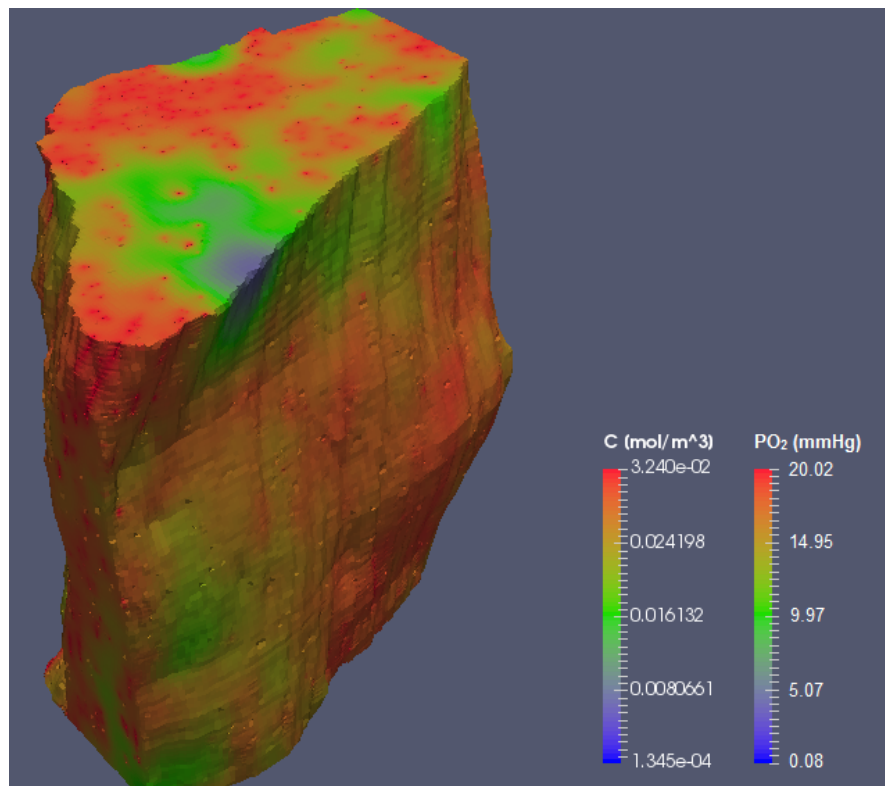
7.6 Summary

An overview of existing mathematical models for modelling oxygen delivery to muscle tissue was presented, with particular respect to image-based models. The main equations used in modelling the oxygen delivery were introduced and the implementation of these equations in this work was presented. It was shown that the

vascular network obtained through μ CT imaging of Microfil-perfused muscle samples is incapable of supplying sufficient oxygen to the tissue. However, utilising the phase contrast-based SR CT images to assess oxygen supply in the different dietary groups showed that 3D morphological parameters are better predictors of tissue oxygenation than 2D parameters.

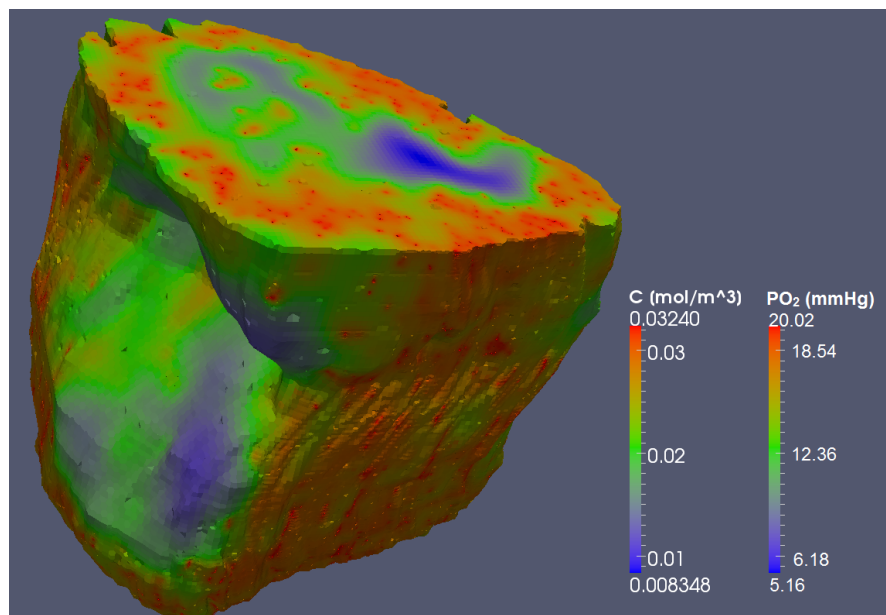


(a) CC muscle oxygenation

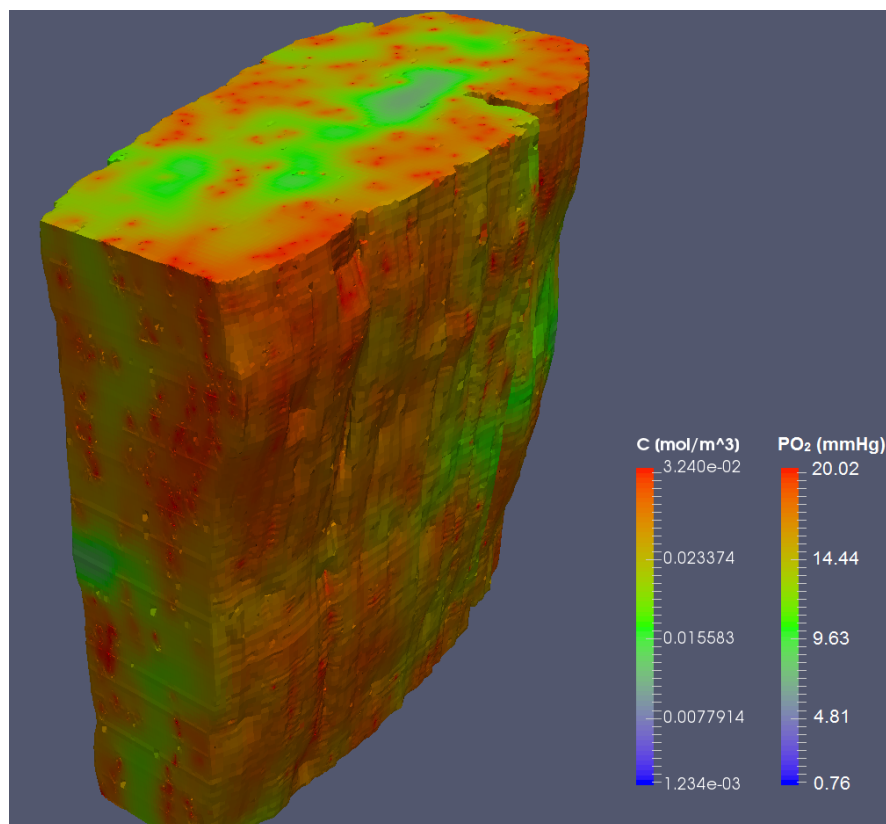


(b) CHF muscle oxygenation

Figure 7.8: **Tissue oxygenation with Michaelis-Menten consumption for exemplary muscle of the CC and CHF group.** The oxygen diffuses from the red blood cells, where it is at its highest concentration, to the tissue where it is consumed.



(a) HFC muscle oxygenation



(b) HFHF muscle oxygenation

Figure 7.9: Tissue oxygenation with Michaelis-Menten consumption for exemplary muscle of the HFC and HFHF group. The oxygen diffuses from the red blood cells, where it is at its highest concentration, to the tissue where it is consumed.

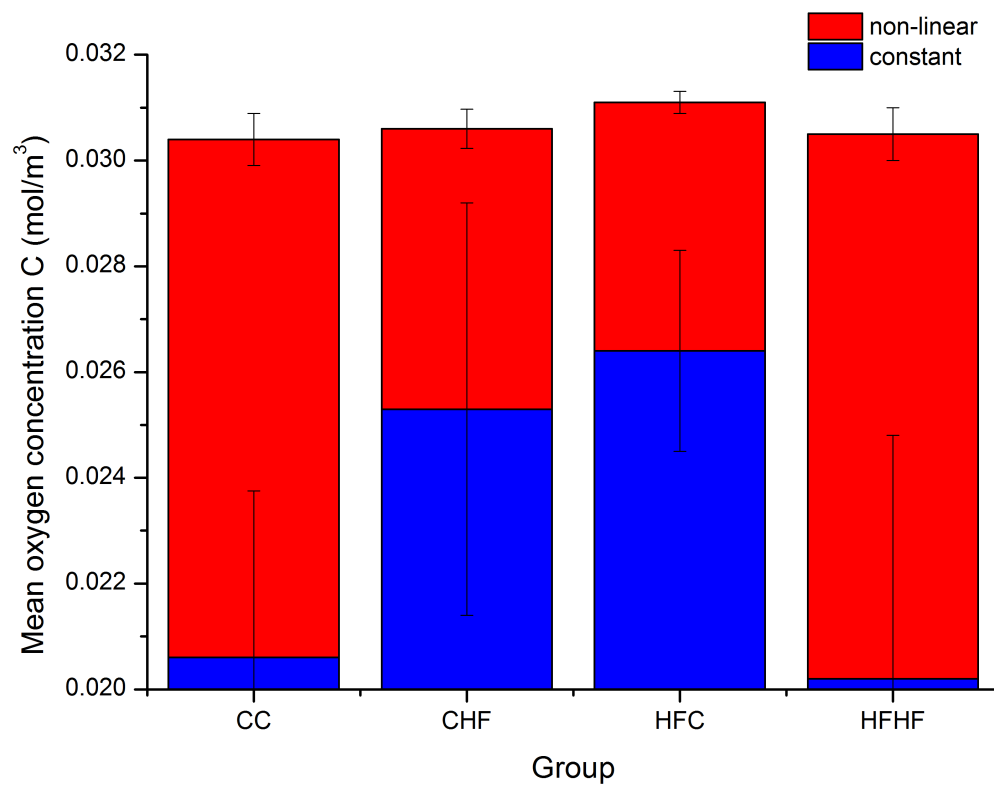
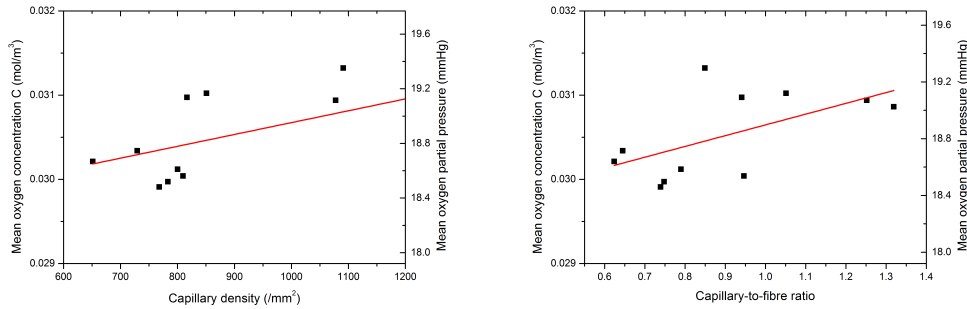
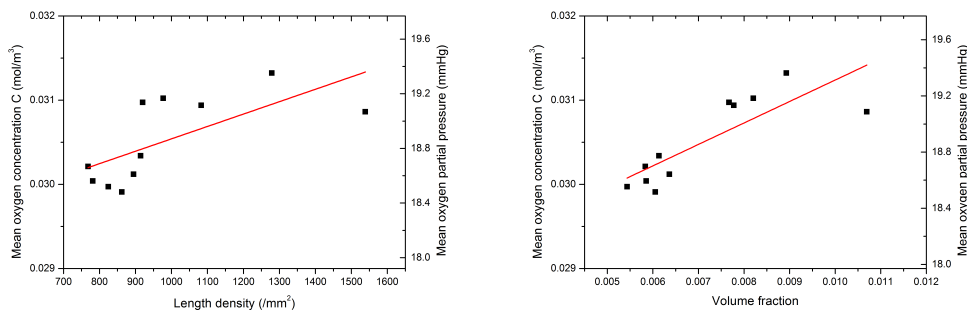


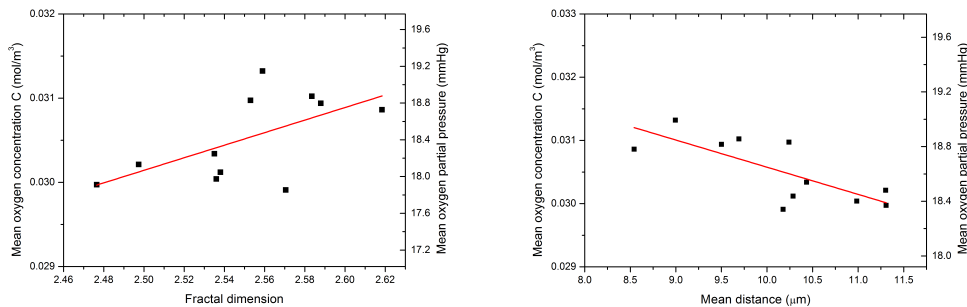
Figure 7.10: **Mean tissue oxygen concentration for non-linear Michaelis-Menten kinetics (red) and constant consumption (blue).** The means (\pm standard deviation) are given for all groups. $N=5$ for CC and $n=3$ or $n=2$ for CHF, HFC and HFHF groups for constant or non-linear consumption, respectively. Due to non-physiological negative concentrations the variability is significantly larger in the case of constant consumption.



(a) Capillary density vs. mean oxygen concentration $R^2 = 0.30$ (b) Capillary-to-fibre ratio vs. mean oxygen concentration $R^2 = 0.26$



(c) Length density vs. mean oxygen concentration $R^2 = 0.40$ (d) Volume fraction vs. mean oxygen concentration $R^2 = 0.63$



(e) Fractal dimension vs. mean oxygen concentration $R^2 = 0.28$ (f) Mean distance to capillary vs. mean oxygen concentration $R^2 = 0.52$

Figure 7.11: Tissue oxygen concentration dependence on structural measures for all muscles. The mean tissue oxygenation based on Michaelis-Menten kinetics has been plotted against the computed structural parameters. A linear regression line was fitted for each plot and the quality of the fit was determined as R^2 . The best fits exist for the measures of volume fraction and mean distance whilst capillary density, fractal dimension and capillary-to-fibre ratios are poor predictors of tissue oxygenation.

Chapter 8

Conclusions and future work

Image-based modelling of skeletal muscle oxygenation is a challenging process. At present, only a few models are based on 3D physiological data. As the microvasculature is a complex 3D network its structure needs to be assessed in according detail to obtain information about its capability to deliver oxygen. A wide range of imaging methods for soft tissue imaging exists, but only few provide the capability to capture small capillaries at whole organ scale. Structural parameters that are currently in use to investigate this capability in health and disease need to be assessed by mathematical modelling of tissue oxygenation to evaluate their relevance. This thesis developed a new work flow of obtaining images of the 3D architecture of the murine skeletal muscle vasculature, performed structural analysis on the networks and employed a mathematical model to simulate the oxygen flow out of the vessels into the tissue.

Figure 8.1 displays requirements regarding the workflow from the point when images of the microvasculature have been obtained until the final analysis of the results. Clearly, this process is very time expensive and requires dedicated resources. Furthermore, each step of the workflow involved a number of processes in which limitations arose, some of which could be circumvented but not all. These limitations were discussed in the respective chapters and are summarised in table 8.1. Overall, this limits the trust we can put into the total numbers of the results of this study. Nevertheless, the workflow was applied consistently to each muscle, thereby granting confidence in the relationships obtained from the structural analysis and the link between structural parameters and muscle tissue oxygenation.

X-ray phase contrast computed tomography has been shown to enable the visualisation of red blood cells within the muscle microvasculature in a fashion that allows for further image-based modelling of oxygen supply to the muscle tissue. This was not possible using more traditional contrasting methods such as perfusion of the microvasculature and staining of the muscle tissue to enhance soft tissue contrast for

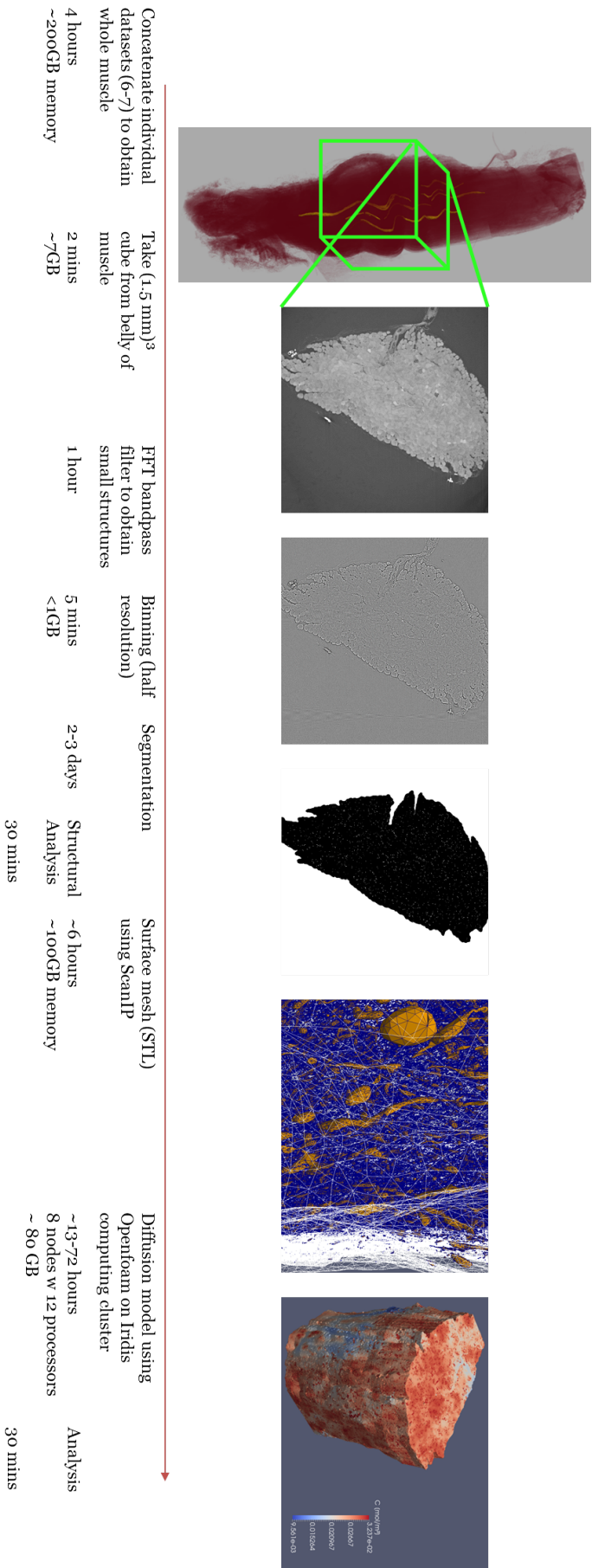


Figure 8.1: Implemented workflow of image-based modelling including times and requirements for each step.

Process	Limitations	Circumvention
Sample Preparation		
Different stresses on animal	Differing RBC numbers	-
Fixation	Shrinkage	Clamp muscle
Dehydration	Shrinkage	Clamp muscle
Imaging		
Sample-to-detector distance	Resulting edge enhance- ment and contrast	Parametric Study
Scintillator skew	Sharpness and greylevels	Post-imaging correction
Phase-retrieval parameters	Resulting edge enhance- ment and contrast	Parametric study around current optimum
Processing and segmentation		
Bandpass filtering	Highlighting too many/few features	Parametric Study
Thresholding	Pre-segmenting too many/few features	Parametric Study
Manual segmentation	Incorrect segmentation	-
Segmentation of RBCs only	Incorrect modelling results	Segment all features
Validation of SR CT images		
Microtoming	Shearing	numerous trials
Dewaxing	RBCs flowing away	-
Inexperience in staining	background staining	numerous trials
Image correlation methods	wrong numbers	optimization
Counting bias	wrong results	second blinded observer

Table 8.1: **Tabulation of all processes in the workflow and limitations that may have arisen with ways of circumvention.** The workflow from sample preparation over imaging and validation is error prone, but it was applied in a consistent manner. Therefore, the relationships determined for structural parameters and tissue oxygenation are valid.

μ CT imaging. Apart from visualisation of blood vessels, phase contrast-based SR CT further enabled the detection of changes in muscle spindle density and intramuscular fat content in an animal model of developmental priming, consistent with previous literature. This thesis showed that in animals fed a fat-rich diet post weaning led to the development of features typical for the metabolic syndrome [Torrens *et al.*, 2012], such as increased muscle volume and fat volume or decreased muscle fibre number per unit volume of muscle and spindle density. It has further become clear that a double high-fat diet in dam and offspring has a significantly negative effect on the number of muscle fibres per muscle volume and fat content. This could be an indication for the decline in muscle performance as observed in mice fed a HF diet [Tam *et al.*, 2015] and offspring of dams fed a “junk food” diet [Bayol *et al.*, 2009].

However, no dependence on dietary group of structural parameters assessing the capillary network were observed, other than the mean distance to the next red blood cell for each point in the muscle tissue, i.e., the RBC spacing. This parameter was closely linked to the tissue oxygenation capabilities of the capillary network. In

conclusion, maternal and offspring diet affect the spacing of the recruited/perfused capillary and possibly that of all capillaries, which was closely linked to muscle tissue oxygenation as also discussed in Frisbee *et al.* [2016].

To summarise, this thesis has expanded the body of knowledge in the following:

- it has been shown that skeletal muscle microvasculature can be visualised in 3D using phase contrast SR CT such that structural parameters can be determined;
- it is possible to image red blood cells rather than the vasculature itself, which enables image-based modelling with realistic haematocrit information;
- 3D structural parameters, i.e., volume fraction and RBC spacing, have been shown to have a greater ability in predicting muscle tissue oxygenation than traditionally used 2D measures capillary density and capillary-to-fibre ratio;
- the combination of maternal and offspring high-fat diet influences the spacing of RBCs, but appears to have no effect on other structural measures.

8.1 Future work

A first step in future work should be the segmentation of all different soft tissue features in a control muscle and to include the different oxygen diffusion/consumption behaviours of each of the different tissues in the mathematical model of tissue oxygenation. This would allow the analysis of how important the presence and identification of these tissues is.

Furthermore, as it was assumed that oxygen diffuses in the same way out of all types of microvessels for the modelling of the muscle perfusion in the Microfil perfused muscle. In a next step different mass transfer coefficients for the different microvessels should be considered and potentially the diffusion of oxygen into capillaries from neighbouring arterioles. For modelling based on the images of the unstained muscles it should be taken into account that not all red blood cells are fully saturated with oxygen at all times. To this end it would be possible to measure the distance of each red blood cell to the next artery/arteriole (which is possible if these are segmented individually) and weigh the oxygen saturation accordingly. At the same time a random algorithm for the oxygen saturation of the RBCs could also be used (with the same total available oxygen) to investigate how important such a weighing function would be.

Additionally, as the length scales of RBCs ($d = 5 \mu\text{m}$) and muscle tissue ($D = 2 \text{ mm}$) are very different and in fact $d/D \ll 1$ it would be in the interest of saving computational resources to consider a homogenization technique for modelling [Daly & Roose, 2015]. However, for these techniques it is necessary that the red blood cells be reasonably

uniformly distributed within the tissue volume, which in this very case was still to be investigated.

More future work could also include the further modelling of the influence of tortuosity on oxygen perfusion as outlined in appendix C. Further work should take into account different consumption rates and the influence of additional blood vessels.

Figure 3.1 in chapter 3 showed that the only other imaging technique that may provide sufficient resolution while penetrating a whole mouse soleus muscle would be light sheet fluorescence microscopy (LSFM) and to use it to build a three dimensional image after fluorescence staining of the vascular endothelium. The LSF microscope at the biomedical imaging unit at Southampton general hospital (SGH) involves five laser diodes, working at 405 nm, 488 nm, 561 nm, 640 nm and 785 nm, respectively [Page, 2014]. If clearing of the muscle tissue can be performed with sufficient quality and a fluorescent stain of the vascular endothelium can be found that diffuses sufficiently through a large muscle volume it would be possible to do comparative imaging - at least of a cubic volume from the belly region of the muscle - and compare results regarding structural parameters from this imaging technique and SR CT. As staining for histology is possible in muscle that has previously been imaged using SR CT this could be done subsequently, so as to provide a best comparison.

Furthermore, in the report presented for continuation towards a PhD and in the proposal for the SLS I had suggested to grow vascular networks *in vitro* in a growth medium and image these using phase contrast imaging as well. The *in vitro* grown vascular networks would be divided into a control group and a group challenged by addition of an adipose environment to study the impact of this outside the body. The growth of these networks was trialled by collaborators at SGH but remained unsuccessful until imaging at the SLS. Consequently the project was dropped. However, it is still a problem of interest, especially as not only the influence of an adipose environment but also the possibly positive influence of VEGF factors or other enzymes could be tested. For further work I would therefore suggest to take this project up again; although 3D imaging in the first instance would not be essential and until good results were obtained light microscopy and/or confocal microscopy might well be sufficient to assess the resulting networks.

Finally, in the course of this PhD and in conjunction with two IP projects in 2014/2015 and 2015/2016 with students Deck Tan and Marie Wallis, respectively, I had begun to investigate the optimization of setting for phase contrast imaging on the Zeiss/Versa 510, see appendix D. To an extent this has already been performed by Bidola *et al.* [2015]. However, first trials based on an unperfused control muscle suggested that indeed the source-to-sample and sample-to-detector distances for visualisation of the soft tissues in muscle are required to be significantly larger than suggested by Bidola *et al.* [2015]. However, implementation of the Paganin phase retrieval for the datasets obtained on the Versa 510 was not yet successful and it was thus not possible to

compare contrast-to-noise ratios based on the phase retrieved reconstructions and compare the resulting images with the gold standard SLS images. Ideally it will be possible to continue this work and perform the phase retrieval and ultimately publish a paper building upon the work of Bidola *et al.* [2015].

Appendix A

Imaging methods

A.1 Light based methods

A.1.1 Light microscopy

Light microscopy (LM) was the first form of microscopy, introduced around 1600 as a single lens microscope. Since then light microscopy has evolved and reached its interim maximum resolution of $0.2\text{ }\mu\text{m}$ in the 19th century. Recently, methods have been developed to image at so-called *superresolution*, i.e. in the range of tens of nanometers [Murphy & Davidson, 2012].

Different forms of light microscopy exist, i.e., polarising, phase contrast and fluorescence microscopy. These use different techniques to make specimen features visible. Fluorescence microscopy uses autofluorescence or fluorescence of a specific stain to make features visible in different colours, whereas phase-contrast microscopy can detect the different phase-shifts of the light coming through a sample. Similarly, a polarising microscope detects the change in light polarisation [Murphy & Davidson, 2012].

A relatively recent development of LM is the so-called lightsheet fluorescence microscopy (LSFM), where a laser is used to create a green light sheet, which excites a $4\text{ }\mu\text{m}$ thick plane within the sample and detects the fluorescent response [Santi, 2011]. This technique is able to image samples up to 1 cm^3 , which prevents the highly destructive sectioning of samples for viewing with LM. The in-plane resolution of LSFM is close to that of LM, i.e., about $1\text{ }\mu\text{m}$ [Santi, 2011]. Samples need to be auto-fluorescent or be stained with fluorescent markers to be excited and emit a response signal.

A.1.2 Confocal laser scanning microscopy

Confocal laser scanning microscopy (CLSM) is fluorescence microscopy with the advantage that it has a greater depth of field due to the reduction of out of focus light via a pinhole. As CLSM is based on fluorescence, staining of samples is necessary, unless they are autofluorescent. The depth of field is limited to 50-100 μm and a CLSM can achieve a resolution of about 100 nm [Kiessling *et al.*, 2010]. Some studies have reported a penetration depth of up to 1500 μm [Dickie *et al.*, 2006]. CLSM has been used to image the 3D microvasculature in skeletal muscle by Cebasek *et al.* [2010], Murakami *et al.* [2010], Lee & Smith [2008b], Benedict *et al.* [2011] and Janacek *et al.* [2009].

A.1.3 Photon laser scanning microscopy

An imaging technique that has proven to be very useful for the imaging of *in vivo* samples is single-photon and multi-photon laser scanning microscopy (SPLSM, MPLSM) used by Jain *et al.* [2013] to image microvasculature in an area of 150 μm or 600 μm around a tumour. For the imaging, window interfaces are inserted into the mouse. This is necessary, as tissue penetration is only 400-1000 μm [Kiessling *et al.*, 2010]. The resolution that can be obtained with this technique goes down to a few micrometres [Lechleiter *et al.*, 2002].

A.1.4 Optical coherence tomography/optical microangiography

Optical coherence tomography (OCT) is a non-invasive technique based on the interference of two light arms, a sample arm that is reflected from the sample and a reference arm that is reflected by a mirror Leahy [2012]. OCT can be expanded to observe Doppler shift created by moving RBCs (then called DOCT), which is useful for *in vivo* imaging [Vakoc *et al.*, 2012]. The depth limit of an OCT system is usually no more than 2 mm, the interferometer resolution is 5-10 μm and the transverse resolution varies from 5-30 μm , depending on the focused beam size [Vakoc *et al.*, 2012]. OCT and MPLSM are techniques that can be used to complement results obtained by μCT .

A.1.5 Laser speckle contrast imaging

Laser speckle (LS) is based on the effect of interference after illumination of tissue by a laser. The speckle pattern changes with the movement of red blood cells, which causes a blurring of the image, depending on the velocity of the movement. The speckle pattern is then recorded using a camera and colour-coded for visualisation. Penetration depth into tissue is between 500 μm and 1 mm [Hecht *et al.*, 2012]. LS

contrast imaging is also used for *in vivo* imaging, e.g. Rege *et al.* [2012] use laser speckle imaging to observe processes in wound healing angiogenesis. An advantage of this method is that it can measure vessels of diameter down to 10 – 15 μm without the necessity to use a staining agent and the field of view can have a size of 6 mm \times 6 mm [Rege *et al.*, 2012].

A.1.6 Laser doppler flowmetry

Laser Doppler flowmetry (LDF) uses the Doppler frequency shift resulting from scattering of coherent light by moving objects, e.g. moving RBCs in the microcirculation [Leahy, 2012]. In single point LDF, the measurements are taken using optical fibres guiding the light between laser source, tissue and detector. This method is very prone to errors, as minor movement may change the light path within the optical fibres. Similarly, temperature variability can have a noise effect on the measurements [Leahy, 2012]. Furthermore, LDF works with arbitrary units such as flux, which makes quantification of measurements difficult. The measurement depth of LDF depends on the source-detector distance and is usually less than 1 mm. The spatial resolution of LDF is about 10 μm [Michelson *et al.*, 2001]. This makes the actual resolution of different capillaries impossible.

A.2 Electron based methods

A.2.1 Scanning electron microscopy

Scanning electron microscopy (SEM) uses of a high-voltage electron beam, to excite the atoms on the surface of the specimen material. These then emit secondary electrons or backscatter the electrons of the beam, which is recorded by detectors within the SEM. Thereby, a quasi three dimensional image of the surface is created [Thornton, 1968]. High-resolution SEM reach resolutions of about 2 nm [Kiessling *et al.*, 2010]. SEM has often been used for the imaging and quantification of vascular corrosion casts [Konerding *et al.*, 1995], [Konerding *et al.*, 1999], [Konerding *et al.*, 2001], [Folarin *et al.*, 2010].

Recent developments permit three dimensional imaging via SEM, by including an automated diamond knife in the machine. This technique is known as *serial block-face SEM*. As with TEM, ultrathin sections of the sample are cut away from the surface. However, instead of scanning the section cut, it is disposed of and the new specimen surface is scanned [Page, 2014].

A.2.2 Transmission electron microscopy

Transmission electron microscopy (TEM) is based on illumination of the specimen by an electron beam in comparison to normal light in LM. Due to scattering of the electrons when hitting a material of high atomic Z-number within the sample or them just passing through the sample, contrast is achieved, as only the electrons passing straight through an aperture behind the specimen are collected by the objective lens. For this, the samples must be relatively thin cut, i.e. about 100 nm at the most [Kiessling *et al.*, 2010], using an Ultramicrotome. TEM yields a much better resolutions than LM, i.e., of about 0.2 nm, which makes it very useful for the scanning of very small features within the endothelial cell wall, e.g., the vesicles. High-resolution TEM was later introduced and permits a resolution below 50 pm. However, the sensitivity of the instruments is very high and requires special conditions, such that no vibrations and external magnetic fields interfere when the machine is operated [Kiessling *et al.*, 2010].

The disadvantage of TEM is the lengthy procedure of cutting ultra-thin sections.

A.3 X-ray based methods

A.3.1 Micro-computed tomography

Micro-computed tomography (μ CT) is a non-destructive 3D imaging techniques that makes use of the different X-ray absorption coefficients of different materials. Images are obtained at 360 degrees of a sample, which are then reconstructed to form an volumetric representation of the sample [Landis & Keane, 2010].

The advantages of μ CT are its non-destructive nature, the low resolution that can be obtained and a relative scanning speed when compared to other 3D imaging techniques [Kiessling *et al.*, 2010]. μ CT can reach a resolution of 700 nm which can be lowered further when using synchrotron-based μ CT (SR CT), where the X-ray spectrum is monochromatic. Even higher resolutions of tens of nanometers can be achieved using so-called X-ray nanotomography (nano-CT). This is based on the same principles, but usually involves optical elements, such as Kirkpatrick-Baez (KB) mirrors or Bragg multiplier systems between source and sample, to create a magnified image on the detector [Withers, 2007]. A KB mirror system is for example implemented at the European Synchrotron Radiation Facility (ESRF) at beamline ID16A-NI, where imaging down to 10 nm image resolution at 17 keV is possible [Hesse *et al.*, 2015, ESR, 2016].

A.4 Magnetic pulse based methods

A.4.1 Micro-magnetic resonance imaging

Micro-magnetic resonance imaging (μ MRI) is based on the alignment of a proton's spin when subjected to a static magnetic field. If the magnetic field is pulsed the spin orientation changes and the spin changes back to the initial orientation with a delay to the magnetic field. This delay, called spin echo, can be measured as a change in voltage in the magnetic coils and is different for different types of material. Usage of magnetic field gradients then enables the localization of respective tissues and a three dimensional image is reconstructed using a Fourier transform based backprojection algorithm.

μ -MRI has high soft-tissue contrast [Morishige *et al.*, 2010], however, the spatial resolution is limited to about 60 μ m [Kim *et al.*, 2012]. Also, imaging is relatively slow in comparison to other techniques [Kiessling *et al.*, 2010]. Its advantage in comparison to μ CT is its suitability for *in vivo* imaging, as no radiation is present therefore no harm is done to the animal unless ferromagnetic objects are present.

A.5 Positron based methods

A.5.1 Positron emission tomography

Micro positron emission tomography (micro-PET) is based on the emission of positrons from a radioactive material injected into the tissue. These travel through the tissue and collide with electrons, thereby emitting a pair of photons which can be recorded by detectors. However, due to the short travel distance of the positrons, the spatial resolution of micro-PET is limited to about 2 mm [Leahy, 2012]. PET is often used jointly with μ CT or in its more advanced form of single photon emission computed tomography (SPECT), which has a slightly better resolution of 1 mm [Leahy, 2012]. This combination of imaging methods allows for the observation of trafficking of substances and particles through the body [Kircher *et al.*, 2008], [Nahrendorf *et al.*, 2009].

A.6 Acoustic waves based methods

A.6.1 Photoacoustic tomography

In photoacoustic tomography (PAT) a short-pulsed laser beam excites the RBCs, which expand through the increase in temperature and thereby emit ultrasonic waves of high

frequency [Leahy, 2012]. From these waves, the RBCs can be localized and a 3D image of the microcirculation can be reconstructed. However, ultrasonic waves are scattered by tissue, thereby limiting the depth of field to about 1 mm. The lateral resolution of PAT is about 50 μm [Leahy, 2012]. Laufer *et al.* [2012] uses PAT for preclinical *in vivo* imaging of tumour vasculature, as it allows the dynamic observation of tumour growth.

Appendix B

Histology protocols

The following protocols were provided by the histochemistry research unit of the University of Southampton and are copyrighted.

B.1 H&E stain

Method:

1. Dewax sections in clearene, hydrate through graded alcohols to water
2. Wash in distilled water for 5 minutes
3. Stain in Mayers Haematoxylin for 5 minutes
4. "Blue" in running tap water for 5 minutes
5. Stain in eosin for 5 minutes
6. Rinse very briefly in distilled water
7. Dehydrate through alcohols (1min each), clear in clearene (2mins each) and mount in pertex

Results:

Nuclei - Blue/Black

Cytoplasm - Varying shades of pink

Muscle Fibres - Deep pinky red

Red blood cells, eosinophils - orange red

Fibrin - deep red

B.2 Avidin biotin-peroxidase technique for paraffin sections

Method: Includes avidin biotin and culture medium blocking stages. All stages are at room temperature unless otherwise stated.

1. Deparaffinise sections in clearane (2x10mins) and rehydrate through graded alcohols (3x5mins) to 70%.
2. Inhibit endogenous peroxidase with 0.5% hydrogen peroxide in methanol (make fresh), 10 mins.
3. Wash TBS 3x2mins.
4. Perform microwave pretreatment (see B.3) for antigen retrieval procedure for primary antibody.
5. Drain slides and apply avidin solution, 20mins.
6. Rinse TBS, 3x2mins.
7. Drain slides and apply biotin solution, 20mins.
8. Rinse TBS, 3x2mins.
9. Drain slides and apply culture medium, 20mins.
10. Drain slides and apply primary antibodies at appropriate dilutions, incubate overnight at 4°C.
11. Wash TBS, 3x5mins.
12. Drain slides and apply biotinylated second stage antibodies at appropriate dilutions, 30mins.
13. Wash TBS, 3x5mins.
14. Drain slides and apply avidin biotin-peroxidase complexes at appropriate dilution, 30mins.
15. Wash TBS, 3x5mins.
16. Drain slides and apply DAB, 5mins.
17. Rinse in TBS.
18. Wash in running tap water, 5mins.
19. Counterstain sections with Mayer's haematoxylin.
20. Blue sections in running tap water, 5mins.
21. Dehydrate through graded alcohols (3x1min), clear in clearane (3x2mins) and mount in pertex.

B.3 Microwave pretreatment

Buffer Formula - 0.01 M Citrate buffer pH 6.0

Citric acid crystals 2.1 g

Distilled Water 1000 ml

Mix and adjust pH to 6.0 with 1M sodium hydroxide (approximate 25 ml)

Method:

1. Fill three plastic staining racks with 24 slides (leaving one gap) and place each in a polythene box. To maintain a constant load 3 racks and boxes are always used. Use blank slides if necessary
2. Fill each box with 330 ml of prepared buffer Place the perforated lid firmly on the box.
3. Place the 3 boxes in the microwave, placing each one at the edge of the plate, evenly spaced with a small gap between each box.
4. Set the microwave to 25 minutes and 50% power. Start and allow to run.
5. When the time has elapsed, remove one box at a time. CARE AS IT WILL BE HOT - WEAR INSULATED GLOVES AND FACE SHIELD. Remove the lid and fill quickly with cold running water. Leave all 3 racks in running water for 2-3 minutes.
6. Place the slides back in the staining trays, wash in TBS 2x5mins, before continuing with the IHC protocol.

B.4 Martius yellow scarlet blue (MSB) trichrome

Method:

1. Dewax sections in clearane, hydrate through graded alcohols to water
2. Stain with Weigert's haematoxylin, 5mins.
3. Blue in running tap water, 5mins.
4. Rinse in 95% alcohol.
5. Stain with Martius Yellow, 2mins.
6. Rinse in water.

7. Stain with Crystal Ponceau, 10mins.
8. Wash in water.
9. Treat with Phosphotungstic acid solution, 5mins.
10. Stain with aniline blue, 5mins.
11. Wash and blot dry.
12. Dehydrate through alcohols (1min each), clear in clearane (2mins each) and mount in pertex.

Appendix C

Testing the Influence of Tortuosity

C.1 Hypothesis

Based on the study of the work of Al-Shammari *et al.* [2012], the question of how realistic two-dimensional modelling of tissue oxygenation was posed. Clearly, if the assumption holds that all blood vessels are straight and parallel to each other, then there is no difference in a two-dimensional and a three-dimensional model if the transverse section the 2D model is based on was cut perfectly perpendicular to the blood vessels. However, the more tortuous the blood vessels are, the more the nutrient flow in z-direction may have to be taken into account. To our knowledge only little work has been performed towards studying the difference in nutrient diffusion patterns for different vessel tortuosities. This was done by Goldman & Popel [2000] who investigated the influence of tortuosity and anastomoses on tissue oxygenation and the work of Penta & Ambrosi [2015] who investigated the influence of tortuosity on hydraulic conductivity and the consequences for drug delivery in cancerous networks. Goldman & Popel [2000] found that a tortuous network resulted in a slightly higher tissue PO_2 than straight networks, i.e., 21 ± 5.67 as opposed to 20 ± 5.6 mmHg, which was not a significant difference. However, the authors looked at a set number of parallel blood vessels with only one kind of tortuosity, which a sinusoidal wave of $50 \mu\text{m}$ wavelength and $8 \mu\text{m}$ amplitude. Penta & Ambrosi [2015] showed a significant decrease (50%) of drug concentration for tortuous vessel networks in comparison to straight networks.

Therefore, it was of interest to investigate the difference in tissue oxygenation for different metabolic consumption rates and a number of different vessel tortuosities.

C.2 Model

A blood vessel was modelled with varying tortuosity within a tissue segment. Table C.1 describes the parameters that were used to define the model. The blood vessel tortuosity was described by a parametric sinusoidal wave:

$$\begin{pmatrix} x \\ y \\ z \end{pmatrix} = \begin{pmatrix} a \sin(bs) \\ 0 \\ s \end{pmatrix} \quad \text{with } s \in [H1 - H2, \dots, H2]. \quad (\text{C.1})$$

This parametric curve gives the centre point for a circle with radius $d/2$ that is swept along it in z -direction, which results in a tortuous blood vessel. The tissue segment was modelled by a cylinder of height H with hexagonal base. The side length of the cylinder is given in table C.1. The blood vessel was placed in the middle of the cylinder. The resulting geometry is shown in figure C.1.

The choice of the hexagonal form was based on the hexagonal distribution of blood vessels within muscle tissue and all parameters were chosen to reflect physiological values.

In order to compare the simulation results to those done on 2D sections, the same simulations were performed on a cross-section of the blood vessel and tissue geometry. The height QZ of this cross-section varies along the height of the cylinder. Two types of equations have been solved, one simple diffusion equation (7.15) and one diffusion-reaction equation (7.6). The boundary conditions were as described for the image-based model in chapter 7, i.e. equations (7.9), (7.10). Both the 3D and the 2D model could be solved using just one COMSOL model, as the cross-section can be defined by including a *Component* model that is created by intersecting 3D model and a pre-defined workplane (at height QZ). The parameters c , a and QZ , as seen in table C.1, were changed after each simulation, so that all simulations for all parameter combinations could be run as a batch simulation. This was done by defining a *parametric sweep* in the study. However, due to extensive memory requirements of the program it was necessary to run separate programs for different c .

C.2.1 Results

The model was run for $c = 1, \dots, 4$ for $t \in [0, \dots, 2]$ s and a parameter sweep over a and QZ as in table C.1. The graphical results for $a = 3$ and $QZ = 15\mu\text{m}$ for the 3D and 2D model at the start and end time are displayed in figures C.2 and C.4(a). Visually, no difference can be observed (note the constant legend). However, when integrating the concentration over the volume or intersection surfaces (and correcting the result for the missing third dimension) and comparing the differences at all time steps and for different a , as shown in C.4, it becomes apparent that the increasing amplitude plays a

Variable	Value [unit]	Description
H	100 [μm]	height
b	$2\pi \frac{c}{H}$	sinus parameter
d	8.7 [μm]	vessel diameter
$hexag$	$10 + \frac{d}{2}$ [μm]	side length of hexagon
c	[1, ..., 4]	number of curves
a	[0, 0.5, ..., 3]	sinus amplitude
$H2$	$H + 10$ [μm]	
$H1$	H [μm]	
QZ	[0, $H/20$, ..., H]	height of cross-section

Table C.1: **Geometric parameters used in the modelling of the influence of tortuosity on tissue oxygenation.** A cylindric capillary is created within a hexagonal tissue segment. Tortuosity in the vessel is induced in the form of sinusoidal oscillations.

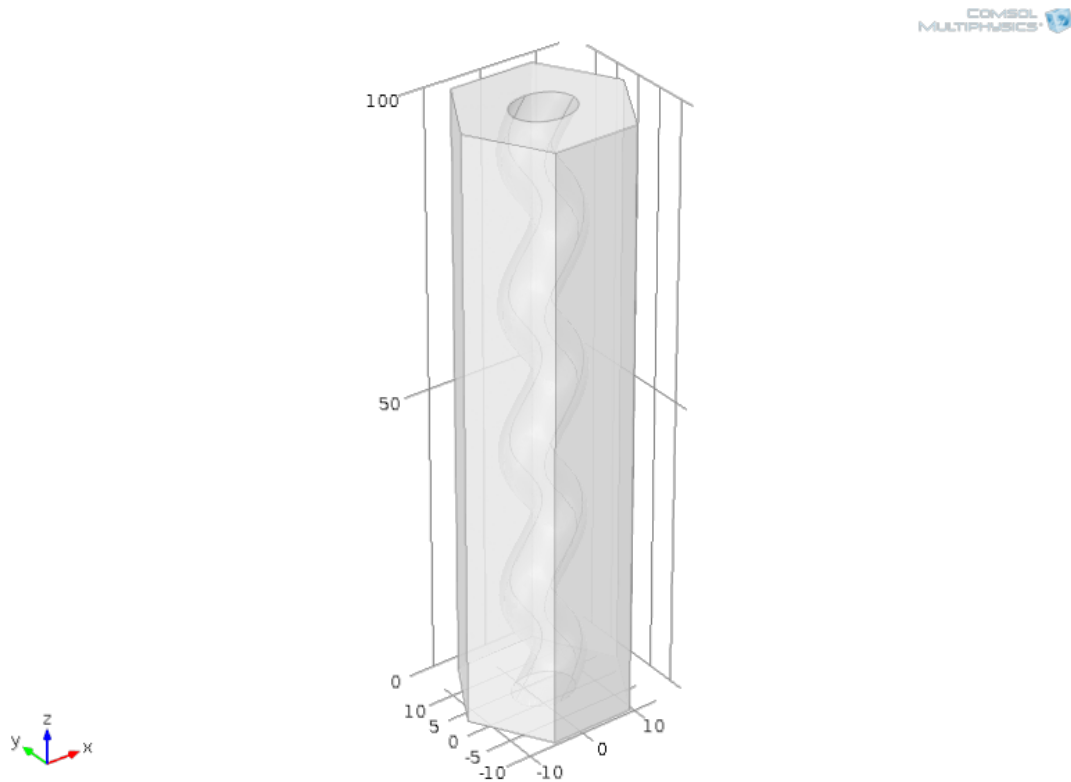


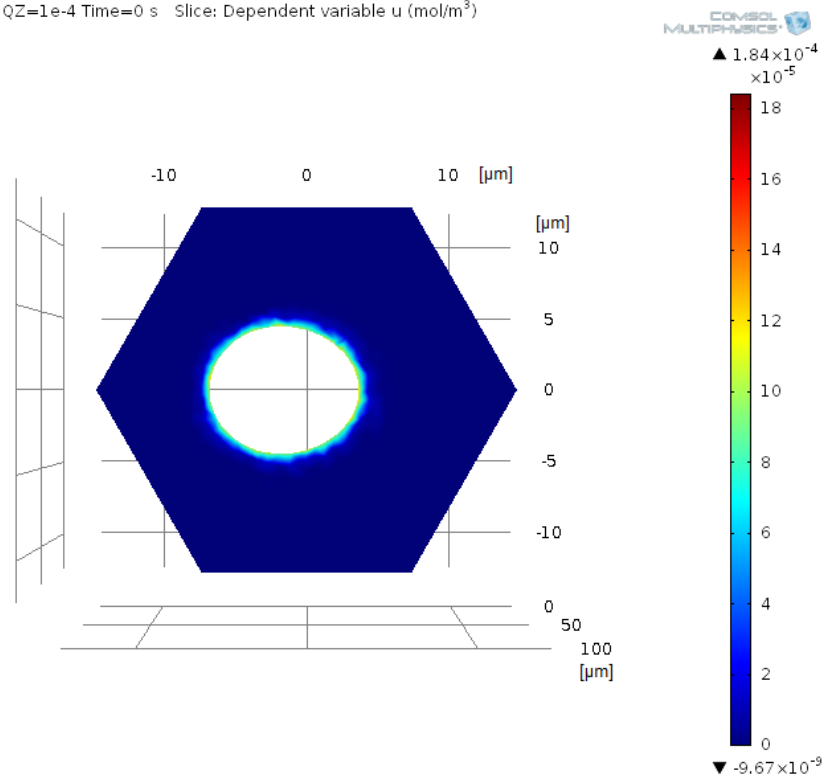
Figure C.1: **Three-dimensional model geometry of the tortuous blood vessel in a hexagonal tissue segment, for $a = 3$, $c = 4$.**

role for the time it takes for the muscle to be fully perfused and also in the difference between 3D and 2D case. The 2D surface is perfused faster than the 3D volume for all $c = 1, \dots, 4$. In all cases and for all times the 3D concentration in the tissue is slightly higher than in the 2D case, this varies between 0.66% and 5.96% from $c = 1$ and $a = 1$ and $c = 4$ and $a = 3$ for $t = 0$ in both cases. The maximum error once the solution has reached its steady state is 0.07% for $c = 4$ and $a = 3$.

C.2.2 Discussion

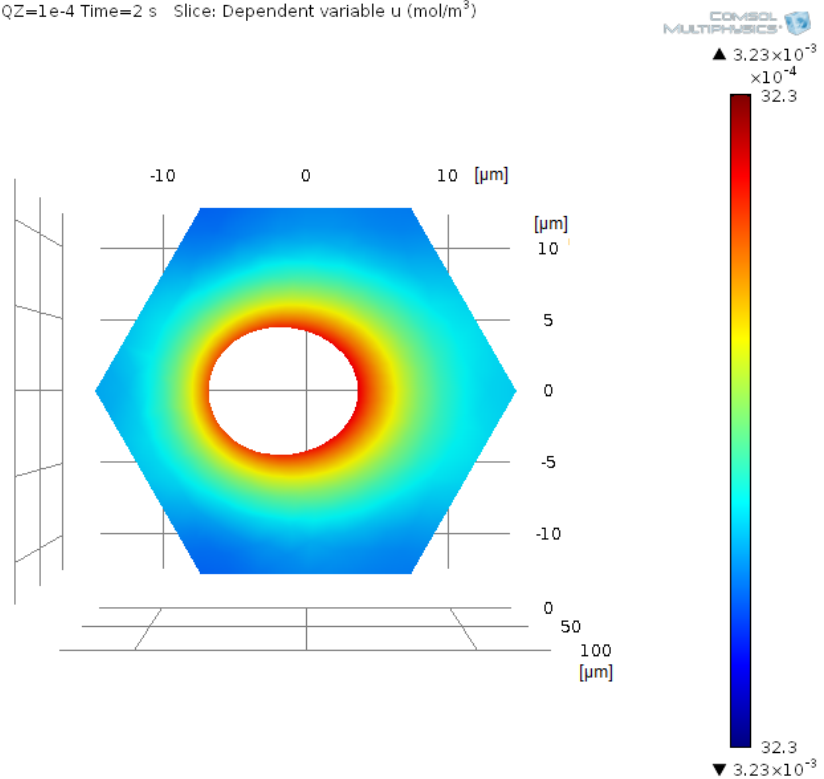
The results for $c = 1, \dots, 4$ for the employed tortuosity model have been presented. As would be expected, the difference between 2D and 3D case increase with increasing a and c and diminish as the solutions reaches the steady case. It is desirable to extend the model to include different consumption rates of oxygen, i.e., consumption at rest and at exercise, which we expect to broaden the differences between 2D and 3D case even further.

a=3, QZ=1e-4 Time=0 s Slice: Dependent variable u (mol/m³)



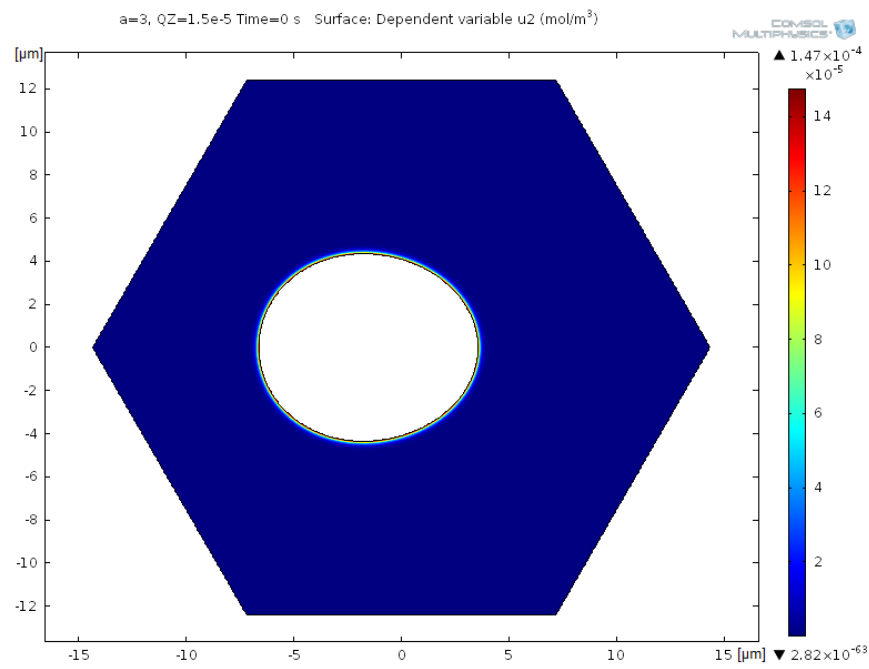
(a)

a=3, QZ=1e-4 Time=2 s Slice: Dependent variable u (mol/m³)

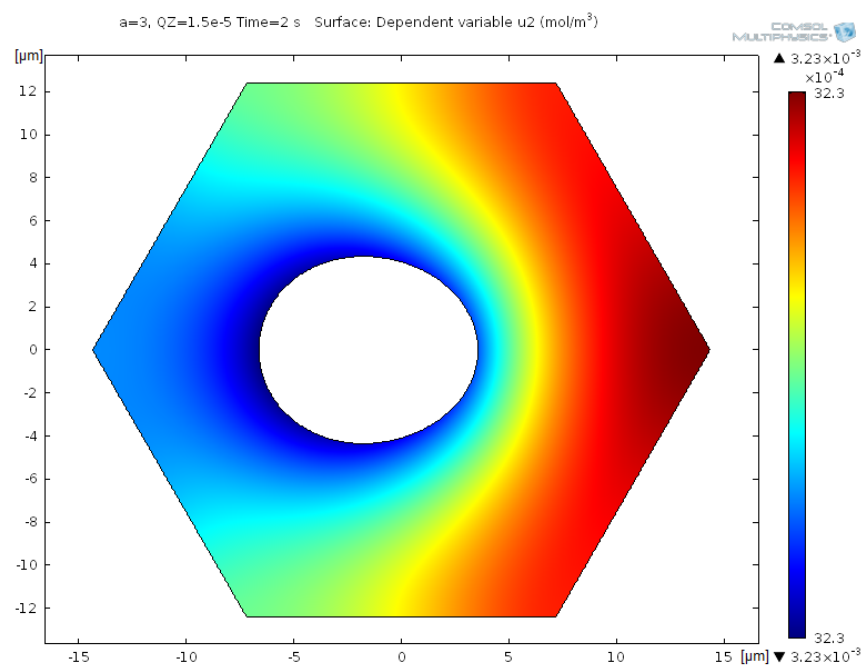


(b)

Figure C.2: 3D results for $t = 0$ and $t = 2$ for $c = 4$.

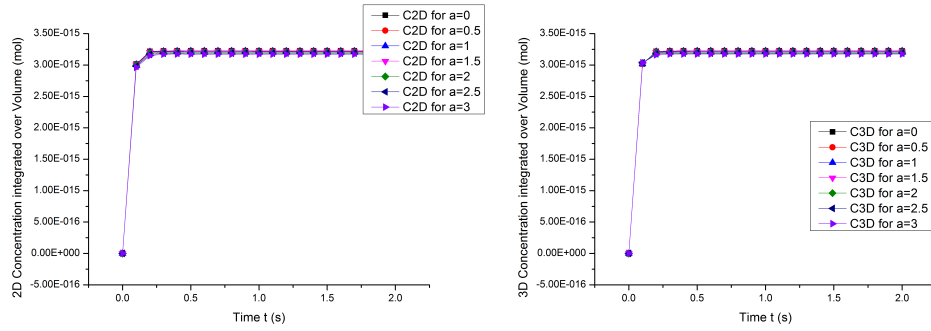


(a)

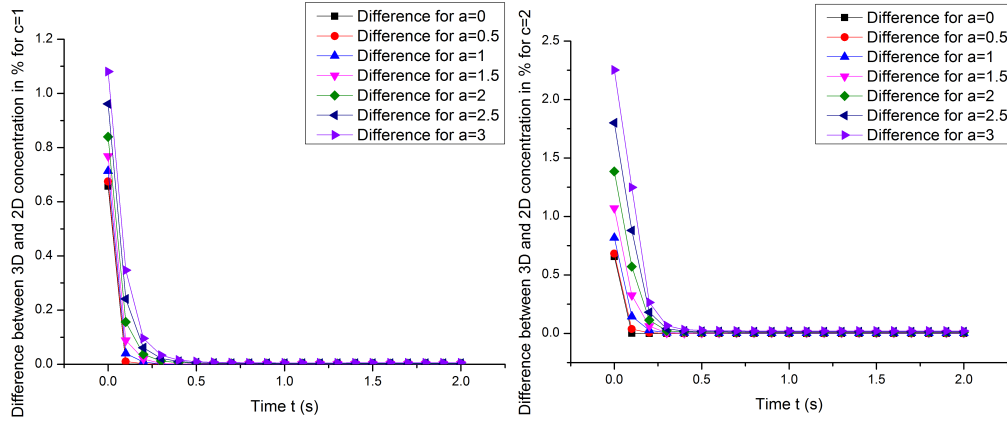


(b)

Figure C.3: 2D results for $t = 0$ and $t = 2$ for $c = 4$.

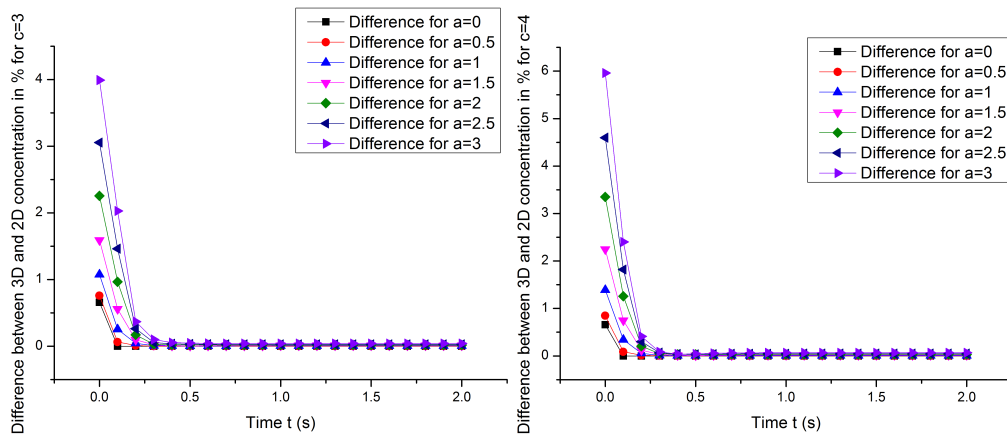


(a) Surface integration of 2D concentration for $c = 4$ (b) Surface integration of 3D concentration for $c = 4$



(c) $c = 1$

(d) $c = 2$



(e) $c = 3$

(f) $c = 4$

Figure C.4: **Model evaluation for $c = 1$ and $c = 4$.** With increasing a and increasing c the difference between 3D and 2D case increases before both reach the steady state solution.

Appendix D

Phase contrast imaging using the Zeiss Versa 510

As synchrotron access is limited and by application only it is desirable to enable lab-based phase contrast μ CT imaging of comparable quality. To this end, initial experiments have been performed on the Zeiss/Xradia Versa 510 system.

Zeiss/Xradia recommends imaging at 40kV/3W using the 4X objective for best phase contrast results. Therefore, an unperfused soleus muscle of the control group (CC) was imaged at 40kV/3W with an exposure time of 27 s and 1901 projections. Figure D.1 shows a slice of the resulting scan. It is obvious that the scanning settings were imperfect, especially the propagation distances were very small, when compared to the synchrotron, see table D.1. However, this could not easily be increased at the same energy as otherwise the exposure time rises strongly which results in very long scanning times. Further consultation with Zeiss/Xradia then led us to perform a short study on source-to-sample and sample-to-detector distances as well as on energies. In order to be able to compare the distances between the different systems, one needs to keep in mind that the synchrotron source is significantly more brilliant, i.e. has a higher photon flux, than the lab based system. The relationship between the sample-to-detector distance sd_S at the synchrotron and the Versa's source-to-sample ss_V and sample-to-detector sd_V distance can be related by the equation (from the Fresnel scaling theorem Paganin *et al.* [2002]):

$$sd_S = \frac{ss_V \cdot sd_V}{ss_V + sd_V} \quad (D.1)$$

Scanning was tested at 80kV and 7W with 2001 projections and the different distances displayed in table D.1. The corresponding slices from the reconstructions are shown in figure D.2. Visually it appears that the best phase-contrast results are obtained at the highest propagation distance. This distance is similar to the distance chosen for

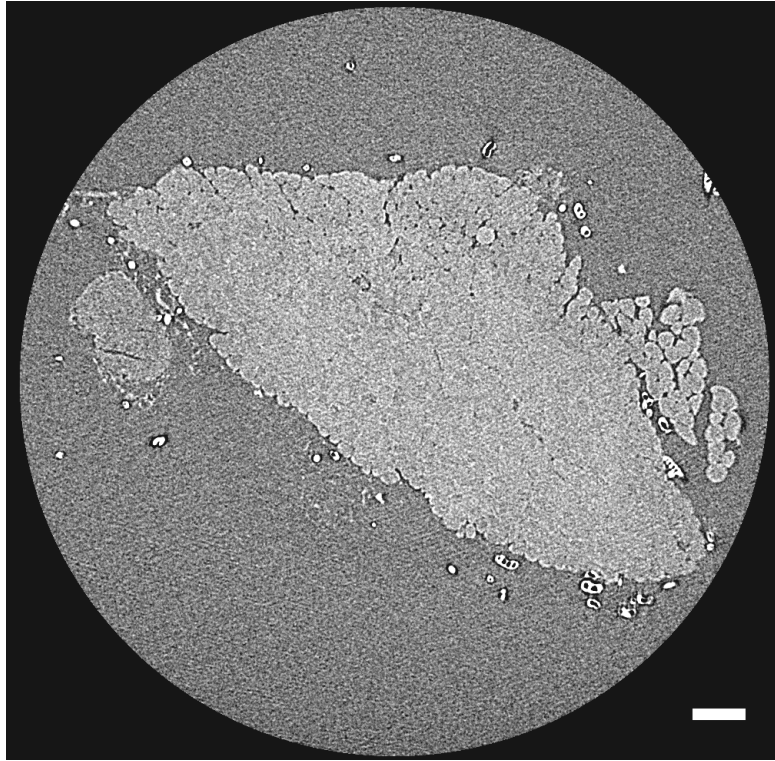


Figure D.1: **Slice of reconstructed volume of first phase contrast test using the Versa 510 system.** The tissue contrast is very low. The only feature discernible is a muscle spindle. The scale bar represents 100 μm .

Scan	Energy [kV]	Power [W]	Source-RA distance [mm]	Detector-RA distance [mm]	Synchrotron distance [mm]	pixel size [μm]
0	40	3	28.11	104.00	22.13	1.43
1	80	7	45.00	163.99	35.31	1.45
2	80	7	60.00	220.00	47.14	1.44
3	80	7	75.00	275.01	58.93	1.44

Table D.1: **Scan settings for Versa 510 distance trial.** The corresponding Synchrotron distances were computed using Equation D.1.

scanning at the SLS (60 mm), see also figure D.3 where intensity profile over fringes were displayed. However, some streak artefacts are visible in figures D.2(b) and D.2(c). This is due to photon starvation, as relatively low exposure times were used (11, 15 and 20 seconds, respectively). This also explains why SNR and CNR were best at the lowest propagation distance, see table D.2.

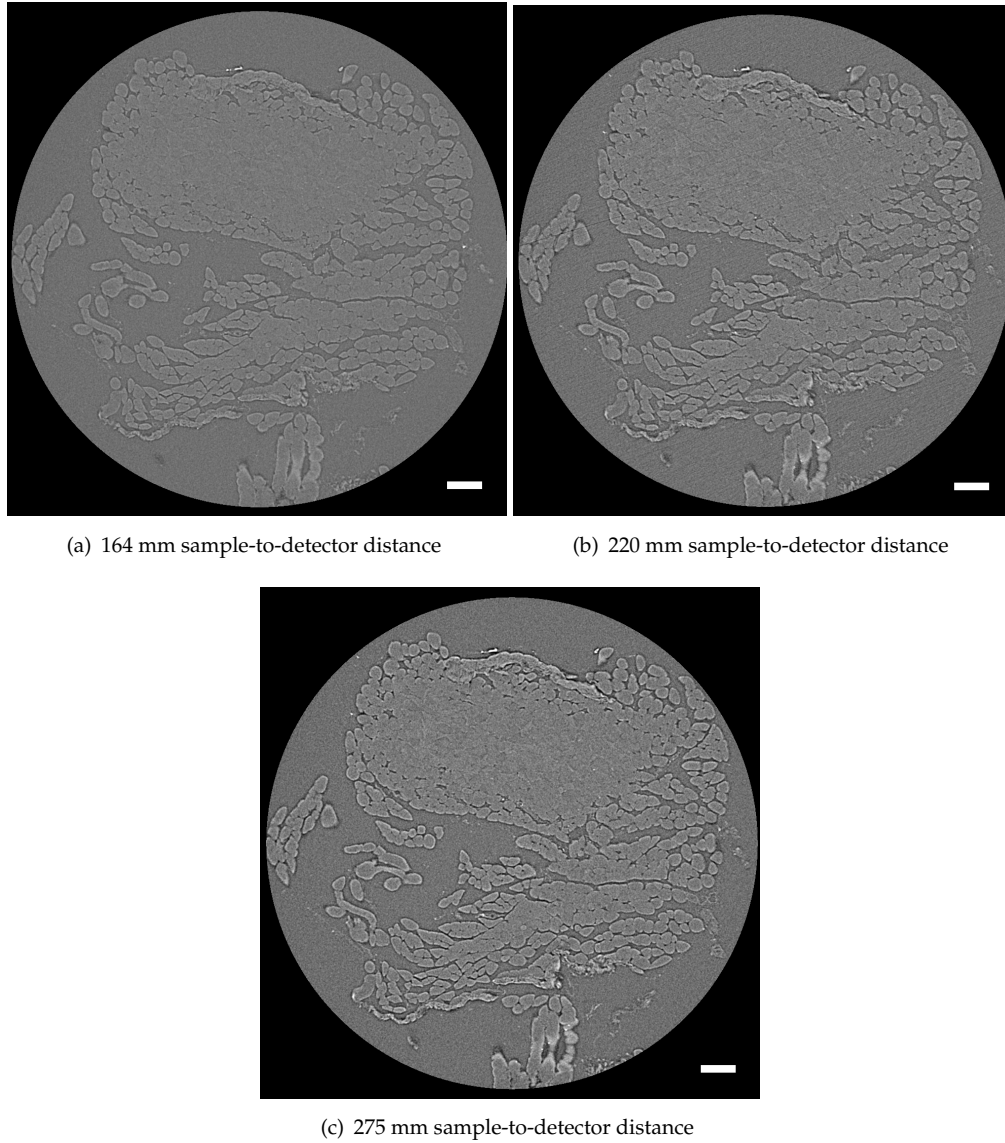


Figure D.2: **Slices of distance trial on the Xradia Versa 510 system.** The phase-contrast visually increases with the further distance. However, some streak artifacts are visible in D.2(b) and D.2(c). This is probably due to photon starvation. Scale bars are 100 μm .

Detector distance [mm]	SNR	CNR
164	21.73	2.36
220	10.24	1.14
275	14.73	1.13

Table D.2: **SNR and CNR for the Versa distance trial.** Computed according to Equations (4.3) and (4.4). The highest values are apparent at a sample-to-detector distance of 164 mm, which is the shortest distance studied.

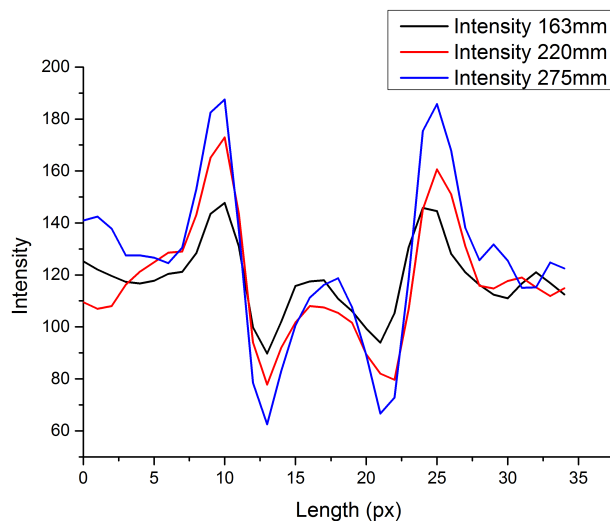


Figure D.3: **Intensity profile for comparison of edge-enhancement for different sample-to-detector distances.** Clearly, the intensity of the edge-enhancement increases with propagation distance.

D.1 Repeated experiments as by Bidola *et al.* [2015]

In the context of an IP project by student Marie Wallis further repeated experiments as conducted by Bidola *et al.* [2015] in an attempt to recreate results. The experimental work presented in this section was performed by Berit Zeller-Plumhoff, whilst the data analysis was performed by Marie Wallis after consultation with Berit Zeller-Plumhoff. The work was presented in the IP report submitted by Marie Wallis.

As in Bidola *et al.* [2015] a 0.5mm thick teflon sheet was to determine the mean energy of the X-ray beam when imaging at a voltage of 40keV. This mean energy was found to be 12.2keV in contrast to 13.1keV determined by [Bidola *et al.*, 2015]. The difference may be due to slight differences in the source design. The CNR on radiographs of the teflon sheet for different source-to-sample and sample-to-detector distances as in Experiment II in [Bidola *et al.*, 2015] was computed. Additionally the influence of increasing the exposure time was tested. The exposure time was chosen so that the photon count in flat field images at all distances remained similar and increased with the square of the change in distance, i.e., doubling the distance led to quadrupling the exposure time. See table D.3 for the different source to sample distances and exposure times.

Figure D.4 shows the important influence that the exposure time has in this case on the CNR. If adjusted the stark decrease of the CNR is counterweighted and the CNR remains on a high level.

Position	Source-to-sample distance [mm]	Sample-to-detector distance [mm]	Exposure time [s]
RI	10	60	5
RII	20	120	5
RIII	40	240	5
RII _{adj}	20	120	20
RIII _{adj}	40	240	82

Table D.3: **Source-to-sample and sample-to-detector distances chosen for the experiments, as in experiment I from Bidola *et al.* [2015].** The exposure time was adjusted for the longer propagation distances RII and RIII to account for the decrease of photon counts on the detector.

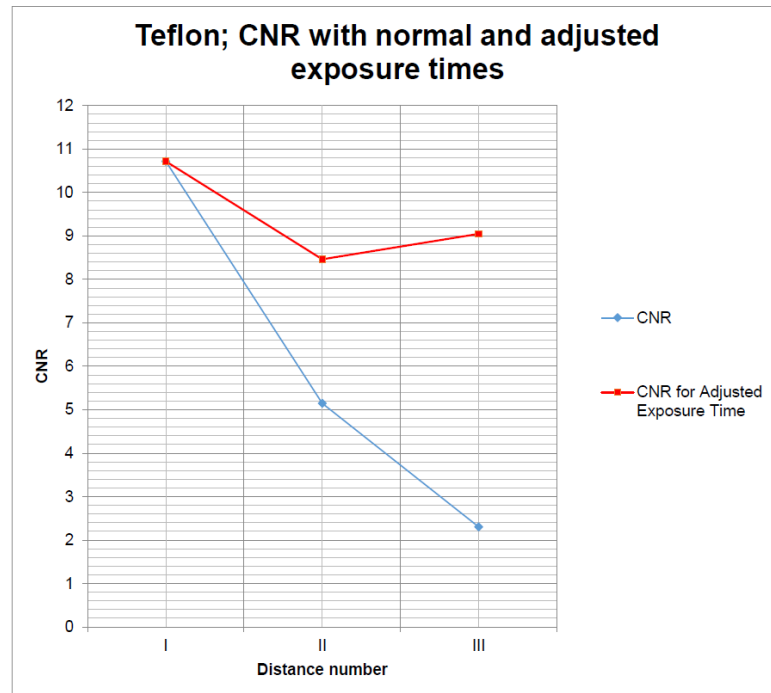


Figure D.4: **CNR of radiographs of teflon sheet as in experiment II in [Bidola *et al.*, 2015].** Whilst the CNR decreases starkly at constant exposure time for increasing source-to-sample and sample-to-detector distances it remains high if the exposure time is adjusted for the changing distances. This image was taken from the IP report submitted by Marie Wallis.

Tomographic imaging of an unperfused mouse muscle was conducted using scanning parameters as in experiment II in [Bidola *et al.*, 2015], with and without adjusted exposure times. Unfortunately, implementation of phase retrieval failed in the time available for the IP project and has not yet been enabled. However, simple FBP based reconstruction was performed and can be visually compared to the phase retrieved images from the SLS, see figures D.5 and D.6 for a zoom onto soft tissue features. It can clearly be seen that features such as neuromuscular spindles and nerves can be observed, but only at distance RIII with adjusted exposure time (RIII_{adj}).

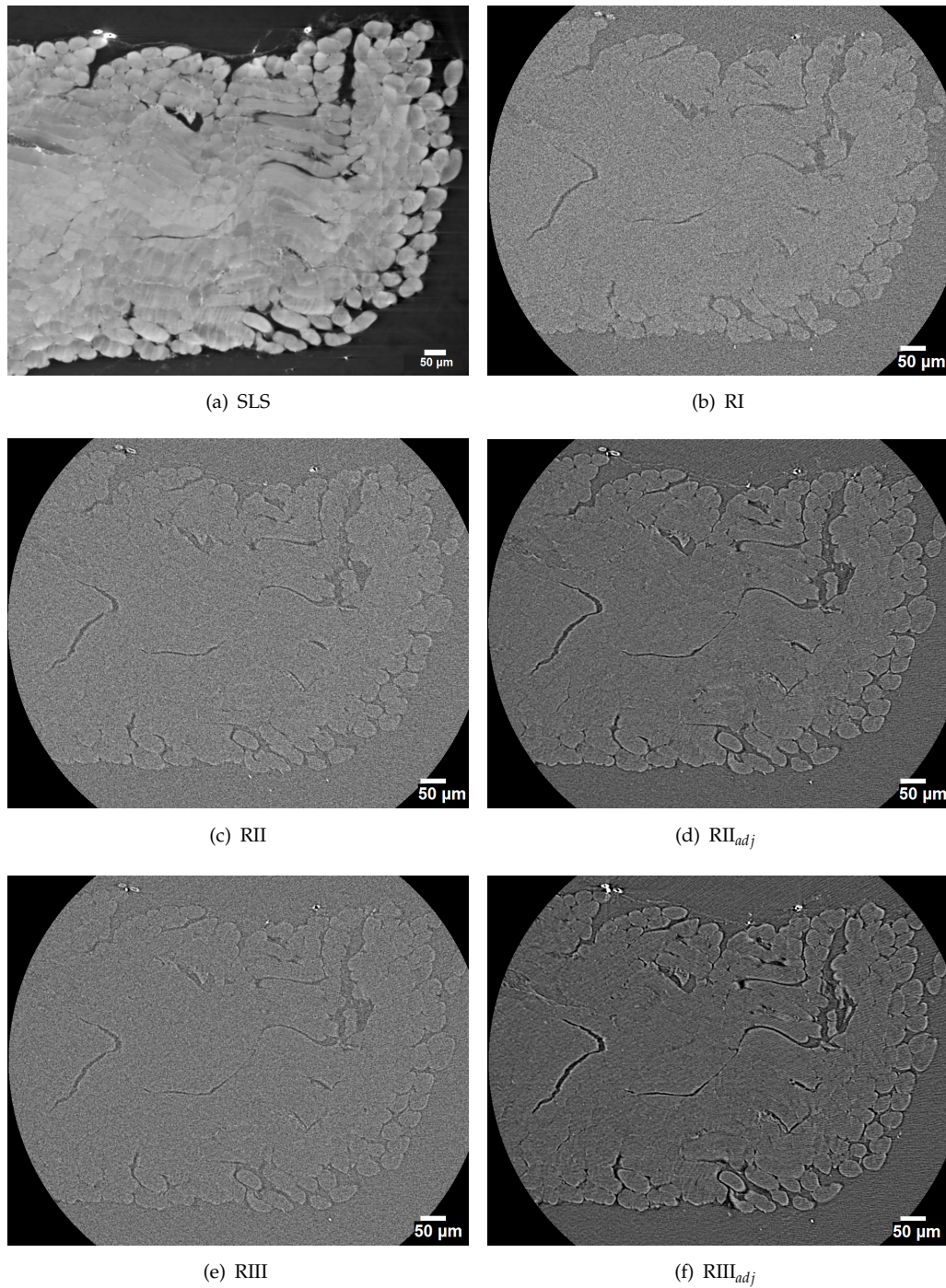


Figure D.5: Comparison of correlated slices of phase contrast-based tomography obtained at the synchrotron (D.5(a)) and for different propagation distances on the Versa 510 system. Propagation distances were increasing from RI (D.5(b)) to RII (D.5(c)) and RIII (D.5(e)) as in Bidola *et al.* [2015], see table D.3. Subfigures D.5(d)) and D.5(f) are for distances RII and RIII, respectively, with adjusted exposure time. Scale bars represent 50 μm .

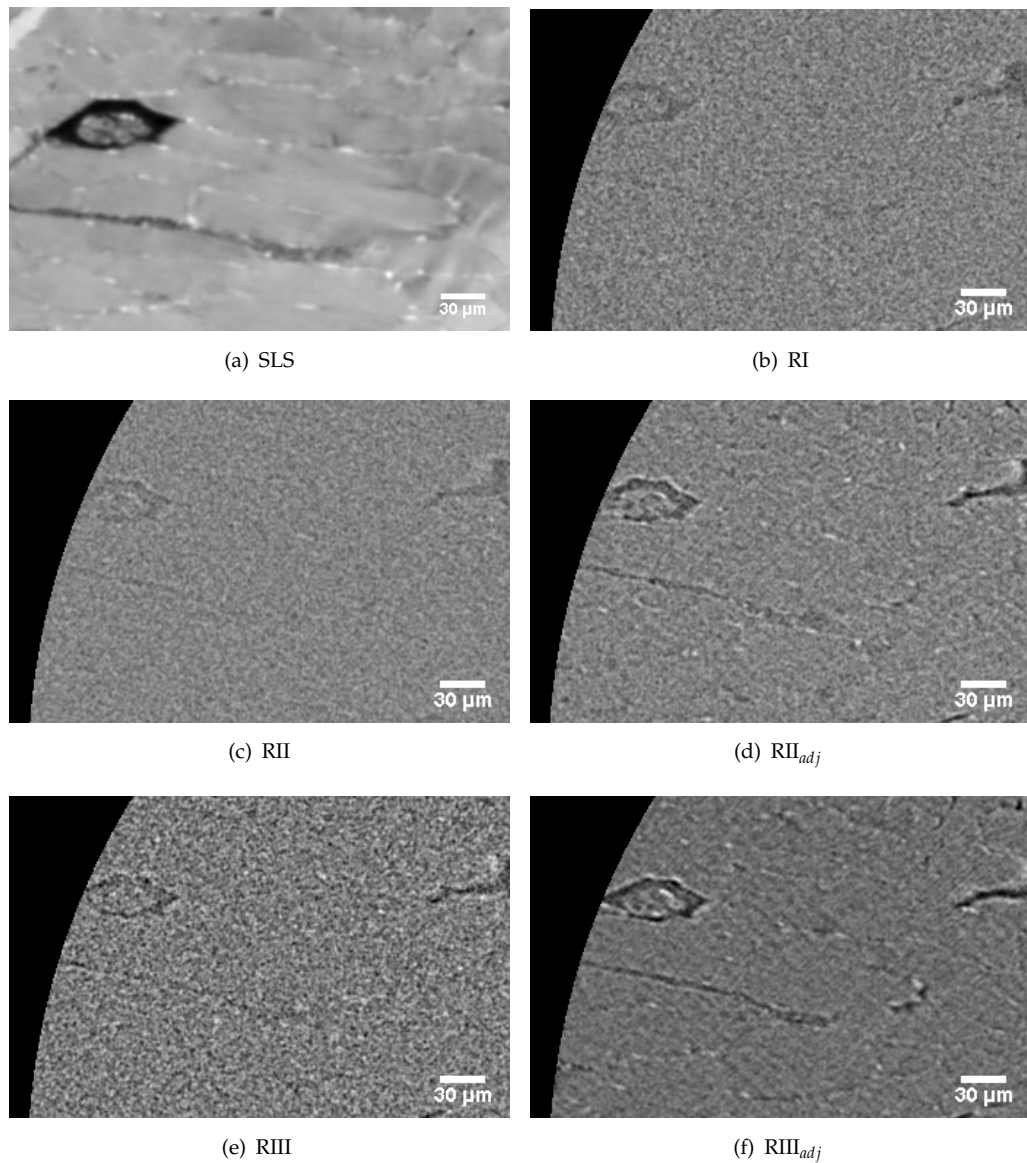


Figure D.6: **Zoom onto nerve and muscle spindle in correlated slices in figure D.5 from SLS and Versa 510 systems.** Soft tissue contrast is high in the SLS image, however, in the images obtained on the Versa 510 system it is only possible to differentiate muscle tissue, nerves and muscle spindles at distance RIII with adjusted exposure time (RIII_{adj}).

Bibliography

2013 (09.2013). *3D Model of Diamond Light Source*.

2016. *Henke Database*.

2016. <http://www.openfoam.com/>.

2016. *ID16A Beamline specifications*.

2016. *X-ray worx*.

Ainge, H., Thompson, C., Ozanne, S. E., & Rooney, K. B. 2011. A systematic review on animal models of maternal high fat feeding and offspring glycaemic control. *Int J Obes (Lond)*, **35**(3), 325–335.

Al-Shammari, A. A., Gaffney, E. A., & Egginton, S. 2012. Re-evaluating the Use of Voronoi Tessellations in the Assessment of Oxygen Supply from Capillaries in Muscle. *Bulletin of Mathematical Biology*, **74**(9), 2204–2231.

Al-Shammari, A. A., Gaffney, E. A., & Egginton, S. 2014. Modelling capillary oxygen supply capacity in mixed muscles: capillary domains revisited. *J Theor Biol*, **356**, 47–61.

Alberts, Bruce. 2002. *Molecular biology of the cell*. 4th edn. New York: Garland Science.

Als-Nielsen, J., & McMorrow, Des. 2011. *Elements of modern X-ray physics*. [electronic resource] / Jens Als-Nielsen, Des McMorrow. ill. (some col.) Electronic reproduction. Palo Alto, Calif. : ebrary, 2011.

Armitage, J. A., Khan, I. Y., Taylor, P. D., Nathanielsz, P. W., & Poston, L. 2004. Developmental programming of the metabolic syndrome by maternal nutritional imbalance: how strong is the evidence from experimental models in mammals? *J Physiol*, **561**(Pt 2), 355–77.

Ashton, J. R., West, J. L., & Badea, C. T. 2015. In vivo small animal micro-CT using nanoparticle contrast agents. *Front Pharmacol*, **6**, 256.

Atwood, R. C., Lee, P. D., Konerding, M. A., Rockett, P., & Mitchell, C. A. 2010. Quantitation of Microcomputed Tomography-Imaged Ocular Microvasculature. *Microcirculation*, **17**(1), 59–68.

- Audet, G. N., Fulks, D., Stricker, J. C., & Olfert, I. M. 2013. Chronic delivery of a thrombospondin-1 mimetic decreases skeletal muscle capillarity in mice. *PLoS One*, **8**(2), e55953.
- Badea, C. T., Johnston, S., Johnson, B., Lin, M., Hedlund, L. W., & Johnson, G. A. 2008. A dual micro-CT system for small animal imaging - art. no. 691342. *Medical Imaging 2008: Physics of Medical Imaging, Pts 1-3*, **6913**, 91342–91342.
- Bancroft, John D., & Gamble, Marilyn. 2008. *Theory and practice of histological techniques*. 6th edn. Philadelphia: Churchill Livingstone Elsevier.
- Banks, R. W. 2006. An allometric analysis of the number of muscle spindles in mammalian skeletal muscles. *J Anat*, **208**(6), 753–68.
- Bauer, T. A., Reusch, J. E., Levi, M., & Regensteiner, J. G. 2007. Skeletal muscle deoxygenation after the onset of moderate exercise suggests slowed microvascular blood flow kinetics in type 2 diabetes. *Diabetes Care*, **30**(11), 2880–5.
- Bayol, S. A., Simbi, B. H., & Stickland, N. C. 2005. A maternal cafeteria diet during gestation and lactation promotes adiposity and impairs skeletal muscle development and metabolism in rat offspring at weaning. *J Physiol*, **567**(Pt 3), 951–61.
- Bayol, S. A., Macharia, R., Farrington, S. J., Simbi, B. H., & Stickland, N. C. 2009. Evidence that a maternal "junk food" diet during pregnancy and lactation can reduce muscle force in offspring. *Eur J Nutr*, **48**(1), 62–5.
- Benedict, K. F., Coffin, G. S., Barrett, E. J., & Skalak, T. C. 2011. Hemodynamic Systems Analysis of Capillary Network Remodeling During the Progression of Type 2 Diabetes. *Microcirculation*, **18**(1), 63–73.
- Berkman, Elliot T., & Reise, Steven Paul. 2012. *A conceptual guide to statistics using SPSS*. Thousand Oaks, CA. ; London: SAGE.
- Bidola, P. M., Zanette, I., Achterhold, K., Holzner, C., & Pfeiffer, F. 2015. Optimization of propagation-based phase-contrast imaging at a laboratory setup. *Opt Express*, **23**(23), 30000–13.
- Binder, N. K., Hannan, N. J., & Gardner, D. K. 2012. Paternal Diet-Induced Obesity Retards Early Mouse Embryo Development, Mitochondrial Activity and Pregnancy Health. *Plos One*, **7**(12).
- Bolland, B. J. R. F., Kanczler, J. M., Dunlop, D. G., & Oreffo, R. O. C. 2008. Development of in vivo mu CT evaluation of neovascularisation in tissue engineered bone constructs. *Bone*, **43**(1), 195–202.
- Bonamy, A. K., Bendito, A., Martin, H., Andolf, E., Sedin, G., & Norman, M. 2005. Preterm birth contributes to increased vascular resistance and higher blood pressure in adolescent girls. *Pediatr Res*, **58**(5), 845–9.

- Boney, C. M., Verma, A., Tucker, R., & Vohr, B. R. 2005. Metabolic syndrome in childhood: association with birth weight, maternal obesity, and gestational diabetes mellitus. *Pediatrics*, **115**(3), e290–6.
- Bos, C., Hoofd, L., & Oostendorp, T. 1995. Mathematical-Model of Erythrocytes as Point-Like Sources. *Mathematical Biosciences*, **125**(2), 165–189.
- Bouxsein, M. L., Boyd, S. K., Christiansen, B. A., Guldberg, R. E., Jepsen, K. J., & Muller, R. 2010. Guidelines for Assessment of Bone Microstructure in Rodents Using Micro-Computed Tomography. *Journal of Bone and Mineral Research*, **25**(7), 1468–1486.
- Bravin, A., Coan, P., & Suortti, P. 2013. X-ray phase-contrast imaging: from pre-clinical applications towards clinics. *Physics in Medicine and Biology*, **58**(1), R1–R35.
- Bronnikov, A. V. 1999. Reconstruction formulas in phase-contrast tomography. *Optics Communications*, **171**(4-6), 239–244.
- Bruce, K. D., Cagampang, F. R., Argenton, M., Zhang, J. L., Ethirajan, P. L., Burdge, G. C., Bateman, A. C., Clough, G. F., Poston, L., Hanson, M. A., McConnell, J. M., & Byrne, C. D. 2009. Maternal High-Fat Feeding Primes Steatohepatitis in Adult Mice Offspring, Involving Mitochondrial Dysfunction and Altered Lipogenesis Gene Expression. *Hepatology*, **50**(6), 1796–1808.
- Bullitt, E., Gerig, G., Pizer, S. M., Lin, W., & Aylward, S. R. 2003. Measuring tortuosity of the intracerebral vasculature from MRA images. *IEEE Trans Med Imaging*, **22**(9), 1163–71.
- Burrell, J. S., Bradley, R. S., Walker-Samuel, S., Jamin, Y., Baker, L. C. J., Boulton, J. K. R., Withers, P. J., Halliday, J., Waterton, J. C., & Robinson, S. P. 2012. MRI measurements of vessel calibre in tumour xenografts: Comparison with vascular corrosion casting. *Microvascular Research*, **84**(3), 323–329.
- Burvall, A., Lundstrom, U., Takman, P. A., Larsson, D. H., & Hertz, H. M. 2011. Phase retrieval in X-ray phase-contrast imaging suitable for tomography. *Opt Express*, **19**(11), 10359–76.
- Butcher, J. T., Stanley, S. C., Brooks, S. D., Chantler, P. D., Wu, F., & Frisbee, J. C. 2014. Impact of increased intramuscular perfusion heterogeneity on skeletal muscle microvascular hematocrit in the metabolic syndrome. *Microcirculation*, **21**(8), 677–87.
- Caro, Colin G., Pedley, T.J., Schroter, R.C., & Seed, W.A. 2012. *The mechanics of the circulation*. 2nd edn. Cambridge: Cambridge University Press.
- Caton, J. S., Reed, J. J., Aitken, R. P., Milne, J. S., Borowicz, P. P., Reynolds, L. P., Redmer, D. A., & Wallace, J. M. 2009. Effects of maternal nutrition and stage of gestation on body weight, visceral organ mass, and indices of jejunal cellularity, proliferation, and vascularity in pregnant ewe lambs. *J Anim Sci*, **87**(1), 222–35.

- Cebasek, V., Radochova, B., Ribaric, S., Kubinova, L., & Erzen, I. 2006. Nerve injury affects the capillary supply in rat slow and fast muscles differently. *Cell Tissue Res*, **323**(2), 305–12.
- Cebasek, V., Erzen, I., Vyhnaľ, A., Janacek, J., Ribaric, S., & Kubinova, L. 2010. The estimation error of skeletal muscle capillary supply is significantly reduced by 3D method. *Microvascular Research*, **79**(1), 40–46.
- Chapman, D., Thomlinson, W., Johnston, R. E., Washburn, D., Pisano, E., Gmur, N., Zhong, Z., Menk, R., Arfelli, F., & Sayers, D. 1997. Diffraction enhanced x-ray imaging. *Phys Med Biol*, **42**(11), 2015–25.
- Clark, B. A., Alloosh, M., Wenzel, J. W., Sturek, M., & Kostrominova, T. Y. 2011. Effect of diet-induced obesity and metabolic syndrome on skeletal muscles of Ossabaw miniature swine. *Am J Physiol Endocrinol Metab*, **300**(5), E848–57.
- Clark, D. P., & Badea, C. T. 2014. Micro-CT of rodents: state-of-the-art and future perspectives. *Phys Med*, **30**(6), 619–34.
- Clark, D. P., Ghaghada, K., Moding, E. J., Kirsch, D. G., & Badea, C. T. 2013. In vivo characterization of tumor vasculature using iodine and gold nanoparticles and dual energy micro-CT. *Physics in Medicine and Biology*, **58**(6), 1683–1704.
- Clark, M. G. 2008. Impaired microvascular perfusion: a consequence of vascular dysfunction and a potential cause of insulin resistance in muscle. *Am J Physiol Endocrinol Metab*, **295**(4), E732–50.
- Cloetens, P., Ludwig, W., Baruchel, J., Van Dyck, D., Van Landuyt, J., Guigay, J. P., & Schlenker, M. 1999. Holotomography: Quantitative phase tomography with micrometer resolution using hard synchrotron radiation x rays. *Applied Physics Letters*, **75**(19), 2912–2914.
- Clough, G. F., & Norman, M. 2011. The Microcirculation: A Target for Developmental Priming. *Microcirculation*, **18**(4), 286–297.
- Clough, G. F., Turzyniecka, M., Walter, L., Krentz, A. J., Wild, S. H., Chipperfield, A. J., Gamble, J., & Byrne, C. D. 2009. Muscle Microvascular Dysfunction in Central Obesity Is Related to Muscle Insulin Insensitivity but Is Not Reversed by High-Dose Statin Treatment. *Diabetes*, **58**(5), 1185–1191.
- Clough, G. F., L'Esperance, V., Turzyniecka, M., Walter, L., Chipperfield, A. J., Gamble, J., Krentz, A. J., & Byrne, C. D. 2011. Functional dilator capacity is independently associated with insulin sensitivity and age in central obesity and is not improved by high dose statin treatment. *Microcirculation*, **18**(1), 74–84.
- Connor, Dean M., & Zhong, Zhong. 2014. Diffraction-Enhanced Imaging. *Current Radiology Reports*, **2**(7), 1–11.

- Cooper, L. J., Heppell, J. P., Clough, G. F., Ganapathisubramani, B., & Roose, T. 2015. An Image-Based Model of Fluid Flow Through Lymph Nodes. *Bull Math Biol*.
- Costello, P. M., Rowlerson, A., Astaman, N. A., Anthony, F. E., Sayer, A. A., Cooper, C., Hanson, M. A., & Green, L. R. 2008. Peri-implantation and late gestation maternal undernutrition differentially affect fetal sheep skeletal muscle development (vol 586, pg 2371, 2008). *Journal of Physiology-London*, **586**(23), 5833–5833.
- Craigmyle, M. B. L. 1986. *A colour atlas of histology*. 2nd edn. Wolfe medical atlases ; London: Wolfe Medical.
- Culver, J. C., & Dickinson, M. E. 2010. The effects of hemodynamic force on embryonic development. *Microcirculation*, **17**(3), 164–78.
- Daly, K.R., & Roose, T. 2015. Homogenization of two fluid flow in porous media. *Proceedings of the Royal Society a-Mathematical Physical and Engineering Sciences*, **471**(2176).
- Dapp, C., Schmutz, S., Hoppeler, H., & Fluck, M. 2004. Transcriptional reprogramming and ultrastructure during atrophy and recovery of mouse soleus muscle. *Physiol Genomics*, **20**(1), 97–107.
- Davidson, Y. S., Clague, J. E., Horan, M. A., & Pendleton, N. 1999. The effect of aging on skeletal muscle capillarization in a murine model. *J Gerontol A Biol Sci Med Sci*, **54**(10), B448–51.
- Degenhardt, K., Wright, A. C., Horng, D., Padmanabhan, A., & Epstein, J. A. 2010. Rapid 3D Phenotyping of Cardiovascular Development in Mouse Embryos by Micro-CT With Iodine Staining. *Circulation-Cardiovascular Imaging*, **3**(3), 314–U138.
- Degens, H., Deveci, D., Botto-Van Bemden, A., Hoofd, L. J. C., & Egginton, S. 2006. Maintenance of heterogeneity of capillary spacing is essential for adequate oxygenation in the soleus muscle of the growing rat. *Microcirculation*, **13**(6), 467–476.
- DeLano, F. A., Schmid-Schonbein, G. W., Skalak, T. C., & Zweifach, B. W. 1991. Penetration of the systemic blood pressure into the microvasculature of rat skeletal muscle. *Microvasc Res*, **41**(1), 92–110.
- Denies, M. S., Johnson, J., Maliphol, A. B., Bruno, M., Kim, A., Rizvi, A., Rustici, K., & Medler, S. 2014. Diet-induced obesity alters skeletal muscle fiber types of male but not female mice. *Physiol Rep*, **2**(1), e00204.
- Despopoulos, Agamemnon, Despopoulos, Agamemnon, Silbernagel, Stefan, & Publishers., Thieme Medical. 2009. *Color atlas of physiology*. [electronic resource] / Agamemnon Despopoulos, Stefan Silbernagl ; color plates by Wolf-Rüdiger Gay and Astrid Rothenburger. Color Atlas of Physiology (Online) Taschenatlas der Physiologie (Online) ill. Made available through: Thieme ElectronicBook Library. Specialty: Physiology. undamentals and cell physiology – Nerve and muscle, physical work –

- Autonomic nervous system (ANS) – Blood – Respiration – Acid-base homeostasis – Kidneys, salt, and water balance – Cardiovascular system – Thermal balance and thermoregulation – Nutrition and digestion – Hormones and reproduction – Central nervous system and senses. Also available in print. System requirements: World Wide Web browser, internet connectivity, Adobe Acrobat reader. Mode of access: World Wide Web.
- Detombe, S. A., Dunmore-Buyze, J., Petrov, I. E., & Drangova, M. 2013. X-ray dose delivered during a longitudinal micro-CT study has no adverse effect on cardiac and pulmonary tissue in C57BL/6 mice. *Acta Radiol*, **54**(4), 435–41.
- Diaz-Flores, L., Gutierrez, R., Saez, F. J., Diaz-Flores, L., Jr., & Madrid, J. F. 2013. Telocytes in neuromuscular spindles. *J Cell Mol Med*, **17**(4), 457–65.
- Dickie, R., Bachoo, R. M., Rupnick, M. A., Dallabrida, S. M., DeLoid, G. M., Lai, J., DePinho, R. A., & Rogers, R. A. 2006. Three-dimensional visualization of microvessel architecture of whole-mount tissue by confocal microscopy. *Microvascular Research*, **72**(1-2), 20–26.
- Doube, M., Klosowski, M. M., Arganda-Carreras, I., Cordelieres, F. P., Dougherty, R. P., Jackson, J. S., Schmid, B., Hutchinson, J. R., & Shefelbine, S. J. 2010. BoneJ: Free and extensible bone image analysis in ImageJ. *Bone*, **47**(6), 1076–9.
- Dowd, B. A., Campbell, G. H., Marr, R. B., Nagarkar, V., Tipnis, S., Axe, L., & Siddons, D. P. 1999. Developments in synchrotron x-ray computed microtomography at the National Synchrotron Light Source. *Developments in X-Ray Tomography II*, **3772**, 224–236.
- Downey, C. M., Singla, A. K., Villemaire, M. L., Buie, H. R., Boyd, S. K., & Jirik, F. R. 2012. Quantitative Ex-Vivo Micro-Computed Tomographic Imaging of Blood Vessels and Necrotic Regions within Tumors. *Plos One*, **7**(7).
- Drake, A. J., & Reynolds, R. M. 2010. Impact of maternal obesity on offspring obesity and cardiometabolic disease risk. *Reproduction*, **140**(3), 387–98.
- Duan, J., Hu, C., Luo, S., Zhao, X., & Wang, T. 2013. Microcomputed tomography with diffraction-enhanced imaging for morphologic characterization and quantitative evaluation of microvessel of hepatic fibrosis in rats. *PLoS One*, **8**(10), e78176.
- Edwards, M. H., Gregson, C. L., Patel, H. P., Jameson, K. A., Harvey, N. C., Sayer, A. A., Dennison, E. M., & Cooper, C. 2013. Muscle size, strength, and physical performance and their associations with bone structure in the Hertfordshire Cohort Study. *J Bone Miner Res*, **28**(11), 2295–304.
- Egginton, S., & Ross, H. F. 1992. *Oxygen transport in biological systems : modelling of pathways from environment to cell*. Society for Experimental Biology Seminar series. Cambridge ;: New York, NY Cambridge University Press.

- Eggleton, C. D., Vadapalli, A., Roy, T. K., & Popel, A. S. 2000. Calculations of intra-capillary oxygen tension distributions in muscle. *Mathematical Biosciences*, **167**(2), 123–143.
- Elahi, M. M., Cagampang, F. R., Mukhtar, D., Anthony, F. W., Ohri, S. K., & Hanson, M. A. 2009. Long-term maternal high-fat feeding from weaning through pregnancy and lactation predisposes offspring to hypertension, raised plasma lipids and fatty liver in mice. *Br J Nutr*, **102**(4), 514–9.
- Elektronensynchrotron, Deutsches. 2016. *Desy Webpage*.
- Ellis, C. G., Goldman, D., Hanson, M., Stephenson, A. H., Milkovich, S., Benlamri, A., Ellsworth, M. L., & Sprague, R. S. 2010. Defects in oxygen supply to skeletal muscle of prediabetic ZDF rats. *Am J Physiol Heart Circ Physiol*, **298**(6), H1661–70.
- Ellsworth, M. L., & Pittman, R. N. 1990. Arterioles Supply Oxygen to Capillaries by Diffusion as Well as by Convection. *American Journal of Physiology*, **258**(4), H1240–H1243.
- Erzen, I., Janacek, J., & Kubinova, L. 2011. Characterization of the capillary network in skeletal muscles from 3D data. *Physiol Res*, **60**(1), 1–13.
- Everitt, Brian. 2002. *The Cambridge dictionary of statistics*. [electronic resource] / B.S. Everitt. Statistics ill. ; 26 cm. Electronic reproduction. Palo Alto, Calif. : ebrary, 2009.
- Faulkes, Zen. 2016. *Murine soleus muscle image*.
- Fedosov, D. A., Caswell, B., Popel, A. S., & Karniadakis, G. E. 2010. Blood Flow and Cell-Free Layer in Microvessels. *Microcirculation*, **17**(8), 615–628.
- Folarin, A. A., Konerding, M. A., Timonen, J., Nagl, S., & Pedley, R. B. 2010. Three-dimensional analysis of tumour vascular corrosion casts using stereoinaging and micro-computed tomography. *Microvasc Res*, **80**(1), 89–98.
- Ford, N. L., Thornton, M. M., & Holdsworth, D. W. 2003. Fundamental image quality limits for microcomputed tomography in small animals. *Med Phys*, **30**(11), 2869–77.
- Fraser, G. M., Goldman, D., & Ellis, C. G. 2013. Comparison of Generated Parallel Capillary Arrays to Three-Dimensional Reconstructed Capillary Networks in Modeling Oxygen Transport in Discrete Microvascular Volumes. *Microcirculation*, **20**(8), 748–763.
- Fraser, G. M., Morton, J. S., Schmidt, S. M., Bourque, S., Davidge, S. T., Davenport, M. H., & Steinback, C. D. 2015. Reduced uterine perfusion pressure decreases functional capillary density in skeletal muscle. *Am J Physiol Heart Circ Physiol*, **309**(12), H2002–7.

- Fratini, M., Bukreeva, I., Campi, G., Brun, F., Tromba, G., Modregger, P., Bucci, D., Battaglia, G., Spano, R., Mastrogiacomo, M., Requardt, H., Giove, F., Bravin, A., & Cedola, A. 2015. Simultaneous submicrometric 3D imaging of the micro-vascular network and the neuronal system in a mouse spinal cord. *Sci Rep*, **5**, 8514.
- Freeman, D. J. 2010. Effects of maternal obesity on fetal growth and body composition: implications for programming and future health. *Semin Fetal Neonatal Med*, **15**(2), 113–8.
- Frisbee, J. C. 2003. Impaired skeletal muscle perfusion in obese Zucker rats. *Am J Physiol Regul Integr Comp Physiol*, **285**(5), R1124–34.
- Frisbee, J. C. 2005. Hypertension-independent microvascular rarefaction in the obese Zucker rat model of the metabolic syndrome. *Microcirculation*, **12**(5), 383–392.
- Frisbee, J. C., Wu, F., Goodwill, A. G., Butcher, J. T., & Beard, D. A. 2011. Spatial heterogeneity in skeletal muscle microvascular blood flow distribution is increased in the metabolic syndrome. *Am J Physiol Regul Integr Comp Physiol*, **301**(4), R975–86.
- Frisbee, J. C., Goodwill, A. G., Frisbee, S. J., Butcher, J. T., Wu, F., & Chantler, P. D. 2016. Microvascular perfusion heterogeneity contributes to peripheral vascular disease in metabolic syndrome. *J Physiol*, **594**(8), 2233–43.
- Fry, B. C., Lee, J., Smith, N. P., & Secomb, T. W. 2012. Estimation of Blood Flow Rates in Large Microvascular Networks. *Microcirculation*, **19**(6), 530–538.
- Fukumura, D., & Jain, R. K. 2008. Imaging angiogenesis and the microenvironment. *APMIS*, **116**(7-8), 695–715.
- Fukumura, D., Duda, D. G., Munn, L. L., & Jain, R. K. 2010. Tumor microvasculature and microenvironment: novel insights through intravital imaging in pre-clinical models. *Microcirculation*, **17**(3), 206–25.
- Gagnon, L., Sakadzic, S., Lesage, F., Musacchia, J. J., Lefebvre, J., Fang, Q., Yucel, M. A., Evans, K. C., Mandeville, E. T., Cohen-Adad, J., Polimeni, J. R., Yaseen, M. A., Lo, E. H., Greve, D. N., Buxton, R. B., Dale, A. M., Devor, A., & Boas, D. A. 2015. Quantifying the microvascular origin of BOLD-fMRI from first principles with two-photon microscopy and an oxygen-sensitive nanoprobe. *J Neurosci*, **35**(8), 3663–75.
- Garcia-Sanz, A., Rodriguez-Barbero, A., Bentley, M. D., Ritman, E. L., & Romero, J. C. 1998. Three-dimensional microcomputed tomography of renal vasculature in rats. *Hypertension*, **31**(1), 440–444.
- Gaudio, E., Pannarale, L., & Marinozzi, G. 1984. A Tridimensional Study of Microcirculation in Skeletal-Muscle. *Vascular Surgery*, **18**(6), 372–381.

- Gazit, Y., Berk, D. A., Leunig, M., Baxter, L. T., & Jain, R. K. 1995. Scale-invariant behavior and vascular network formation in normal and tumor tissue. *Phys Rev Lett*, **75**(12), 2428–2431.
- Geiger, S.R., Renkin, E.M., & Michel, C.C. 1984. *The cardiovascular system: Microcirculation*. American Physiological Society.
- Georgi, M. K., Vigilance, J., Dewar, A. M., & Frame, M. D. 2011. Terminal Arteriolar Network Structure/Function and Plasma Cytokine Levels in db/db and ob/ob Mouse Skeletal Muscle. *Microcirculation*, **18**(3), 238–251.
- Ghaghada, K. B., Badea, C. T., Karumbaiah, L., Fettig, N., Bellamkonda, R. V., Johnson, G. A., & Annapragada, A. 2011. Evaluation of tumor microenvironment in an animal model using a nanoparticle contrast agent in computed tomography imaging. *Acad Radiol*, **18**(1), 20–30.
- Ghanavati, S., Yu, L. X., Lerch, J. P., & Sled, J. G. 2013. A perfusion procedure for imaging of the mouse cerebral vasculature by X-ray micro-CT. *J Neurosci Methods*.
- Gluckman, Peter D., Beedle, Alan, & Hanson, Mark A. 2009. *Principles of evolutionary medicine*. [electronic resource] / Peter Gluckman, Alan Beedle, Mark Hanson. ill., maps. Electronic reproduction. Palo Alto, Calif. : ebrary, 2013.
- Goldman, D. 2008. Theoretical Models of Microvascular Oxygen Transport to Tissue. *Microcirculation*, **15**(8), 795–811.
- Goldman, D., & Popel, A. S. 1999. Computational modeling of oxygen transport from complex capillary networks. Relation to the microcirculation physiome. *Adv Exp Med Biol*, **471**, 555–63.
- Goldman, D., & Popel, A. S. 2000. A computational study of the effect of capillary network anastomoses and tortuosity on oxygen transport. *Journal of Theoretical Biology*, **206**(2), 181–194.
- Goldman, D., & Popel, A. S. 2001. A computational study of the effect of vasomotion on oxygen transport from capillary networks. *Journal of Theoretical Biology*, **209**(2), 189–199.
- Goldman, D., Bateman, R. M., & Ellis, C. G. 2004. Effect of sepsis on skeletal muscle oxygen consumption and tissue oxygenation: interpreting capillary oxygen transport data using a mathematical model. *Am J Physiol Heart Circ Physiol*, **287**(6), H2535–44.
- Goldman, D., Bateman, R. M., & Ellis, C. G. 2006. Effect of decreased O₂ supply on skeletal muscle oxygenation and O₂ consumption during sepsis: role of heterogeneous capillary spacing and blood flow. *Am J Physiol Heart Circ Physiol*, **290**(6), H2277–85.

- Gould, D. J., Vadakkan, T. J., Poche, R. A., & Dickinson, M. E. 2011. Multifractal and Lacunarity Analysis of Microvascular Morphology and Remodeling. *Microcirculation*, **18**(2), 136–151.
- Gould, I. G., & Linninger, A. A. 2015. Hematocrit distribution and tissue oxygenation in large microcirculatory networks. *Microcirculation*, **22**(1), 1–18.
- Greene, A. S., Tonellato, P. J., Lui, J., Lombard, J. H., & Cowley, A. W., Jr. 1989. Microvascular rarefaction and tissue vascular resistance in hypertension. *Am J Physiol*, **256**(1 Pt 2), H126–31.
- Gregor, Tomáš, Kochová, Petra, Eberlová, Lada, Nedorost, Lukáš, Prosecká, Eva, Liška, Václav, Mírka, Hynek, Kachlík, David, Pirner, Ivan, Zimmermann, Petr, Králíčková, Anna, Králíčková, Milena, & Tonar, Zbyněk. 2012. Correlating Micro-CT Imaging with Quantitative Histology, Injury and Skeletal Biomechanics. *InTech*.
- Grimes, David Robert, Kannan, Pavitra, Warren, Daniel R., Markelc, Bostjan, Bates, Russell, Muschel, Ruth, & Partridge, Mike. 2016. Estimating oxygen distribution from vasculature in three-dimensional tumour tissue. *Journal of The Royal Society Interface*, **13**(116).
- Groso, A., Abela, R., & Stampanoni, M. 2006. Implementation of a fast method for high resolution phase contrast tomography. *Optics Express*, **14**(18), 8103–8110.
- Hannon-Fletcher, Mary, & Maxwell, Perry. 2009. *Advanced techniques in diagnostic cellular pathology*. [electronic resource] / edited by Mary Hannon-Fletcher and Perry Maxwell. ill. (some col.) ; 25 cm. Electronic reproduction. Palo Alto, Calif. : ebrary, 2009.
- Hanson, M., & Gluckman, P. 2011. Developmental origins of noncommunicable disease: population and public health implications. *American Journal of Clinical Nutrition*, **94**(6), 1754s–1758s.
- Hanson, M., Godfrey, K. M., Lillycrop, K. A., Burdge, G. C., & Gluckman, P. D. 2011. Developmental plasticity and developmental origins of non-communicable disease: Theoretical considerations and epigenetic mechanisms. *Progress in Biophysics & Molecular Biology*, **106**(1), 272–280.
- Hecht, Nils, Schneider, UlfC, Woitzik, Johannes, & Vajkoczy, Peter. 2012. *Laser Speckle Imaging*. Springer Protocols Handbooks. Humana Press. Chap. 41, pages 517–523.
- Heinzer, S., Krucker, T., Stampanoni, M., Abela, R., Meyer, E. P., Schuler, A., Schneider, P., & Muller, R. 2006. Hierarchical microimaging for multiscale analysis of large vascular networks. *Neuroimage*, **32**(2), 626–636.
- Henke, B. L., Gullikson, E. M., & Davis, J. C. 1993. X-Ray Interactions - Photoabsorption, Scattering, Transmission, and Reflection at E=50-30,000 Ev, Z=1-92. *Atomic Data and Nuclear Data Tables*, **54**(2), 181–342.

- Hesse, B., Varga, P., Langer, M., Pacureanu, A., Schrof, S., Mannicke, N., Suhonen, H., Maurer, P., Cloetens, P., Peyrin, F., & Raum, K. 2015. Canalicular Network Morphology is the Major Determinant of the Spatial Distribution of Mass Density in Human Bone Tissue: Evidence by Means of Synchrotron Radiation Phase-Contrast nano-CT. *Journal of Bone and Mineral Research*, **30**(2), 346–356.
- Hildebrand, T., & Rüegsegger, P. 1997. A new method for the model-independent assessment of thickness in three-dimensional images. *Journal of Microscopy*, **185**(1), 67–75.
- Honig, C. R., & Gayeski, T. E. 1982. Correlation of O₂ transport on the micro and macro scale. *Int J Microcirc Clin Exp*, **1**(4), 367–80.
- Hoofd, L. 1995. Calculation of Oxygen Pressures in Tissue with Anisotropic Capillary Orientation .1. 2-Dimensional Analytical Solution for Arbitrary Capillary Characteristics. *Mathematical Biosciences*, **129**(1), 1–23.
- Hounsfield, G.N. 1973. Computerized transverse axial scanning (tomography): Part 1. Description of system. *The British Journal of Radiology*, **46**(552), 1016–1022.
- Hsieh, Jiang. 2009. *Computed tomography principles, design, artifacts, and recent advances*. [electronic resource] : Jiang Hsieh. ill.) : digital file. "SPIE digital library." Title from PDF t.p. (viewed on Feb. 25, 2010). Also available in print version.
- Hsieh, Jiang. 2015. *Computed tomography : principles, design, artifacts, and recent advances*. Third edition. edn. SPIE Press monograph ;.
- Hu, D. D., Chen, Y., Bihi, A., Li, X. M., Wang, T. L., Wang, B. E., & Zhao, X. Y. 2014. A new conversation between radiology and pathology-identifying microvascular architecture in stages of cirrhosis via diffraction enhanced imaging in vitro. *PLoS One*, **9**(2), e87957.
- Hudlicka, O. 1985. Development and Adaptability of Microvasculature in Skeletal Muscle. *Journal of Experimental Biology*, **115**(Mar), 215–228.
- Huisken, J., & Stainier, D. Y. 2009. Selective plane illumination microscopy techniques in developmental biology. *Development*, **136**(12), 1963–75.
- Humeau-Heurtier, A., Mahe, G., & Abraham, P. 2015. Microvascular blood flow monitoring with laser speckle contrast imaging using the generalized differences algorithm. *Microvasc Res*, **98**, 54–61.
- Huxley, R., Neil, A., & Collins, R. 2002. Unravelling the fetal origins hypothesis: is there really an inverse association between birthweight and subsequent blood pressure? *Lancet*, **360**(9334), 659–65.
- Huxley, R. R., & Neil, H. A. 2004. Does maternal nutrition in pregnancy and birth weight influence levels of CHD risk factors in adult life? *Br J Nutr*, **91**(3), 459–68.

- Jacobsen, J. C. B., Gustafsson, F., & Holstein-Rathlou, N. H. 2003. A model of physical factors in the structural adaptation of microvascular networks in normotension and hypertension. *Physiological Measurement*, **24**(4), 891–912.
- Jacobsen, J. C. B., Hornbech, M. S., & Holstein-Rathlou, N. H. 2011. Significance of microvascular remodelling for the vascular flow reserve in hypertension. *Interface Focus*, **1**(1), 117–131.
- Jain, R. K. 1987a. Transport of molecules across tumor vasculature. *Cancer Metastasis Rev*, **6**(4), 559–93.
- Jain, R. K. 1987b. Transport of molecules in the tumor interstitium: a review. *Cancer Res*, **47**(12), 3039–51.
- Jain, R. K., Munn, L. L., & Fukumura, D. 2013. Measuring angiogenesis and hemodynamics in mice. *Cold Spring Harb Protoc*, **2013**(4), 354–8.
- Janacek, J., Cebasek, V., Kubinova, L., Ribaric, S., & Erzen, I. 2009. 3D Visualization and Measurement of Capillaries Supplying Metabolically Different Fiber Types in the Rat Extensor Digitorum Longus Muscle During Denervation and Reinnervation. *Journal of Histochemistry & Cytochemistry*, **57**(5), 437–447.
- Japee, S. A., Pittman, R. N., & Ellis, C. G. 2005. A new video image analysis system to study red blood cell dynamics and oxygenation in capillary networks. *Microcirculation*, **12**(6), 489–506.
- Jenkins, M. J., Edgley, A. J., Sonobe, T., Umetani, K., Schwenke, D. O., Fujii, Y., Brown, R. D., Kelly, D. J., Shirai, M., & Pearson, J. T. 2012. Dynamic Synchrotron Imaging of Diabetic Rat Coronary Microcirculation In Vivo. *Arteriosclerosis Thrombosis and Vascular Biology*, **32**(2), 370–U466.
- Jensen, T. H., Bech, M., Binderup, T., Bottiger, A., David, C., Weitkamp, T., Zanette, I., Reznikova, E., Mohr, J., Rank, F., Feidenhans'l, R., Kjaer, A., Hojgaard, L., & Pfeiffer, F. 2013. Imaging of metastatic lymph nodes by X-ray phase-contrast micro-tomography. *PLoS One*, **8**(1), e54047.
- Jung, A., Faltermeier, R., Rothoerl, R., & Brawanski, A. 2005. A mathematical model of cerebral circulation and oxygen supply. *J Math Biol*, **51**(5), 491–507.
- Jurgens, K. D., Peters, T., & Gros, G. 1994. Diffusivity of myoglobin in intact skeletal muscle cells. *Proc Natl Acad Sci U S A*, **91**(9), 3829–33.
- Kak, A., & Slaney, M. 1988. 5. *Aliasing Artifacts and Noise in CT Images*. Pages 177–201.
- Kalender, Willi. 2011. *Computed tomography : fundamentals, system technology, image quality, applications*. 3rd rev. edn. Erlangen: Publicis Publishing.

- Kamoun, W. S., Chae, S. S., Lacorre, D. A., Tyrrell, J. A., Mitre, M., Gillissen, M. A., Fukumura, D., Jain, R. K., & Munn, L. L. 2010. Simultaneous measurement of RBC velocity, flux, hematocrit and shear rate in vascular networks. *Nature Methods*, **7**(8), 655–U78.
- Kerkhof, G. F., Breukhoven, P. E., Leunissen, R. W., Willemsen, R. H., & Hokken-Koelega, A. C. 2012. Does preterm birth influence cardiovascular risk in early adulthood? *J Pediatr*, **161**(3), 390–396 e1.
- Kherlopian, A. R., Song, T., Duan, Q., Neimark, M. A., Po, M. J., Gohagan, J. K., & Laine, A. F. 2008. A review of imaging techniques for systems biology. *BMC Syst Biol*, **2**, 74.
- Kiessling, F., Razansky, D., & Alves, F. 2010. Anatomical and microstructural imaging of angiogenesis. *European Journal of Nuclear Medicine and Molecular Imaging*, **37**, S4–S19.
- Kim, E., Stamatelos, S., Cebulla, J., Bhujwala, Z., Popel, A., & Pathak, A. 2012. Multiscale Imaging and Computational Modeling of Blood Flow in the Tumor Vasculature. *Annals of Biomedical Engineering*, **40**(11), 2425–2441.
- Kircher, M. F., Grimm, J., Swirski, F. K., Libby, P., Gerszten, R. E., Allport, J. R., & Weissleder, R. 2008. Noninvasive in vivo imaging of monocyte trafficking to atherosclerotic lesions. *Circulation*, **117**(3), 388–395.
- Kirkpatrick, Lee A., & Feeney, Brooke C. 2013. *A simple guide to IBM SPSS® statistics : for version 20.0*. International edn. Australia ; United Kingdom: Wadsworth : Cengage Learning.
- Kistner, A., Jacobson, L., Jacobson, S. H., Svensson, E., & Hellstrom, A. 2002. Low gestational age associated with abnormal retinal vascularization and increased blood pressure in adult women. *Pediatr Res*, **51**(6), 675–80.
- Kistner, A., Celsi, G., Vanpee, M., & Jacobson, S. H. 2005. Increased systolic daily ambulatory blood pressure in adult women born preterm. *Pediatr Nephrol*, **20**(2), 232–3.
- Kokkorigiannis, T. 2004. Somatic and intramuscular distribution of muscle spindles and their relation to muscular angiotypes. *J Theor Biol*, **229**(2), 263–80.
- Kondo, H., Fujino, H., Murakami, S., Nagatomo, F., Roy, R. R., & Ishihara, A. 2011. Regressed three-dimensional capillary network and inhibited angiogenic factors in the soleus muscle of non-obese rats with type 2 diabetes. *Nutr Metab (Lond)*, **8**(1), 77.
- Konerding, M. A., Miodonski, A. J., & Lametschwandtner, A. 1995. Microvascular corrosion casting in the study of tumor vascularity: A review. *Scanning Microscopy*, **9**(4), 1233–1244.

- Konerding, M. A., Malkusch, W., Klapthor, B., van Ackern, C., Fait, E., Hill, S. A., Parkins, C., Chaplin, D. J., Presta, M., & Denekamp, J. 1999. Evidence for characteristic vascular patterns in solid tumours: quantitative studies using corrosion casts. *British Journal of Cancer*, **80**(5-6), 724–732.
- Konerding, M. A., Fait, E., & Gaumann, A. 2001. 3D microvascular architecture of pre-cancerous lesions and invasive carcinomas of the colon. *British Journal of Cancer*, **84**(10), 1354–1362.
- Krogh, A. 1919a. The number and distribution of capillaries in muscles with calculations of the oxygen pressure head necessary for supplying the tissue. *J Physiol*, **52**(6), 409–15.
- Krogh, A. 1919b. The rate of diffusion of gases through animal tissues, with some remarks on the coefficient of invasion. *J Physiol*, **52**(6), 391–408.
- Krogh, A. 1919c. The supply of oxygen to the tissues and the regulation of the capillary circulation. *J Physiol*, **52**(6), 457–74.
- Krucker, T., Lang, A., & Meyer, E. P. 2006. New polyurethane-based material for vascular corrosion casting with improved physical and imaging characteristics. *Microscopy Research and Technique*, **69**(2), 138–147.
- Kuh, D., Bassey, J., Hardy, R., Aihie Sayer, A., Wadsworth, M., & Cooper, C. 2002. Birth weight, childhood size, and muscle strength in adult life: evidence from a birth cohort study. *Am J Epidemiol*, **156**(7), 627–33.
- Kuliga, K. Z., McDonald, E. F., Gush, R., Michel, C., Chipperfield, A. J., & Clough, G. F. 2014. Dynamics of microvascular blood flow and oxygenation measured simultaneously in human skin. *Microcirculation*, **21**(6), 562–73.
- Lametschwandtner, A., Lametschwandtner, U., & Weiger, T. 1984. Scanning electron microscopy of vascular corrosion casts—technique and applications. *Scan Electron Microsc*, 663–95.
- Lametschwandtner, A., Lametschwandtner, U., & Weiger, T. 1990. Scanning electron microscopy of vascular corrosion casts—technique and applications: updated review. *Scanning Microsc*, **4**(4), 889–940; discussion 941.
- Landis, E. N., & Keane, D. T. 2010. X-ray microtomography. *Materials Characterization*, **61**(12), 1305–1316.
- Lang, S., Muller, B., Dominiotto, M. D., Cattin, P. C., Zanette, I., Weitkamp, T., & Hieber, S. E. 2012. Three-dimensional quantification of capillary networks in healthy and cancerous tissues of two mice. *Microvascular Research*, **84**(3), 314–322.
- Lang, S., Zanette, I., Dominiotto, M., Langer, M., Rack, A., Schulz, G., Le Duc, G., David, C., Mohr, J., Pfeiffer, F., Muller, B., & Weitkamp, T. 2014. Experimental comparison of

- grating- and propagation-based hard X-ray phase tomography of soft tissue. *Journal of Applied Physics*, **116**(15).
- Laufer, J., Johnson, P., Zhang, E., Treeby, B., Cox, B., Pedley, B., & Beard, P. 2012. In vivo preclinical photoacoustic imaging of tumor vasculature development and therapy. *Journal of Biomedical Optics*, **17**(5).
- Leahy, Martin J. 2012. *Microcirculation imaging*. [electronic resource] / edited by Martin J. Leahy. ill. Electronic reproduction. Palo Alto, Calif. : ebrary, 2011.
- Lechleiter, J. D., Lin, D. T., & Sieneart, I. 2002. Multi-photon laser scanning microscopy using an acoustic optical deflector. *Biophysical Journal*, **83**(4), 2292–2299.
- Lee, J., & Smith, N. 2008a. Development and application of a one-dimensional blood flow model for microvascular networks. *Proceedings of the Institution of Mechanical Engineers Part H-Journal of Engineering in Medicine*, **222**(H4), 487–511.
- Lee, J., & Smith, N. 2008b. Theoretical Modeling in Hemodynamics of Microcirculation. *Microcirculation*, **15**(8), 699–714.
- Levick, J. Rodney. 2003. *An introduction to cardiovascular physiology*. 4th edn. London: Arnold.
- Li, T. C., Ota, S., Kim, J., Wong, Z. J., Wang, Y., Yin, X. B., & Zhang, X. 2014. Axial Plane Optical Microscopy. *Scientific Reports*, **4**.
- Linderman, J. R., & Boegehold, M. A. 1996a. Arteriolar network growth in rat striated muscle during juvenile maturation. *International Journal of Microcirculation-Clinical and Experimental*, **16**(5), 232–239.
- Linderman, R., & Boegehold, M. 1996b. Maturation changes in striated muscle microvasculature: Structural and functional aspects. *6th World Congress for Microcirculation*, 915–919.
- Lionikas, A., Smith, C. J., Smith, T. L., Bunger, L., Banks, R. W., & Bewick, G. S. 2013. Analyses of muscle spindles in the soleus of six inbred mouse strains. *J Anat*, **223**(3), 289–96.
- Liu, G., Qutub, A. A., Vempati, P., Mac Gabhann, F., & Popel, A. S. 2011. Module-based multiscale simulation of angiogenesis in skeletal muscle. *Theor Biol Med Model*, **8**, 6.
- Lo, A., Fuglevand, A. J., & Secomb, T. W. 2003. Oxygen delivery to skeletal muscle fibers: effects of microvascular unit structure and control mechanisms. *Am J Physiol Heart Circ Physiol*, **285**(3), H955–63.
- Lorthois, S., & Cassot, F. 2010. Fractal analysis of vascular networks: insights from morphogenesis. *J Theor Biol*, **262**(4), 614–33.

- Lundstrom, U., Larsson, D. H., Burvall, A., Takman, P. A., Scott, L., Brismar, H., & Hertz, H. M. 2012. X-ray phase contrast for CO₂ microangiography. *Phys Med Biol*, **57**(9), 2603–17.
- Ma, L., Ma, S., He, H., Yang, D., Chen, X., Luo, Z., Liu, D., & Zhu, Z. 2010. Perivascular fat-mediated vascular dysfunction and remodeling through the AMPK/mTOR pathway in high-fat diet-induced obese rats. *Hypertens Res*, **33**(5), 446–53.
- Maeda, H., Kurose, T., & Kawamata, S. 2015. Regulation of the microvascular circulation in the leg muscles, pancreas and small intestine in rats. *Springerplus*, **4**, 295.
- Maltin, C. A. 2008. Muscle development and obesity: Is there a relationship? *Organogenesis*, **4**(3), 158–69.
- Margaritondo, Giorgio. 2002. *Elements of synchrotron light : for biology, chemistry, and medical research*. Oxford: Oxford University Press.
- Marone, F., & Stampanoni, M. 2012. Regridding reconstruction algorithm for real-time tomographic imaging. *J Synchrotron Radiat*, **19**(Pt 6), 1029–37.
- Masters, B. R. 2004. Fractal analysis of the vascular tree in the human retina. *Annu Rev Biomed Eng*, **6**, 427–52.
- Mathieu-Costello, O. 1987. Capillary tortuosity and degree of contraction or extension of skeletal muscles. *Microvasc Res*, **33**(1), 98–117.
- Mathieu-Costello, O., Potter, R. F., Ellis, C. G., & Groom, A. C. 1988. Capillary configuration and fiber shortening in muscles of the rat hindlimb: correlation between corrosion casts and stereological measurements. *Microvasc Res*, **36**(1), 40–55.
- Mathieu-Costello, O., Hoppeler, H., & Weibel, E. R. 1989. Capillary tortuosity in skeletal muscles of mammals depends on muscle contraction. *J Appl Physiol* (1985), **66**(3), 1436–42.
- Mayer, J., Swoger, J., Ozga, A. J., Stein, J. V., & Sharpe, J. 2012. Quantitative measurements in 3-dimensional datasets of mouse lymph nodes resolve organ-wide functional dependencies. *Comput Math Methods Med*, **2012**, 128431.
- Mayo, S. C., Stevenson, A. W., & Wilkins, S. W. 2012. In-Line Phase-Contrast X-ray Imaging and Tomography for Materials Science. *Materials*, **5**(5), 937–965.
- McComas, Alan J. 1996. *Skeletal muscle : form and function*. Champaign, IL: Human Kinetics.
- McDonald, S. A., Marone, F., Hintermuller, C., Mikuljan, G., David, C., Pfeiffer, F., & Stampanoni, M. 2009. Advanced phase-contrast imaging using a grating interferometer. *J Synchrotron Radiat*, **16**(Pt 4), 562–72.

- McDougall, S. R., Anderson, A. R. A., Chaplain, M. A. J., & Sherratt, J. A. 2002. Mathematical modelling of flow through vascular networks: Implications for tumour-induced angiogenesis and chemotherapy strategies. *Bulletin of Mathematical Biology*, **64**(4), 673–702.
- Medina, G. 2015. *tex.stackexchange.com*.
- Meng, H., Bentley, T. B., & Pittman, R. N. 1993. Myoglobin content of hamster skeletal muscles. *J Appl Physiol* (1985), **74**(5), 2194–7.
- Metscher, B. D. 2009. MicroCT for Developmental Biology: A Versatile Tool for High-Contrast 3D Imaging at Histological Resolutions. *Developmental Dynamics*, **238**(3), 632–640.
- Meyer, E. P., Beer, G. M., Lang, A., Manestar, M., Krucker, T., Meier, S., Mihic-Probst, D., & Groscurth, P. 2007. Polyurethane elastomer: A new material for the visualization of cadaveric blood vessels. *Clinical Anatomy*, **20**(4), 448–454.
- Michelson, G., Welzenbach, J., Pal, I., & Harazny, J. 2001. Functional imaging of the retinal microvasculature by scanning laser Doppler flowmetry. *Int Ophthalmol*, **23**(4-6), 327–35.
- Milburn, A. 1973. The early development of muscle spindles in the rat. *J Cell Sci*, **12**(1), 175–95.
- Mizutani, R., & Suzuki, Y. 2012. X-ray microtomography in biology. *Micron*, **43**(2-3), 104–115.
- Moding, E. J., Clark, D. P., Qi, Y., Li, Y. F., Ma, Y., Ghaghada, K., Johnson, G. A., Kirsch, D. G., & Badea, C. T. 2013. Dual-Energy Micro-Computed Tomography Imaging of Radiation-Induced Vascular Changes in Primary Mouse Sarcomas. *International Journal of Radiation Oncology Biology Physics*, **85**(5), 1353–1359.
- Mondy, W. L., Cameron, D., Timmermans, J. P., De Clerck, N., Sasov, A., Casteleyn, C., & Piegel, L. A. 2009a. Computer-aided design of microvasculature systems for use in vascular scaffold production. *Biofabrication*, **1**(3).
- Mondy, W. L., Cameron, D., Timmermans, J. P., De Clerck, N., Sasov, A., Casteleyn, C., & Piegel, L. A. 2009b. Micro-CT of Corrosion Casts for Use in the Computer-Aided Design of Microvasculature. *Tissue Engineering Part C-Methods*, **15**(4), 729–738.
- Morishige, K., Kacher, D. F., Libby, P., Josephson, L., Ganz, P., Weissleder, R., & Aikawa, M. 2010. High-Resolution Magnetic Resonance Imaging Enhanced With Superparamagnetic Nanoparticles Measures Macrophage Burden in Atherosclerosis. *Circulation*, **122**(17), 1707–1715.

- Moschandreou, T. E., Ellis, C. G., & Goldman, D. 2011. Influence of tissue metabolism and capillary oxygen supply on arteriolar oxygen transport: A computational model. *Mathematical Biosciences*, **232**(1), 1–10.
- Mozzarelli, A., & Bettati, S. 2011. Chemistry and Biochemistry of Oxygen Therapeutics From Transfusion to Artificial Blood Preface. *Chemistry and Biochemistry of Oxygen Therapeutics: From Transfusion to Artificial Blood*, Xxiii–Xxiv.
- Muller, K. A., Ryals, J. M., Feldman, E. L., & Wright, D. E. 2008. Abnormal muscle spindle innervation and large-fiber neuropathy in diabetic mice. *Diabetes*, **57**(6), 1693–701.
- Murakami, S., Fujino, H., Takeda, I., Momota, R., Kumagishi, K., & Ohtsuka, A. 2010. Comparison of Capillary Architecture between Slow and Fast Muscles in Rats Using a Confocal Laser Scanning Microscope. *Acta Medica Okayama*, **64**(1), 11–18.
- Murphy, Douglas B., & Davidson, Michael W. 2012. *Fundamentals of light microscopy and electronic imaging*. [electronic resource] / Douglas B. Murphy, Michael W. Davidson. ill. Electronic reproduction. Palo Alto, Calif. : ebrary, 2011.
- Musa, M. G., Torrens, C., & Clough, G. F. 2014. The microvasculature: a target for nutritional programming and later risk of cardio-metabolic disease. *Acta Physiologica*, **210**(1), 31–45.
- Nahrendorf, M., Keliher, E., Panizzi, P., Zhang, H., Hembrador, S., Figueiredo, J.-l., Aikawa, E., Kelly, K., Libby, P., & Weissleder, R. 2009. F-4V for PET-CT imaging of VCAM-1 expression in inflammatory atherosclerosis. *JACC Cardiovascular Imaging*, **2**, 1213–1222.
- Nair, P. K., Hellums, J. D., & Olson, J. S. 1989. Prediction of Oxygen-Transport Rates in Blood Flowing in Large Capillaries. *Microvascular Research*, **38**(3), 269–285.
- Nair, P. K., Huang, N. S., Hellums, J. D., & Olson, J. S. 1990. A Simple-Model for Prediction of Oxygen-Transport Rates by Flowing Blood in Large Capillaries. *Microvascular Research*, **39**(2), 203–211.
- Nebuloni, L., Kuhn, G. A., Vogel, J., & Muller, R. 2014. A novel in vivo vascular imaging approach for hierarchical quantification of vasculature using contrast enhanced micro-computed tomography. *PLoS One*, **9**(1), e86562.
- Nesch, I., Fogarty, D. P., Tzvetkov, T., Reinhart, B., Walus, A. C., Khelashvili, G., Muehleman, C., & Chapman, D. 2009. The design and application of an in-laboratory diffraction-enhanced x-ray imaging instrument. *Rev Sci Instrum*, **80**(9), 093702.
- Nixon, Mark S., & Aguado, Alberto S. 2008. *Feature extraction and image processing*. [electronic resource] / Mark S. Nixon, Alberto S. Aguado. ill. ; 25 cm. Title from e-book title screen (viewed July 4, 2008). Electronic reproduction. UK : MyiLibrary, 2008 Available via World Wide Web. Access may be limited to MIL affiliated libraries.

- Nuyt, A. M. 2008. Mechanisms underlying developmental programming of elevated blood pressure and vascular dysfunction: evidence from human studies and experimental animal models. *Clin Sci (Lond)*, **114**(1), 1–17.
- Osborne, D. R., Yan, S., Stuckey, A., Pryer, L., Richey, T., & Wall, J. S. 2012. Characterization of X-ray Dose in Murine Animals Using microCT, a New Low-Dose Detector and nanoDot Dosimeters. *PLoS One*, **7**(11), e49936.
- Paganin, D., Mayo, S. C., Gureyev, T. E., Miller, P. R., & Wilkins, S. W. 2002. Simultaneous phase and amplitude extraction from a single defocused image of a homogeneous object. *Journal of Microscopy-Oxford*, **206**, 33–40.
- Page, Anton. 2014. *private communication*.
- Pai, V. M., Kozlowski, M., Donahue, D., Miller, E., Xiao, X. H., Chen, M. Y., Yu, Z. X., Connelly, P., Jeffries, K., & Wen, H. 2012. Coronary artery wall imaging in mice using osmium tetroxide and micro-computed tomography (micro-CT). *Journal of Anatomy*, **220**(5), 514–524.
- Pampaloni, F., Chang, B. J., & Stelzer, E. H. K. 2015. Light sheet-based fluorescence microscopy (LSFM) for the quantitative imaging of cells and tissues. *Cell and Tissue Research*, **360**(1), 129–141.
- Parkins, C. S., Fowler, J. F., Maughan, R. L., & Roper, M. J. 1985. Repair in mouse lung for up to 20 fractions of X rays or neutrons. *Br J Radiol*, **58**(687), 225–41.
- Patel, H. P., Syddall, H. E., Martin, H. J., Stewart, C. E., Cooper, C., & Sayer, A. A. 2010. Hertfordshire sarcopenia study: design and methods. *BMC Geriatr*, **10**, 43.
- Patel, H. P., White, M. C., Westbury, L., Syddall, H. E., Stephens, P. J., Clough, G. F., Cooper, C., & Sayer, A. A. 2015. Skeletal muscle morphology in sarcopenia defined using the EWGSOP criteria: findings from the Hertfordshire Sarcopenia Study (HSS). *BMC Geriatr*, **15**, 171.
- Pauwels, E., Van Loo, D., Cornillie, P., Brabant, L., & Van Hoorebeke, L. 2013. An exploratory study of contrast agents for soft tissue visualization by means of high resolution X-ray computed tomography imaging. *Journal of Microscopy*, **250**(1), 21–31.
- Peitgen, Heinz-Otto, Jürgens, Hartmut, & Saupe, Dietmar. 1992. *Chaos and fractals : new frontiers of science*. New York: Springer.
- Penta, R., & Ambrosi, D. 2015. The role of the microvascular tortuosity in tumor transport phenomena. *J Theor Biol*, **364**, 80–97.
- Pfeiffer, F., Weitkamp, T., Bunk, O., & David, C. 2006. Phase retrieval and differential phase-contrast imaging with low-brilliance X-ray sources. *Nature Physics*, **2**(4), 258–261.

- Pinzer, B. R., Cacquevel, M., Modregger, P., McDonald, S. A., Bensadoun, J. C., Thuerling, T., Aebischer, P., & Stampanoni, M. 2012. Imaging brain amyloid deposition using grating-based differential phase contrast tomography. *Neuroimage*, **61**(4), 1336–46.
- Pittman, R. N. 2011. Oxygen gradients in the microcirculation. *Acta Physiol (Oxf)*, **202**(3), 311–22.
- Pittman, R. N. 2013. Oxygen transport in the microcirculation and its regulation. *Microcirculation*, **20**(2), 117–37.
- Pladys, P., Sennlaub, F., Brault, S., Checchin, D., Lahaie, I., Le, N. L. O., Bibeau, K., Cambonie, G., Abran, D., Brochu, M., Thibault, G., Hardy, P., Chemtob, S., & Nuyt, A. M. 2005. Microvascular rarefaction and decreased angiogenesis in rats with fetal programming of hypertension associated with exposure to a low-protein diet in utero. *American Journal of Physiology-Regulatory Integrative and Comparative Physiology*, **289**(6), R1580–R1588.
- Poole, D. C., Mathieu-Costello, O., & West, J. B. 1989. Capillary tortuosity in rat soleus muscle is not affected by endurance training. *Am J Physiol*, **256**(4 Pt 2), H1110–6.
- Poole, D. C., Batra, S., Mathieucostello, O., & Rakusan, K. 1992. Capillary Geometrical Changes with Fiber Shortening in Rat Myocardium. *Circulation Research*, **70**(4), 697–706.
- Poole, D. C., Copp, S. W., Ferguson, S. K., & Musch, T. I. 2013. Skeletal muscle capillary function: contemporary observations and novel hypotheses. *Exp Physiol*, **98**(12), 1645–58.
- Popel, A. S. 1989. Theory of oxygen transport to tissue. *Crit Rev Biomed Eng*, **17**(3), 257–321.
- Pries, A. R., & Secomb, T. W. 2009. Origins of heterogeneity in tissue perfusion and metabolism. *Cardiovascular Research*, **81**(2), 328–335.
- Pries, A. R., Secomb, T. W., Gaehtgens, P., & Gross, J. F. 1990. Blood-Flow in Microvascular Networks - Experiments and Simulation. *Circulation Research*, **67**(4), 826–834.
- Quercioli, A., Pataky, Z., Montecucco, F., Carballo, S., Thomas, A., Staub, C., Di Marzo, V., Vincenti, G., Ambrosio, G., Ratib, O., Golay, A., Mach, F., Harsch, E., & Schindler, T. H. 2012. Coronary vasomotor control in obesity and morbid obesity: contrasting flow responses with endocannabinoids, leptin, and inflammation. *JACC Cardiovasc Imaging*, **5**(8), 805–15.
- Radon, J. 1917. Über die Bestimmung von Funktionen durch ihre Integralwerte längs gewisser Mannigfaltigkeiten. *Berichte der Sächsischen Akademie der Wissenschaften, Leipzig, Mathematisch-Physische Klasse*, **69**, 262–277.

- Razavi, H., Dusch, M. N., Zarafshar, S. Y., Taylor, C. A., & Feinstein, J. A. 2012. A method for quantitative characterization of growth in the 3-D structure of rat pulmonary arteries. *Microvasc Res*, **83**(2), 146–53.
- Rege, A., Thakor, N. V., Rhie, K., & Pathak, A. P. 2012. In vivo laser speckle imaging reveals microvascular remodeling and hemodynamic changes during wound healing angiogenesis. *Angiogenesis*, **15**(1), 87–98.
- Rkhezay-Jaf, J., O'Dowd, J. F., & Stocker, C. J. 2012. Maternal Obesity and the Fetal Origins of the Metabolic Syndrome. *Curr Cardiovasc Risk Rep*, **6**(5), 487–495.
- Rochow, Theodore George, & Tucker, Paul Arthur. 1994. *Introduction to microscopy by means of light, electrons, X rays, or acoustics*. 2nd edn. The language of science. New York: Plenum Press.
- Rodriguez-Porcel, M., Lerman, A., Ritman, E. L., Wilson, S. H., Best, P. J. M., & Lerman, L. O. 2000. Altered myocardial microvascular 3D architecture in experimental hypercholesterolemia. *Circulation*, **102**(17), 2028–2030.
- Roseboom, T. J., van der Meulen, J. H. P., Osmond, C., Barker, D. J. P., Ravelli, A. C. J., Schroeder-Tanka, J. M., van Montfrans, G. A., Michels, R. P. J., & Bleker, O. P. 2000. Coronary heart disease after prenatal exposure to the Dutch famine, 1944–45. *Heart*, **84**(6), 595–598.
- Ruifrok, A. C., & Johnston, D. A. 2001. Quantification of histochemical staining by color deconvolution. *Anal Quant Cytol Histol*, **23**(4), 291–9.
- Rutland, C. S., Latunde-Dada, A. O., Thorpe, A., Plant, R., Langley-Evans, S., & Leach, L. 2007. Effect of gestational nutrition on vascular integrity in the murine placenta. *Placenta*, **28**(7), 734–42.
- Safaeian, N., Sellier, M., & David, T. 2010. A computational model of hemodynamic parameters in cortical capillary networks. *J Theor Biol*.
- Samuelsson, A. M., Matthews, P. A., Argenton, M., Christie, M. R., McConnell, J. M., Jansen, E. H., Piersma, A. H., Ozanne, S. E., Twinn, D. F., Remacle, C., Rowlerson, A., Poston, L., & Taylor, P. D. 2008. Diet-induced obesity in female mice leads to offspring hyperphagia, adiposity, hypertension, and insulin resistance: a novel murine model of developmental programming. *Hypertension*, **51**(2), 383–92.
- Santi, P. A. 2011. Light Sheet Fluorescence Microscopy: A Review. *Journal of Histochemistry & Cytochemistry*, **59**(2), 129–138.
- Sayer, A. A., & Cooper, C. 2005. Fetal programming of body composition and musculoskeletal development. *Early Hum Dev*, **81**(9), 735–44.
- Sayer, A. A., Syddall, H., Martin, H., Patel, H., Baylis, D., & Cooper, C. 2008. The developmental origins of sarcopenia. *J Nutr Health Aging*, **12**(7), 427–32.

- Schindelin, J., Arganda-Carreras, I., Frise, E., Kaynig, V., Longair, M., Pietzsch, T., Preibisch, S., Rueden, C., Saalfeld, S., Schmid, B., Tinevez, J. Y., White, D. J., Hartenstein, V., Eliceiri, K., Tomancak, P., & Cardona, A. 2012. Fiji: an open-source platform for biological-image analysis. *Nature Methods*, **9**(7), 676–682.
- Schittny, J. C., Barre, S. F., Mokso, R., Haberthur, D., Semmler-Behnke, M., Kreyling, W. G., Tsuda, A., & Stampanoni, M. 2011. High-Resolution Phase-Contrast Imaging of Submicron Particles in Unstained Lung Tissue. *10th International Conference on X-Ray Microscopy*, **1365**, 384–387.
- Schneider, P., Krucker, T., Meyer, E., Ulmann-Schuler, A., Weber, B., Stampanoni, M., & Muller, R. 2009. Simultaneous 3D Visualization and Quantification of Murine Bone and Bone Vasculature Using Micro-Computed Tomography and Vascular Replica. *Microscopy Research and Technique*, **72**(9), 690–701.
- Secomb, T. W. 2011. Mechanics and computational simulation of blood flow in microvessels. *Medical Engineering & Physics*, **33**(7), 800–804.
- Secomb, T. W. 2015. Krogh-cylinder and infinite-domain models for washout of an inert diffusible solute from tissue. *Microcirculation*, **22**(1), 91–8.
- Secomb, T. W., & Hsu, R. 1994. Simulation of O₂ Transport in Skeletal-Muscle - Diffusive Exchange between Arterioles and Capillaries. *American Journal of Physiology*, **267**(3), H1214–H1221.
- Secomb, T. W., Alberding, J. P., Hsu, R., Dewhirst, M. W., & Pries, A. R. 2013. Angiogenesis: An Adaptive Dynamic Biological Patterning Problem. *Plos Computational Biology*, **9**(3).
- Segovia, S. A., Vickers, M. H., Gray, C., & Reynolds, C. M. 2014. Maternal obesity, inflammation, and developmental programming. *Biomed Res Int*, **2014**, 418975.
- Sen, S., Carpenter, A. H., Hochstadt, J., Huddleston, J. Y., Kustanovich, V., Reynolds, A. A., & Roberts, S. 2012. Nutrition, weight gain and eating behavior in pregnancy: a review of experimental evidence for long-term effects on the risk of obesity in offspring. *Physiol Behav*, **107**(1), 138–45.
- Sinha, R., Dufour, S., Petersen, K. F., LeBon, V., Enoksson, S., Ma, Y. Z., Savoye, M., Rothman, D. L., Shulman, G. I., & Caprio, S. 2002. Assessment of skeletal muscle triglyceride content by (1)H nuclear magnetic resonance spectroscopy in lean and obese adolescents: relationships to insulin sensitivity, total body fat, and central adiposity. *Diabetes*, **51**(4), 1022–7.
- Skalak, Richard, & Chien, Shu. 1987. *Handbook of Bioengineering*. New York: McGraw-Hill.

- Soukup, T., Zacharova, G., & Smerdu, V. 2002. Fibre type composition of soleus and extensor digitorum longus muscles in normal female inbred Lewis rats. *Acta Histochemica*, **104**(4), 399–405.
- Stead, R., Musa, M. G., Bryant, C. L., Lanham, S. A., Johnston, D. A., Reynolds, R., Torrens, C., Fraser, P. A., & Clough, G. F. 2016. Developmental conditioning of endothelium-derived hyperpolarizing factor-mediated vasorelaxation. *J Hypertens*, **34**(3), 452–63.
- Tam, C. S., Power, J. E., Markovic, T. P., Yee, C., Morsch, M., McLennan, S. V., & Twigg, S. M. 2015. The effects of high-fat feeding on physical function and skeletal muscle extracellular matrix. *Nutr Diabetes*, **5**, e187.
- Tapp, R. J., Ness, A., Williams, C., Howe, L. D., Tilling, K., Witt, N., Chaturvedi, N., Mc, G. Thom S. A., & Hughes, A. D. 2013. Differential effects of adiposity and childhood growth trajectories on retinal microvascular architecture. *Microcirculation*, **20**(7), 609–16.
- Taschereau, R., Chow, P. L., & Chatziioannou, A. F. 2006. Monte carlo simulations of dose from microCT imaging procedures in a realistic mouse phantom. *Med Phys*, **33**(1), 216–24.
- Tateishi, N., Suzuki, Y., Tanaka, J., & Maeda, N. 1997. Imaging of oxygen saturation and distribution of erythrocytes in microvessels. *Microcirculation*, **4**(4), 403–12.
- Thomas, M. M., Trajcevski, K. E., Coleman, S. K., Jiang, M., Di Michele, J., O'Neill, H. M., Lally, J. S., Steinberg, G. R., & Hawke, T. J. 2014. Early oxidative shifts in mouse skeletal muscle morphology with high-fat diet consumption do not lead to functional improvements. *Physiol Rep*, **2**(9).
- Thornell, L. E., Carlsson, L., Eriksson, P. O., Liu, J. X., Osterlund, C., Stal, P., & Pedrosa-Domellof, F. 2015. Fibre typing of intrafusal fibres. *J Anat*, **227**(2), 136–56.
- Thornton, P. R. 1968. *Scanning electron microscopy: applications to materials and device science*. London,: Chapman & Hall.
- Toma-Dasu, I., & Dasu, A. 2013. Modelling tumour oxygenation, reoxygenation and implications on treatment outcome. *Comput Math Methods Med*, **2013**, 141087.
- Torrens, C., Snelling, T. H., Chau, R., Shanmuganathan, M., Cleal, J. K., Poore, K. R., Noakes, D. E., Poston, L., Hanson, M. A., & Green, L. R. 2009. Effects of pre- and periconceptual undernutrition on arterial function in adult female sheep are vascular bed dependent. *Experimental Physiology*, **94**(9), 1024–1033.
- Torrens, C., Ethirajan, P., Bruce, K.D., Cagampang, F.R.A., Siow, R.C.M., & al., et. 2012. Interaction between Maternal and Offspring Diet to Impair Vascular Function and Oxidative Balance in High Fat Fed Male Mice. *PLoS ONE*, **7**(12).

- Trajcevski, K. E., O'Neill, H. M., Wang, D. C., Thomas, M. M., Al-Sajee, D., Steinberg, G. R., Ceddia, R. B., & Hawke, T. J. 2013. Enhanced lipid oxidation and maintenance of muscle insulin sensitivity despite glucose intolerance in a diet-induced obesity mouse model. *PLoS One*, **8**(8), e71747.
- Umetani, K., & Fukushima, K. 2013. X-ray intravital microscopy for functional imaging in rat hearts using synchrotron radiation coronary microangiography. *Review of Scientific Instruments*, **84**(3).
- Vakoc, B. J., Fukumura, D., Jain, R. K., & Bouma, B. E. 2012. Cancer imaging by optical coherence tomography: preclinical progress and clinical potential. *Nature Reviews Cancer*, **12**(5), 363–368.
- van der Merwe, E. L., & Kidson, S. H. 2010. Advances in imaging the blood and aqueous vessels of the ocular limbus. *Experimental Eye Research*, **91**(2), 118–126.
- Vasquez, S. X., Gao, F., Su, F., Grijalva, V., Pope, J., Martin, B., Stinstra, J., Masner, M., Shah, N., Weinstein, D. M., Farias-Eisner, R., & Reddy, S. T. 2011. Optimization of MicroCT Imaging and Blood Vessel Diameter Quantitation of Preclinical Specimen Vasculature with Radiopaque Polymer Injection Medium. *Plos One*, **6**(4).
- Vickers, M. H. 2011. Developmental programming of the metabolic syndrome - critical windows for intervention. *World J Diabetes*, **2**(9), 137–48.
- Vidal, F. P., Letang, J. M., Peix, G., & Cloetens, P. 2005. Investigation of artefact sources in synchrotron microtomography via virtual X-ray imaging. *Nuclear Instruments & Methods in Physics Research Section B-Beam Interactions with Materials and Atoms*, **234**(3), 333–348.
- Walpole, J., Papin, J. A., & Peirce, S. M. 2013. Multiscale computational models of complex biological systems. *Annu Rev Biomed Eng*, **15**, 137–54.
- Walter, I., & Klaus, S. 2014. Maternal high-fat diet consumption impairs exercise performance in offspring. *J Nutr Sci*, **3**, e61.
- Walton, L. A., Bradley, R. S., Withers, P. J., Newton, V. L., Watson, R. E., Austin, C., & Sherratt, M. J. 2015. Morphological Characterisation of Unstained and Intact Tissue Micro-architecture by X-ray Computed Micro- and Nano-Tomography. *Sci Rep*, **5**, 10074.
- Wang, Z., Hauser, N., Singer, G., Trippel, M., Kubik-Huch, R. A., Schneider, C. W., & Stampanoni, M. 2014. Non-invasive classification of microcalcifications with phase-contrast X-ray mammography. *Nat Commun*, **5**, 3797.
- Weitkamp, T., Diaz, A., David, C., Pfeiffer, F., Stampanoni, M., Cloetens, P., & Ziegler, E. 2005. X-ray phase imaging with a grating interferometer. *Opt Express*, **13**(16), 6296–304.

- Wiernsperger, N., Nivoit, P., De Aguiar, L. G., & Bouskela, E. 2007. Microcirculation and the metabolic syndrome. *Microcirculation*, **14**(4-5), 403–38.
- Wilkins, S. W., Gureyev, T. E., Gao, D., Pogany, A., & Stevenson, A. W. 1996. Phase-contrast imaging using polychromatic hard X-rays. *Nature*, **384**(6607), 335–338.
- Withers, P. J. 2007. X-ray nanotomography. *Materials Today*, **10**(12), 26–34.
- Wolf, Emil. 2007. *Introduction to the Theory of Coherence and Polarization of Light*. Cambridge, UK: Cambridge University Press.
- Wu, F., Beard, D. A., & Frisbee, J. C. 2011. Computational analyses of intravascular tracer washout reveal altered capillary-level flow distributions in obese Zucker rats. *J Physiol*, **589**(Pt 18), 4527–43.
- Wust, R. C., Gibbings, S. L., & Degens, H. 2009. Fiber capillary supply related to fiber size and oxidative capacity in human and rat skeletal muscle. *Adv Exp Med Biol*, **645**, 75–80.
- Xie, B. H., Miao, P., Sun, Y. H., Wang, Y. T., & Yang, G. Y. 2012. Micro-Computed Tomography for Hemorrhage Disruption of Mouse Brain Vasculature. *Translational Stroke Research*, **3**, S174–S179.
- Xu, R. D., Franchi, F., Miller, B., Crane, J. A., Peterson, K. M., Psaltis, P. J., Harris, P. C., Lerman, L. O., & Rodriguez-Porcel, M. 2013. Polycystic Kidneys Have Decreased Vascular Density: A Micro-CT Study. *Microcirculation*, **20**(2), 183–189.
- Zanette, I., Weitkamp, T., Le Duc, G., & Pfeiffer, F. 2013. X-ray grating-based phase tomography for 3D histology. *Rsc Advances*, **3**(43), 19816–19819.
- Zhang, M., Peng, G., Sun, D., Xie, Y., Xia, J., Long, H., Hu, K., & Xiao, B. 2014. Synchrotron radiation imaging is a powerful tool to image brain microvasculature. *Med Phys*, **41**(3), 031907.
- Zhu, X. Y., Chade, A. R., Porcel, M. R., Bentley, M. D., Ritman, E. L., Lerman, A., & Lerman, L. O. 2004. Cortical microvascular remodeling in the stenotic kidney - Role of increased oxidative stress. *Arteriosclerosis Thrombosis and Vascular Biology*, **24**(10), 1854–1859.
- Zienkiewicz, O. C., Taylor, Robert L., Zhu, J. Z., & Zienkiewicz, O. C. 2005. *The finite element method its basis and fundamentals*. [electronic resource] : O.C. Zienkiewicz, R.L. Taylor, J.Z. Zhu. ill. (some col.) Previous ed.: 2000. "In the present edition we have decided not to pursue the course of having three contiguous volumes but rather we treat the whole work as an assembly of three separate works, each one capable of being used without the others ... The two further volumes form again separate books ... The first of these is entitled The Finite Element Method in Solid and Structural

Mechanics and the second is a text entitled The Finite Element Method in Fluid Dynamics."—Pref. Electronic reproduction. Palo Alto, Calif. : ebrary, 2009.